

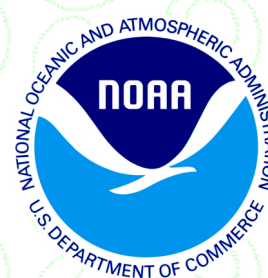
42<sup>nd</sup> NOAA Climate Diagnostics and Prediction Workshop  
Special Issue

*Norman, OK*



# Climate Prediction S&T Digest

<https://doi.org/10.7289/V5/CDPW-NWS-42ND-2018>



April 2018

**NWS Science & Technology Infusion Climate Bulletin Supplement**

## **Inside this issue:**

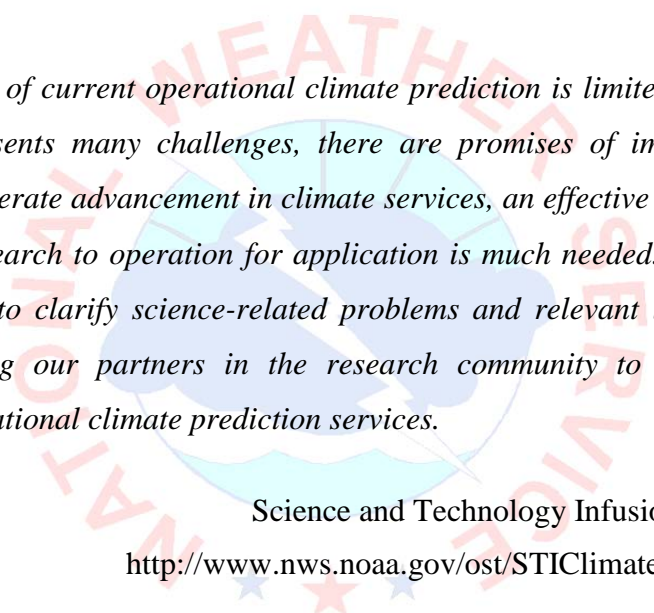
1. Recent events
2. Subseasonal to seasonal extremes
3. Climate services
4. High latitude variability
5. Drought and pluvial events
6. Subseasonal to seasonal predictability
7. Climate diagnostics, prediction, and analyses

Appendix

Workshop Photo Gallery

## **NOAA's National Weather Service**

Office of Science and Technology  
Integration  
1325 East West Highway  
Silver Spring, MD 20910  
Climate Prediction Center  
5830 University Research Court  
College Park, MD 20740

The seal of the National Weather Service is centered in the background. It features a circular design with a blue outer ring containing the words "NATIONAL WEATHER SERVICE" in white. Inside the ring is a stylized globe with a white arrow pointing upwards and to the right. The globe is set against a light blue background with white clouds.

*Although the skill of current operational climate prediction is limited and the research on the topic presents many challenges, there are promises of improvement on the horizon. To accelerate advancement in climate services, an effective mechanism of S&T infusion from research to operation for application is much needed. This bulletin has been established to clarify science-related problems and relevant issues identified in operation, inviting our partners in the research community to work together on improvement of national climate prediction services.*

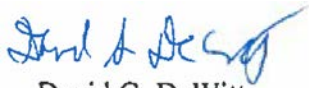
Science and Technology Infusion Climate Bulletin  
<http://www.nws.noaa.gov/ost/STIClimateBulletin/index.htm>

National Weather Service  
National Oceanic and Atmospheric Administration  
U.S. Department of Commerce

## PREFACE

It is with great pleasure that the Climate Prediction Center (CPC) and the Office of Science and Technology Integration (STI) offer you this synthesis of the 42<sup>nd</sup> Climate Diagnostics and Prediction Workshop (CDPW). The CDPW remains a must attend workshop for the climate monitoring and prediction community. As is clearly evident in this digest, considerable progress is being made both in our ability to monitor and predict climate. The purpose of this digest is to ensure that climate research advances are shared with the broader community and also transitioned into operations. This is especially important as NOAA works to enhance climate services both across the agency and with external partners. We hope you find this digest to be useful and stimulating. And please drop me a note if you have suggestions to improve the digest.

I would like to thank Dr. Jiayu Zhou of the Office of Science and Technology Integration, for developing the digest concept and seeing it through to completion. This partnership between STI and CPC is an essential element of NOAA climate services.



David G. DeWitt

Director, Climate Prediction Center  
National Centers for Environmental Prediction  
NOAA's National Weather Service





# CONTENTS

<b>OVERVIEW</b>	1
<b>1 RECENT EVENTS</b>	3
California from drought to deluge within the framework of winter stationary waves <i>Simon Wang, Emily Becker, Jinho Yoon, and Rob Gillies</i>	4
Diagnosing the atypical extreme precipitation events under weakly forced synoptic setting: The West Virginia flood (June 2016) and beyond <i>Binod Pokharel, S.-Y. Simon Wang, Yen-Heng Lin, Lin Zhao, and Robert Gillies</i>	8
An overview of the 2016-17 La Niña and return to neutral conditions <i>Michelle L'Heureux</i>	14
Relation between a Rossby wave-breaking event and enhanced convective activities in August 2016 <i>Kazuto Takemura, Yutaro Kubo, and Shuhei Maeda</i>	18
The sudden onset of the 2017 northern High Plains drought <i>Muthuvel Chelliah and David Miskus</i>	23
The Australian climate of 2016: A strong negative Indian Ocean Dipole dominates <i>Catherine Ganter, Andrew Watkins, and Felicity Gamble</i>	28
Causality and sub-seasonal predictability of the 2016 Yangtze River extreme rainfall <i>Xing Yuan, Shanshan Wang, and Zeng-Zhen Hu</i>	31
<b>2 SUBSEASONAL TO SEASONAL EXTREMES</b>	33
Skillful empirical subseasonal prediction of landfalling atmospheric river activity using the Madden-Julian Oscillation and the Quasi-biennial Oscillation <i>Bryan D. Mundhenk, Elizabeth A. Barnes, Eric D. Maloney, and Cory F. Baggett</i>	34
The impact of El Niño Southern Oscillation on winter and early spring U.S. tornado outbreaks <i>Ashton Robinson Cook, Lance M. Leslie, David B. Parsons, and Joseph T. Schaefer</i>	35
Extratropical impacts on Atlantic tropical cyclone activity via Rossby wave breaking <i>Zhuo Wang</i>	36
Developing an experimental week 2-4 severe weather outlook for the United States <i>Hui Wang, Alima Diawara, Arun Kumar, and David DeWitt</i>	38
Gulf of Mexico influence on sub-seasonal and seasonal severe thunderstorm frequency <i>Maria J. Molina, John T. Allen, and Vittorio A. Gensini</i>	42
Short-term climate extremes: Probabilistic forecasts from a multi-model ensemble <i>Emily J. Becker and Huug van den Dool</i>	46
CFSv2-based hybrid dynamical-statistical model for week 3 to 4 forecasts of Atlantic/Pacific tropical storm activity <i>Christina Finan, Hui Wang, and Jae Schemm</i>	49

<b>3 CLIMATE SERVICES</b>	53
Delivering impact-based seasonal outlooks for South Central Texas <i>Larry J. Hopper, Jr., M. Lenz, T. Dickinson, and J. W. Zeitler</i>	54
Improving impact-based seasonal outlooks for South Central Texas <i>Ty Dickinson, Larry Hopper, and Mark Lenz</i>	62
Forecasting long-term water supply using stochastic methods with trend consideration: A study on Lake Meredith in the Canadian River Basin in Texas <i>John Zhu and Nelun Fernando</i>	70
Tracking progress on NOAA's MAPP-CTB projects: Accelerating transition of research advances into improved operational capabilities <i>Jiayu Zhou and David DeWitt</i>	76
<b>4 HIGH LATITUDE VARIABILITY</b>	85
Diagnosing extremes and trends of seasonal temperatures in Alaska <i>John E. Walsh and Brian Brettschneider</i>	86
Atmosphere-sea ice coupling processes in observations and CMIP5 <i>Qinghua Ding, Michelle L'Heureux, Kirstin Harnos, Nathaniel Johnson, and Mitch Bushuk</i>	91
Searching for Arctic temperature trends and extremes from original station records <i>Taneil Uttal</i>	93
New pathway of tropical influences on Arctic subseasonal warming events in the troposphere <i>Yen-Heng Lin and S.-Y. Simon Wang</i>	97
Stratospheric influence on MJO-AO teleconnections in the subseasonal to seasonal (S2S) models <i>Laura M. Ciasto, Michelle L'Heureux, Kirstin Harnos, and Jason C. Furtado</i>	101
Prediction of seasonal Arctic sea ice extent using the NMME <i>Kirstin Harnos, Michelle L'Heureux, Qin Zhang, and Qinghua Ding</i>	105
Multi-week prediction skill assessment of Arctic sea ice variability in the CFSv2 <i>Yanyun Liu, Wanqiu Wang, and Arun Kumar</i>	110
<b>5 DROUGHT AND PLUVIAL EVENTS</b>	115
Subseasonal prediction of warm season drought in North America <i>Hailan Wang, Yehui Chang, Siegfried D. Schubert, and Randal D. Koster</i>	116
Diagnosing extreme drought characteristics across the globe <i>Ehsan Najafi, Indrani Pal, and Reza M. Khanbilvardi</i>	121
Future projections of U.S. drought and pluvial event characteristics <i>Elinor R Martin</i>	126
Long-term variation of US land surface hydrological extremes <i>Yun Fan and Huug van den Dool</i>	130

Improving CPC's handling of long-term temperature trends <i>Stephen Baxter</i>	136
Drought characteristics in two agro-climatic zones in Sub-Sahara Africa <i>Ayansina Ayanlade, Maren Radeny, John F. Morton, and Tabitha Muchaba</i>	140
Probabilistic drought forecasts based on the Northern American Multi-Model Ensemble (NMME) <i>Li Xu and Kingtse C. Mo</i>	144
<b>6 SUBSEASONAL TO SEASONAL PREDICTABILITY</b>	149
An assessment of subseasonal forecast using extended Global Ensemble Forecast System (GEFS) <i>Yuejian Zhu, Wei Li, Eric Sinsky, Hong Guan, Xiaqiong Zhou, and Dingchen Hou</i>	150
Investigating the potential for seasonal snowfall forecasts at CPC <i>Stephen Baxter</i>	154
Improving the stable surface layer in the NCEP Global Forecast System <i>Weizhong Zheng, Michael Ek, Kenneth Mitchell, Helin Wei, and Jesse Meng</i>	158
<b>7 CLIMATE DIAGNOSTICS, PREDICTION, AND ANALYSES</b>	161
Changing snowpack-streamflow relationships in the Rio Grande headwaters <i>David S. Gutzler and Shaleene B. Chavarria</i>	162
Impact of high vertical resolution in an oceanic general circulation model on sea surface temperature simulation <i>Ying Zhang, Wanqiu Wang, and Arun Kumar</i>	163
Empirical teleconnection-based standards for U.S. temperature and precipitation predictability at Weeks 3 and 4 <i>Daniel S. Harnos, Laura M. Ciasto, Nathaniel C. Johnson, Michelle L'Heureux, Cristiana Stan, and Adam D. Allgood</i>	167
Extratropical-Tropical interactions over Ethiopia <i>Endalkachew Bekele Biratu and Wassila Thiaw</i>	173
Developing an NMME probability threshold based seasonal forecast tool <i>Mingyue Chen, Arun Kumar, and David DeWitt</i>	175
Seasonal prediction of North American temperature and precipitation using the Calibration, Bridging, and Merging (CBaM) method <i>Sarah Strazzo, Dan Collins, Andrew Schepen, Q. J. Wang, Emily Becker, and Liwei Jia</i>	177
Correlation of regional sea-level variability mechanism, sub-mesoscale dynamics, climate variability and development of Sea-Level Variability Predicting Models (SLVPM) <i>Virendra Goswami</i>	181
<b>APPENDIX</b>	
Workshop photo gallery	183



## OVERVIEW

NOAA's 42<sup>nd</sup> Climate Diagnostics and Prediction Workshop was held in Norman, Oklahoma on 23-26 October 2017. The workshop was hosted by the School of Meteorology at the University of Oklahoma and was co-sponsored by the Climate Prediction Center (CPC) of the National Centers for Environmental Prediction (NCEP) and the Climate Services Branch (CSB) of the National Weather Service (NWS).

The workshop focused on five major themes, with an emphasis on climate prediction, monitoring, attribution, and diagnostics related to:

1. Recent high-impact weather, climate, and water events, such as the 2016-17 La Niña and its transition from the 2015-16 El Niño and the repeated atmospheric river events of January 2017 impacting the North Pacific;
2. Subseasonal-to-seasonal (S2S) extremes and hazards, such as severe weather;
3. Drought and pluvial events, with particular focus on the Great Plains;
4. High-latitude and Arctic variability and change, and linkages with the lower latitudes;
5. Climate prediction applications for decision support services.

The workshop featured daytime oral presentations, invited speakers, and discussions with a poster session event in one evening.

This Digest is a collection of extended summaries of the presentations contributed by participants. The workshop is continuing to grow and expected to provide a stimulus for further improvements in climate monitoring, diagnostics, prediction, applications and services.





# 1. RECENT EVENTS

42<sup>nd</sup> NOAA Annual Climate Diagnostics and  
Prediction Workshop

23-26 October 2017, Norman, Oklahoma

## California from Drought to Deluge Within the Framework of Winter Stationary Waves

S.-Y. Simon Wang<sup>1,2</sup>, Emily Becker<sup>3</sup>, Jin-Ho Yoon<sup>4</sup>, and Robert Gillies<sup>1,2</sup>

<sup>1</sup>*Utah Climate Center, Utah State University, Logan, UT*

<sup>2</sup>*Department of Plants, Soils and Climate, Utah State University, Logan, UT*

<sup>3</sup>*NOAA Climate Prediction Center, College Park, MD*

<sup>4</sup>*School of Earth Sciences and Environmental Engineering,  
Gwangju Institute of Science and Technology, Gwangju, South Korea*

### 1. Introduction

The multiyear drought in California (2012-2016) was broken by a dramatic reversal in the form of extreme precipitation and flooding in early 2017. The widespread floods led to the declaration of yet another State of Emergency, this time from a very different perspective vis-a-vis the 2014 drought. Many studies that were motivated by the post-2014 drought have focused on the persistent high-pressure ridge stationed off the West Coast during the height of the drought (GRL-AGU 2015; Wang *et al.* 2014; Swain *et al.* 2014). In the winter of 2016-2017, an enhanced low-pressure trough appeared in the same location, initiating and directing sequential atmospheric river events toward California and causing high precipitation. We would like to underline that the dramatic appearance of this enhanced trough in 2016-2017 is “the other side of the coin”; this flip side was implied and even projected in some previous studies (Wang *et al.* 2014; Singh *et al.* 2016; Yoon *et al.* 2015a) analyzing the drought-producing ridge.

### 2. Diagnostics

One prominent feature associated with the drought winters of 2013-2015 was the extreme warm-West/cool-East surface temperature anomaly pattern in North America, accompanied by a pronounced “ridge-trough” circulation pattern in the upper atmosphere. Collectively, this temperature-wave pattern is referred to as the North American winter “dipole” (Singh *et al.* 2016; Yoon *et al.* 2015a; Wang *et al.* 2015; Swain *et al.* 2016), which coincides with the winter-mean stationary waves (indicated in Figure 1 by contours and “x/+”). The winter stationary waves establish the climatologically warmer west and colder east forming the surface temperature division of North America. Any perturbation of the climatological ridge in the west can excite downwind amplification of the eastern trough through Rossby wave dispersion and vice versa, so the two are very much anticorrelated (Wang *et al.* 2014). Consequently, an amplification of the stationary wave leads to enhancement of such differences in the atmospheric circulation and surface temperature, while a weakened stationary wave reverses it.

In early 2017, the cool-West/warm-East surface temperature pattern did indeed suggest a reversal of the dipole from that of the 2013-2015 winters. By plotting the 250-hPa geopotential height anomalies ( $\Delta Z$ ) during November 2016-January 2017, one can observe an opposite-phase wave pattern (Figure 1a), as compared to that for the 2013-2014 drought winter (Figure 1b). Spatial correlation analysis of  $\Delta Z$  computed between the two winters yielded a significant value of -0.86, supporting their reverse correspondence. Figure 1c displays the dipole index constructed by the  $\Delta Z$  difference between the ridge and trough centers, following previous studies (Wang *et al.* 2014; Singh *et al.* 2016). The 2016-2017 winter features a significantly low value, in contrast to the record high value in 2013-2014, suggesting that the 2016-2017 winter circulation leading to the California deluge resembles a reversal of the 2013-2015 situation. Though not shown here, the detrended sea surface temperature anomalies (SSTA) in the 2013-2014 and 2016-2017 winters are also

opposite, with a significant spatial correlation of  $-0.7$  in the North Pacific Ocean. More importantly, the 7-year running variance of the dipole index (Figure 1c light blue line) shows a pronounced increase since the beginning of the 21st century, and this dipole amplification is projected to continue (Yoon *et al.* 2015; Wang *et al.* 2015).

To further illustrate the dipole's association with winter precipitation anomalies in North America, we constructed the correlation maps of November–January (NDJ) precipitation with the dipole index for two periods (a) before and (b) after 1985, in comparison with that of three other indices: El Niño/Southern Oscillation (ENSO, *i.e.* the Nino3.4 SSTA), the North Pacific Pattern (NP), and the Pacific Decadal Oscillation (PDO) from <https://www.esrl.noaa.gov/psd/data/climateindices/list/>. As shown in Figure 2, the dipole's correlation with precipitation has been significant over much of the West Coast ( $p < 0.01$ ) encompassing northern and central California, and consistently so throughout the different periods. By comparison, the precipitation correlation with ENSO is much lower and highly fluctuating, averaging to only half of that of the dipole ( $0.32$ ). Precipitation correlations with NP and PDO reveal weak and unstable association in California (Figure 2). Therefore, given the dipole's persistently high correlation with the California precipitation, its observed and projected amplification implies an increased impact on California's water cycle extremes, which could translate to severe drought and excessive deluge.

There is always a component of internal variability in the atmosphere that underlies the persistence of the North Pacific circulation anomalies and unique regional processes that increase event extremeness (*i.e.* without external forcing from either SSTA or of anthropogenic origin). However, a large body of research (GRL-AGU 2015) has shown evidence of remote teleconnections to North Pacific circulation stagnation through pronounced atmospheric Rossby waves of tropical origin. Warming in the West Pacific (Funk *et al.* 2014), North Pacific (Hartmann 2015), the ENSO region (Stevenson *et al.* 2012), and even the Indian Ocean (McDonald *et al.* 2016) can amplify the drought-producing ridge with differing patterns and temporal characteristics (Funk *et al.* 2014). Coupled model studies (Yoon *et al.* 2015a) have connected the strengthening of the relationship between the dipole and California's precipitation to relevant climate

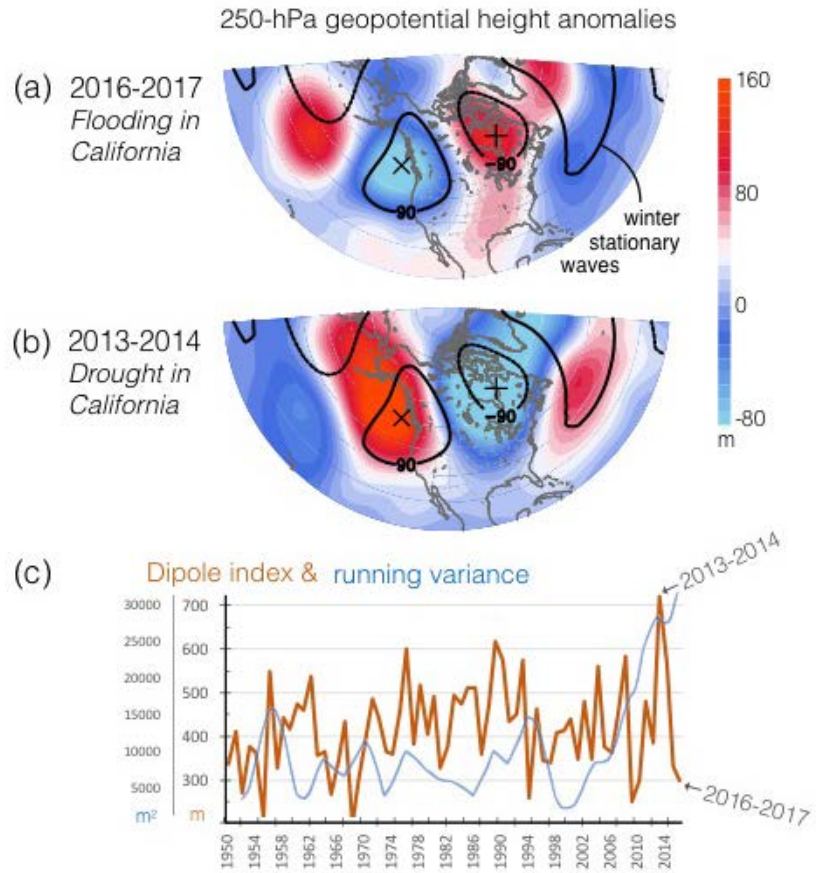


**Fig. 1** November–January climatological geopotential height at 250 hPa (contour, with the zonal mean removed) depicting the atmospheric stationary waves, overlaid with the anomalies (shading) during (a) the flooding winter of 2016–2017 and (b) the drought winter of 2013–2014. The dipole location is indicated by  $\times$  and  $+$  symbols over North America. Notice the geographical coincidence of each year's circulation anomalies with the dipole location and the apparent opposite patterns between the two winters. (c) The dipole index from 1950 to 2017 (orange line) along with its 7-year running variance (light blue). Data source is the NCAR/NCEP Global Reanalysis.

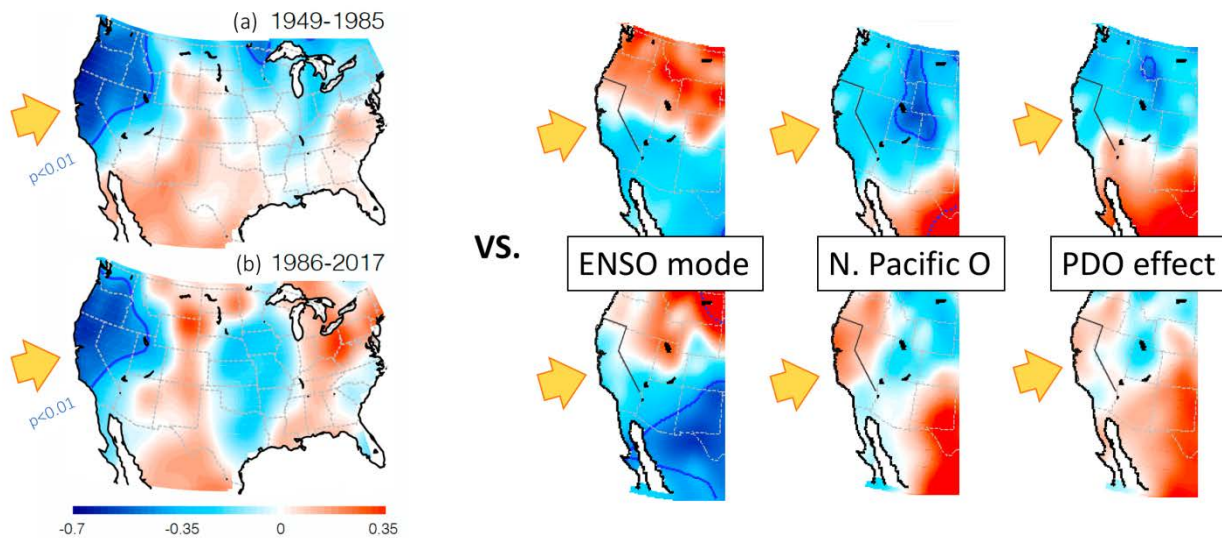


**Fig. 2** Correlation maps of the November-January precipitation correlated with (from left to right) the dipole, ENSO, NP, and PDO indices during (a) an earlier period of 1949-1985 and (b) the latter period of 1986-2017. The thick contours outline significant values at the 99% confidence interval. Notice the consistently high correlations over the West Coast with the dipole including California. Precipitation data: PRECipitation REConstruction over Land (PREC/L).

oscillations with resulting projections of an increase of both drought and deluge. Other factors such as midlatitude internal atmospheric dynamics could power drought conditions regardless of ENSO conditions (Teng and Branstator 2016). Furthermore, the extent to which the warming Arctic interacts with the mid-latitude circulation and its influence on the dipole amplification has also entered the debate (Kim *et al.* 2014) suggesting that future sea ice loss may drive large changes in the regional circulation over the North Pacific (Blackport and Kushner 2017). The alternation of extreme wet/dry seasons every few years prompts the growth of vegetation, which increases “fuel” for wildfires and further increase fire danger days (Yoon *et al.* 2015b).

### 3. Future direction

Despite the debate concerning the causes of the drought-producing ridge in the Northeast Pacific Ocean, the various hypotheses about natural variability did suggest one thing in common: the flip-flop nature of the anomalous circulation. In other words, the amplified ridge in one winter can turn into a deepened trough in another and this tendency appears to have intensified (Figure 1c). Motivated by these recent studies, we suggest that future exploration of extreme climate anomalies in California should focus on attributing the linkages between North American winter atmospheric conditions and teleconnections under a projected warming climate. To improve the predictability of future climate extremes, the community can benefit from having coordinated numerical experiments with multiple models, with region-specific analyses on quantifying the relative importance of the internal/external factors. A cohesive evaluation and assessment should, in theory, result in more well-informed mitigation plans and water management to offset the future hazards and risks that are implied in a warming climate.

(This summary has been adopted from Wang *et al.* 2017.)

### References

- Blackport, R., and P. J. Kushner, 2017: Isolating the atmospheric circulation response to Arctic sea ice loss in the coupled climate system. *J. Climate*, **30**, 2163-2185.
- Funk, C., A. Hoell, and D. Stone, 2014: Examining the contribution of the observed global warming trend to the California droughts of 2012/13 and 2013/14 [in "Explaining Extremes of 2013 from a Climate Perspective"]. *Bull. Amer. Meteor. Soc.*, **95**, S11-S15.

- GRL-AGU, 2015: The ongoing California Drought of 2012-2015: A testbed for understanding regional climate extremes in a warming world.  
[http://agupubs.onlinelibrary.wiley.com/agu/issue/10.1002/\(ISSN\)1944-8007.CALDROUGHT1/](http://agupubs.onlinelibrary.wiley.com/agu/issue/10.1002/(ISSN)1944-8007.CALDROUGHT1/).
- Hartmann, D. L., 2015: Pacific sea surface temperature and the winter of 2014. *Geophys. Res. Lett.*, **42**, 1894-1902. doi:10.1002/2015GL063083.
- Kim, B.-M., and Co-authors, 2014: Weakening of the stratospheric polar vortex by Arctic sea-ice loss. *Nat Commun.*, **5**, doi:10.1038/ncomms5646.
- MacDonald, G. M., and Co-authors, 2016: Prolonged California aridity linked to climate warming and Pacific sea surface temperature. *Sci. Rep.*, **6**, 33325, doi:10.1038/srep33325.
- Singh, D., and Co-authors, 2016: Recent amplification of the North American winter temperature dipole. *J. Geophys. Res.: Atmos.*, **121**, 9911-9928. doi:10.1002/2016JD025116.
- Stevenson, S., and Co-authors, 2012: Will there be a significant change to El Niño in the twenty-first century? *J. Climate*, **25**, 2129-2145.
- Swain, D. L. , and Co-authors, 2014: The extraordinary California drought of 2013/2014: Character, context, and the role of climate change [in "Explaining Extremes of 2013 from a Climate Perspective"]. *Bull. Amer. Meteor. Soc.*, **95**, S3-S7.
- Swain, D. L., D. E. Horton, D. Singh, and N. S. Diffenbaugh, 2016: Trends in atmospheric patterns conducive to seasonal precipitation and temperature extremes in California. *Sci. Adv.*, **2**, e1501344.
- Teng, H., and G. Branstator, 2016: Causes of extreme ridges that induce California droughts. *J. Climate*, **30**, 1477-1492.
- Wang, S.-Y., J.-H. Yoon, E. Becker, and R. Gillies, 2017: California from drought to deluge. *Nat. Climate Change*, **7**, 465-468.
- Wang, S.-Y., L. Hipps, R. R. Gillies, and J.-H. Yoon, 2014: Probable causes of the abnormal ridge accompanying the 2013-2014 California drought: ENSO precursor and anthropogenic warming footprint. *Geophys. Res. Lett.*, **41**, 3220-3226. doi:10.1002/2014GL059748.
- Wang, S.-Y., W.-R. Huang, and J.-H. Yoon, 2015: The North American winter 'dipole' and extremes activity: A CMIP5 assessment. *Atmos. Sci. Lett.*, **16**, 338-345.
- Yoon, J.-H., and Co-authors, 2015a: Increasing water cycle extremes in California and in relation to ENSO cycle under global warming. *Nat. commun.*, **6**, doi: 10.1038/ncomms9657.
- Yoon, J.-H., and Co-authors, 2015b: Extreme fire season in California: A glimpse into the future? [in "Explaining Extremes of 2014 from a Climate Perspective"]. *Bull. Am. Meteorol. Soc.*, **96**, S5-S9.

## Diagnosing the Atypical Extreme Precipitation Events Under Weakly Forced Synoptic Setting: The West Virginia Flood (June 2016) and Beyond

Binod Pokharel<sup>1,2</sup>, S.-Y. Simon Wang<sup>1,2</sup>, Yen-Heng Lin<sup>2</sup>, Lin Zhao<sup>3</sup>, and Robert Gillies<sup>1,2</sup>

<sup>1</sup>*Utah Climate Center, Utah State University, Logan, UT, USA*

<sup>2</sup>*Department of Plants, Soils and Climate, Utah State University, Logan, UT*

<sup>3</sup>*Northwest Institute of Eco-Environment and Resources, Chinese Academy of Sciences, Lanzhou, China*

### 1. Introduction

June 2016 saw concurrent extreme climate/weather events in the U.S., with scorching heat (Liberto, 2016) in the Southwest associated with an upper-atmospheric ridge and record flooding in West Virginia. The ridge condition on 23 June induced a series of mid-tropospheric short waves that propagated across the Ohio valley, producing the “1-in-1000-year” precipitation event in West Virginia with 10 inches of 24-h rainfall (Grote and Dyer 2017; Corrigan *et al.* 2017; Perfater *et al.* 2017). The extreme precipitation in West Virginia was not associated with a deep synoptic trough, but occurred during the prevailing mid-level northwesterly flow (NWF) setting (Fig. 1a). The ridge type weather pattern that is commonly considered as the warm and pleasant weather condition, have occasionally created extreme weather including the 2012 DC derechos (Fig. 1c). The predominant ridge and NWF setting are related to summer outbreaks of thunderstorms (Johns 1982) and convectively induced windstorms or derechos (Johns and Hirt 1987; Bentley and More 1998). However, most of the climate projection studies overlooked the NWF severe weather outbreaks as they focused on strong low-pressure systems which are sustained by large-scale baroclinic forcing (*e.g.*, Weaver *et al.* 2016; Feng *et al.* 2016; Feng *et al.* 2012; Jiang *et al.* 2006; Berg *et al.* 2015). The aforementioned extreme events occurring under the “weakly forced” synoptic setting, *i.e.* the continental-scale ridge with the NWF or the so-called warm season pattern (Johns 1982, 1993), prompted us to question whether and how such storms may have changed.

This study is targeted at diagnosing the climatology and variation of weak sub-synoptic-scale features in the central U.S. associated with the propagating mesoscale convective systems (MCSs) during early to mid-summer. The majority of these sub-synoptic features embedded in the NWF are generated on the east of the Rocky Mountains and propagate across the northern plains in the form of serial short-wave perturbations, referred to as the mid-tropospheric perturbations (MPs; Wang *et al.* 2009, 2011a, b). MPs provide the forcing for the progressive MCSs when they travel a long distance creating extreme weather events (Wang *et al.* 2011a, b), but the climate variation linked to their genesis and steering mechanism has not been explored. This study presents a method to track MPs by using reanalysis data and discusses the variation and trend of MPs.

### 2. Data sources and methodology

We use the 3-hourly North American Regional Reanalysis (NARR, Mesinger *et al.* 2006) data as the main dataset to calculate the MPs. We also utilize the NCEP-NARR reanalysis R1 data and the Storm Prediction Center's Warning storm reports compiled from the Coordination Meteorologist (WCM) website (<http://www.spc.noaa.gov/wcm/>). The storm report has been used to construct the NWF outbreak frequency (John 1982). However, storm observations originate from sighting and are highly dependent of population; this presents a data quality problem due to human and population biases (Weiss *et al.* 2002; Gallus *et al.* 2008). During the course of 38 years (1979-2016), the perturbations are calculated based on the midlevel winds and relative vorticity at 600-hPa for the June, July and August. Because the average life cycle of MPs is 48 hours (Wang *et al.* 2011a), the vorticity field is filtered using both low- and high-pass filters in order to retain the MPs characteristics. To exclude the synoptic-scale trough, the filtered vorticity is masked out by



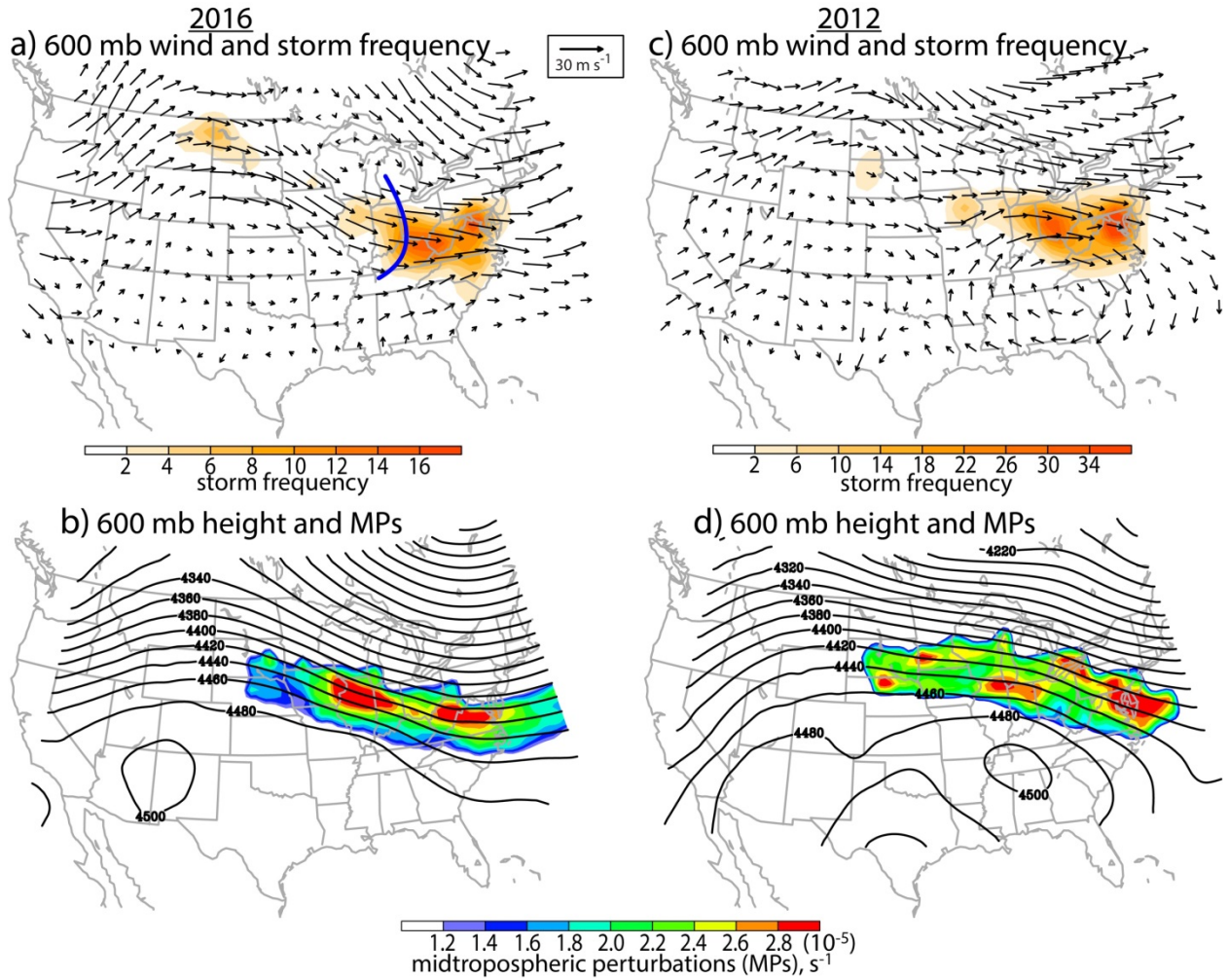


**Fig. 1** Synoptic conditions storm frequency and MPs during two extreme weather events of June 2016 (left panel) and June 2012 (right panel). a) and c) are the 600-hPa wind (vectors) with storm (wind, hail and tornado) frequency (shading) from storm reports. Blue curve in a) shows the shortwave trough. b) and d) are the 600-hPa height (contours) with MPs (shading). The MPs (storm frequency) and 600-hPa height, are averaged (added) from the 21–24 June and 28–30 June for 2016 and 2012, respectively. The wind vectors in a) and c) are taken from the middle of the extreme events at 18Z on 23 June 2016 and at 00Z on 30 June 2012, respectively.

applying the circulation criteria; this excludes the region of negative stream function. Moisture is an important precursor for the MP-related convective activity and, therefore, further moisture criteria is applied in which vertically integrated precipitable water should be larger than certain thresholds (we use 24 mm in this study). Finally, the root-mean-square of vorticity (RMSVORT) is averaged weekly from June to August. The storm report data are used for verification by mapping onto a  $1^\circ \times 1^\circ$  grid mesh and averaging similarly with RMSVORT.

### 3. MPs events and climatology

#### 3.1 Case analysis

The 2016 West Virginia flood and the 2012 Mid-Atlantic derecho, both occurring in late June, serve to exemplify the extreme events related to NWF outbreaks. In both events, the mid- to upper-level high pressure was centered over the southcentral U.S. spreading prevailing NWF from the northern plains to the mid-Atlantic regions. The 2012 NWF produced several damaging hail and wind events throughout the Midwest

and Mid-Atlantic regions in 2012 (Fig. 1c) while 2016 system produced 8-10 inches of precipitation in West Virginia within 12-24 hours (NOAA NCEI, 2016) in addition to the wind and hail damage (Fig. 1a).

The noticeable difference with the 2016 case was the presence of a mid-level shortwave trough on the 23<sup>rd</sup> of June (Fig. 1a). Such a shortwave feature was not present in the June 2012 case when the Derecho propagated with the MP (Fig. 1c). We note both cases show a good agreement between the storm track (Fig. 1a and c) and propagated MPs (Fig. 1b and d). More detailed comparison between the two cases is given in Box 1.

### 3.2 Climatology and variability of MPs

The 38-year climatology of RMSVORT shows similar pattern with the 10-year, manually tracked MP climatology by Wang *et al.* (2011a, b). The spatial distribution of the MP climatology developed here is also in good agreement with the derecho frequency in mid-summer (Guastini and Bosart 2016; John and Hirt 1987). The MP frequency peaks in the three-week period of 17 June to 7 July, which is adopted to examine the interannual variability using the empirical orthogonal function (EOF). As shown in Fig. 2, the first and fourth EOFs reveal the MP spatial pattern that is most relevant to 2016's West Virginia case, including the Upper Midwest track and the increased frequency in the East Coast. EOF1 reveals the main track of MPs (Fig. 2a) while its corresponding principal component (PC1, not shown) correlates well with the storm frequency (Fig. 2b). EOF4 (Fig. 2e) reveals the east-west fluctuation of MPs and its PC correlates with

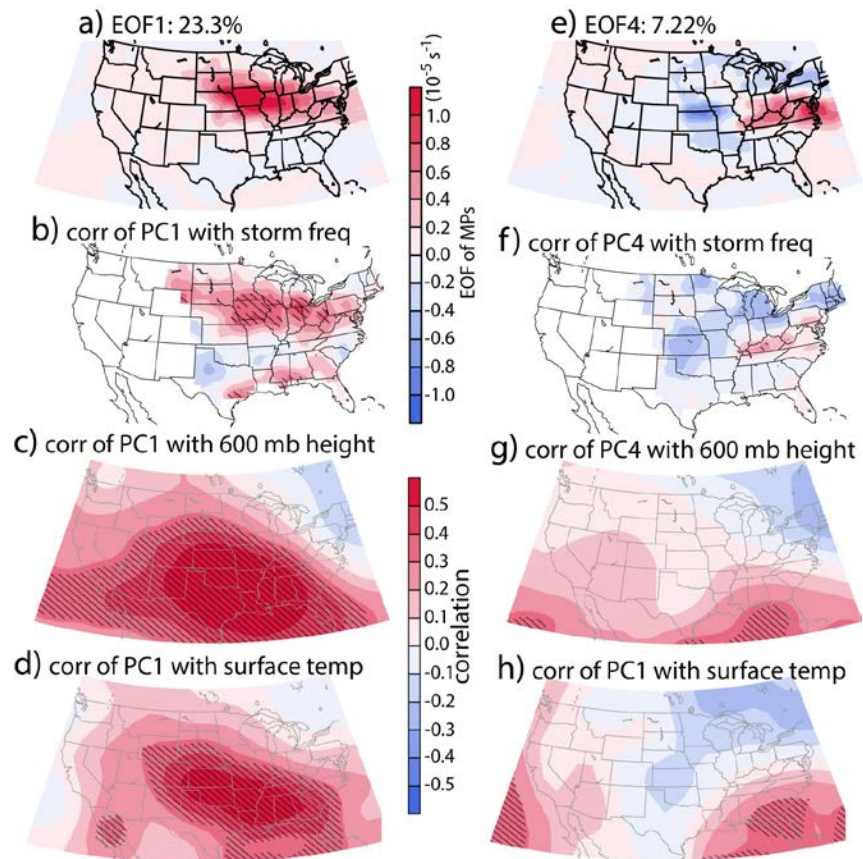


**Fig. 2** Interannual variation of MPs a) first EOF and e) fourth EOF from 17June to 7July for 38 years (1979-2016). Temporal correlation of PC1 and PC4 with June-July average of storm frequency ((b) and (f)), 600-hPa height ((c) and (g)), and surface temperature ((d) and (h)), respectively. Hatched areas indicate significant values with  $p < 0.05$ .

#### Box 1

##### COMPARISON OF TWO EXTREME EVENTS BETWEEN JUNE 2012 AND 2016

Even though we applied a moisture criteria in our MPs calculation, a continuous source of moisture plays an important role to create the extreme precipitation. During the 2016 case, the low-level jet and mid-level shortwave provided continuous moisture from the Gulf of Mexico (GoM), helping to create deep convection (figure not shown). The hydrometeor mixing ratio was significant during the 2016 event – as high as 100-hPa – indicating the extreme magnitude of the continuous source of moisture and mid-level shortwave moisture pooling. However, the 2012 derecho case shows slightly different flow – mainly at low levels – reducing the moisture supply from the GoM. Another noticeable difference between these two cases is that the location of the high pressure center was located westward during the 2016 case compared to a more eastward placement during the 2012 event.

the eastward shift of extreme weather (Fig. 2f), similar to the one over West Virginia in 2016 which has the largest values of PC1 and PC4. Though not shown, we note that the north-south shift of MPs is reflected in EOF2 and it resembles the 2012 storm track with a high PC2 value.

Since EOF1 depicts the major MP track and mimics the NWF outbreaks (Fig. 2b), we analyzed the anomalous circulations associated with PC1. The correlation map of 600-hPa geopotential height with PC1 (Fig. 2c) shows a predominant anticyclone centered in the southern U.S. providing enhanced NWF conditions. Surface air temperature in the southern U.S. increases correspondingly during high PC1 (Fig. d). By comparison, PC4 is positively correlated only with increased meridional gradient of the geopotential height over the mid-Atlantic region (Fig. 2g) and this corresponds with the increased storm frequency and warmer air in the southeast US (Fig. 1h). We further diagnosed the correlation of PC1 with GoM SST for different months and observed that the Gulf SST seems to respond during the early summer months (not shown). We also observe an increasing trend in the MP frequency as well as PC1 (Fig. 3). The increasing trend of MPs is even larger after 1990 (not shown), suggesting a post-1990 increase in MPs and arguably in NWF outbreaks.

#### 4. Discussion

Climate models have a difficulty producing weakly forced storms and resultant extreme precipitation and this drawback may affect how the models project future climate extremes. To understand the extent to which devastating floods like the one in West Virginia will occur relies on how well climate models depict the NWF synoptic settings and embedded MPs. The present objective analysis for the MP climatology is intended to help develop metrics that will evaluate model projections of the MP track. Future work will also include the diagnosis of larger-scale teleconnections associated with the circulation setting relevant to the MP track and frequency (*e.g.*, Fig. 2). Preliminary analysis not included here has indicated that ENSO does not correlate with the MP frequency, but the Pacific-North American (PNA) and the Arctic Multidecadal Oscillation (AMO) do. During the positive phase of AMO and PNA, the MP frequency over the Midwest and Mid-Atlantic region seems to enhance.

#### References

- Bentley, M. L., and T. L. Mote, 1998: A climatology of derecho-producing mesoscale convective systems in the central and eastern United States, 1986-95. Part I: Temporal and spatial distribution. *Bull. Amer. Meteor. Soc.*, **79**, 2527-2540.

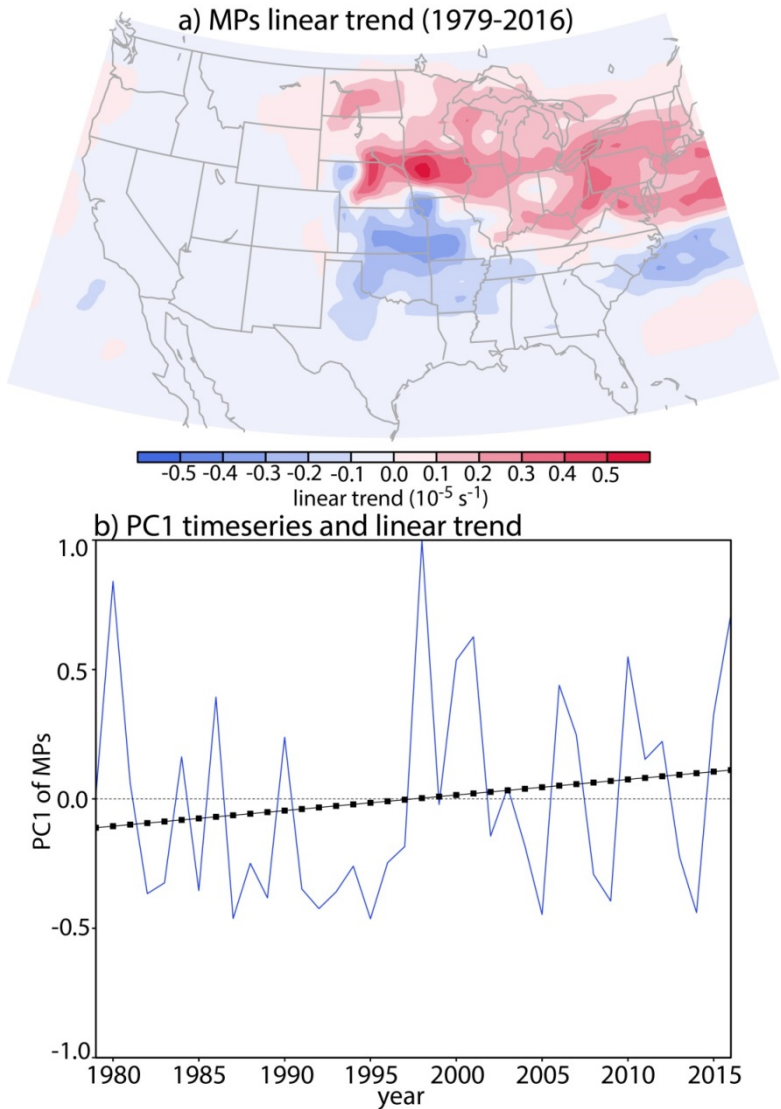


**Fig. 3** (a) Linear trend (slope multiplied by number of years which is 38 years here) of MPs and (b) timeseries of PC1 (blue line) with linear trend line (black line) from 1979 to 2016.



- Berg, L. K., L. D. Riihimaki, Y. Quan, H. Yan, and M. Huang, 2015: The low-level jet over the southern Great Plains determined from observations and reanalysis and its impact on moisture transport. *J. Climate*, **28**, 6682-6706.
- Corrigan, P., S. J. Keighton, R. Stonefield, and R. H. Grumm, 2017: The West Virginia historic and devastating floods of 23 June 2016: Summary of impacts and National Weather Service decision support services. *97<sup>th</sup> AMS Annual Meeting*, Seattle, WA, 22-27 Jan 2017. <https://ams.confex.com/ams/97Annual/webprogram/Paper316125.html>
- Liberto, T. D., 2016: Scorching heat breaks the Southwest in mid-June 2016. *NOAA Climate.gov*, <https://www.climate.gov/news-features/event-tracker/scorching-heat-bakes-southwest-mid-june-2016>.
- Feng, Z., L. R. Leung, S. Hagos, R. A. Houze, C. D. Burleyson, and K. Balaguru, 2016: More frequent intense and long-lived storms dominate the springtime trend in central US rainfall, *Nat. Commun.*, **7**:13429, DOI: 10.1038/ncomms13429.
- Feng, Z., X. Dong, B. Xi, S. A. McFarlane, A. Kennedy, B. Lin, and P. Mannis, 2012: Life cycle of midlatitude deep convective systems in a Lagrangian framework, *J. Geophys. Res.*, **117**, D23201, doi:10.1029/2012JD018362.
- Gallus W. A., N. A. Snook, and E. V. Johnson, 2008: Spring and summer severe weather reports over the Midwest as a function of convective mode: a preliminary study. *Wea. Forecast*, **23**, 101–113.
- Grote, T., and J. L. Dyer, 2017: Preliminary assessment of the hydrometeorology and hydrology of the June 2016 Greenbrier River flooding, West Virginia. *97<sup>th</sup> AMS Annual Meeting*, Seattle, WA, 22-27 Jan 2017. <https://ams.confex.com/ams/97Annual/webprogram/Paper310934.html>
- Guastini, C. T., and L. F. Bosart, 2016: Analysis of a progressive derecho climatology and associated formation environments. *Mon. Wea. Rev.*, **144**, 1363-1382.
- Jiang, X., N.-C. Lau, and S. A. Klein, 2006: Role of eastward propagating convection systems in the diurnal cycle and seasonal mean of summertime rainfall over the U.S. Great Plains. *Geophys. Res. Lett.*, **33**, L19809, doi:10.1029/2006GL027022.
- Johns R. H., 1982: A synoptic climatology of northwest flow severe weather outbreaks. Part I: nature and significance. *Mon. Wea. Rev.*, **110**, 1653–1663.
- Johns R. H., 1993: Meteorological conditions associated with bow echo development in convective storms. *Wea. Forecast*, **8**, 294–299.
- Johns R. H., and W. D. Hirt, 1987: Derechos: widespread convectively induced windstorms. *Wea. Forecast*, **2**, 32–49.
- Mesinger F., and Co-authors, 2006: North American regional reanalysis. *Bull. Am. Meteorol. Soc.*, **87**, 343–360.
- NOAA National Centers for Environmental Information (NCEI), 2016: State of the climate: Synoptic discussion -June 2016, <https://www.ncdc.noaa.gov/sotc/synoptic/201606>.
- Perfater, S., S. M. Martinaitis, B. Albright, J. J. Gourley, M. J. Bonder, B. Cosgrove, M. Klein, Z. L. Flaming, T.C. Meyer, R. Clark III, and D.R. Novak, 2017: Experimental results and joint testbed collaboration of the West Virginia flood event of June 23-24, 2016. *97<sup>th</sup> AMS Annual Meeting*, Seattle, WA, 22-27 Jan 2017. <https://ams.confex.com/ams/97Annual/webprogram/Paper310829.html>
- Wang S.-Y., Chen T. C. and Taylor S. E., 2009: Evaluations of NAM forecasts on midtropospheric perturbation-induced convective storms over the U.S. Northern Plains. *Wea. Forecast*, **24**, 1309–1333. doi:10.1175/2009WAF2222185.1
- Wang, S.-Y., T.-C. Chen, and J. Correia, 2011a: Climatology of summer midtropospheric perturbations in the U.S. northern plains. Part I: influence on northwest flow severe weather outbreaks. *Clim. Dyn.*, **36**, 793–810.
- Wang, S.-Y., T.-C. Chen, and E. S. Takle, 2011b: Climatology of summer midtropospheric perturbations in the U.S. northern plains. Part II: large-scale effects of the Rocky Mountains on genesis. *Clim. Dyn.*, **36**, 1221-1237.

- 
- Weaver, S. J., S. Baxter, and K. Harnos, 2016: Regional changes in the interannual variability of U.S. warm season precipitation. *J. Climate*, **29**, 5157-5173.
- Weiss S. J., J. A. Hart, and P. R. Janish, 2002: An examination of severe thunderstorm wind report climatology: 1970–1999. *21<sup>st</sup> conference on severe local storms*, San Antonio, TX, 14 August 2002.  
[https://ams.confex.com/ams/SLS\\_WAF\\_NWP/techprogram/paper\\_47494.htm](https://ams.confex.com/ams/SLS_WAF_NWP/techprogram/paper_47494.htm)

## An Overview of the 2016-17 La Niña and Return to Neutral Conditions

Michelle L'Heureux

<sup>1</sup>Climate Prediction Center, NOAA/NWS/NCEP, College Park, MD

### 1. ENSO evolution and forecasts during 2016-17

A very brief and weak La Niña followed the major El Niño of 2015-16. NOAA Climate Prediction Center (CPC) issued its first La Niña Watch in April 2016, during the decay of the major El Niño of 2015-16 (L'Heureux *et al.*, 2017). At that time, most model forecasts were strongly anticipating a transition to a moderate La Niña by Northern Hemisphere summer 2016 (Niño-3.4 index values between  $-1^{\circ}\text{C}$  and  $-1.4^{\circ}\text{C}$ ). The grey lines in Fig. 1 show that ensemble mean forecasts of Niño-3.4 from the North American Multi-Model Ensemble (NMME), initialized in early-mid 2016, were much colder than what actually occurred (black line). That most ensemble members from the NMME were too cold was reflected in the very negative Log Skill Scores (LSS) for almost all forecast leads for the target month of July 2016 (Fig. 2- top and middle panels).

By August 2016, sea surface temperature (SST) anomalies in the Niño-3.4 region ( $5^{\circ}\text{S}$ - $5^{\circ}\text{N}$ ,  $120^{\circ}\text{W}$ - $170^{\circ}\text{W}$ ) decreased to near  $-0.5^{\circ}\text{C}$ . By then the models were forecasting borderline La Niña or ENSO-neutral conditions for the upcoming fall and winter, so there was much uncertainty whether the period would qualify as a historical La Niña episode as classified by NOAA (requiring 5 consecutive 3-month overlapping seasons at or less than  $-0.5^{\circ}\text{C}$  in the Niño-3.4 index). As a result, a La Niña Advisory was not issued until early November 2016 when it became more certain that the event would last long enough to meet NOAA's criteria.

Not only did the NMME predict too cold conditions in Niño-3.4 during the summer of 2016, but for runs made in mid-to-late 2016, the majority of model members were also indicating too cold conditions for early 2017. Figure 2 (bottom panel) shows that NMME forecasts of Niño-3.4 had a negative bias for April 2017, particularly at longer forecast leads. While the individual forecast members are not displayed for other target months, this bias occurred at longer leads for targets during January-March 2017 as well (Fig. 2- top panel). Thus, the majority of models were anticipating La Niña to last longer than it did, abruptly ending by January 2017 and returning to ENSO-neutral.

In retrospect, the 2016-17 La Niña ended up as one of the weakest and shortest episodes in the ERSSTv5 data (Huang *et al.*, 2017) extending back to 1950, lasting exactly five consecutive seasons from July-

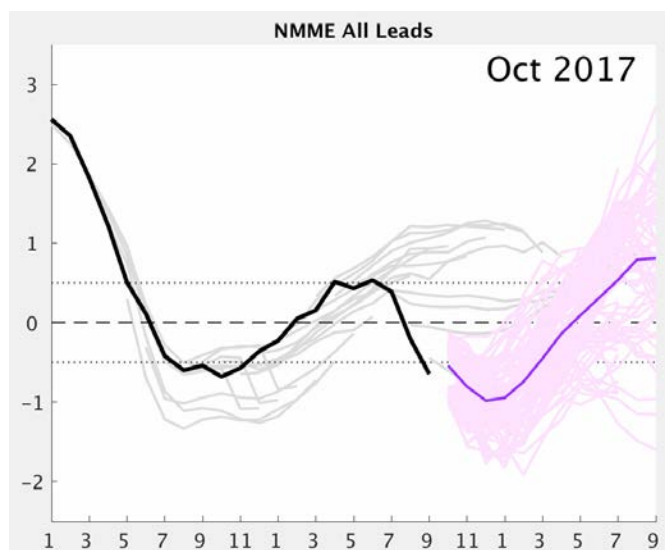


**Fig. 1** Observed monthly Niño-3.4 index values (black line) from daily OISST (Reynolds *et al.* 2007) and once monthly forecasts of Niño-3.4 from the North American Multi-Model (NMME) from January 2016 through October 2017 (grey lines showing ensemble means). The pink and purple lines show the NMME forecast ensemble initialized in October 2017. The x-axis shows the month and the y-axis shows the Niño-3.4 index value. Departures are formed by removing monthly means during 1982-2010.



September (JAS) 2016 – November-January (NDJ) 2016-17 (with a maximum amplitude of  $-0.7^{\circ}\text{C}$ ). Notably, the La Niña of 2016-17 was so marginal that the Bureau of Meteorology in Australia never reached its own La Niña thresholds, meaning it is debatable whether the 2016-17 La Niña was robust enough to be considered a full-blown event.

## 2. Global temperature, precipitation, and circulation anomalies during NDJ 2016-17 and their relation with ENSO

CPC defines the Northern Hemisphere winter season as the December-January (DJF) average, but because La Niña officially only lasted through NDJ 2016-17 (see previous section), the analysis in this section is only presented for NDJ. The left column of Fig. 3 shows observed climate anomalies during NDJ 2016-17 and the right column shows the regression of these climate anomalies onto the Niño-3.4 index, which helps to diagnose the anomalies linearly associated with ENSO (note: there are also non-linear anomalies, but these are not presented herein). The regression patterns presented in the right column are multiplied by a factor and multiplied by minus one, so that the La Niña anomalies can be seen more clearly and compared with the observations. In the top right corner of each row, the spatial correlation (with the spatial mean removed) between the observations and the ENSO regression is displayed for 500-hPa geopotential height and winds (top row), surface temperature (middle row), and precipitation (bottom row).

Among all the variables, the largest spatial correlation ( $r=-0.42$ ) or match between the observed anomalies and the expected linear ENSO pattern occurs for precipitation (Fig. 3, bottom row). Corresponding to La Niña, NDJ 2016-17 precipitation was enhanced over the Maritime Continent and Southeast Asia, northwestern Australia, over parts of southern Africa (excluding the southern tip), and over most of northern South America. Reduced precipitation occurred over parts of southern Brazil and northern Argentina. While the La Niña pattern emerged over parts of the globe, over the contiguous southern United States, the expected drier-than-average pattern did not materialize (with the exception of Florida) and instead the pattern was largely average or wetter-than-average.

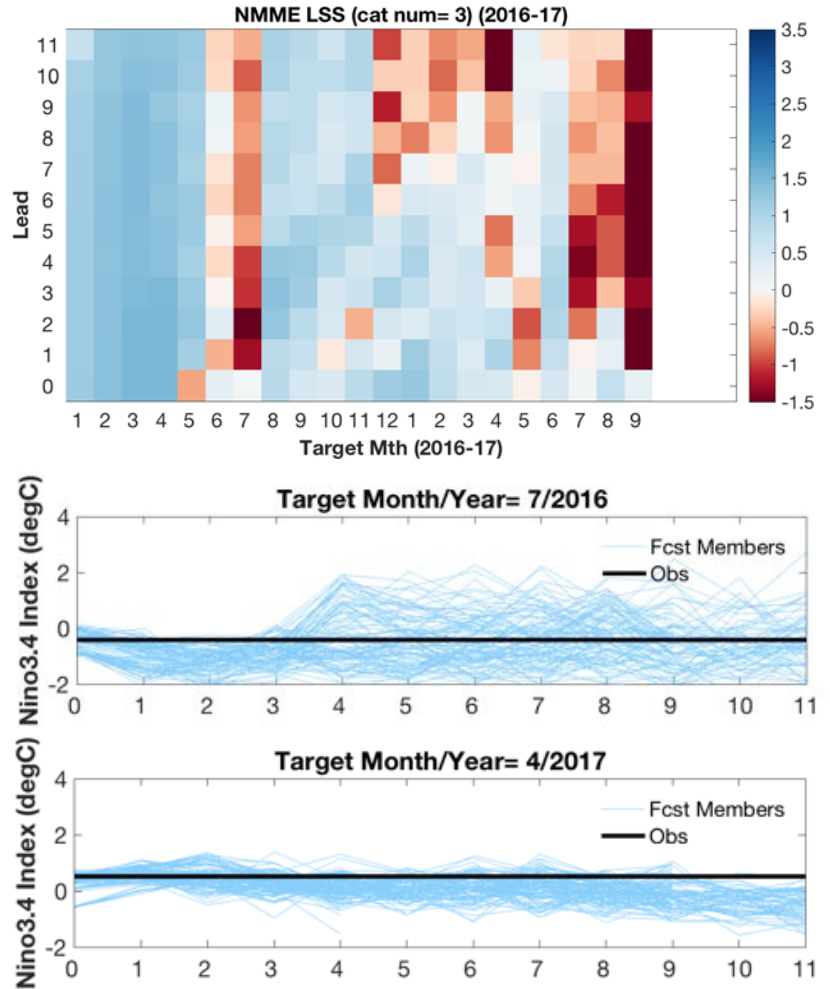


**Fig. 2** (top panel) The Logarithmic Skill Score (LSS) of the Niño-3.4 index for target months between January 2016 and September 2017 out to 12-months lead from the NMME (more info on LSS in Tippett *et al.*, 2017). Red shading indicates skill that is worse than climatological forecasts and blue shading indicates skill better than climatological forecasts. Also shown are the forecasts of Niño-3.4 for all ~100 members from the NMME (blue lines) for targets of July 2016 (middle panel) and for April 2017 (bottom panel). The horizontal black line shows the observed Niño-3.4 index value for that target month. On the x-axis is the lead time in months.

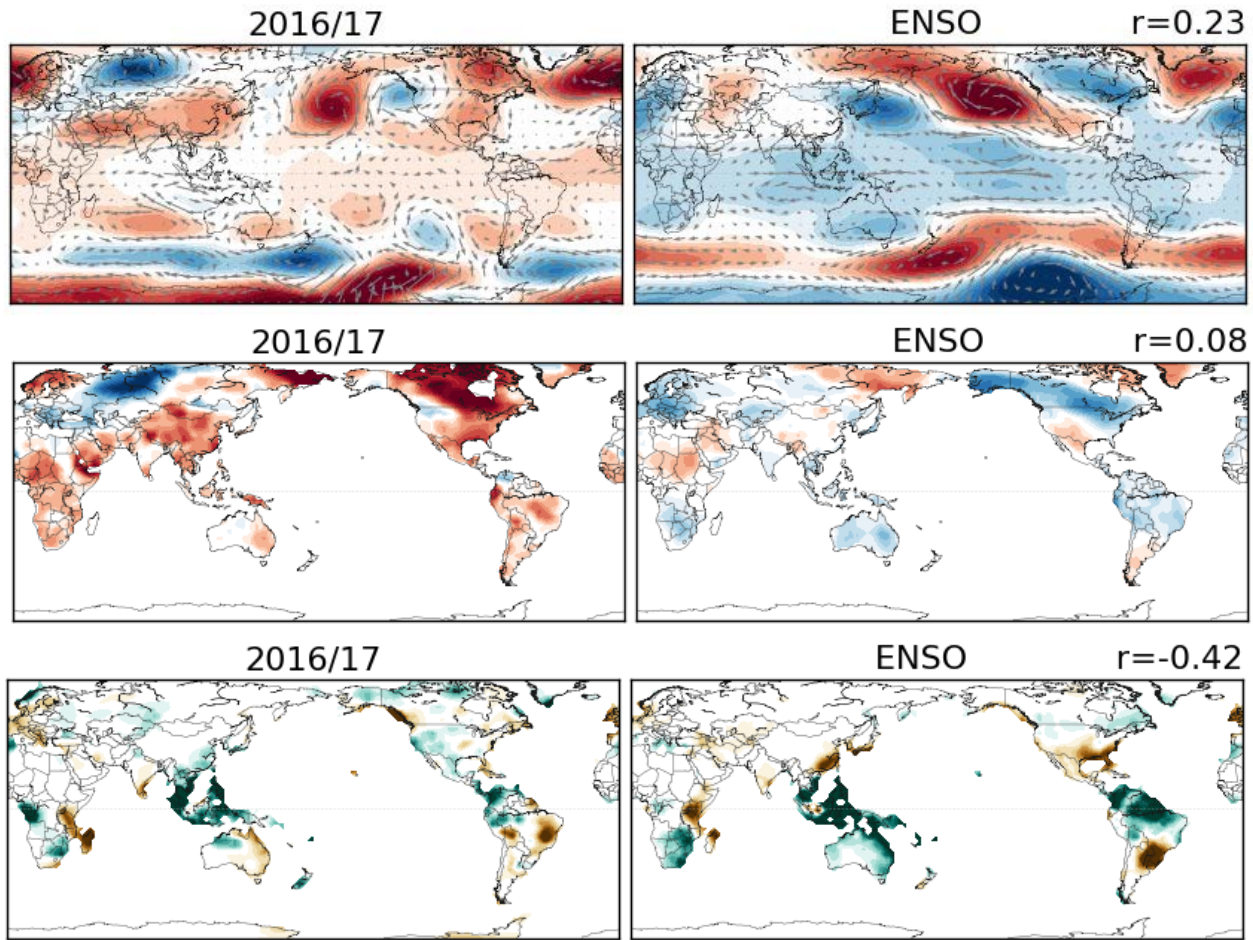


**Fig. 3** November 2016-January 2017 (NDJ) anomalies of 500-hPa geopotential height and winds (top row), surface temperature (middle row), and precipitation (bottom row). The left column shows the observational data, while the right column shows the reconstruction for 2016-17 (weighted regression map of the Niño-3.4 index). The reconstruction is multiplied by a factor of eight to aid comparison. The  $r$ -values show the spatial correlation coefficient between the observational and the reconstructed anomalies (cosine weighted by latitude). Geopotential height and wind data is from the NCEP/NCAR Reanalysis, the temperature is from the gridded GHCN+CAMS dataset (Fan and van den Dool, 2008), and precipitation data is from the gridded Precipitation Reconstruction Dataset (PREC) dataset (Chen *et al.*, 2002). Departures are formed by removing monthly means during 1981-2010.

Figure 4 shows scatterplots between the Niño-3.4 index values and the NDJ 2016-17 spatial correlations (red dot) relative to other NDJ seasons between 1979-2016 (black dots) for 500-hPa geopotential height (left panel), surface temperature (middle panel), and precipitation (right panel). At the top of each panel in Fig. 4, the temporal correlation is provided between the Niño-3.4 index value and the spatial correlations (between the observed maps and the ENSO regression). From this analysis, it is clear that precipitation and 500-hPa heights have the strongest linkage with Niño-3.4 ( $r$  is  $\sim 0.9$ ), meaning that larger values of Niño-3.4 are generally associated with larger spatial correlations. Phrased another way, the similarity between the observed global anomalies and the “expected” ENSO pattern is higher with stronger ENSO events. That NDJ 2016-17 was a marginal La Niña with index values closer to -0.5, it follows that the spatial correlations indicated in Fig. 3 are not particularly high.

In fact, one interesting aspect of the NDJ 2016-17 anomalies was how dissimilar the 500-hPa heights were from the ENSO regression (Fig. 3 - top two panels and Figure 4 - left panel). The spatial correlations were positive ( $r=0.23$ ), meaning the anomalous height pattern was mostly opposite of what would be expected during La Niña. In particular, the global tropics during NDJ 2016-17 were remarkable for its above-average

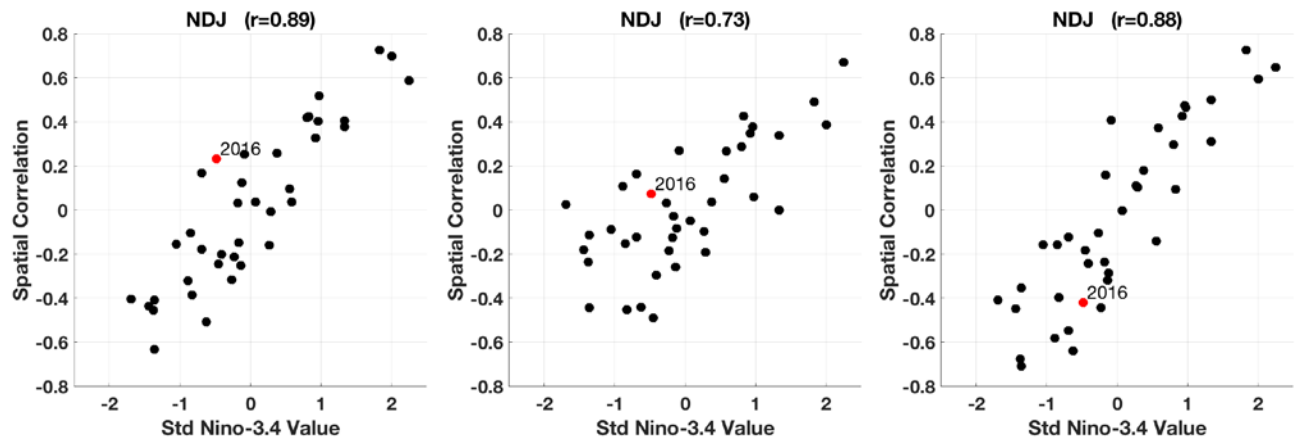


**Fig. 4** Scatterplots of the spatial correlation between the ENSO regression maps of 500mb geopotential height (left panel), temperature (middle panel) and precipitation (right panel) and the observed anomalies. The spatial correlation coefficient is on the y-axis and the seasonal average Nino-3.4 index value is on the x-axis. Each dot represents a single year between 1982-2017. The red dot indicates the 2016-17 La Niña (the spatial correlations are also presented in Fig. 3). At the top of each panel are the temporal correlations between the Niño-3.4 values (x-axis) and the spatial correlations (y-axis). The spatial mean is removed.

heights, which are typically below average during La Niña. Also, in the Southern Hemisphere mid-to-high latitudes, the circulation anomalies were reflective of a negative state of the Southern Annular Mode or Antarctic Oscillation, which is usually positive during La Niña. Only over the North Pacific Ocean did an anomalous anticyclone emerge, which is consistent with a retracted Asian jet stream, a common signal during La Niña. The poor fit of the circulation pattern during NDJ 2016-17 has some parallels with other marginal La Niña events (see the black dots surrounding the red dot in Fig. 4- left), but it was certainly striking.

Finally, the correspondence between the expected surface temperature pattern and the observations were very close to zero ( $r=0.08$ ), indicating little fit between the two. This is evident by the large areas of above-average temperature anomalies that are not commonly seen during La Niña, when below-average temperatures tend to prevail over the globe (Fig. 3- middle row). However, Fig. 4 (middle panel) clearly shows that a weak correspondence between the observations and ENSO regression is often the case during a weak La Niña such as the one that occurred in 2016-17.

*Acknowledgements.* The ENSO forecast team: Anthony Barnston, Emily Becker, Gerry Bell, Tom Di Liberto, Jon Gottschalck, Mike Halpert, Zeng-Zhen Hu, Nathaniel Johnson, Wanqiu Wang, Yan Xue.

## References

- Chen, M., P. Xie, J. E. Janowiak, and P. A. Arkin, 2002: Global land precipitation: A 50-yr monthly analysis based on gauge observations. *J. Hydrometeorol.*, **3**, 249–266.
- Fan, Y., and H. van den Dool, 2008: A global monthly land surface air temperature analysis for 1948-present. *J. Geophys. Res.: Atmos.*, **113**, D01103, doi:10.1029/2007JD008470.
- Huang, B., and Co-authors, 2017: Extended reconstructed sea surface temperature, version 5 (ERSSTv5): Upgrades, validations, and intercomparisons. *J. Climate*, **30**, 8179–8205.
- L’Heureux, M.L., and Co-authors, 2017: Observing and predicting the 2015/16 El Niño. *Bull. Amer. Meteor. Soc.*, **98**, 1363–1382.
- Reynolds, R. W., T. M. Smith, C. Liu, D. B. Chelton, K. S. Casey, and M. G. Schlax, 2007: Daily high-resolution-blended analyses for sea surface temperature. *J. Climate*, **20**, 5473–5496.
- Tippett, M.K., M. Ranganathan, M. L’Heureux, A. Barnston, and T. DelSole, 2017: Assessing probabilistic predictions of ENSO phase and intensity from the North American Multimodel Ensemble. *Clim Dyn.* <https://doi.org/10.1007/s00382-017-3721-y>.

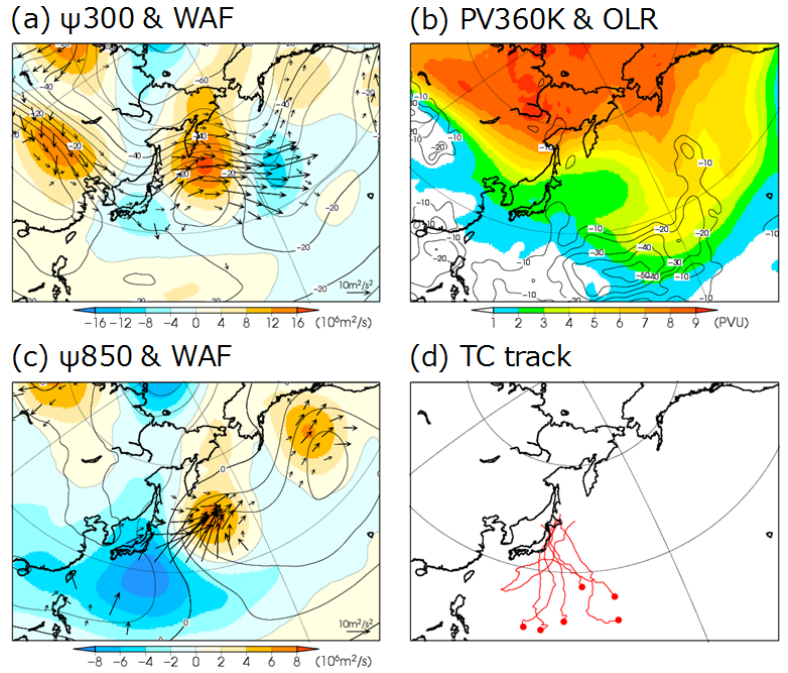




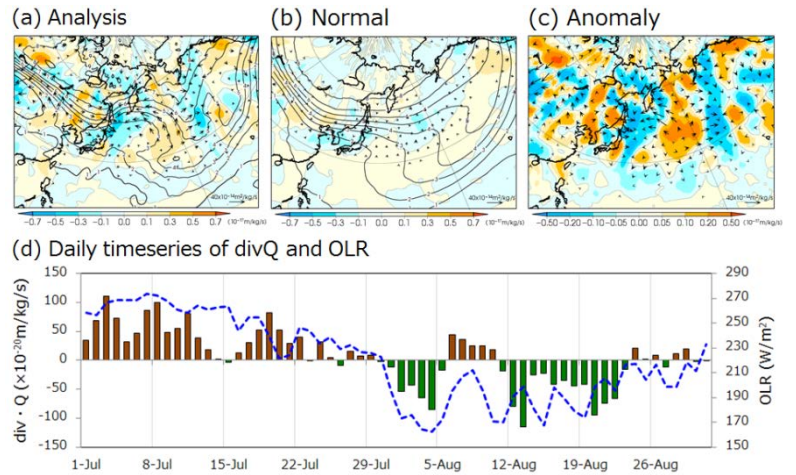
### 3. Results

Figure 2 shows 300-hPa and 850-hPa stream function anomalies and 360-K isentropic PV and OLR anomalies averaged in August 2016. The wave patterns of the circulation anomalies in the upper troposphere are observed along the Asian jet stream over an area extending from Eurasia to the seas east of Japan (Fig. 2a). An omega-shaped blocking high, with distinct anti-cyclonic circulation anomalies and an associated meridional PV overturning and southward intrusion of the high PV (Fig. 2b), is observed to the east of Japan. On the other hand, convective activities are enhanced over latitude bands near 20°N to the southwest of the high PV (contour lines in Fig. 2b). Six tropical cyclones formed over the seas south to southeast of Japan in the month (Fig. 2d), corresponding to the enhanced convective activities (Fig. 2b). In the lower troposphere, large-scale cyclonic circulation anomalies are clearly observed over the wide area in the sub-tropical western North Pacific (Fig. 2c), indicating not only circulation accompanied by the tropical cyclones but also a Rossby-wave response to the enhanced convective activities.

To examine the dynamic relation between the southward intrusion of the high PV and the enhanced convective activities based on the quasi-geostrophic (QG) theory, vertical motion induced by the QG balance was diagnosed using Q-vectors field. In the Q-vectors and its divergence derived from the monthly mean in August 2016 shown in Fig. 3, convergence anomalies are seen along just south of the area (near 20°N; Fig. 3c) where the stronger-than-normal southward intrusion of high PV is observed (Figs. 3a and 3b), indicating that QG upward motion is induced due to temperature advection or vertical derivatives of vorticity advection. A daily time series for the Q-vectors divergence over the same area (bars in Fig. 3d) indicates convergence, particularly two



**Fig. 2** Monthly mean (a) 300-hPa and (c) 850-hPa stream function (contour lines) and its anomalies (shading); contour lines at intervals of  $5 \times 10^6 \text{ m}^2/\text{s}$ ; WAF (vector) and (b) OLR anomalies (contour lines at intervals of 10  $\text{W/m}^2$ , positive anomaly values omitted); and 360-K PV (shading at intervals of 1 PVU) in August 2016. The red closed circle and lines in (d) shows the points of origin for the typhoon formed over the seas south to southeast of Japan in the month and its best tracks, respectively, based on data from JMA.



**Fig. 3** (a) Actual, (b) normal, and (c) anomalous Q-vectors at 500 hPa (vector; unit:  $\text{m}^2/\text{kg/s}$ ) and its divergence (shading; unit:  $\text{m/kg/s}$ ) derived from monthly mean in August 2016. The contour lines in (a) and (b) show 360-K PV at intervals of 1 PVU. (d) Daily time series of the Q-vectors divergence (brown bars denote divergence and green ones denote convergence) and OLR (blue dashed lines) averaged over 15°N–25°N and 150°E–180°E.

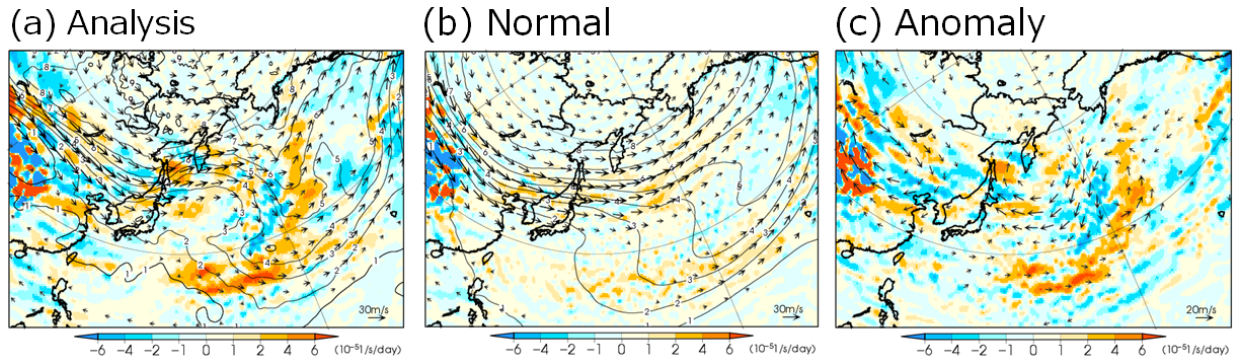


**Fig. 4** Monthly mean (a) actual, (b) normal, and (c) anomalous vertical differences (200 to 850 hPa) of vorticity advection (shading; unit:  $10^{-5}/s/day$ ) by QG horizontal wind (vector) in August 2016. The contour lines in (a) and (b) show 360-K PV at intervals of 1 PVU.

or three peaks of strong convergence during the period from end of July to late August. The time variation of the Q-vectors divergence is consistent with that of OLR, indicating that the QG upward motion induced by the high PV primarily contributed to the enhanced convective activities over the sub-tropical western North Pacific (Figs. 2b and 2c).

Figure 4 shows vertical differences of vorticity advection by QG horizontal wind between 200 hPa and 850 hPa. In association with cyclonic vorticity advection due to stronger-than-normal southward wind in the upper troposphere, positive anomalous vertical differences of the vorticity advection are seen (Fig. 4) over and around the area where the Q-vectors convergence anomalies are observed (Fig. 3) and south of the intruding high PV (Fig. 2b). Warm-air advection in the mid-troposphere, which is one of the factors that induces the QG upward motion, is not clearly seen over and around the same area (not shown). For the influence of extra-tropical circulation on the sub-tropical circulation in August 2016, the Q-vector and vorticity budget diagnoses indicate that the RWB to the east of Japan and the associated strong mid-Pacific trough contribute to the enhanced convective activities over the sub-tropical western North Pacific through the QG upward motion.

An inter-annual time series of 350-K PV averaged over the area east of Japan and OLR anomalies and Q-vector divergence averaged over latitude bands near  $20^{\circ}N$  in the western Pacific (Figs. 5a, 5b and 5c) indicates the lowest on record in August 2016 since 1979 and that they exhibit the significant characteristics of the circulation mentioned above. These characteristics suggest that compared with the normal, a Rossby-wave packet that propagated along the Asian jet stream converged to the east of Japan and contributed the enhanced convective activities through the QG upward motion and the associated formation of tropical cyclones.

To assess the impact of the tropical convective activities on the atmospheric circulation, a deterministic numerical

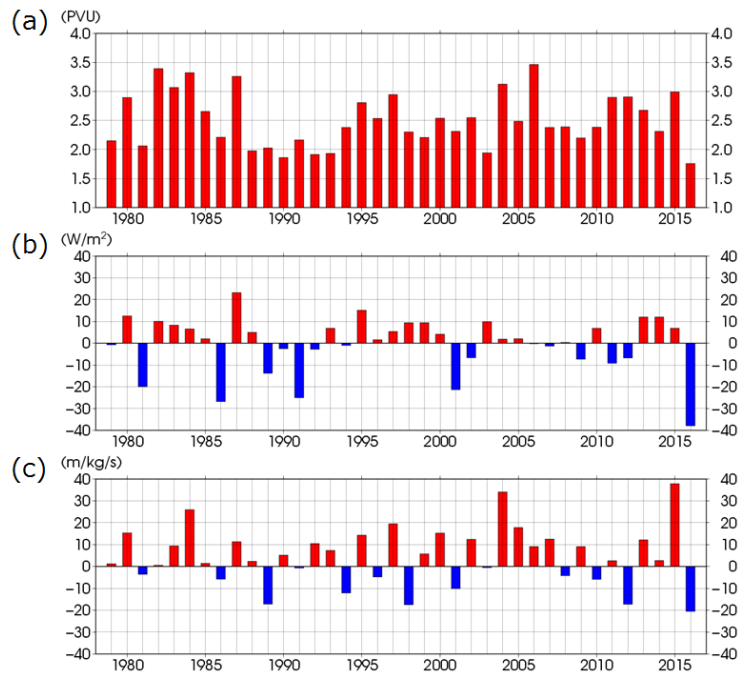


**Fig. 5** For August, from 1979 to 2016, inter-annual time series of monthly mean (a) 350-K PV (PVU) averaged over  $35^{\circ}N-45^{\circ}N$  and  $150^{\circ}E-180^{\circ}E$ ; (b) OLR anomalies ( $W/m^2$ ) averaged over  $15^{\circ}N-25^{\circ}N$  and  $150^{\circ}E-180^{\circ}E$ ; and (c) Q-vectors divergence anomalies ( $10^{-17} m/kg/s$ ) averaged over  $15^{\circ}N-25^{\circ}N$  and  $150^{\circ}E-180^{\circ}E$ .



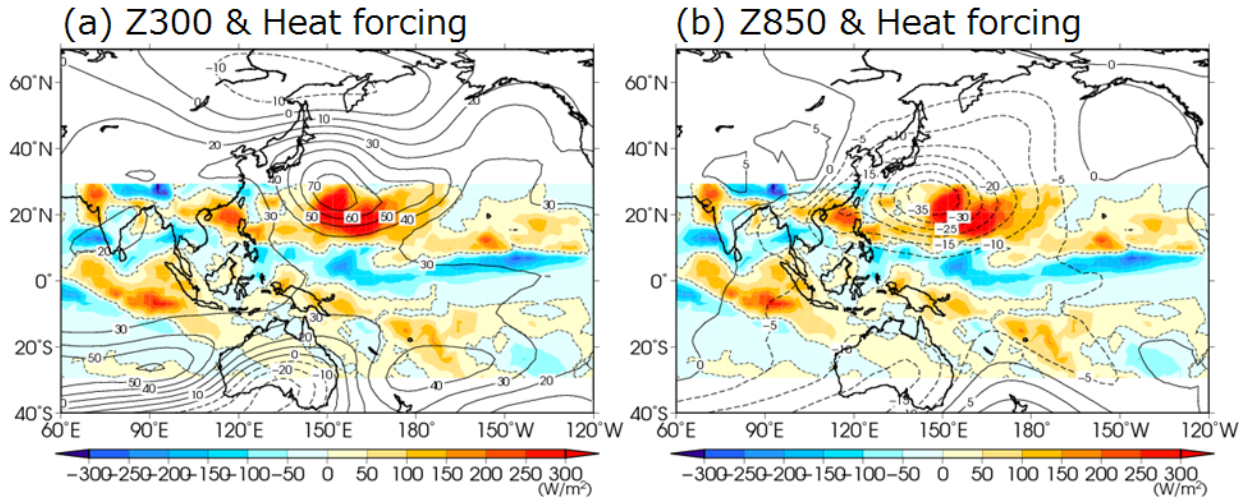


**Fig. 6** Steady linear responses of (a) 300-hPa and (b) 850-hPa height (contour lines) in the LBM to diabatic heating anomalies in the tropics (30°S–30°N) for August 2016 (shading). The anomalies represent deviations from the basic states of the normal in August. The contour intervals is (a) 10 and (b) 5 m. Dashed contours show negative values.

experiment was performed using the LBM. The LBM was solved with monthly mean diabatic heating anomalies over the area from 30°S to 30°N in August 2016. The vertical integrated heating anomalies (shading in Fig. 6) indicate the existence of strong heat sources associated with enhanced convective activities over and around 20°N in the western North Pacific. The LBM responses of 300-hPa and 850-hPa height fields show positive (anti-cyclonic) and negative (cyclonic) anomalies over the seas southeast of Japan, respectively, indicating the Rossby-wave response to the strong heat sources (Figs. 6a and 6b). The responses of cyclonic circulation anomalies at 850 hPa are consistent with the circulation anomalies observed in August 2016 (Fig. 2c), indicating the influences of the enhanced convective activities over the sub-tropical western North Pacific on the large-scale cyclonic circulation anomalies and presumably on the origin and track of the tropical cyclones. By contrast, the responses of anti-cyclonic circulation anomalies at 300 hPa differ from the anomaly patterns observed in August 2016 (Fig. 2a), indicating that the upper tropospheric circulation anomalies primarily formed not by the responses to the enhanced convective activities in the sub-tropical western North Pacific but by the quasi-stationary Rossby-wave propagation from Eurasia along the Asian jet stream (see WAF shown in Fig. 2a).

The results of Q-vectors diagnoses and LBM experiments mentioned above suggest that the RWB to the east of Japan and the quasi-geostrophically induced convection over the sub-tropical western North Pacific contributed to a series of typhoon formations or landfalls, which caused significant wet conditions in eastern and northern Japan in August 2016.

#### 4. Discussion and conclusions

We investigated the dynamic relation between the RWB to the east of Japan and the associated enhanced convective activities over the sub-tropical western North Pacific and their influence on Japan's climate in August 2016. In the monthly mean atmospheric circulation, the quasi-stationary Rossby-wave propagation is observed along the Asian jet stream and resultant wave packet convergence to the east of Japan (*i.e.*, the occurrence of RWB). The RWB accompanies meridional PV overturning and southward intrusion of the high PV in the upper troposphere (*i.e.*, the enhanced mid-Pacific trough). The enhanced convective activities in the sub-tropical western North Pacific are presumed to be mainly associated with the upper tropospheric southward positive vorticity advection through the QG upward motion. The LBM experiment indicates that the 850-hPa cyclonic circulation anomalies over the wide area in the sub-tropical western North Pacific are associated with the Rossby-wave response to the enhanced convective activities. The convective activities and cyclonic circulation anomalies are presumed to be related to the formation of six tropical cyclones and significant wet conditions mainly owing to a series of typhoons passing over eastern to northern Japan.

The Q-vectors and vorticity budget diagnoses infer that the QG upward motion associated with the strong mid-Pacific trough induced the enhanced convective activities in the sub-tropical western North Pacific. To demonstrate the causal relation between them, some impact experiments with the relaxation area over and around the mid-Pacific trough were performed using JMA's operational one-month ensemble prediction system. The results of the experiments indicate the existence of the causal processes from the mid-Pacific trough to the sub-tropical convective activities associated with the QG balance; these results support the inferences mentioned above. The detailed results and discussion will be presented in another paper.

Further investigations are needed to identify the primary factors that caused the significant atmospheric circulation in August 2016, as shown in the interannual time series of some area-averaged elements in Fig. 5. The significant amplification of the blocking high to the east of Japan (Fig. 2a) and the lower tropospheric large-scale cyclonic circulation over the sub-tropical western North Pacific are presumed to be associated with some atmospheric instability with its seasonal basic states. To assess the contribution of the atmospheric instability to the significant amplification, baroclinic and barotropic energy conversion from the basic states defined as the normal to the anomaly patterns will be calculated in future studies and detailed results will be presented.

Although this is a case study for the anomalous summer conditions over and around Japan in August 2016, we expect that studying the dynamic interaction between extratropical and tropical circulation is important to make further progress in both climate system monitoring and seasonal forecasting.

## References

- Kobayashi, S., *et al.* 2015: The JRA-55 reanalysis: General specifications and basic characteristics. *J. Meteor. Soc. Japan*, **93**, 5–48.
- Molinari, J., and D. Vollaro, 2012: A subtropical cyclonic gyre associated with interactions of the MJO and the midlatitude jet. *Mon. Wea. Rev.*, **140**, 343–357.
- Sato, N., K. Sakamoto, and M. Takahashi, 2005: An air mass with high potential vorticity preceding the formation of the marcus convergence zone. *Geophys. Res. Lett.*, **32**, L17801. doi:10.1029/2005GL023572.
- Takaya, K., and H. Nakamura, 2001: A formulation of a phase-independent wave-activity flux for stationary and migratory quasi-geostrophic eddies on a zonally varying basic flow. *J. Atmos. Sci.*, **58**, 608–627.
- Watanabe, M., and M. Kimoto, 2000: Atmospheric-ocean thermal coupling in the Northern Atlantic: A positive feedback. *Quart. J. Roy. Meteor. Soc.*, **126**, 3343–3369.
- Watanabe, M., and M. Kimoto, 2001: Corrigendum. *J. Roy. Meteor. Soc.*, **127**, 733–734.

## **The Sudden Onset of the 2017 Northern High Plains Drought**

Muthuvel Chelliah and David Miskus

*Climate Prediction Center, NOAA/NWS/NCEP, College Park, MD*

### **1. Introduction**

Across the Northern Great Plains (NGP) states of the United States, in large parts of Montana, North Dakota and South Dakota, drought like conditions emerged suddenly in spring 2017, which progressively got worse quickly in late spring and summer lasting throughout the year, and the drought conditions have not eased even in early 2018. This brief note describes the conditions under which the NGP drought emerged, whether its emergence could have been identified a bit earlier, and for how long it is likely to last.

### **2. Drought fact and 2017 NGP condition**

The first and foremost fact about this or any other drought is the very obvious, that, it is the consequence of the lack of, or significant deficit in, the “normal/expected precipitation” in a given region during a “certain time” of the year. The severity, extent and longevity of the resulting drought depend on how much the precipitation deficit is from normal levels, and for how long that deficit lasts. If that “certain time” of the year happens to be among the few months in the main rainy season for that region, then the consequences of the rainfall deficit possibly leading to the local drought is certain, and that drought conditions will probably last until next year when the rainfall season returns. In Fig. 1 is shown the sequence of weekly United States Drought Monitor (USDM) maps beginning with the week of 2nd May 2017 map, until the 18th May 2017 map. From these USDM maps, it appears that drought conditions were declared in very late May in eastern Montana and the Dakotas at the D0 level of drought and quickly spreading and intensifying in the subsequent weeks to the maximum D4 category by August and September (bottom two big panels of Fig.1). At the beginning of this sequence of maps, except for a small patch of drought in the southeast US, drought free conditions prevailed in general over much of the country, and by the end of summer into early fall, the Northern Plains Drought was the dominant meteorological event and newsmaker in the country.

### **3. Early detection of drought onset**

Even though, once the Northern Great Plains (NGP) drought was forecast well, in successive months after the drought got established, the quick emergence and the sudden development of the drought caught many local farmers by surprise, and there was even an inkling if the NGP Drought was not “declared” even earlier, during the onset period. We will address this issue partly by using Figures 2 and 3. In Fig. 2, is shown the 1-month (1<sup>st</sup> column), 2-months (middle column), and 3-months (last column) accumulated precipitation deficit (yellow/red) and surplus (blue/green) in months ending Jan 2017 through May 2017. Medium percent of annual precipitation during the different 3-month calendar seasons for the United States (courtesy of Rich Tinker, CPC/NCEP) are shown in Fig. 3. Here we highlight the main precipitation season May-June-July (MJJ) for the Northern Plain states, the region of drought under study here. Note that in the NGP states, even though over half to two thirds (possibly above) of the annual rain falls during MJJ months, the region begins to get some early rain in late March and April, which is critical to the farmers there, after the rigid winter cold, when much of the surface is frozen. Here, the pre-rainy season Feb-Mar-Apr (FMA) gets about 15-20 percent of the median rainfall. But in 2017, as can be seen in Fig. 2 (middle/last columns across April), as indicated by a red square, there has already been a deficit building up towards end of April, which must have been a warning sign for possible emerging drought. Precipitation deficit/excess maps like Fig. 2 (which can be made at any day of the month) made in the last week of April or first week of May, for the preceding contiguous 30, 60 or 90 days (not shown here) period accumulations, show in fact, that even by late April or early May, the clear warning signs of developing dryness and an emerging drought, are already in place.

With the established deficit already in place in the region, if the “expected rain” did not arrive in successive week(s), the caution/alarm bells should have triggered to initiate the drought warning there. But it was not done until very late May, when the US drought monitor caught the drought condition.

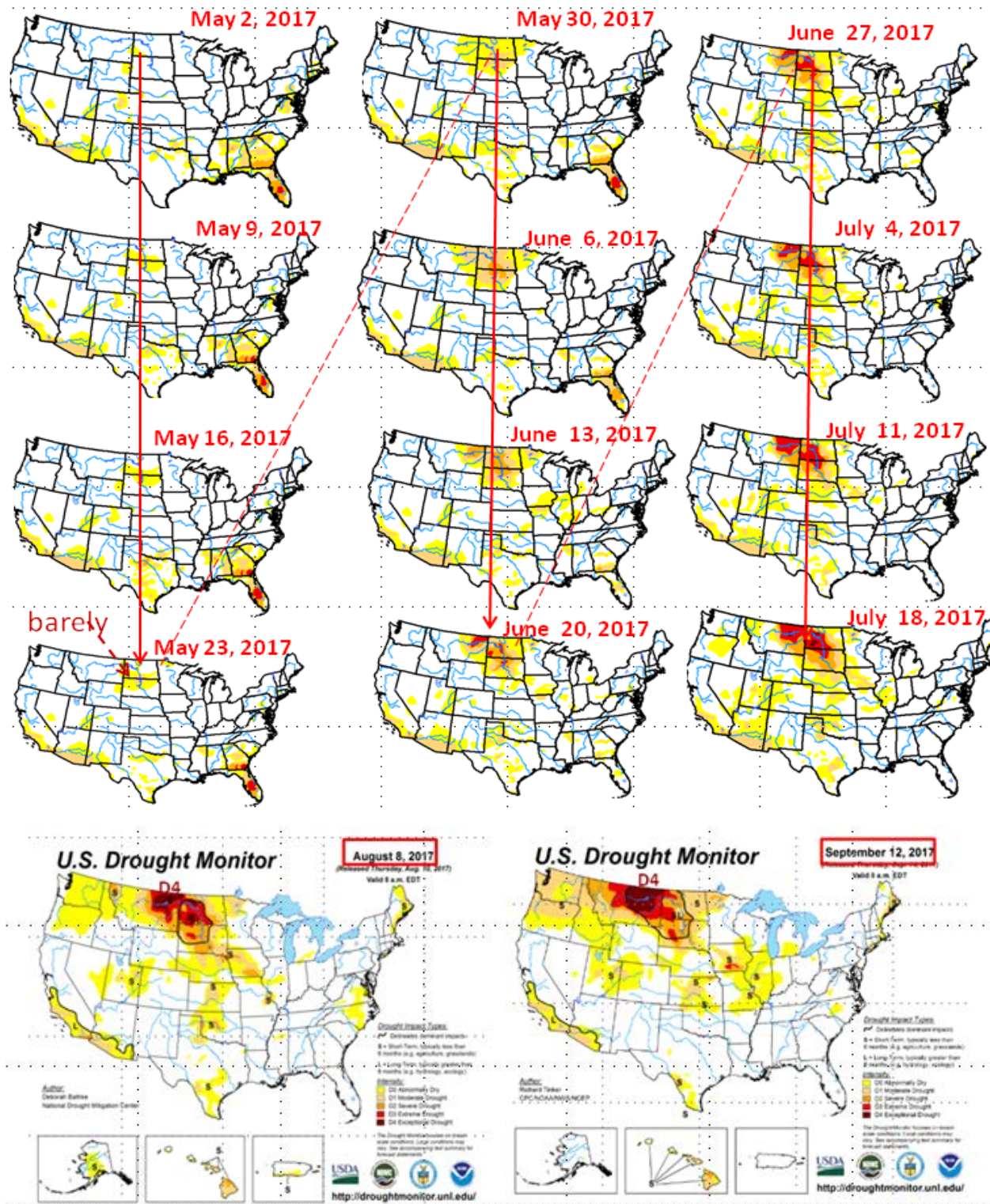


**Fig.1** The weekly U.S. Drought Monitor at various stages of the 2017 Great Northern Plains Drought. The top 12 panels are weekly sequential DM maps and the last two are at peak drought stage.



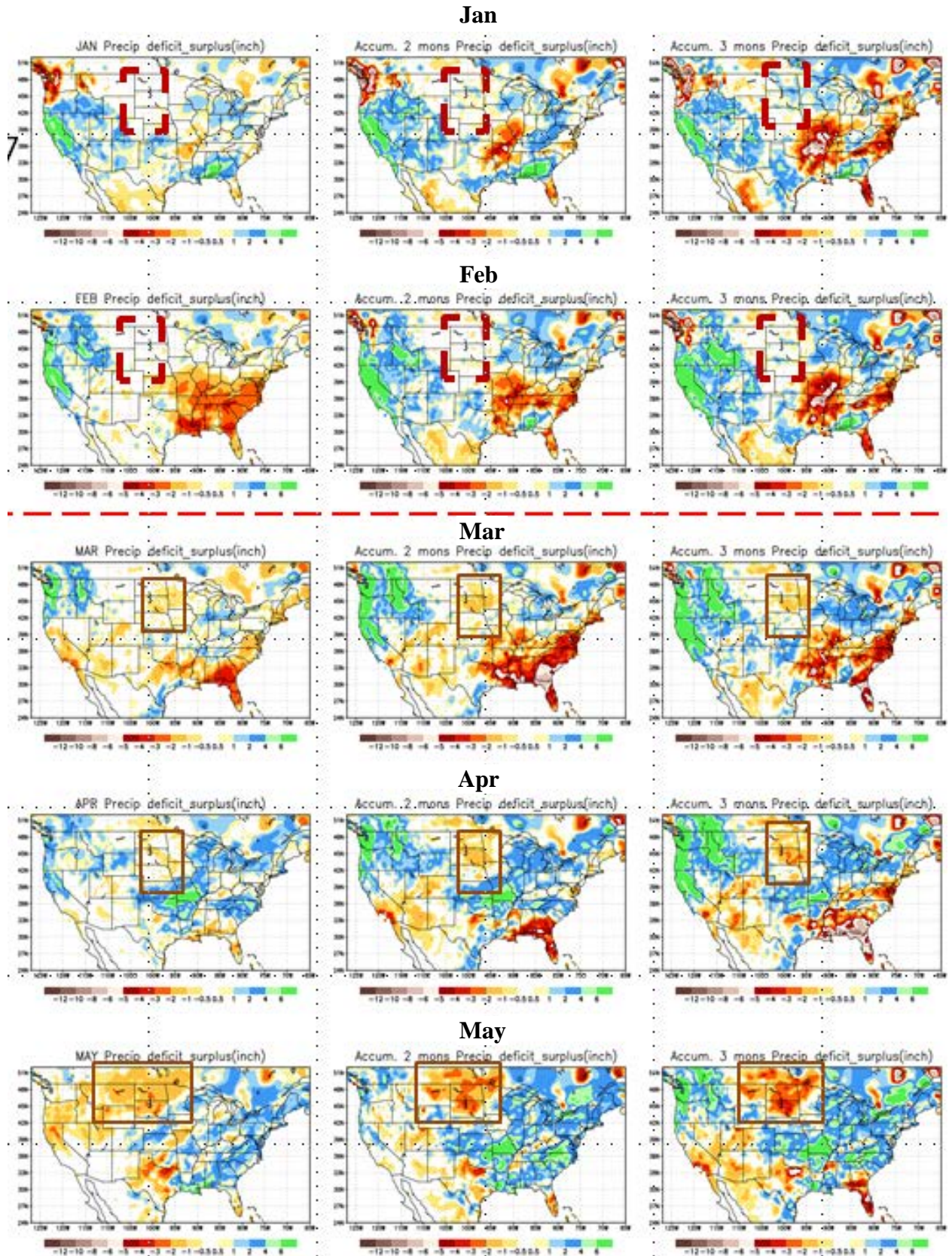


**Fig. 2** 1-mon (1<sup>st</sup> column), 2-months (middle column), and 3-months (last column) accumulated precipitation Deficit (yellow/red) Surplus (blue/green) in months ending Jan through May 2017.



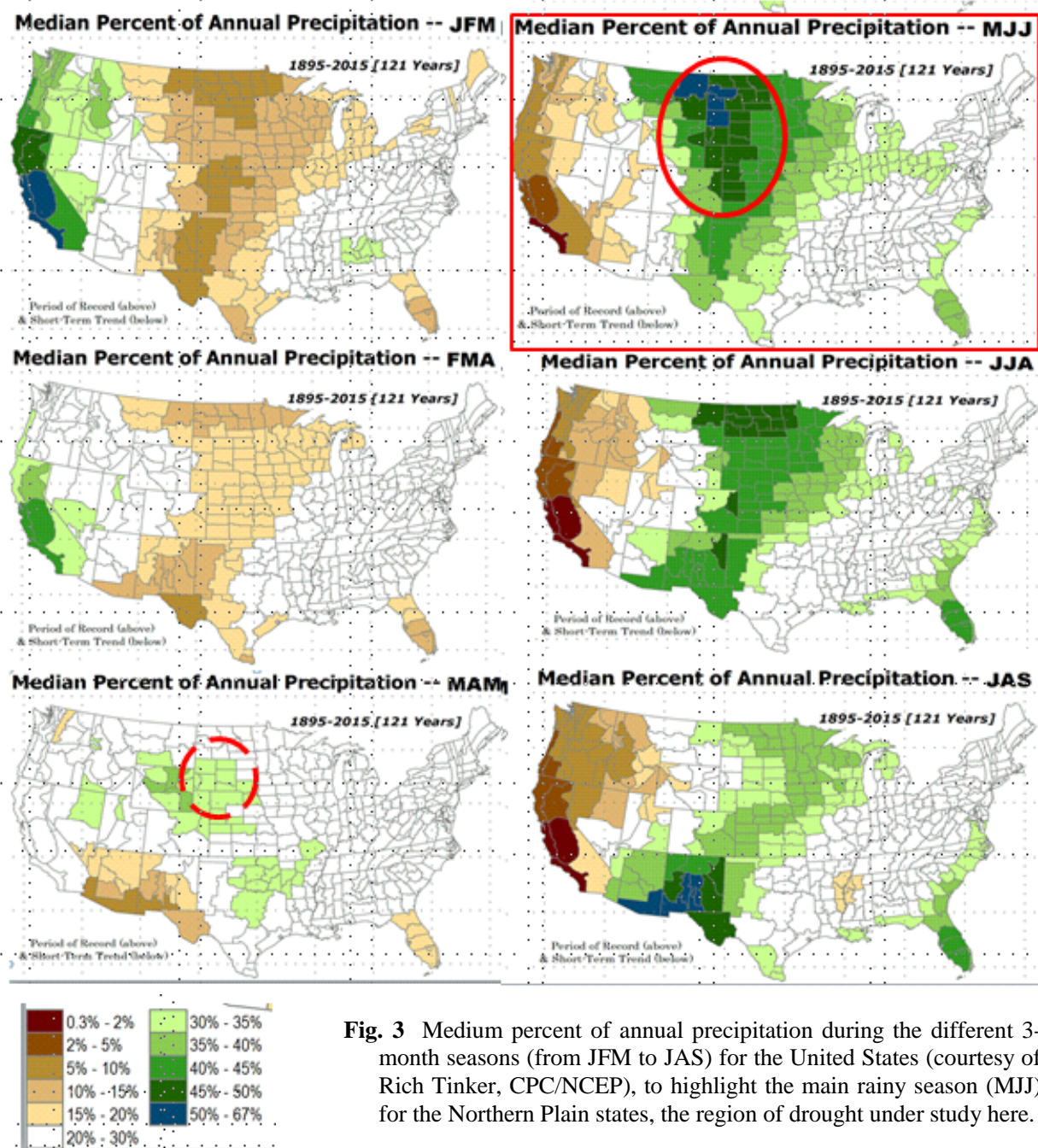


**Fig. 3** Medium percent of annual precipitation during the different 3-month seasons (from JFM to JAS) for the United States (courtesy of Rich Tinker, CPC/NCEP), to highlight the main rainy season (MJJ) for the Northern Plain states, the region of drought under study here.

The monthly drought outlook (MDO) issued on April 30, 2017 (Fig. 4) or the seasonal drought outlook (SDO) issued on both 20 April or 18 May did not indicate any drought in the NGP. Only the MDO issued on 31 May pointed to a drought in the region and that it was likely to persist.

#### 4. Remarks

In closing, why was such a delay? In retrospect, a few reasons come to mind. First, this NGP states is not the typical region that drought usually occurs, so overall possibly less attention was given to the region (rarity, low population density (?), *etc.*). Second, until just a few months earlier (late 2016/early 2017) the major focus and more attention had been on the other two major drought areas in more “important” drought prone regions namely California and the southeast US. Also the focus was centered on the totally unexpected rains

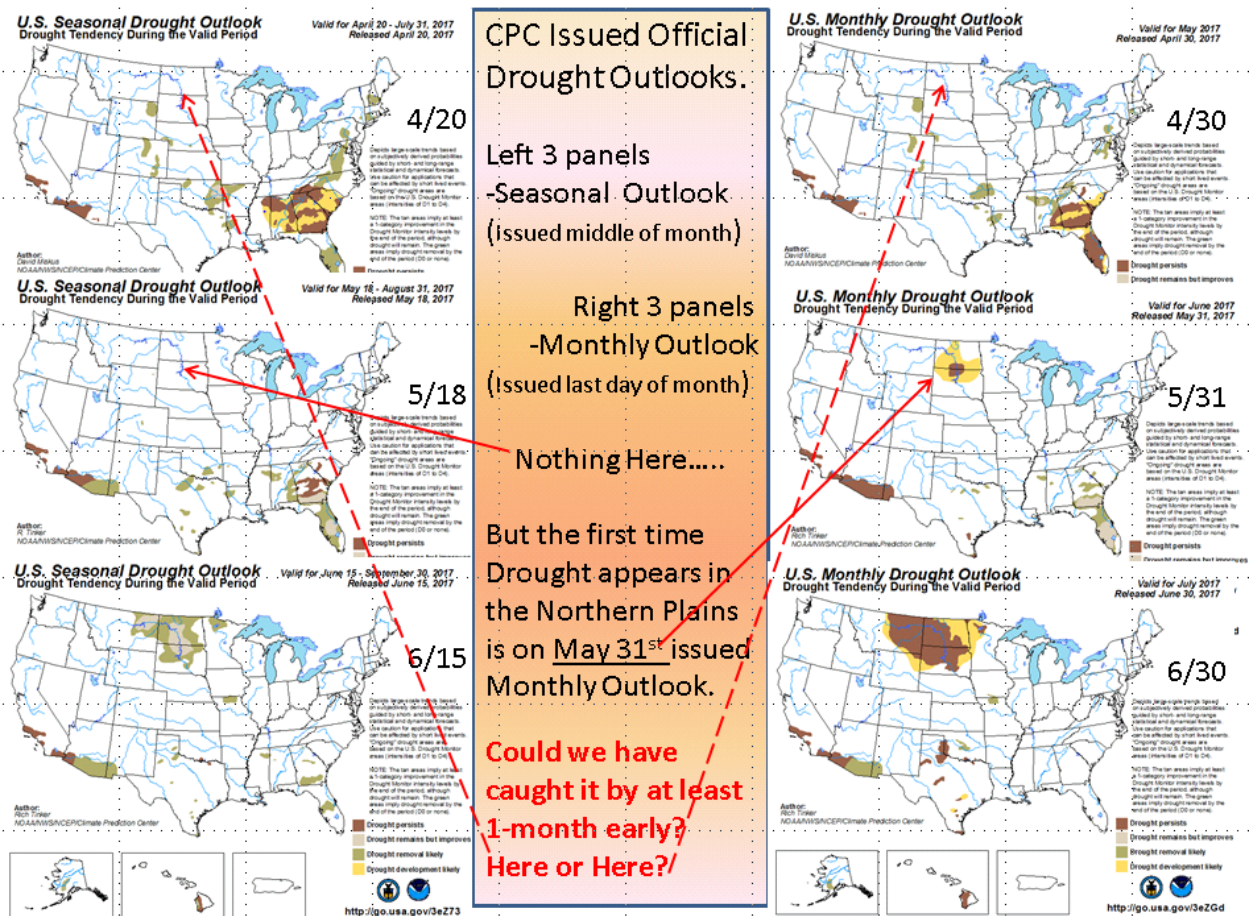


**Fig. 4** Monthly Drought Outlooks issued in April, May and June 2017 on the right panels, and the Seasonal drought outlooks issued in the middle of the same months on the left.

in California during 2016/2017 La Nina winter which abruptly ended the long lasted drought in that region and the gradual improvement in the drought in the southeast US. Thirdly, and more importantly, the NMME models and the official forecasts (not shown here) called for above normal MJJ seasonal rain in the region (which of course did not happen!), and consequently the NLDAS models followed suit to return the dryness towards normal (did not verify!). These are valuable lessons learned from this NGP drought, and it is hoped that the onset of the 2018 rainy season (possibly a good one!) will probably end the drought in the region which started in spring 2017.

## The Australian Climate of 2016: A Strong Negative Indian Ocean Dipole Dominates

Catherine Ganter, Andrew Watkins, and Felicity Gamble  
*Australian Bureau of Meteorology, Melbourne Australia*

### 1. Introduction/Overview

The very strong 2015–16 El Niño brought dry conditions to many parts of Australia right up until its decay in the austral autumn (March to May). But then the climate flipped: May to November 2016 saw the Australian climate, and indeed many locations surrounding the Indian Ocean, dominated by a strong negative Indian Ocean Dipole (IOD) event, which resulted in very wet conditions across Australia, particularly in the south.

### 2. The Indian Ocean Dipole (IOD)

The IOD (Saji *et al.* 1999, Saji and Yamagata 2003 a, b) is defined by the difference in sea surface temperature anomalies between the western and eastern tropical Indian Ocean (see Fig. 1). A negative phase of the IOD is indicated by cooler than average waters closer to Africa and warmer than average waters closer to Indonesia. These warmer waters close to Indonesia act to favour convection to the northwest of Australia, triggering a Rossby wave train that encourages lower pressures over southeast Australia (Lim and Hendon 2017) and more moisture into the Australian region (Risbey *et al.* 2009). Cooler waters and hence subsiding air in the west reduce rainfall in eastern Africa/Horn of Africa. Typically, IOD events develop during May or June, peak around October, and rapidly decay by November or early December. The IOD pattern is unable to form during December to April. This is because the monsoon trough shifts south over the IOD regions, changing the wind patterns, and upsetting the east/west circulation over the tropical Indian Ocean.

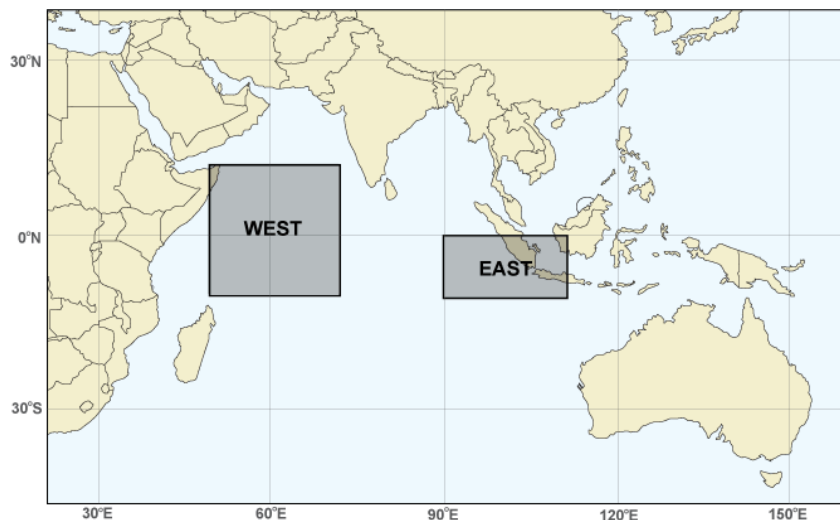


**Fig. 1** East and west nodes of the Indian Ocean Dipole. West node covers the area from 50°E to 70°E and 10°S to 10°N while east node covers the area from 90°E to 110°E and 10°S to 0°S. Source: Australian Bureau of Meteorology.

### 3. Event development

In March and April 2016 (Australian Bureau of Meteorology 2016 a, b), international climate models were suggesting the development of a negative IOD event. Event onset occurred slightly sooner than forecast, with a dipole pattern developing in late May, reaching peak strength in July (Fig. 2), which then persisted through to the end of October. Values were strongly negative at times, with the monthly IOD index value for July the most negative since reliable records began in 1960. Historical index values are based upon the NOAA Extended Reconstructed Sea Surface Temperature Version 5 (ERSST v5), Huang *et al.* 2017, sourced from: <http://www.esrl.noaa.gov/psd/>.



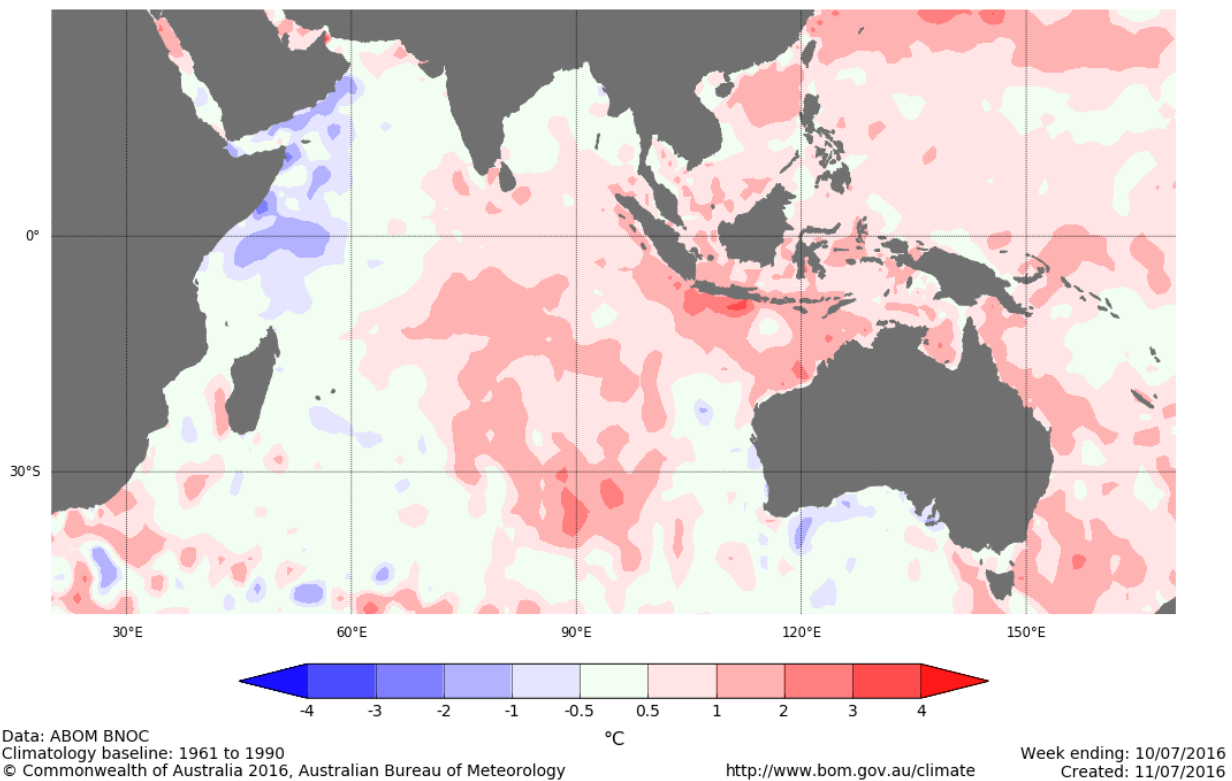


**Fig. 2** Sea surface temperature anomalies showing the negative Indian Ocean Dipole (IOD) pattern during the week ending 10 July 2016. The negative IOD pattern is characterized by cooler than average waters near the Horn of Africa, and warmer than average waters off the Indonesian islands of Sumatra and Java. Source: Australian Bureau of Meteorology.

#### 4. Rainfall effect and Australian cropping season

The strong negative IOD heralded wetter conditions for much of southern Australia, and helped bring Australia its wettest May to September period in 117 years of national rainfall records (Fig. 3). This was a much needed turnaround for previously drought-affected regions in Victoria and inland Queensland.

The end of the negative IOD event in November, and a subsequent return to near-average rainfall and temperatures, meant the Australian grain crop of 2016 had experienced a near-perfect growing-season climate. Ideal conditions for the grain crop are good rainfall and few frosts during its growing season, and little rainfall or heatwaves during the harvest time, which is typically around November or December. These ideal growing conditions in 2016 resulted in Australia's largest winter grain crop on record, around 30 per cent above the previous record set in 2011–12 (ABARES 2018).

In contrast, eastern Africa continued to experience dry conditions, with the failure of their long rains (March to May) and short rains (October to December) extending an already significant drought, leading to poor crops and ultimately a food shortage crisis (World Food Program 2016 a, b).

#### References

- Australian Bureau of Agricultural and Resource Economics and Sciences (ABARES), 2018: <http://www.agriculture.gov.au/abares/research-topics/agricultural-commodities/agricultural-commodities-trade-data#austrian-crop-report-data>
- Australian Bureau of Meteorology, 2016a: <http://www.bom.gov.au/climate/model-summary/archive/20160316.archive.shtml>
- , 2016b: <http://www.bom.gov.au/climate/model-summary/archive/20160418.archive.shtml>

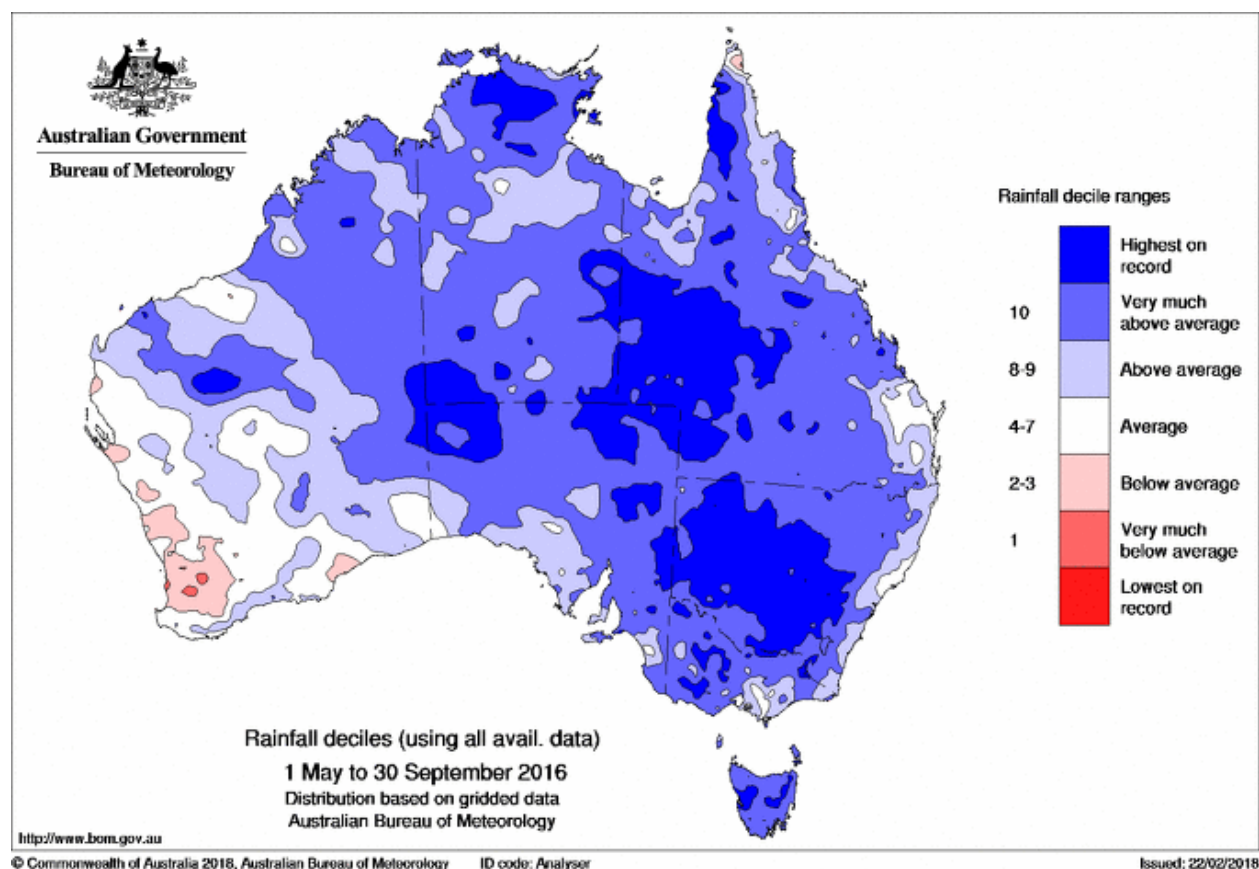


**Fig. 3** Rainfall deciles for May to September 2016 for Australia, based on the 1900–2016 distribution. (Source: Australian Bureau of Meteorology)

- Huang, B., P. W. Thorne, V. F. Banzon, T. Boyer, G. Chepurin, J. Lawrimore, M. J. Menne, T. M. Smith, R. S. Vose, and H. M. Zhang, 2017: Extended reconstructed sea surface temperature version 5 (ERSST.v5): Upgrades, validations and intercomparisons. *J. Climate*, doi:10.1175/JCLI-D-16-0836.1
- Lim, E., and H. H. Hendon, 2017: Causes and predictability of the negative Indian Ocean Dipole and its impact on La Niña during 2016. *Scientific Reports* 7, Article number: 12619, doi:10.1038/s41598-017-12674-z
- Risbey, J. S., M. J. Pook, and P. McIntosh, 2009. On the remote drivers of rainfall variability in Australia. *Mon. Wea. Rev.*, **137**, 3233–3253, <https://doi.org/10.1175/2009MWR2861.1>
- Saji, N. H., B. N. Goswami, P. N. Vinayachandran, and T. Yamagata, 1999: A dipole mode in the tropical Indian Ocean. *Nature*, **401**, 360–363, doi:10.1038/43854
- , and T. Yamagata, 2003a: Structure of SST and surface wind variability during Indian Ocean Dipole mode events: COADS observations. *J. Climate*, **16**, 2735–2751, [https://doi.org/10.1175/1520-0442\(2003\)016<2735:SOSASW>2.0.CO;2](https://doi.org/10.1175/1520-0442(2003)016<2735:SOSASW>2.0.CO;2)
- , and T. Yamagata, 2003b: Possible impacts of Indian Ocean Dipole mode events on global climate. *Climate Research*, **5**, 151–169.
- World Food Program, 2016a: Eastern African growing season 2016 (long rains). Recovering from El Niño. <http://documents.wfp.org/stellent/groups/public/documents/ena/wfp283668.pdf>
- , 2016b. East Africa: The 2016 season. Severe drought in the Horn of Africa. <http://documents.wfp.org/stellent/groups/public/documents/ena/wfp289530.pdf>

## Causality and Sub-seasonal Predictability of the 2016 Yangtze River Extreme Rainfall

Xing Yuan<sup>1</sup>, Shanshan Wang<sup>2</sup>, and Zeng-Zhen Hu<sup>3</sup>

<sup>1</sup>Key Laboratory of Regional Climate-Environment for Temperate East Asia (RCE-TEA),  
Institute of Atmospheric Physics, Chinese Academy of Sciences, Beijing, China

<sup>2</sup>Institute of Arid Meteorology, CMA, Lanzhou, China

<sup>3</sup>Climate Prediction Center, NCEP/NWS/NOAA, College Park, MD

### 1. Introduction

In June-July 2016, a barrage of extreme rainfall hit the middle and lower reaches of Yangtze River in eastern China, which caused severe urban inundations in big cities such as Wuhan and Nanjing, and resulted in direct economic loss of 70 billion RMB (about 10 billion US dollars). The rainfall anomaly exceeded 300-400 mm within 10 days, and was ranked as the 1st heaviest 10-day rainfall since 1951 (Yuan *et al.*, 2018). Understanding the causality and predictability of the 2016 Yangtze River extreme rainfall is crucial for flooding early warning and adaptation in a changing climate.

The Yangtze extreme rainfall was supposed to be associated with the 2015/16 big El Niño, nevertheless its spatial pattern was different from the 1997/98 El Niño-induced Yangtze River extreme rainfall. The June-July mean rainfall was regressed against NINO3.4 index during preceding DJF, and it is found that the ENSO forced teleconnection pattern shifts from southeastern China to the middle and lower reaches of Yangtze River after 2000, resulting in a pattern that is similar to the 2016 extreme rainfall (Fig. 1). This suggests the northward shift of the ENSO forced teleconnection may increase the risk of extreme rainfall over Yangtze River.

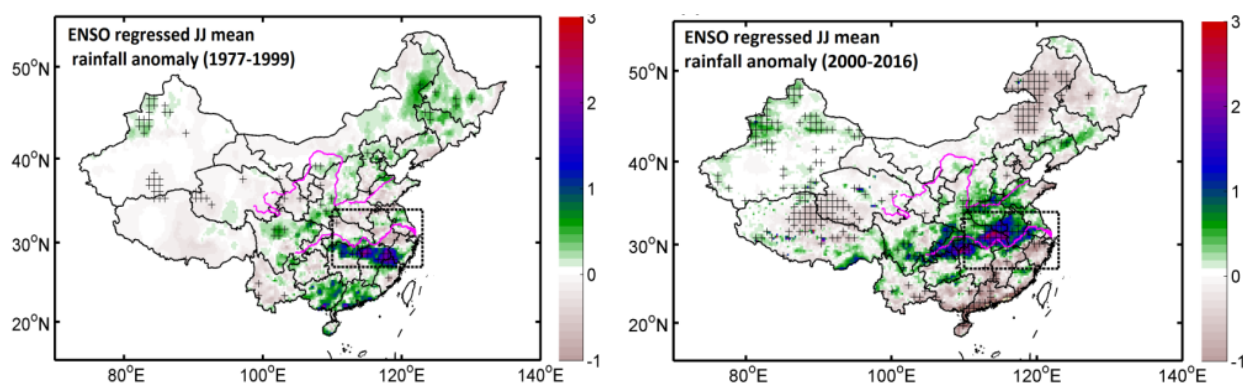


**Fig. 1** Decadal change in ENSO-East Asian summer rainfall teleconnection. Regressed June-July mean rainfall anomaly (mm/day) against NINO3.4 SST in the preceding December-February during 1977-1999 and 2000-2016 respectively, where the stippling indicates a 90% confidence level.

### 2. Causality and potential sub-seasonal predictability

To explore the causality of the risk change, CMIP5 model simulations with all and natural only forcings were used. CMIP5 models seem to over-represent the ENSO-seasonal mean rainfall teleconnection and under-represent the ENSO-extreme rainfall teleconnection, but the models' simulations on the teleconnection pattern can be improved to some extent with the consideration of anthropogenic forcings, suggesting that anthropogenic climate change may play an important role in influencing the likelihood of the Yangtze River

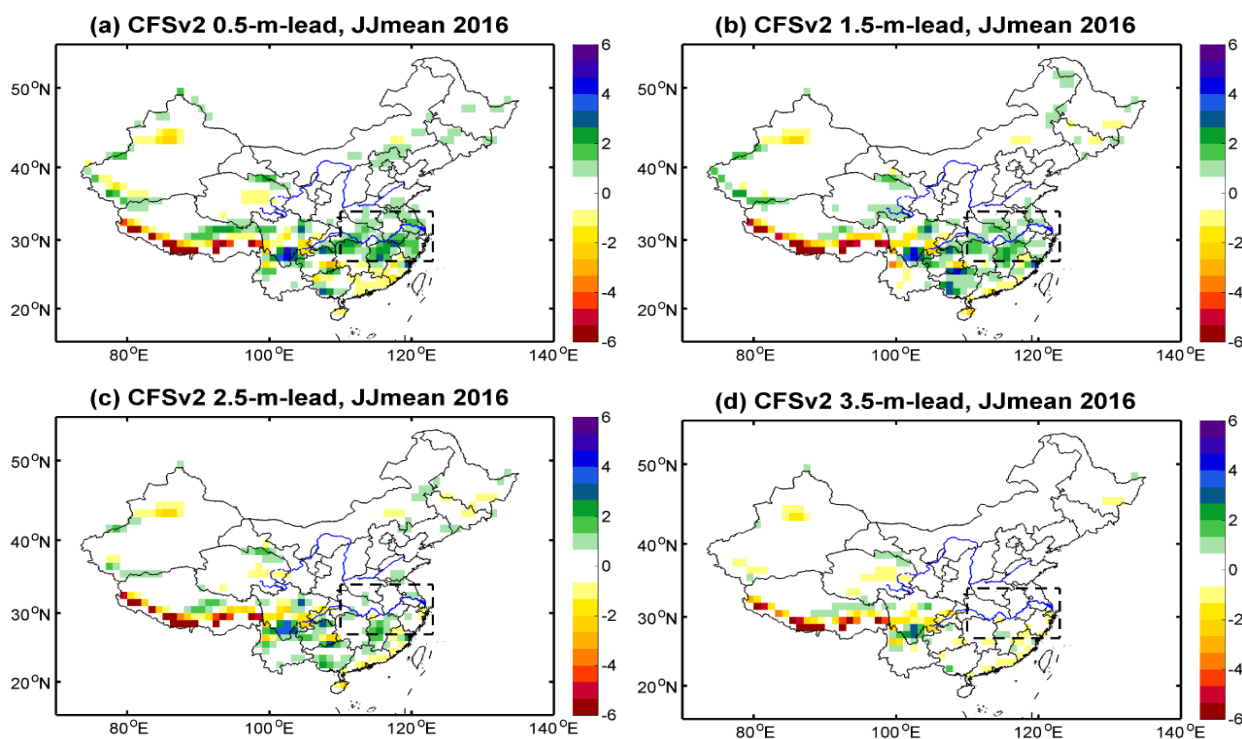


**Fig. 2** June-July mean rainfall anomaly in 2016 predicted by CFSv2 at different lead times.

extreme rainfall. In fact, anthropogenic climate change has increased risk of 2016 Yangtze River extreme summer rainfall by 1/3, and it could reach 2/3 in El Niño years (please see Yuan *et al.* 2018 for details).

CFSv2 model roughly captured the rainfall anomaly at 1.5-month lead, with an underestimation of the magnitude (Fig. 2). The sub-seasonal predictability of the Yangtze River extreme rainfall was investigated by using CFSv2 hindcasts and real-time forecast with a “perfect model” assumption. It is found that the potential predictability of atmospheric moisture flux, which is a key factor for extreme rainfall, is higher than the potential predictability of the extreme rainfall at sub-seasonal time scale (Wang and Yuan 2018). This suggests that atmospheric moisture flux may also be a good indicator for extreme rainfall prediction such as 2016 at sub-seasonal scale.

## References

- Yuan, X., S. Wang, and Z.-Z. Hu, 2018: Do climate change and El Niño increase likelihood of Yangtze River extreme rainfall? *Bull. Amer. Meteor. Soc.*, **99**, S113-S117, doi:10.1175/BAMS-D-17-0089.1
- Wang, S., and X. Yuan, 2018: Extending seasonal predictability of Yangtze River summer floods. *Hydrol. Earth Syst. Sci. Discuss.*, <https://doi.org/10.5194/hess-2018-112>, in review.

## 2. SUBSEASONAL TO SEASONAL EXTREMES

42<sup>nd</sup> NOAA Annual Climate Diagnostics and  
Prediction Workshop

23-26 October 2017, Norman, Oklahoma





## Skillful Empirical Subseasonal Prediction of Landfalling Atmospheric River Activity Using the Madden-Julian Oscillation and the Quasi-biennial Oscillation

Bryan D. Mundhenk, Elizabeth A. Barnes, Eric D. Maloney, and Cory F. Baggett

*Department of Atmospheric Science, Colorado State University, Fort Collins, CO*

### ABSTRACT

Upon landfall, atmospheric rivers (ARs)—plumes of intense water vapor transport—often trigger weather and hydrologic extremes. Presently, no guidance is available to alert decision makers to anomalous AR activity within the subseasonal time scale (~2–5 weeks). Here, we construct and evaluate an empirical prediction scheme for anomalous AR activity based solely on the initial state of two prominent modes of tropical variability: the Madden-Julian oscillation (MJO) and the quasi-biennial oscillation (QBO). The MJO—the dominant mode of intraseasonal variability in the tropical troposphere—modulates landfalling AR activity along the west coast of North America by exciting large-scale circulation anomalies over the North Pacific. In light of emerging science regarding the modulation of the MJO by the QBO—the dominant mode of interannual variability in the tropical stratosphere—we demonstrate that the MJO–AR relationship is further influenced by the QBO. Evaluating the prediction scheme over 36 boreal winter seasons, we find skillful subseasonal “forecasts of opportunity” when knowledge of the MJO and the QBO can be leveraged to predict periods of increased or decreased AR activity (Fig. 1). Certain MJO and QBO phase combinations provide empirical subseasonal predictive skill for anomalous AR activity that exceeds that of a state-of-the-art numerical weather prediction model. Given the wide-ranging impacts associated with landfalling ARs, even modest gains in the subseasonal prediction of anomalous AR activity may support decision making and benefit numerous sectors of society.

This work was published in *npj Climate and Atmospheric Science* in 2018.

### References

Mundhenk, B., E. A. Barnes, E. Maloney, and C. F. Baggett, 2018: Skillful empirical subseasonal prediction of landfalling atmospheric river activity using the Madden-Julian Oscillation and the Quasi-biennial Oscillation. *npj Climate and Atmospheric Science*, doi: 10.1038/s41612-017-0008-2.

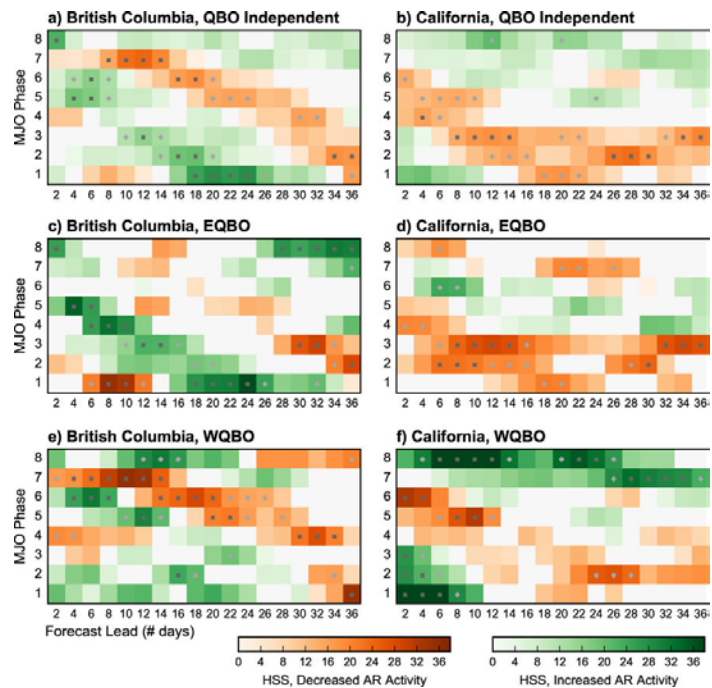


**Fig. 1** Heidke skill score (HSS) values as a function of MJO phase (y axis) and forecast lead time (x axis) for the British Columbia (left column) and California (right column) landfall boundaries, (a, b) independent of the state of the QBO, as well as conditioned on (c, d) easterly QBO (EQBO) and (e, f) westerly QBO (WQBO). Only conditional combinations where the HSS is positive are shaded. The shading is based on the dominant AR activity response: decreased activity (oranges) or increased activity (greens). Statistical significance of the skill scores is denoted by the light gray diamonds ( $\geq 80$ th percentile) and dark gray squares ( $\geq 90$ th percentile), based on 1000 block bootstrap samples.



## The Impact of El Niño Southern Oscillation on Winter and Early Spring U.S. Tornado Outbreaks

Ashton Robinson Cook<sup>1</sup>, Lance M. Leslie<sup>2</sup>, David B. Parsons<sup>2</sup>, and Joseph T. Schaefer<sup>3</sup>

<sup>1</sup>NOAA Storm Prediction Center and School of Meteorology, University of Oklahoma, Norman, Oklahoma

<sup>2</sup>School of Meteorology, University of Oklahoma, Norman, Oklahoma

<sup>3</sup>Embry-Riddle Aeronautical University, Daytona Beach, Florida

### ABSTRACT

In recent years, the topic of seasonal predictability of tornado outbreaks has attracted the attention of researchers. Previous studies on this matter have focused mainly on the influence of global circulation patterns (*e.g.*, El Niño Southern Oscillation (ENSO), North Atlantic Oscillation, Pacific Decadal Oscillation) on tornado outbreaks. However, these studies have yielded conflicting results of the roles of these climate drivers on tornado intensity and frequency. The present study seeks to establish linkages between ENSO and tornado outbreaks over the U.S. during winter and early spring. These linkages are established in two ways: 1) Statistically, by relating raw counts of tornadoes in outbreaks (defined as six or more tornadoes in a 24-hour period in the U.S. east of the Rocky Mountains), and their destructive potential, to sea surface temperature anomalies observed in the Niño 3.4 region; and 2) Qualitatively, by relating ENSO to shifts in synoptic-scale atmospheric phenomena that influence to tornado outbreaks. The latter approach is critical for interpreting the statistical relationships, thereby avoiding the deficiencies in previous studies that failed to provide physical explanations relating ENSO to shifts in tornado activity. The results suggest shifts in tornado occurrence are clearly related to ENSO. In particular, La Niña conditions consistently foster more frequent and intense tornado activity compared with El Niño, particularly at higher latitudes (Fig. 1). Tornado activity changes are tied not only to the location and intensity of the subtropical jet during individual outbreaks, but also to the positions of surface cyclones, low-level jet streams, and instability axes.

This work has been published in the *Journal of Applied Meteorology and Climatology* in September 2017.

### References

Cook, A.R., L.M. Leslie, D.B. Parsons, and J.T. Schaefer, 2017: The impact of El Niño–Southern Oscillation (ENSO) on winter and early spring U.S. tornado outbreaks. *J. Appl. Meteor. Climatol.*, **56**, 2455–2478, <https://doi.org/10.1175/JAMC-D-16-0249.1>

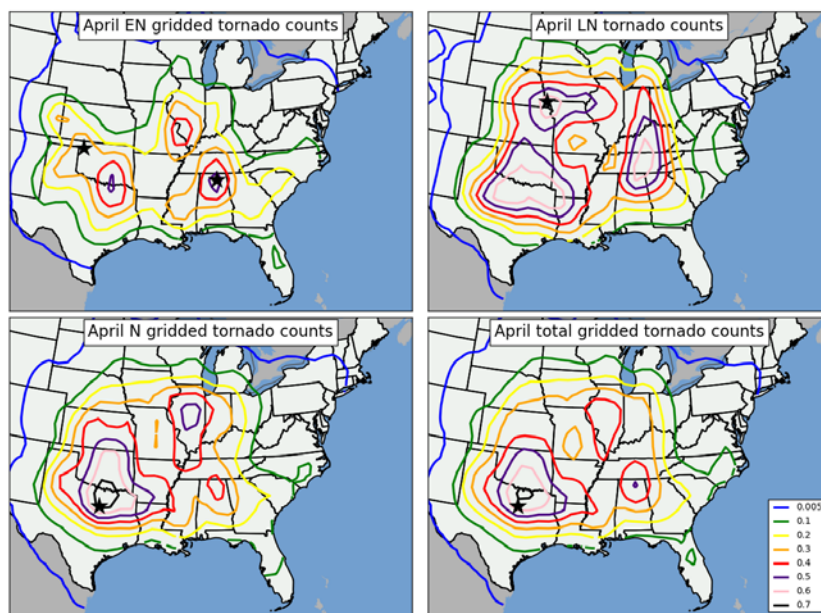


**Fig. 1** Contour plots representing normalized gridded tornado counts during April in each ENSO phase. Tornado data was normalized against the number of April months classified as El Niño (EN), La Niña (LN), and Neutral (N). The black stars indicate locations of maximum normalized tornado occurrences.

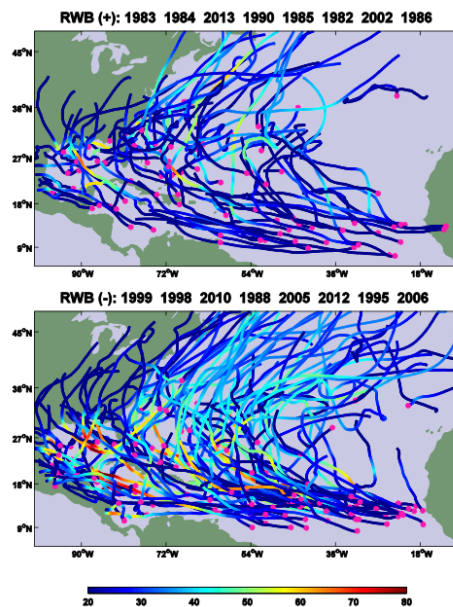
## Extratropical Impacts on Atlantic Tropical Cyclone Activity via Rossby Wave Breaking

Zhuo Wang

University of Illinois at Urbana-Champaign

### ABSTRACT

With warm sea surface temperature (SST) anomalies in the tropical Atlantic and cold SST anomalies in the east Pacific, the unusually quiet hurricane season in 2013 was a surprise to the hurricane community. The authors' analyses suggest that the substantially suppressed Atlantic tropical cyclone (TC) activity in August 2013 can be attributed to frequent breaking of midlatitude Rossby waves, which led to the equatorward intrusion of cold and dry extratropical air. Rossby wave breaking (RWB) perturbs the wind and moisture fields throughout the troposphere in the vicinity of a breaking wave. When RWB occurs more frequently over the North Atlantic, the Atlantic main development region (MDR) is subject to stronger vertical wind shear and reduced tropospheric moisture; the basinwide TC counts are reduced, and TCs are generally less intense, have a shorter lifetime, and are less likely to make landfalls (Fig. 1). A significant negative correlation was found between Atlantic TC activity and RWB occurrence during 1979–2013. The correlation is comparable to that with the MDR SST index and stronger than that with the Niño-3.4 index (Fig. 1).



	RWB+	RWB-
TC #	86	127
HURR#	29	70

Significant correlation btw. RWB and TC was found for July-Oct (1979-2013)

1979-2013	Hurr #	ACE
<b>RWB</b>	<b>-0.68</b>	<b>-0.74</b>
<b>MDR SST</b>	<b>0.64</b>	<b>0.65</b>
<b>Nino3.4</b>	<b>-0.42</b>	<b>-0.37</b>

**Fig. 1** (Left) Composites of TC tracks based on the RWB index; (upper right) the number of named tropical cyclones and hurricanes in eight positive years and eight negative years of the RWB index; (lower right) correlations between the TC activity indices (hurricane counts and accumulated cyclone energy) and climate indices during 1979-2013. (Adapted from Zhang *et al.* 2017)

Further analyses suggest that the variability of RWB occurrence in the western Atlantic is largely independent of that in the eastern Atlantic. The RWB occurrence in the western basin is more closely tied to the environmental variability of the tropical North Atlantic and is more likely to hinder TC intensification or reduce the TC lifetime because of its proximity to the central portion of TC tracks. Consequently, the basinwide TC counts and the accumulated cyclone energy have a strong correlation with western-basin RWB occurrence but only a moderate correlation with eastern-basin RWB occurrence. The results highlight the extratropical impacts on Atlantic TC activity and regional climate via RWB and provide new insights into the variability and predictability of TC activity.

---

The works presented were published in Journal of Climate in 2017 and Journal of Atmospheric Sciences in 2016.

## References

- Zhang, G., Z. Wang, M. Peng, and G. Magnusdottir, 2017: Characteristics and Impacts of Extratropical Rossby Wave Breaking during the Atlantic Hurricane Season, *J. Climate*, **30**, 2363–2379.  
<http://journals.ametsoc.org/doi/abs/10.1175/JCLI-D-16-0425.1>
- Zhang, G., Z. Wang, T. Dunkerton, M. Peng, and G. Magnusdottir, 2016: Extratropical Impacts on Atlantic Tropical Cyclone Activity, *J. Atmos. Sci.*, **73**, 1401–1418.  
<http://journals.ametsoc.org/doi/abs/10.1175/JAS-D-15-0154.1>

## Developing an Experimental Week 2–4 Severe Weather Outlook for the United States

Hui Wang<sup>1</sup>, Alima Diawara<sup>1,2</sup>, Arun Kumar<sup>1</sup>, David DeWitt<sup>1</sup>

<sup>1</sup>Climate Prediction Center, NOAA/NWS/NCEP, College Park, MD

<sup>2</sup>Innovim, LLC, Greenbelt, MD

### 1. Introduction

Developing week 2 to 4 severe weather outlooks is one of the CPC projects under the Office of Science and Technology Policy initiative. The goals of this project are (1) to expand development and perform evaluation of week-2 severe weather model guidance in the first year, and (2) to explore the potential and develop experimental forecast tools for week 3 and 4 severe weather in the second year. The results presented at the workshop focus on week 2 forecast.

Based on different timescales, forecasts can be categorized into three types. One is short-term prediction for several days, mainly determined by initial conditions. Another is seasonal outlook from one month to several seasons. At this timescale, slow evolving components, such as SST, ENSO and AMO, are the sources of predictability. In-between is the extended-range prediction from week 2 to week 4. At this time range, the forecast skill is relatively low mainly due to a lack of source of predictability.

A recent study by Carbin *et al.* (2016) uses the Supercell Composite Parameter (SCP) derived from the CFSv2 45-day forecast to provide extended-range severe weather environment guidance. When SCP is greater than one, it is expected that severe weather will likely occur. Here we take one more step to forecast severe weather based on empirical relationship between model predicted SCP and actual severe weather in historical records.

### 2. Data and methods

The data used in this study consist of both observational data and model forecast. For observations, the Climate Forecast System Reanalysis (CFSR) and local storm report (LSR) are employed. The LSR includes hail, tornado, and damaging wind, as well as their location, time and intensity. The sum of the LSRs for hail, tornado and damaging wind are referred to as LSR3 hereafter. They are re-gridded to a  $0.5^\circ \times 0.5^\circ$  grid. We use the NCEP GEFS 16-day hindcasts for week 2. Hindcast period is from 1996 to 2012. The hindcasts were made every 4 days with 5 members and a  $0.5^\circ \times 0.5^\circ$  resolution. The analysis presented was performed with the 5-member ensemble mean.

Following Carbin *et al.* (2016),

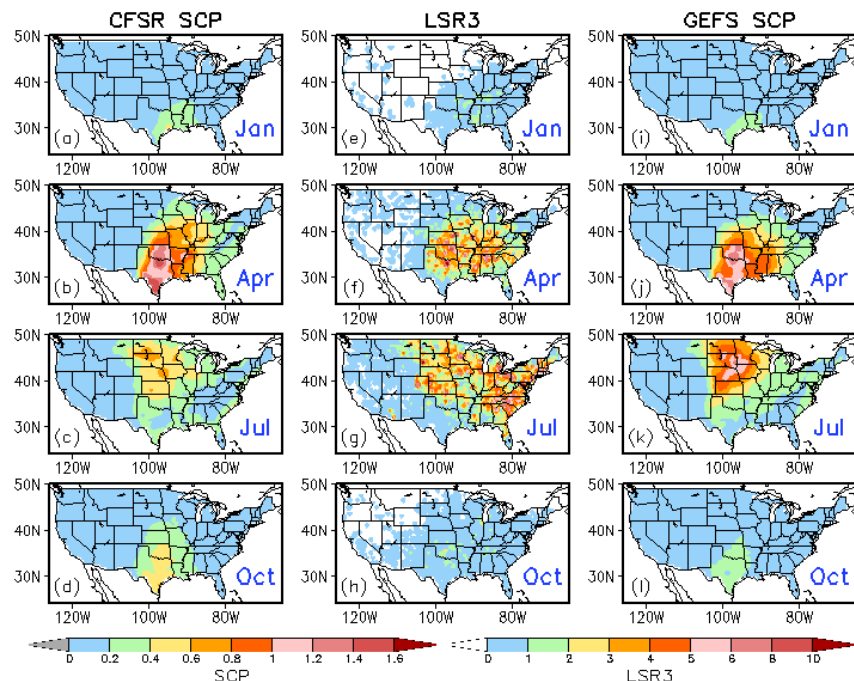


**Fig. 1** Climatological monthly mean daily SCP for January, April, July and October derived from (a–d) CFSR and (i–l) GEFS day-1 forecast and (e–h) observed climatological monthly LSR3 in the period of 1996–2012.



the SCP is defined as

$$\text{SCP} = (\text{CAPE}/1000 \text{ J kg}^{-1}) \times (\text{SRH}/50 \text{ m}^{-2} \text{ s}^{-2}) \times (\text{BWD}/20 \text{ m s}^{-1}),$$

where CAPE is convective available potential energy, SRH storm-relative helicity, and BWD bulk wind difference. The three constants are used to normalize SCP so that when SCP is greater than 1, there is a chance for severe weather to occur.

The forecast model developed in this study is a hybrid dynamical-statistical model (*e.g.*, Wang *et al.* 2009). It uses the dynamical model (GEFS) predicted SCP as a predictor, and then forecast severe weather (LSR3) based on the statistical relationship between model SCP and actual LSR3 in historical records. The forecast skill is cross-validated over the GEFS hindcast period (1996–2012).

### 3. Results

The observed seasonality of SCP is examined first. Figure 1a–d shows the climatological monthly mean daily SCP over the U.S. for January, April, July, and October, respectively, derived from CFSR. The seasonal variation of SCP is characterized by relatively large values of SCP appearing in the Gulf States during winter months. Then SCP intensifies and peaks in spring. The region of the maximums moves northward from the Southern Plain in spring to the Northern Plain in summer. From summer to the following winter, the SCP value decreases and the center of the maximums moves back to the south. The SCP displays strong seasonality over the central U.S. Over the same region, the LSR3 also shows similar seasonality with strong severe weather activity in spring and summer (Fig. 1e–h). During these two seasons, however, there are also strong activities in the eastern U.S. where SCP value is small. Therefore, in terms of seasonal cycle, there is a good correspondence between SCP and LSR3 in the central U.S.

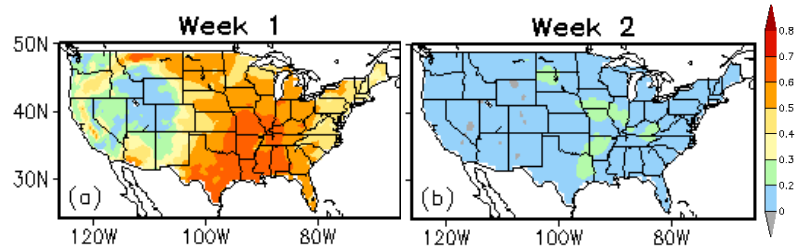


**Fig. 2** Anomaly correlation between SCPs from CFSR and GEFS hindcasts for (a) week 1 and (b) week 2 over the 1996–2012 period.

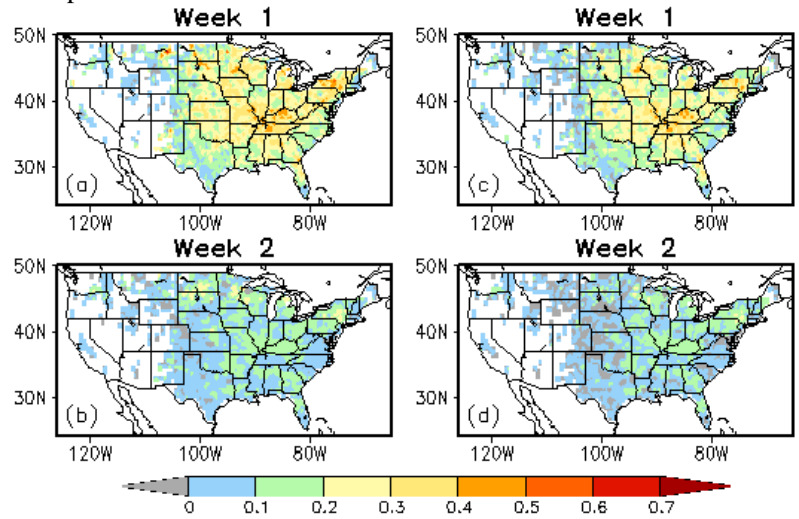


**Fig. 3** Correlations between observed LSR3 and SCP from the GEFS hindcasts for (a) week 1 and (b) week 2 and anomaly correlations between observed LSR3 and predicted LSR3 from the dynamical-statistical model for (c) week 1 and (d) week 2 based on cross-validations over the 1996–2012 GEFS hindcast period.

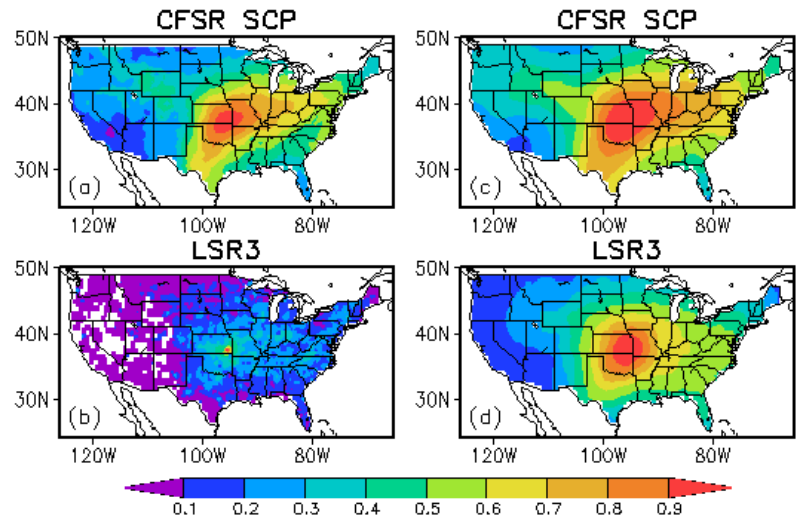


**Fig. 4** One-point correlation map between the observed weekly anomaly (1996–2012) at (95.5°W, 37.5°N) and that at each grid point over the U.S. for (a) CFSR SCP and (b) LSR3 at 0.5°×0.5° grid and for (c) CFSR SCP and (d) LSR3 averaged over 5°×5° boxes, respectively.

For comparing the seasonal cycle between observations and GEFS forecast for SCP, Fig. 1 i–l also shows the long-term monthly mean SCP from the GEFS day-1 forecasts. Overall, the model captures the observed seasonality of SCP. For other leads (day-2 to day-14 forecasts), the monthly climatology of SCP slightly decreases with lead time (not shown).

The GEFS forecast skill for SCP is assessed by anomaly correlation (AC) between GEFS SCP and CFSR SCP. The forecast skill decreases with lead time from day 1 to day 14. Particularly, there is a sharp decrease from day 7 to day 8 (not shown). Consistently, the week-2 forecast skill is much lower than week 1, as shown in Fig. 2.

To develop a hybrid forecast model, we first need to establish some relationship between GEFS predicted SCP and observed LSR3. The relationship is the basis for the dynamical-statistical prediction. Given the strong seasonality of both SCP and LSR3 (Fig. 1), a 3-month moving window is used in the analysis. As an example, Fig. 3a–b shows the correlations between observed LSR3 and GEFS week-1 and week-2 forecasts of SCP, respectively, for March, April, and May (MAM), the peak severe weather season. The correlation with the week-2 forecast is less than the week-1 forecast, indicating a weak relationship between GEFS SCP and LSR3 for week 2.

A linear regression model is developed to forecast the number of severe weather (LSR3) using the GEFS predicted SCP as a predictor and based on their relationship depicted in Fig. 3a–b. The forecast skill is cross-validated over the GEFS hindcast period (1996–2012). The anomaly correlation skills (Fig. 3c–d) for week 1 and week 2 are very similar to the corresponding correlations between GEFS SCP and LSR3 (Fig. 3a–b). The forecast skill is low, especially for week 2.

The difficulty in forecasting severe weather is mainly due to its short lifetime and small spatial scale. Figure 4a–b shows the one-point correlation map for weekly CFSR SCP and LSR3, respectively, at the  $0.5^\circ \times 0.5^\circ$  grid. It is the correlation map between weekly anomaly at one grid point (here  $95.5^\circ\text{W}$ ,  $37.5^\circ\text{N}$ ) and that at every grid point over the U.S. For SCP (Fig. 4a), there are high correlations between the selected grid point and the surrounding grid points, indicating that SCP has a large-scale feature. For LSR3 (Fig. 4b), in contrast, the correlations are small, except the correlation with itself, consistent with the small spatial scale of severe weather. However, when averaging LSR3 over a  $5^\circ \times 5^\circ$  box and then recalculating the one-point correlation map, the result (Fig. 4d) shows much higher spatial coherence for LSR3 and is comparable to that of SCP (Fig. 4c).

Next, we use the  $5^\circ \times 5^\circ$  area-averaged anomalies to reestablish the relationship between model SCP and observed LSR3. Their

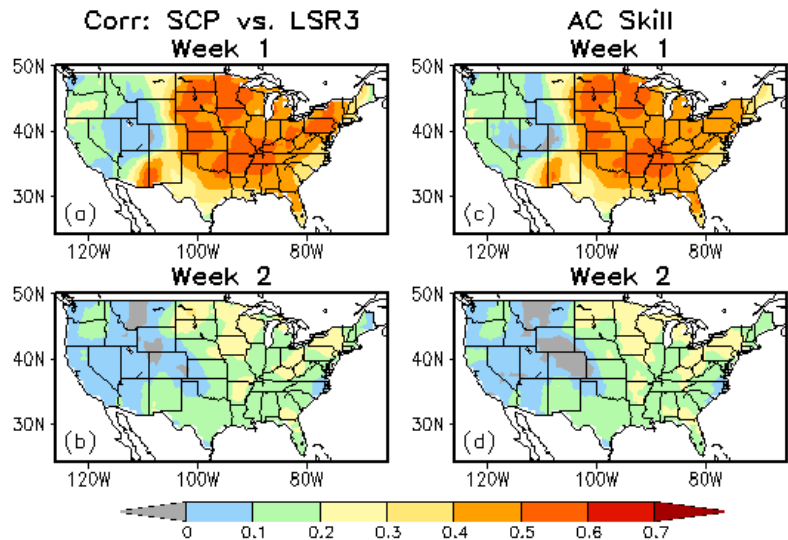


**Fig. 5** Same as Fig. 3, but for anomalies averaged over the  $5^\circ \times 5^\circ$  box.

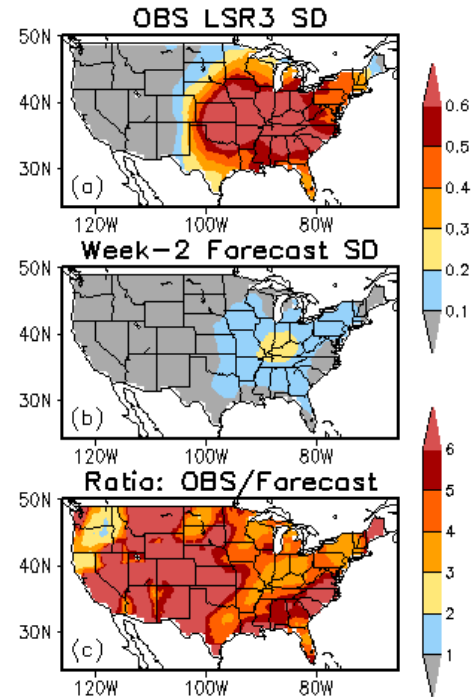


**Fig. 6** Standard deviation of (a) observed weekly LSR3 and (b) week-2 forecast and (c) ratio of the observed standard deviation to the week-2 forecast.



correlations (Fig. 5a–b) are much higher than the  $0.5^\circ \times 0.5^\circ$  grid (Fig. 3a–b) for both week 1 and week 2. Similarly, the forecast skill of the hybrid model is significantly improved (Fig. 5c–d) by using the  $5^\circ \times 5^\circ$  area-averaged anomalies.

Figure 6 shows the spatial distribution of the standard deviation of the observed weekly LSR3 (top) and that of the week-2 forecast (middle) from the hybrid model, respectively, as well as the ratio of the observed standard deviation to the forecast (bottom). The amplitude of the forecasted anomalies is much smaller than the observed. Their ratio is greater than 3 over most of the U.S.

The forecast of the total weekly LSR3 is the hybrid model predicted anomaly plus the observed weekly climatology. Because the amplitude of the forecasted anomalies is much smaller than the observed, the forecast of the total LSR3 tends toward the observed climatology. To avoid this, we can make adjustment for the forecasted anomaly by multiplying it with the ratio in Fig. 6c. In this way, the amplitude of the forecasted anomalies will be closer to the observations. However, this procedure cannot improve the anomaly correlation skill, but may reduce the root-mean-square error of the forecast.

Figure 7 shows an example for the week of May 24 to 30, 2011. On May 24, 2011, there was a tornado outbreak in central and northern Oklahoma. By the end of that day, there were one EF5 tornado, two EF4 and two EF3 tornadoes. Figure 7a is the distribution of weekly total LSR3 with  $5^\circ \times 5^\circ$  area-averages. The week-2 forecast and the adjusted forecast are presented in Fig. 7b and 7c, respectively. For this extreme event, some signals in the week-2 forecast are consistent with the observations.

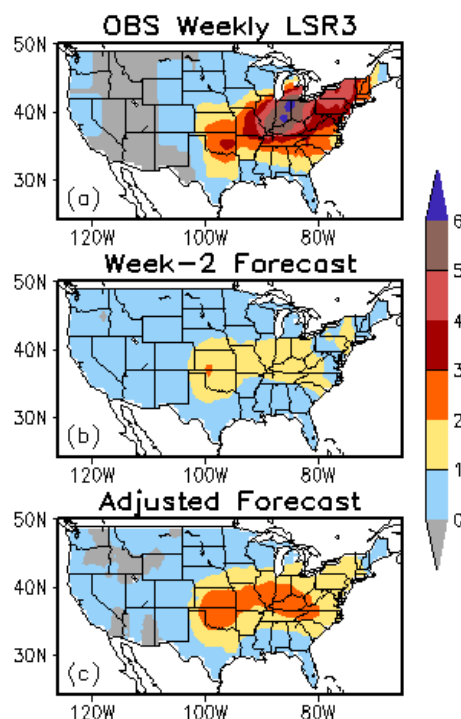


**Fig. 7** (a) Observed weekly LSR3, (b) week-2 forecast, and (c) adjusted week-2 forecast for the week of May 24–30, 2011.

#### 4. Conclusions

Following Carbin's work, the Supercell Composite Parameter (SCP) was selected as a variable to represent the large-scale environment and link the model forecast to actual severe weather. The hybrid model forecasts suggest a low skill for week-2 severe weather. However, the forecast can be improved by using the  $5^\circ \times 5^\circ$  area-averaged anomalies and the adjustment of the amplitude of the forecasted anomalies.

For future work, we plan to extend the analysis for weeks 3 and 4 using the CFSv2 45-day hindcasts and forecasts. Because the forecast skill for week-2 SCP is already low, we will also need to explore other potential predictors for weeks 3 and 4.

**Acknowledgements.** We would like to thank our colleagues Brad Pugh, Daniel Harnos, Jon Gottshalck, and Stephen Baxter at CPC for helpful discussions and Yuejian Zhu and Hong Guan at EMC for providing GEFS model forecast data.

#### References

- Carbin, G. W., M. K. Tippett, S. P. Lillo, and H. E. Brooks, 2016: Visualizing long-range severe thunderstorm environment guidance from CFSv2. *Bull. Amer. Meteor. Soc.*, **97**, 1021–1032.
- Wang H., J.-K. E. Schemm, A. Kumar, W. Wang, L. Long, M. Chellian, G. D. Bell, and P. Peng, 2009: A statistical forecast model for Atlantic seasonal hurricane activity based on the NCEP dynamical seasonal forecast. *J. Climate*, **22**, 4481–4500.

## Gulf of Mexico Influence on Sub-seasonal and Seasonal Severe Thunderstorm Frequency

Maria J. Molina<sup>1</sup>, John T. Allen<sup>1</sup>, and Vittorio A. Gensini<sup>2</sup>

<sup>1</sup>Department of Earth and Atmospheric Sciences, Central Michigan University, Mount Pleasant, MI

<sup>2</sup>Department of Geographic and Atmospheric Sciences, Northern Illinois University, DeKalb, IL

### 1. Introduction

Considerable year-to-year variability is evident in the Storm Prediction Center (SPC) tornado data set, despite inherent non-meteorological limitations (Fig. 1 left panel; Verbout *et al.*, 2006; Doswell *et al.*, 2009; Edwards *et al.*, 2013). Year-to-year variability is also present when considering billion-dollar severe thunderstorm disaster events (Fig. 1 right panel; Smith and Matthews, 2015). A better understanding as to why tornado activity can vary considerably from one year to the next can help the public and insurers better prepare for future severe thunderstorm activity. Previous studies have identified relationships between the climate system and severe thunderstorms during the winter (DJF) and spring (MAM) seasons, including the El Niño-Southern Oscillation (ENSO; Allen *et al.*, 2015; Cook *et al.*, 2017) and Gulf of Mexico (GoM) sea surface temperatures (SSTs; Molina *et al.*, 2016). La Niña has been related to increases in the frequency of tornadic activity across areas east of the Rocky Mountains, due increased leeside cyclogenesis and meridional flow (Allen *et al.*, 2015; Cook *et al.*, 2017). In contrast, El Niño has been associated with decreases in tornado frequency inland of the Gulf Coast (Allen *et al.*, 2015; Cook *et al.*, 2017). Warm (cold) GoM SSTs serve as a source of increased (decreased) moisture and buoyancy for advection towards the contiguous United States (CONUS), potentially contributing to severe thunderstorm development (Molina *et al.*, 2016).

### 2. Methodology

In order to explore the year-to-year variability associated with tornadic activity, the GoM, and ENSO, this study uses the significant tornado parameter (STP; Thompson *et al.*, 2003), serving as an environmental proxy of significant tornadoes (F/EF2+). STP values greater than one have been associated with most F/EF2 or greater intensity tornadoes, while STP values less than one have been associated with mostly non-tornadic

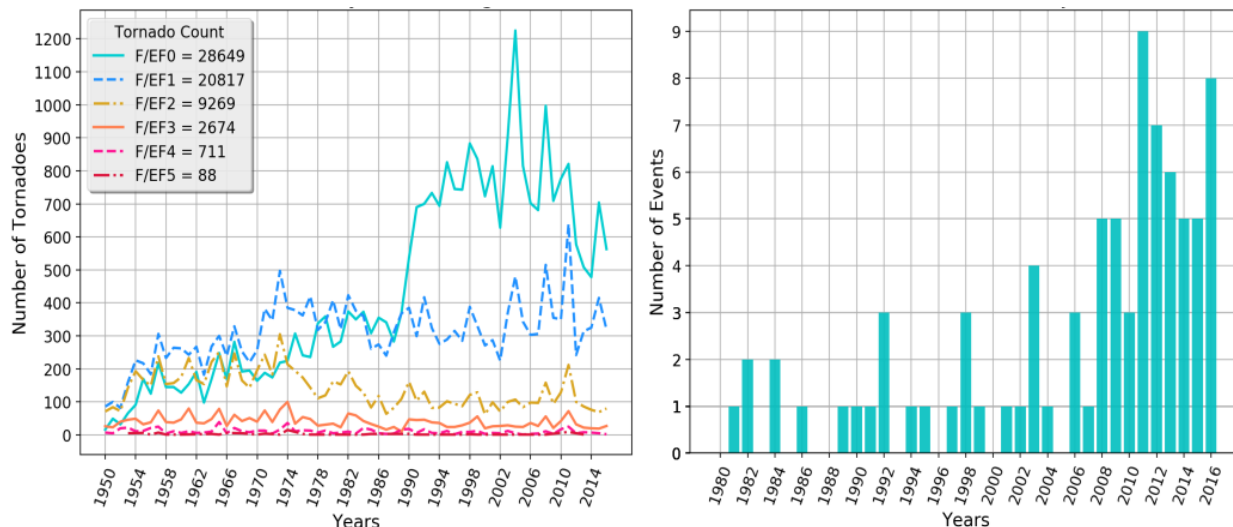


**Fig. 1** Tornadoes (1950-2016) in the U.S. stratified by E/EF intensity (left) and billion-dollar severe thunderstorm disaster events (Consumer Price Index (CPI) adjusted; right).

supercells (Thompson *et al.*, 2003). Mirroring the formulation from Thompson *et al.*, (2003) and Gensini and Marinaro, (2015), STP as used in this study is:

$$STP = \frac{sbCAPE}{1500 \text{ J kg}^{-1}} \times \frac{(2000 - sbLCL)}{1000 \text{ m}} \times \frac{SRH01}{150 \text{ m}^2 \text{ s}^{-2}} \times \frac{BWD06}{20 \text{ m s}^{-1}}$$

where sbCAPE is surface-based convective available potential energy, sbLCL is surface-based lifting condensation level, SRH01 is storm relative helicity from 0-1 km, and BWD06 is bulk wind difference from 0-6 km (Thompson *et al.*, 2003). Using the North American Regional Reanalysis (NARR; 1982-2016) data set of 32 km horizontal grid spacing and 3-hourly temporal resolution (Mesinger *et al.*, 2006), a binary data set was constructed from STP. Grid cells with  $STP \geq 1$  were assigned a value of 1, and grid cells with  $STP < 1$  were assigned a value of zero (named “STP Hours” in this study), where STP Hours encompass a 3-hour time period. A climatology of STP was constructed for DJF and MAM (Fig. 2).

The climatology of DJF 3-hourly mean STP Hours shows values of approximately 10-15 hours across southeast Texas, Louisiana, and southern Arkansas, which is equivalent to about 45 hours of  $STP \geq 1$ . MAM 3-hourly mean STP Hours shows values of greater magnitude than DJF, of approximately 20-40 from eastern Texas to the mid-south region. This is equivalent to approximately 5 full days of  $STP \geq 1$ . A series of composite analyses were run using daily, 0.25-degree resolution SST anomalies (SSTAs; Reynolds *et al.*, 2007) and STP Hours, to explore the relationship between GoM SSTA variability and a favorable tornadic environment. Statistical significance was determined using a 95-percentile, two-tailed test from a bootstrapped set of composite differences.

### 3. Results

Results show that during DJF, the warmest quartile (25%) of GoM SSTAs results in a significant 50-66% increase in STP Hours frequency from northeastern Texas to the Great Lakes region, while the coldest quartile results in a 20-33% decrease in STP Hours frequency across the south (Fig. 3 upper two panels). MAM results show that the warmest GoM quartile results in a significant increase in STP Hours frequency across central Texas, while the coldest GoM quartile results in a significant decrease in STP Hours frequency across the Great Plains (Fig. 3 lower two panels). These results are physically plausible; warmer GoM SSTs make low level moisture more readily available for advection to the CONUS (east of the Rockies), resulting in greater buoyancy available for storm development. These results are consistent when considering ENSO-neutral years (not shown), suggesting that GoM SSTs can serve as an independent predictand for MAM and potentially DJF severe thunderstorms, during ENSO and ENSO-neutral years. It is important to note that a favorable tornado environment does not necessarily lead to convective initiation, and that a number of other severe thunderstorm formation ingredients are necessary in the development of severe convection. Additionally, the STP parameter applied for this analysis is not without limitations. STP is calibrated for identifying conditions favorable to strong tornadoes produced by discrete supercells, and was formulated primarily for the Great Plains, and thus does not account for all strong tornado events (Thompson *et al.*, 2003). Thus, STP will not capture the full range of possible tornado environments. Overall, the results here suggest that GoM weights the likelihood of severe thunderstorm activity and should be considered a predictor for subseasonal and seasonal forecasts of convective weather.

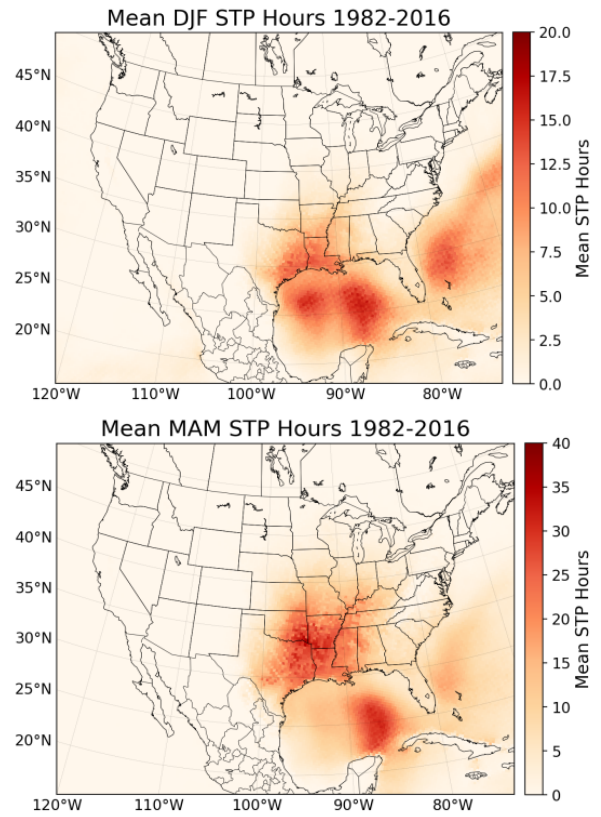


**Fig. 2** 1982-2016 DJF (top) and MAM (bottom) STP Hours climatology.

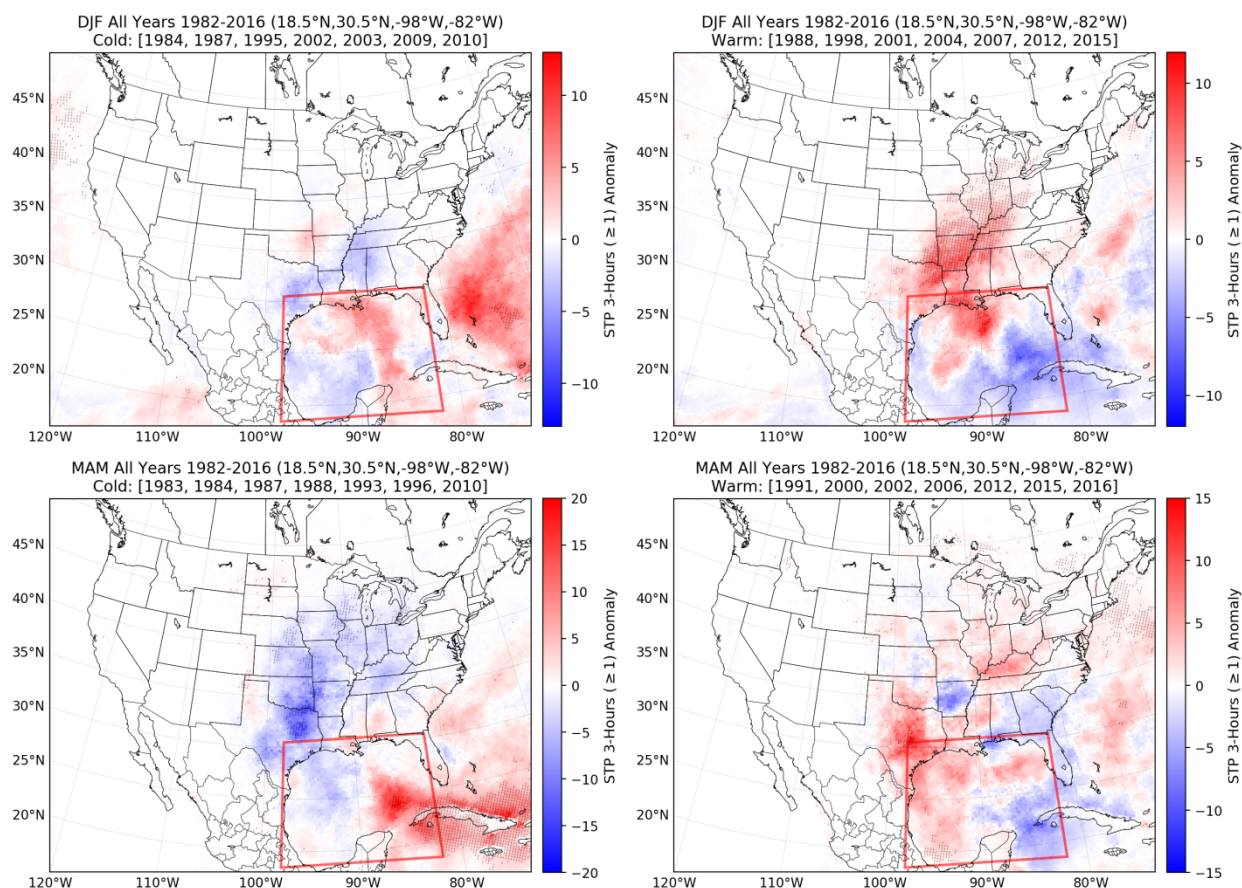


**Fig. 3** GoM coldest (left column) and warmest (right column) SST quartile composites of STP Hours anomalies for DJF (upper panels) and MAM (lower panels).

## References

- Allen, J. T., M. K. Tippett, and A. H. Sobel, 2015: Influence of the El Niño-Southern Oscillation on tornado and hail frequency in the United States. *Nat. Geosci.*, **8**, 278–283, doi:10.1038/ngeo2385.
- Cook, A. R., L. M. Leslie, D. B. Parsons, and J. T. Schaefer, 2017: The impact of the El Niño-Southern Oscillation (ENSO) on winter and early spring US tornado outbreaks. *J. Appl. Meteor. Climatol.*, doi:10.1175/JAMC-D-16-0249.1.
- Doswell, C. A., H. E. Brooks, and N. Dotzek, 2009: On the implementation of the enhanced Fujita scale in the USA. *Atmos. Res.*, **93**, 554–563, doi:10.1016/j.atmosres.2008.11.003.
- Edwards, R., J. G. LaDue, J. T. Ferree, K. Scharfenberg, C. Maier, and W. L. Coulbourne, 2013: Tornado intensity estimation: Past, present, and future. *Bull. Am. Meteor. Soc.*, **94**, 641–653, doi:10.1175/BAMS-D-11-00006.1.
- Gensini, V. A., and A. Marinaro, 2015: Tornado frequency in the United States related to global relative angular momentum. *Mon. Wea. Rev.*, **144**, 801–810, doi:10.1175/MWR-D-15-0289.1.
- Mesinger, F., and Coauthors, 2006: North American Regional Reanalysis. *Bull. Amer. Meteor. Soc.*, **87**, 343–360, doi:10.1175/BAMS-87-3-343.
- Molina, M., R. Timmer, and J. Allen, 2016: Importance of the Gulf of Mexico as a climate driver for US severe thunderstorm activity. *Geophys. Res. Lett.*, **43**, doi:10.1002/2016GL071603.
- Reynolds, R. W., T. M. Smith, C. Liu, D. B. Chelton, K. S. Casey, and M. G. Schlax, 2007: Daily high-resolution-blended analyses for sea surface temperature. *J. Climate*, **20**, 5473–5496, doi:10.1175/2007JCLI1824.1.

- 
- Smith, A. B., and J. L. Matthews, 2015: Quantifying uncertainty and variable sensitivity within the US billion-dollar weather and climate disaster cost estimates. *Natural Hazards*, **77**, 1829–1851.
- Thompson, R. L., R. Edwards, J. A. Hart, K. L. Elmore, and P. Markowski, 2003: Close proximity soundings within supercell environments obtained from the rapid update cycle. *Wea. Forecasting*, **18**, 1243–1261, doi:10.1175/1520-0434(2003)018h1243:CPSWSEi2.0.CO;2.
- Verbout, S.M., H. E. Brooks, L.M. Leslie, and D.M. Schultz, 2006: Evolution of the US tornado database: 1954-2003. *Wea. Forecasting*, **21**, 86–93, doi:10.1175/WAF910.1.



## Short-Term Climate Extremes: Probabilistic Forecasts from a Multi-Model Ensemble

Emily J. Becker and Huug van den Dool

Climate Prediction Center, NOAA/NWS/NCEP, College Park, MD  
 and  
 Innovim, LLC, Greenbelt, MD

### 1. Introduction

This study explores the potential for probabilistic forecasts of extremes in monthly mean 2 m temperature and precipitation rate using the North American Multi-Model Ensemble (NMME; Kirtman *et al.* 2014), an ensemble of state-of-the-art coupled global climate models. Extremes are where the real impact of weather and climate are felt, yet there are currently very few forecasts for short-term climate extremes (STCE). Aggregate skill of deterministic forecasts of STCE (as assessed using the anomaly correlation) has previously been found to be higher than the aggregate skill of all forecasts (Becker *et al.* 2013; Becker 2017). This study examines the skill of a proposed forecast system providing probabilities of occurrence of the 15<sup>th</sup> and 85<sup>th</sup> percentile events, based on climatology.

### 2. Methodology

The NMME currently provides real-time guidance for NOAA's operational short-term climate forecasts, and includes a database of retrospective forecasts (1982-2010), used for bias correction, calibration, and skill studies. Seven models from the NMME contribute to this study: NCEP-CFSv2, Environment Canada's CanCM3 and CanCM4, GFDL's CM2.1 and FLOR, NASA-GEOS5, and NCAR-CCSM4. This study spans the hindcast and forecast period from 1982-2016. Verification data is obtained from the GHCN+CAMS station-to-grid 2 m surface temperature dataset (Fan and van den Dool 2008) and the CMAP precipitation rate dataset (Xie and Arkin 1997).

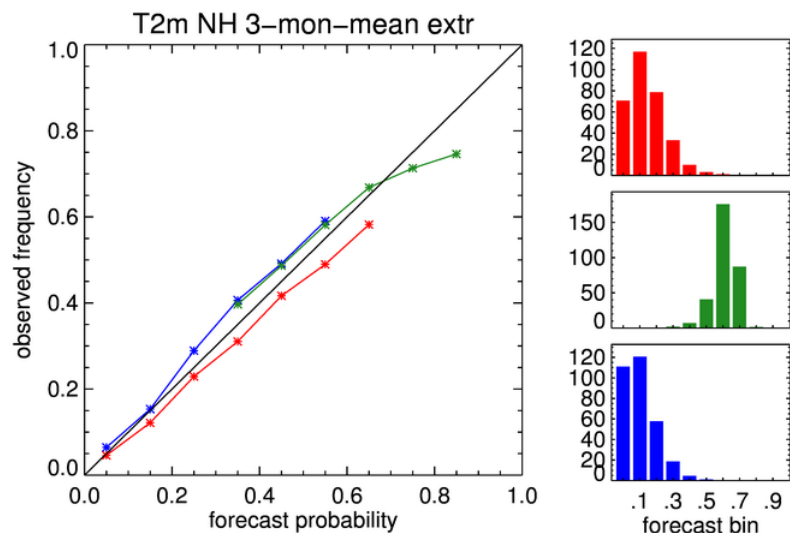


**Fig. 1** 2 m temperature lead-1 3-month-mean reliability diagram showing forecast reliability aggregated over the northern hemisphere and all 12 initial conditions. Forecasts are binned by 10% increments. Histograms show sharpness diagrams, indicating how often each forecast bin was used.

Temperature extremes are herein defined as greater than 1 standard deviation or less than -1 standard deviation away from the mean of the 1982-2010 historical record at each gridpoint. This is very close to the 85<sup>th</sup> and 15<sup>th</sup> percentile. A Gaussian distribution is assumed, but may not be the most accurate fit; this is a point that requires further examination. This study assesses forecast verification, that is, the question of “did the forecast come true?” at a one-month lead for the 3-month mean, over all initial conditions. Forecast probabilities are provided in a 3-category system, where a probability of occurrence is provided for each of the three unequal categories: < -1 standard deviation (SD); > -1 SD and < 1 SD; > 1 SD, very close to 15%/70%/15% climatological likelihood. Observed probabilities are either 1 or 0. Results are compared to

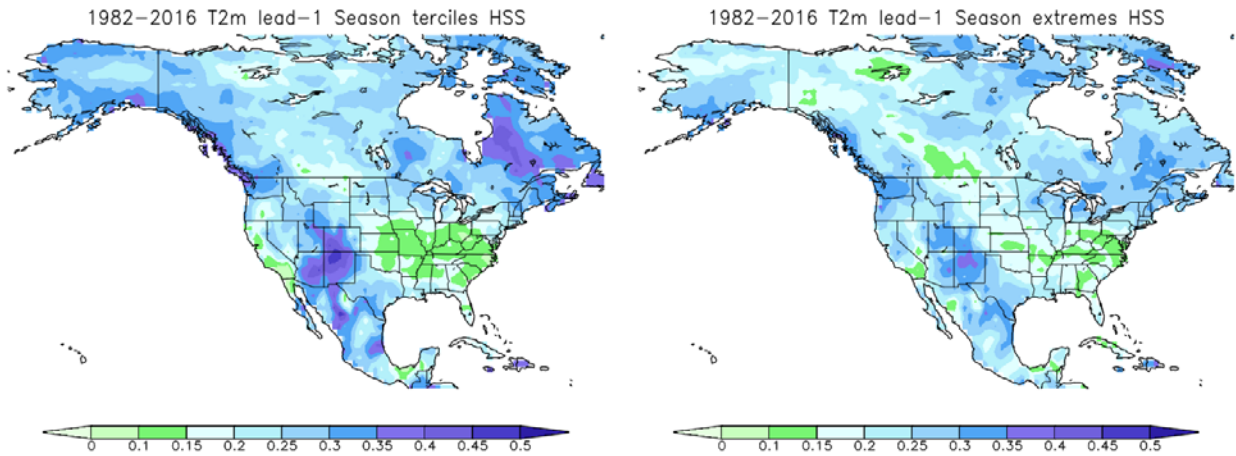


**Fig. 2** Heidke skill score of lead-1 3-month-mean 2 m temperature forecasts, aggregated over all 12 initial conditions. Left panel shows results for the tercile system, right panel for the extremes.

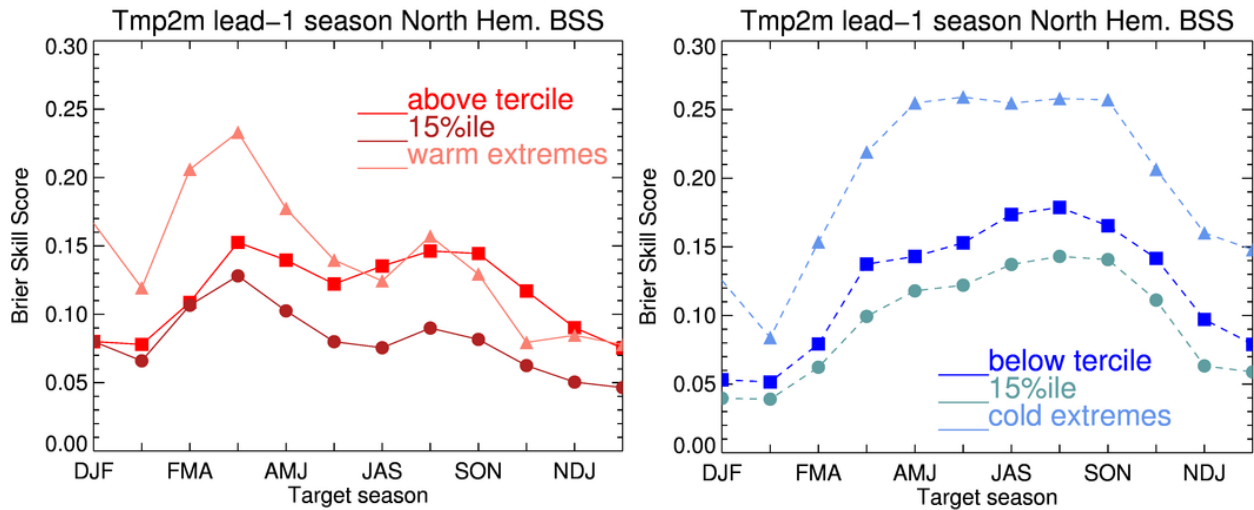


**Fig. 3** Brier skill score of lead-1 3-month-mean 2 m temperature forecast aggregated over the northern hemisphere land. Left panel shows results for the above average tercile, all forecasts in the 15th percentile, and “warm extremes,” where forecasts indicated > 25% probability of an extreme. Right panel shows the same for the below average/cold extremes.

the 3-category, equally likely tercile forecast system that is in use by the Climate Prediction Center: each category has a climatological likelihood of 33.33%. Metrics used in this study include the Brier skill score (BSS), Heidke skill score (HSS), and reliability diagram.

### 3. Results

Cold temperature extremes in the Northern Hemisphere are found to be slightly underforecast in the 1982–2016 data set, while warm extremes are slightly overforecast (Fig. 1); overall, however, the reliability is very good, indicating that forecast probabilities match up with observed frequencies. These are similar patterns to those found when the reliability of the tercile system is assessed. The Heidke skill score for extremes, examined over North America, shows similar annual-aggregate patterns to the terciles, with an area of low skill over the southeastern United States (Fig. 2). In general, HSS of extremes is slightly lower than for terciles; this is not unexpected, given the lower base rate of the extremes (15% climatological threshold). However, in some areas, such as the lower-skill southeastern US, the HSS is slightly higher for the extreme system. When comparing the BSS for the 15/70/15 category system to the BSS of the tercile system, the extremes system results in somewhat lower BSS (Fig. 3). However, when forecasts for extremes are isolated,

in this case by examining only the subset of forecasts where the probability in the extreme category was > 25%, the BSS is found to be generally higher than for forecasts in the tercile system (Fig. 3).

Results for land-only precipitation rate over the northern hemisphere show very low skill for both the extreme and tercile system. Some regions and times show statistically significant positive skill, however. As a forecast for extremes could be issued only when there is reason for confidence, it's possible that a forecast system could be developed for some regions or seasons.

#### 4. Concluding remarks

This is a preliminary study that demonstrates that there is some potential for skillful probabilistic forecasting of extremes. Further experimentation will examine the definition of “extreme”, including possible use of absolute temperature thresholds and the relationship between extreme temperature and precipitation. A large ensemble such as the NMME is valuable in constructing probabilistic forecasts, and further analysis will be necessary to discover valid thresholds for triggering an extreme forecast.

#### References

- Becker, E. J., H. van den Dool, and M. Pena, 2013: Short-term climate extremes: Prediction skill and predictability. *J. Climate*, **26**, 512-531.
- Becker, E. J., 2017: Prediction of short-term climate extremes with a multimodel ensemble. *Climate Extremes: Patterns and Mechanisms*, S.-Y. Wang *et al.* Eds., John Wiley & Sons, Inc. 347-359, doi: 10.1002/9781119068020.ch21
- Fan, Y., and H. van den Dool, 2008: A global monthly land surface air temperature analysis for 1948-present, *J. Geophys. Res.*, **113**, D01103, doi:10.1029/2007JD008470.
- Kirtman, B. P., D. Min, J. M. Infanti, J. L. Kinter, D. A. Paolino, Q. Zhang, H. van den Dool, S. Saha, M. P. Mendez, E. Becker, P. Peng, P. Tripp, J. Huang, D. G. DeWitt, M. K. Tippett, A. G. Barnston, S. Li, A. Rosati, S. D. Schubert, Y.-K. Lim, Z. E. Li, J. Tribbia, K. Pegion, W. Merryfield, B. Denis and E. Wood, 2014: Phase-1 seasonal to interannual prediction, phase-2 toward developing intra-seasonal prediction. *Bull. Amer. Meteor. Soc.*, **95**, 585–601, doi:10.1175/BAMS-D-12-00050.1.
- Xie P., and P. A. Arkin, 1997: Global precipitation: a 17-year monthly analysis based on gauge observations, satellite estimates, and numerical model outputs. *Bull. Amer. Meteor. Soc.*, **78**, 2539-2558.

## CFSv2-based Hybrid Dynamical-Statistical Model for Week 3 to 4 Forecast of Atlantic/Pacific Tropical Storm Activity

Christina Finan, Hui Wang and Jae Schemm

*Climate Prediction Center, NCEP/NWS/NOAA, College Park, MD*

### 1. Introduction

Hybrid models have been utilized to predict tropical cyclone (TC) activity on the seasonal and monthly timescales. Subseasonal variabilities and variations, such as the Madden Julian Oscillation, can enhance or degrade the impacts of TC activity and the likelihood of TC formation. Due to successes in longer-lead forecasts, the NCEP Climate Forecast System v2 (CFSv2) has been used to create a dynamical-statistical model to forecast TC activity for weeks 3 to 4. This is a timescale that sees large variability and improving forecast skill for this time period will bridge a gap between the shorter-lead week-2 forecasts and the longer lead seasonal forecasts. With the improvement of CFSv2 in predicting MJO, the hybrid approach can be applied to predicting TC activity on a shorter timescale. The hybrid model was developed using multiple linear regression relationships derived from CFSv2 forecasts and hindcasts, and observational datasets, similar to that developed for seasonal forecasting (Wang *et al.* 2009). This project uses only CFSv2 data, rather than the North American Multi-model Ensemble, as seen with the seasonal forecasting (Harnos *et al.* 2017), due to availability of data on the daily basis.

### 2. Hybrid model

The model predicts for three northern ocean basins, the Atlantic, the Eastern North Pacific and the Western North Pacific, for 31 weeks of the hurricane season; defined as the first week of May through the last week of November. Three variables, vertical wind shear (VWS), sea level pressure (SLP) and 2-m temperature (T2m) from the CFSv2 dynamical forecasts were tested as predictors for the statistical model. Correlations between the three variables and observed weekly TC days were used to determine the regions of highest correlations for each variable. These area-averaged variables were used as potential predictors in the model to forecast weekly TC days, weekly ACE values and probabilistic forecasts. Multiple and simple linear regression approaches were used to evaluate the potential predictors, performing cross-validations with CFSv2 hindcast data to test each variable individually and all combinations of the three over the 1999 to 2014 period. The results from this test are shown in Fig 1. From this evaluation of forecast skill, 2-meter temperature and vertical wind shear were selected as the best predictors for the model. The same variables, averaged over different regions of skill, were used as predictors for all three basins.

### 3. Forecasts of 2017 hurricane season

Real-time forecasts, both probabilistic and deterministic, were made for weeks 1 to 4 for the 2017 season. For the purpose of this project, we focused on weeks 3 to 4. The deterministic forecasts for the 2017 season are shown in Fig. 2. The correlations between the observed and forecasted values are shown in Table 1. The Eastern North Pacific forecast captured some of the variability in the 2017 season; however, it did over-predict activity for much of the season. The Western

**Table 1** Correlations between the forecasted ACE and observed ACE are shown for week 3 and 4 of 2017 hurricane season for the three basins.

Week	WNP	ENP	ATL
3	0.277	0.474	0.658
4	0.402	0.607	0.657

**Table 2** Heidke skill scores for the probabilistic forecast based on weekly tropical cyclones days are shown for weeks 3 and 4 of 2017 hurricane season for the three basins.

Week	WNP	ENP	ATL
3	-0.09	-1.36	0.07
4	0.14	-1.39	0.09



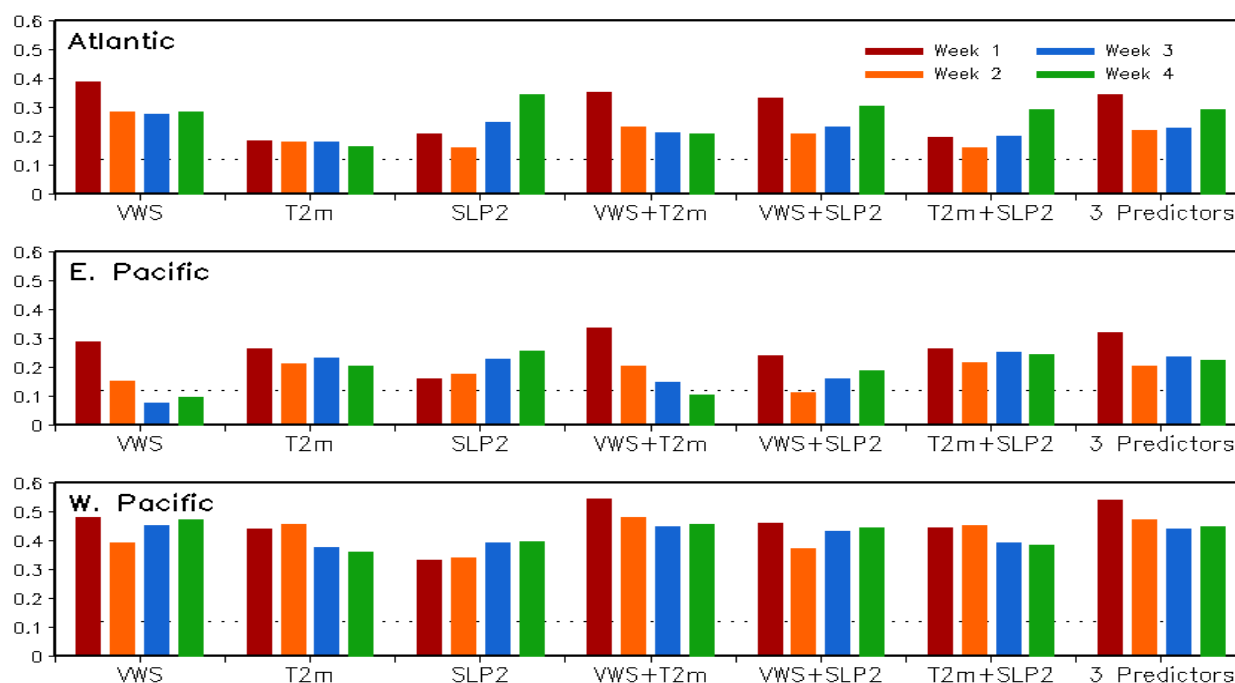


**Fig. 1** Forecast skill for weekly TC activity is shown using the different potential predictors, as well as combinations. These are based on cross-validations over the 1999-2014 period.

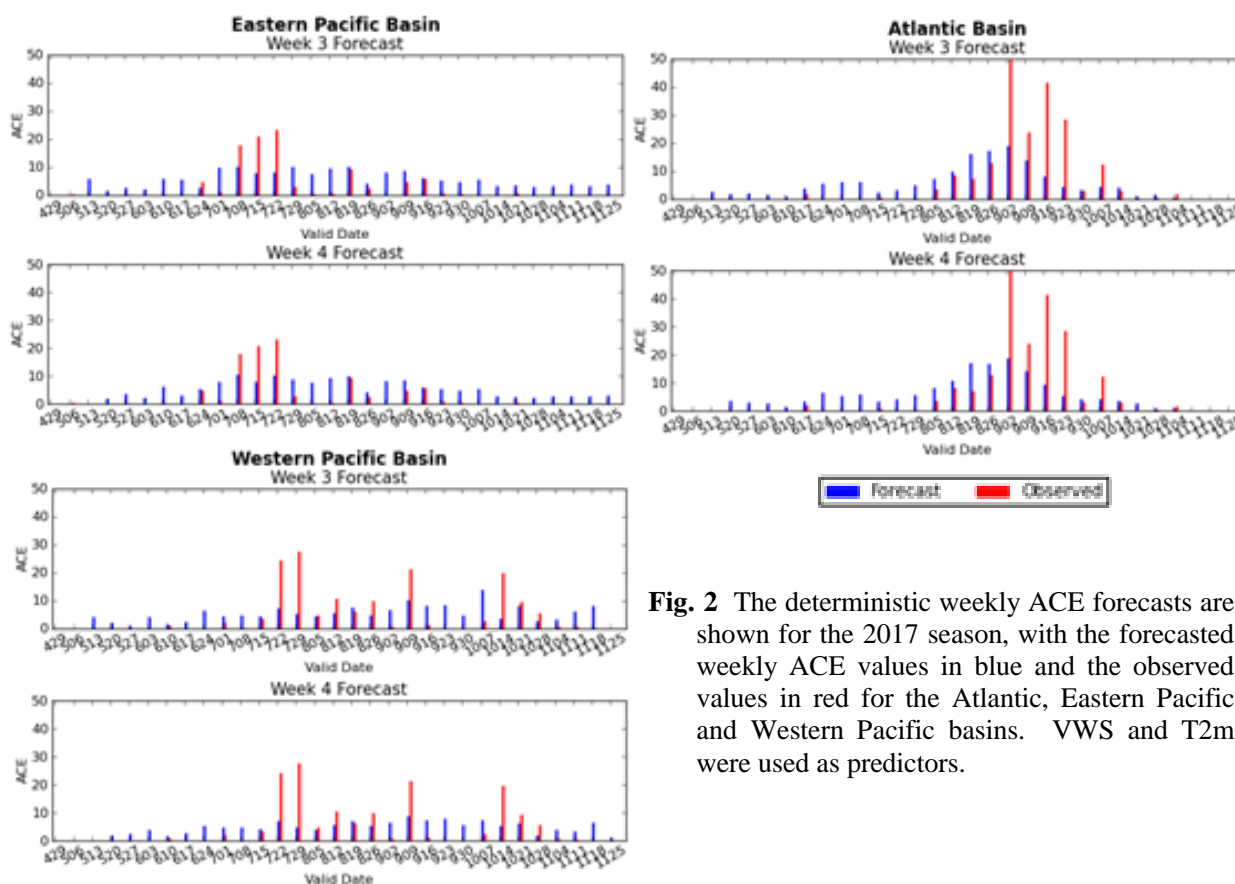


**Fig. 2** The deterministic weekly ACE forecasts are shown for the 2017 season, with the forecasted weekly ACE values in blue and the observed values in red for the Atlantic, Eastern Pacific and Western Pacific basins. VWS and T2m were used as predictors.

North Pacific basin was under-forecast by the model, specifically in the middle of the season. The latter part of the season was actually over-predicted by the model. The model did the best in the Atlantic basin in terms of capturing the peak of activity for the season, though it did fail at capturing the extreme values in the observations. The highest correlations between observed and forecasted activity are for the Atlantic basin, followed by the Eastern North Pacific and Western North Pacific. Overall, week 4 has a higher correlation than week 3 in almost all the basins.

The probabilistic forecasts for weeks 3 and 4 for the 2017 season are shown in Fig 3. The results are for the entire 2017 31-week season, from late April until the end of November. Heidke skill scores for weeks 3 and 4 are shown in Table 2. The hybrid statistical-dynamical model developed for forecasting week 3 and 4 had varied results for the three basins in the probabilistic real-time forecasts through the 2017 season. The Eastern North Pacific had the lowest skill, with negative Heidke skill scores for both weeks 3 and 4. The probabilistic forecast for the Eastern North Pacific basin was above normal for almost the entire season. Further diagnosis into this case is needed to determine what caused such a bias in the probabilistic forecast, when observations were near normal, if not below average. The Western North Pacific had the best skill overall in week 4, but was slightly negative skill for week 3. The Atlantic basin was the most consistent over the two weeks, with a slight positive skill score. In the hindcast evaluation (Fig. 1), the Western North Pacific had the most skill, followed by the Atlantic and then the Eastern North Pacific. The probabilistic forecasts also show a similar pattern, which was to be expected.

#### 4. Future plan

This model will continue to be evaluated and optimized to provide a useful tool to forecasters for the week 3-4 time period. For further improvement, using different combinations of predictors for each basin could yield better results, most specifically for the Eastern North Pacific. Sea level pressure was shown to add

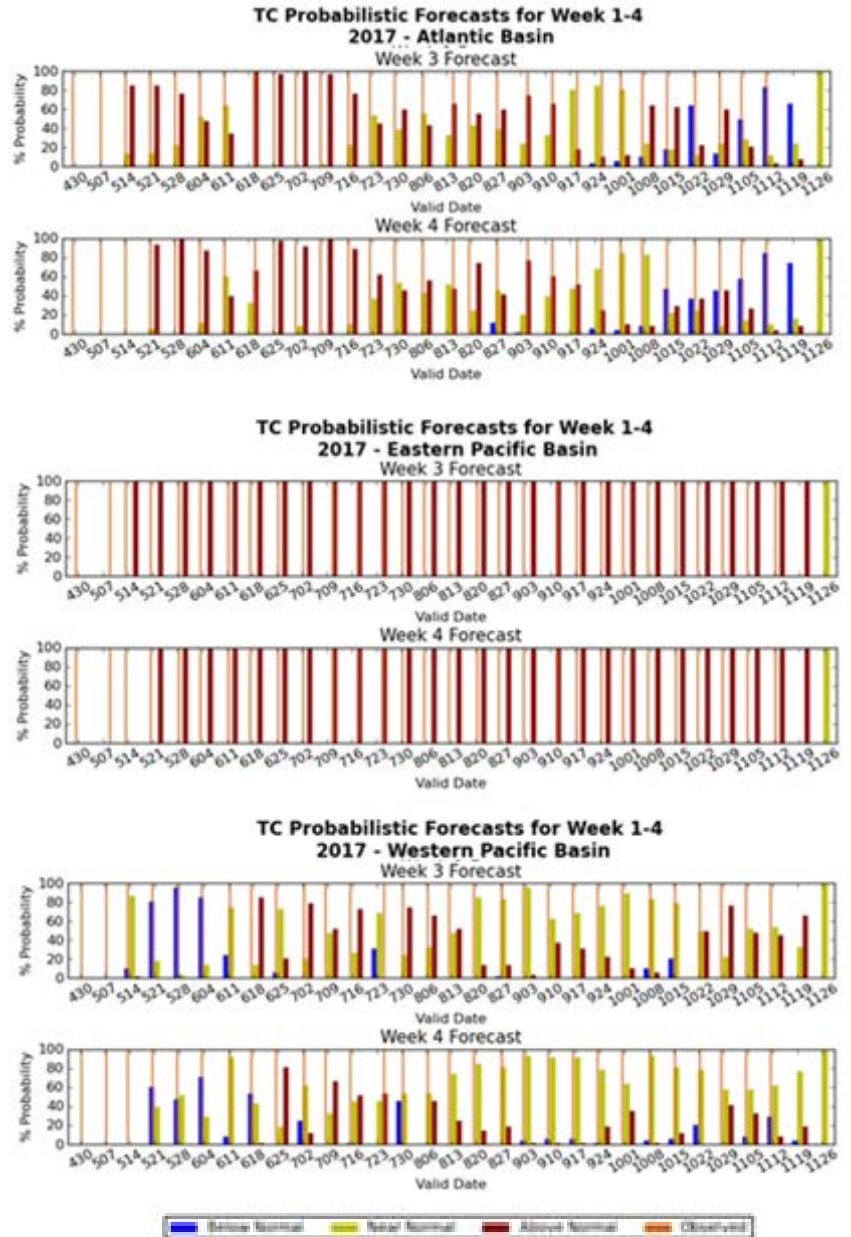


**Fig. 3** The probabilistic forecasts for weeks 3 and 4 for the 2017 season are shown for the Atlantic basin, the Eastern Pacific basin and the Western Pacific basin. Above normal activity is shown in red, near normal in yellow and below normal in blue. Observations are shown in brown, and overlap the category that was observed. Above normal activity is defined as one standard deviation above the mean and below normal activity as one standard deviation below.

skill in the hindcast evaluations for this basin. Another issue highlighted in the real-time forecast was the model's inability to capture extreme values seen in observation. Measures to increase the variability are being considered. Other possibilities considered will be including more recent years in the training period, as well forecasting for weeks 3 and 4 as one time period. Eventually, the goal is to transition this product to an operational framework to act as guidance for week 3-4 tropical forecasts.

## References

- Harnos, D. S., J.-K. E. Schemm, H. Wang, C. A. Finan, 2017: NMME-based hybrid prediction of Atlantic hurricane season activity. *Climate Dyn.*, doi: <https://doi.org/10.1007/s00382-017-3891-7>.
- Wang, H., J.-K. E. Schemm, A. Kumar, W. Wang, L. Long, M. Chelliah, G. D. Bell, and P. Peng, 2009: A statistical forecast model for Atlantic seasonal hurricane activity based on the NCEP dynamical season forecast. *J. Climate*, **22**, 4481-4500.

# 3. CLIMATE SERVICES

42<sup>nd</sup> NOAA Annual Climate Diagnostics and  
Prediction Workshop

23-26 October 2017, Norman, Oklahoma





## Delivering Impact-based Seasonal Outlooks for South Central Texas

Larry J. Hopper, Jr.<sup>1</sup>, M. Lenz<sup>1</sup>, T. Dickinson<sup>2</sup>, and J. W. Zeitler<sup>1</sup>

<sup>1</sup>NOAA/NWS Austin/San Antonio Weather Forecast Office

<sup>2</sup>School of Meteorology, The University of Oklahoma

### 1. Introduction and motivation

Expanding and improving impact-based decision support services (IDSS) to core partners continues to be one of the highest priorities for the National Weather Service (NWS). Seamlessly linking climate and weather through IDSS to support regional and local decision making is listed as one of eleven key concepts for services within the NWS “Weather Ready Nation” (WRN) Roadmap (NWS 2013). Enhancing climate services to help communities, businesses, and governments understand and adapt to climate-related risks is also mentioned as one of six NWS strategic plan goals in the WRN Roadmap. Furthermore, the Weather Research and Forecasting Innovation Act of 2017 (U.S. House of Representatives 2017) codifies funding for subseasonal and seasonal forecasting innovation to enhance national security. Considering that 219 weather and climate disasters between 1980 and 2017 have exceeded \$1 billion in damages (Consumer Price Index (CPI) adjusted to 2017) leading to \$1.5 trillion in losses (NCEI 2018) and thousands of fatalities, building resilience to extreme weather and climate events is critical in helping mitigate losses from these events.

Improving forecasts and IDSS for extreme weather and climate events is critical for Texas, which has experienced 95 of the 219 billion-dollar weather and climate disasters. South Central Texas has recently experienced record floods during May 2015 (Furl *et al.* 2018) and October 2015 (Lin *et al.* 2018) that helped end a catastrophic drought (Nielsen-Gammon 2012) along with the most catastrophic wildfire (Murdoch *et al.* 2016) and costliest hailstorm in Texas history (Hampshire *et al.* 2017), all since 2010. The likelihood of a significant loss of life and property from these events is increasing due to rapid urbanization and population growth in the Austin-San Antonio corridor, which doubled from 2.25 to 4.50 million from 1990 to 2017 and is forecast to increase to 7.59 million by 2046 (IHS Markit 2017). Flash flooding impacts are most critical in the Texas Hill Country and the Austin-San Antonio corridor due to a regular occurrence of heavy rainfall events over a region with steep channel beds and thin soils in small basins that contribute to rapid river rises. These factors combined with hundreds of low water crossings contribute to significant fatality rates caused by regular short return-period events instead of rare, high-casualty events found in other parts of the United States (Ashley and Ashley 2008; Saharia *et al.* 2017).

In order to help local core partners build resilience to high impact and climate events, the Austin/San Antonio NWS Weather Forecast Office (WFO EWX) began delivering local impact-based seasonal outlooks (LIBSOs) in fall 2015. Briefings are first presented to emergency managers (EMs), broadcast media, and other core partners during an interactive webinar that averages 17 participants. Full recordings and specific content slides are then shared on social media and through targeted outreach and media interviews. Over 70 unique core partners have participated in the live webinars, with archived webinars averaging 600 viewers on You Tube and specific social media posts approaching 100,000 views. This paper provides an adaptable structure for how LIBSOs may be created while taking into account antecedent conditions and locally relevant research. Core partner feedback is also briefly discussed to identify strengths and areas for improvement.

### 2. Objectives and structure of LIBSOs

The main objectives of delivering LIBSOs is to brief, educate, and encourage action among EMs, broadcast meteorologists, and other core partners within WFO EWX's county warning area (CWA). Increasing core partners' situational awareness on the potential for high impact weather and climate events

while educating them on the regional seasonal threats and how to interpret NWS and CPC products is especially important for EMs who have a broad range of educational experiences and typically only attend 1-3 training courses or workshops per year (Weaver *et al.* 2014). Figure 1 top panel shows an example slide given during several LIBSOs to explain the meaning of CPC's seasonal outlooks to help prevent core partners from misinterpreting these forecasts, particularly the meaning of probabilities assigned to equally probable tercile categories (above, near or below normal) based on the most recent 30-yr climatological period. Finally, encouraging partners to make decisions or take action to improve preparedness for an increased potential of an extreme weather and climate event in a given season is the most latent and ambitious objective of LIBSOs. However, WFO EWX believes this is an attainable goal through building trust with core partners by delivering outlooks that they believe (and actually are) relatively accurate.

Briefings issued by WFO EWX are approximately 20 minutes in length and are always given on Thursdays at 2 p.m. LT to provide a consistent time block that works best for core partners based on partner surveys discussed in section 4. In addition, this time takes advantage of the Thursday morning issuance of several weekly products including some CPC outlooks and the Drought Monitor (<http://droughtmonitor.unl.edu/>). WFO EWX typically delivers webinars during early December (winter; DJF), early March (spring; MAM), and early June (summer; JJA) after the National Oceanographic and Atmospheric Administration's (NOAA) Hurricane Outlook is issued, matching the expected onset of winter, severe, and tropical weather seasons, respectively. The fall webinar has been issued anywhere from mid-September to mid-October depending on when the reasonable threat of tropical cyclones and excessive heat ends in a given year. This seasonal transition usually coincides with the first strong front that local research suggests is most likely to occur in late September, but may be delayed during El Niño years (Fig. 1 bottom panel). WFOs must determine what months work best for delivering webinars for their CWA based on their seasonal impacts and operational schedules. Quarterly webinars are recommended for WFOs east of the Rocky Mountains, but different schedules may be needed for other CWAs.

All briefings begin by presenting current rainfall anomalies and the Drought Monitor before covering subseasonal and seasonal CPC temperature and precipitation outlooks and any relevant climate

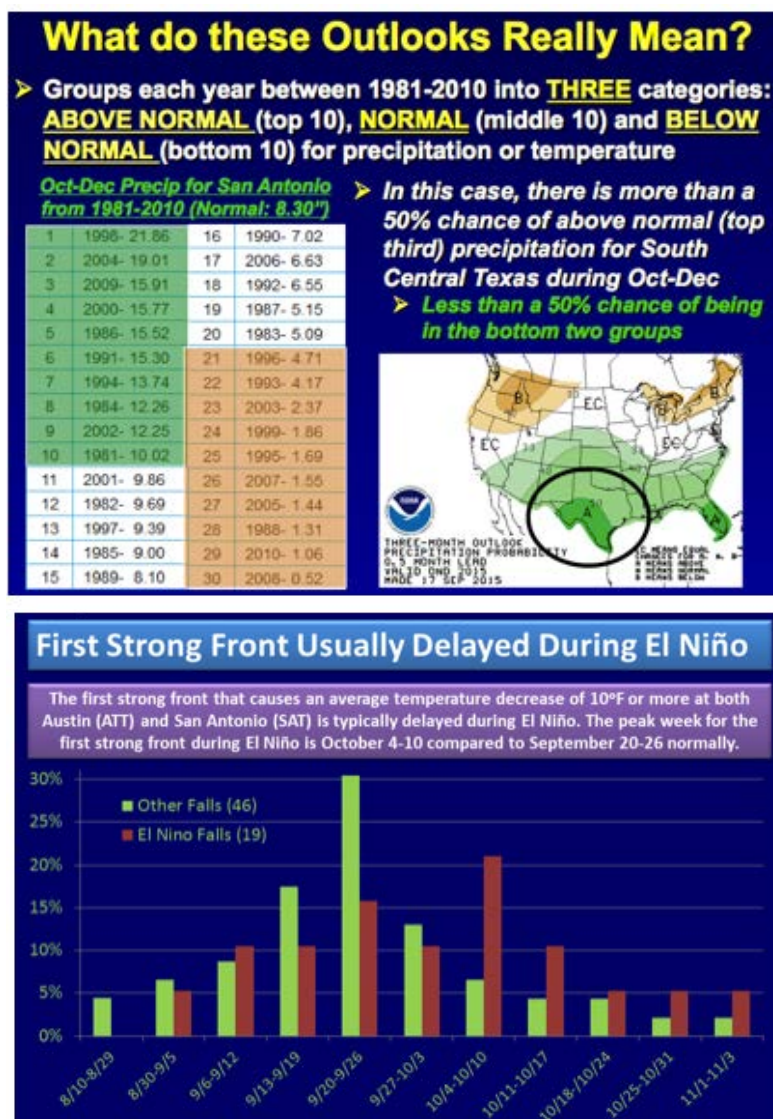


**Fig. 1** Example (top) educational slide given during the fall 2015 South Central Texas LIBSO briefing that shows the seasonal (OND) precipitation outlook issued by CPC on 17 September 2015 and (bottom) locally relevant research slide that shows a histogram of the date of the first strong front of fall during ENSO-neutral and La Niña (green) and El Niño (red).

teleconnections behind them. Locally relevant research that helps provide context and confidence for the national outlooks is discussed next, highlighting common sources of seasonal forecast skill mentioned in Goddard and Hoerling (2006) that CPC staff account for to some extent in the long-lead forecast process (O'Lenic *et al.* 2008). These sources of skill include, but may not be limited to: (1) global climate change, (2) interdecadal variability, (3) El Niño-Southern Oscillation (ENSO), and (4) atmosphere-land surface interactions. Finally, the briefing wraps up with an impacts outlook and questions from core partners attending the live briefing and anyone who views it later online. Archives of South Central Texas LIBSO briefings are available at <https://www.youtube.com/user/NWSSanAntonio/videos>.

### 3. Creating the impacts outlook

An example of an impacts outlook that was issued by WFO EWX during fall 2015 is presented in Fig. 2. Similar to CPC outlooks, a tercile-based approach is used to forecast whether above, near, or below normal impacts are expected for a specific weather type relevant to a particular season. However, WFO EWX's relatively subjective impact outlooks are purely categorical instead of assigning probabilities to a particular tercile as in CPC monthly and seasonal outlooks. Impacts are given for the first and second half of a particular season (or first and last two months if needing to emphasize the first month's forecast) to provide partners with the relative confidence of the forecast through the entire season, including any trends in how impacts may change. Outlooks are produced for severe weather, river and flash flooding, and fire weather for every season, with the addition of winter weather and summertime tropical weather based on the NOAA Hurricane Outlook during those seasons. WFOs in other regions may need to add or remove weather impact types by season depending on their climatology.

Creating the impacts outlook is currently a subjective collaboration between the climate, fire weather, and tropical focal points and service hydrologist at WFO EWX to make sure all weather impact types are consistent. In addition to CPC and NOAA outlooks, antecedent conditions and locally relevant research are given significant consideration when creating the impacts outlook. Single categorical forecasts of above, near, or below normal impacts are usually given for the entire CWA, but multi-county areas whose antecedent conditions or CPC outlooks differ significantly from the rest of the CWA are occasionally featured with a different forecast. The following subsections briefly describe three primary forecast drivers in the context of the first impacts outlook that WFO EWX issued for fall 2015 on 8 October 2015 (Fig. 2).

#### 3.1 Antecedent conditions

Significant wetter (drier) than normal antecedent conditions increase (decrease) the likelihood of flooding while decreasing (increasing) the threat of fire weather and drought going into a particular season, especially when CPC outlooks are forecasting an equal chance of above or below normal precipitation and temperature. Rainfall anomalies are an important antecedent condition that is covered at the beginning of the LIBSO because they are a proxy for soil moisture and potential fuel growth, but streamflow

anomalies along with drought indicators and indices are also important. Prior to the fall 2015 webinar, an abnormally dry July-September period following the wettest April-June period on record in Texas (Furl *et al.* 2018) resulted in 90-day rainfall anomalies that were 10-50% of normal (Fig. 3a), but 180-day rainfall anomalies that were 100-200% of normal (Fig. 3b) across South Central Texas. This triggered the development of a flash drought over the CWA by early fall with below normal streamflow and soil moisture anomalies (not shown) that decreased flood potential going into early fall.

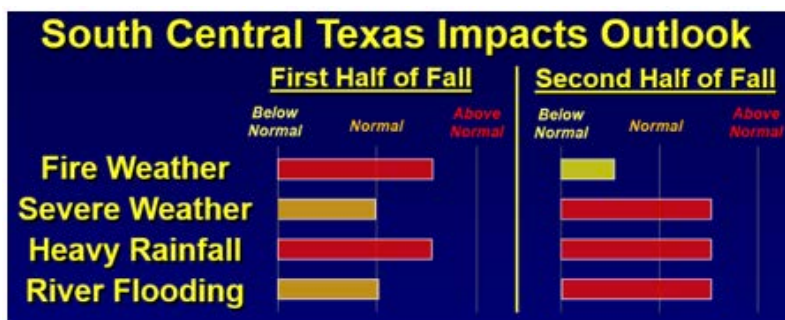


**Fig. 2** Example impacts outlook given during the fall 2015 South Central Texas LIBSO briefing on 8 October 2015. This figure is adapted from its original form in that “First Half of Fall” was “October” and “Second Half of Fall” was “November-December.”



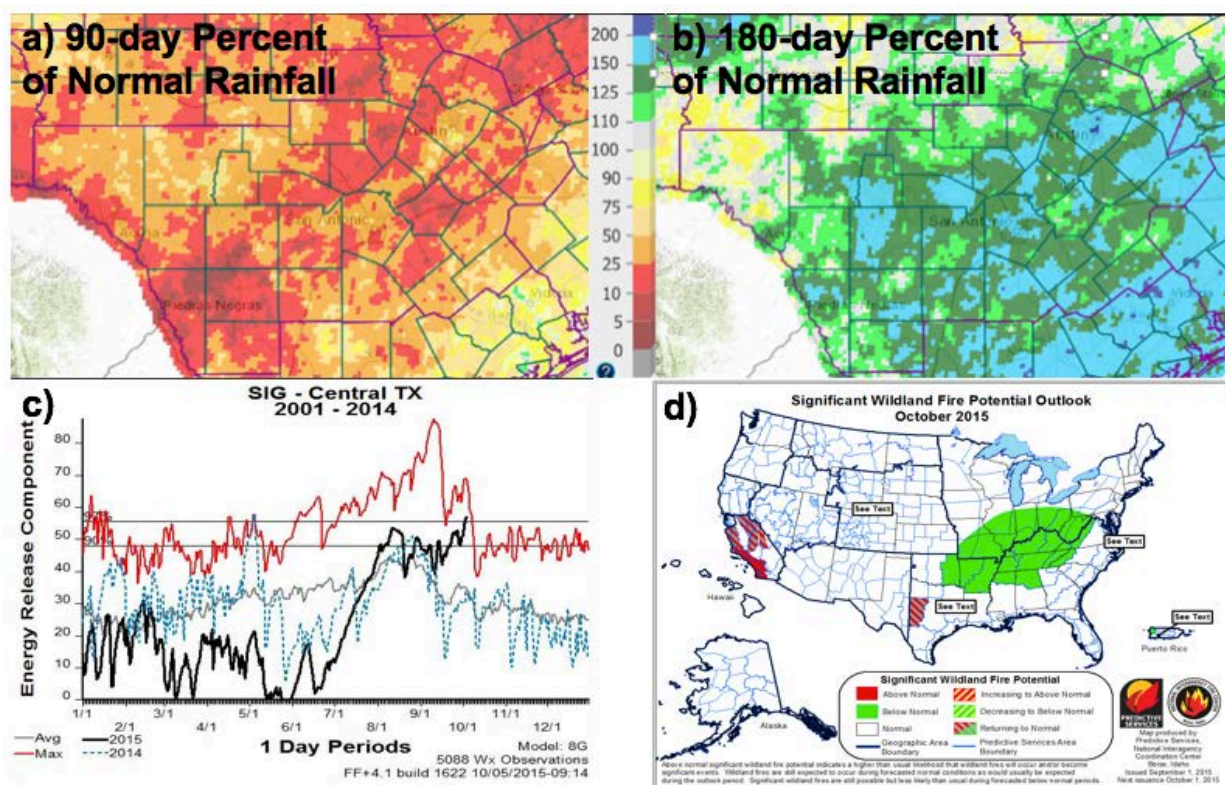


**Fig. 3** Antecedent conditions presented in the fall 2015 South Central Texas LIBSO on 8 October 2015. The panels depict (a) 90-day rainfall anomalies, (b) 180-day rainfall anomalies, (c) Energy Release Components (ERCs) for Central Texas, and (d) the NICC Significant Wildland Fire Potential Outlook for October 2015.

However, excessive fuel growth due to the wet spring and early summer followed by very hot and dry conditions over the next three months set up favorable fire weather conditions by early fall across all of WFO EWX's CWA. Energy Release Component (ERC) trends, that are considered to be a fuel moisture index that reflects the contribution of all live and dead fuels to fire intensity (Bradshaw *et al.* 1983; TICC 2018), increased dramatically across Central Texas during the summer and approached near record levels by the beginning of October (Fig. 3c). Consistent with the ERC trends and rainfall anomalies, the Significant Wildland Fire Potential Outlook issued by the National Interagency Coordination Center (NICC) highlighted the potential for fire weather conditions to increase above normal during October (Fig. 3d). The NICC monthly outlook and antecedent conditions combined with 8- and 14-day CPC outlooks favoring odds tilted towards continued warmer and drier than normal conditions increased forecaster confidence that fire weather conditions would be above normal during October if rainfall did not materialize. However, fire weather impacts would be expected to decrease to below normal as flood impacts increased if CPC's prediction of above normal rainfall for the October-December period materialized (*cf.* Fig. 1 top panel), justifying the reversal of fire weather and flooding impacts highlighted in the impacts outlook (*cf.* Fig. 2).

### 3.2 CPC and NOAA Outlooks

In the absence of significant antecedent conditions, probabilistic monthly and seasonal CPC outlooks following O'Lenic *et al.* (2008) are the primary forecast drivers of the impacts outlook (excluding severe weather). Skill analyses performed by Livezey and Timofeyeva (2008; LT08) at lead times up to 1 year and Peng *et al.* (2012: P12) for 0.5-month lead forecasts issued by CPC display greater skill for temperature than precipitation, most likely due to long-term warming trends associated with climate change. LT08 shows that skill generally does not vary by lead time except for cold season forecasts during non-neutral ENSO conditions, which P12 shows is the dominant contributor to precipitation skill. Both LT08 and P12 display a distinct spatial preference of regions with higher skill that WFOs may evaluate for their CWA by using



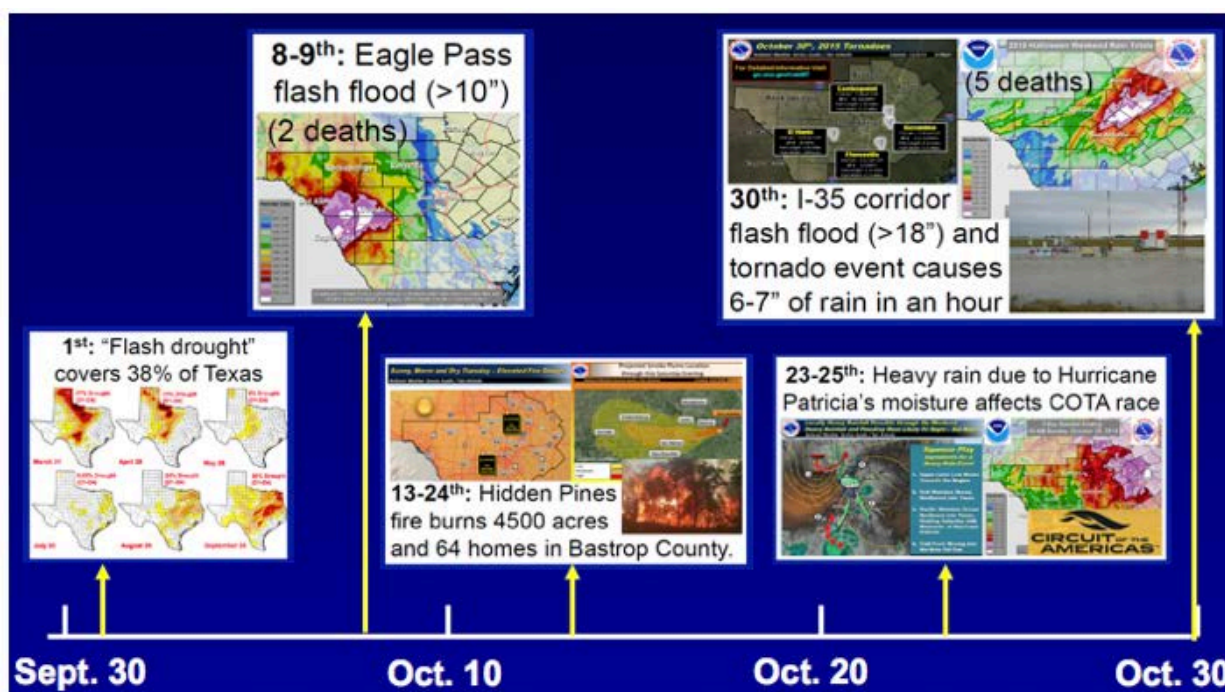


**Fig. 4** October 2015 timeline of fire weather, flooding, and severe weather events in South Central Texas.

NOAA's Local Climate Analysis Tool (LCAT; Timofeyeva-Livezey *et al.* 2015). LCAT analyses (along with figures in P12 and LT08) show that South Central Texas has some of the highest skill scores for precipitation during non-neutral ENSO conditions in all seasons except summer and above average skill for temperature all year regardless of ENSO conditions.

CPC outlooks from 17 September 2015 predicted a greater than a 40% chance of above normal (top third percentile) rainfall for South Central Texas during October and more than a 50% chance of above normal precipitation during the OND period (*cf.* Fig. 1 top panel). Although drier and warmer than normal weather was favored for the two weeks following the briefing, CPC predicted a transition towards wetter and cooler than normal weather evidenced by their 40% chance of below normal temperatures (bottom third percentile) for the OND period (not shown). These high confidence CPC forecasts made possible by one of the three strongest El Niño events since 1950 gave WFO EWX the ability to highlight a reversal from above normal fire weather and drought conditions to above normal flooding impacts during the fall season. In addition, the updated NOAA Hurricane Season Outlook issued on 6 August 2015 forecast a 70% chance of an above normal Pacific hurricane season common during El Niño. This is significant considering that moisture from Pacific storms often causes flooding in South Central Texas during fall when they interact with slow-moving fronts. A timeline of events from October 2015 shown in Fig. 4 shows that this transition from drought and above normal fire weather conditions to flooding did materialize due to two heavy rainfall events in late October.

### 3.3 Locally relevant research

Simplified explanations of locally relevant research also increase WFO EWX's confidence in their impacts outlook and the CPC outlooks behind them. This research ranges from basic local office studies like the one given in Fig. 1 bottom panel that shows the first strong front is delayed during El Niño, to peer-reviewed studies that highlight impacts specific to South Central Texas. Although important for all weather hazards, locally relevant research is most critical for predicting subseasonal and seasonal severe weather impacts for which antecedent conditions and CPC outlooks provide little forecast skill. Several recent studies have shown that La Niña conditions foster more frequent and intense tornado and hail activity across the U.S. relative to El Niño during winter and spring (Cook and Schaefer 2017; Lee *et al.* 2016; Allen *et al.* 2015), suggesting that long-range seasonal prediction of thunderstorm activity is possible. La Niña's linkages with tornado activity and intensity are

most pronounced at higher latitudes in January-March (Cook and Schaefer 2017) and in the Southeast, Ohio River Valley, and Upper Midwest in April-May during the second spring of “resurgent” La Niña episodes (Lee *et al.* 2016). However, significant geographical variations displayed in these studies make performing local research of seasonal severe weather impacts critical. For example, local studies show that La Niña and ENSO-neutral conditions produce the greatest number of severe wind, hail, and tornado reports during spring within WFO EWX’s CWA, but El Niño conditions are associated with twice as many severe reports during late fall and winter compared to La Niña or ENSO-neutral conditions (not shown). Finally, Research-to-Operations (R2O) innovations like the Climate Forecast System, version 2’s (CFSv2; Saha *et al.* 2014) Severe Weather Guidance Dashboard (Carbin *et al.* 2016) may provide additional skill for both LIBSOs and seasonal severe thunderstorm outlooks as the CFSv2 model’s skill improves in the future.

#### 4. Core partner feedback and next steps

Anonymous surveys were administered in October 2017 to 72 core partners who had attended at least one live webinar to receive feedback on how well LIBSOs were serving them and evaluate whether the objectives stated in section 2 were being satisfied. This survey was completed by 22 core partners (15 EMs, 3 broadcast meteorologists, 2 government officials, and 2 other) for a response rate of 31%. These surveys indicated that 82% of respondents use the information to maintain situational awareness, 59% improved their understanding of local weather, and 50% made decisions or took actions to improve preparedness based on the LIBSO. Although there is room for improvement, these surveys suggest that objectives to brief, educate, and encourage actions are being met for at least half of core partners.

Over 90% of core partners who completed the survey indicated that the briefings were useful and understandable, and that presenters were accessible for questions during and after the webinars. More than half of survey respondents indicated that they would like monthly updates between the seasonal briefings (77%) and quarterly email briefings with a short bullet-point summary (59%), changes that WFO EWX plans to make the later in 2018. WFO EWX also began combining river and flash flooding into a single outlook in fall 2017 because river and flash floods typically occur simultaneously in the Texas Hill Country and Austin-San Antonio corridor, a change supported by 64% of core partners and preliminary verification work described in Dickinson *et al.* (2018). Most core partners also indicated that categorical forecasts of above, near, or below normal impacts are easier to understand than a numerical scale, but a large number of respondents are open to utilizing their preferred tercile-based forecasts to provide context for a numerical scale. Assigning probabilities to a particular tercile for each weather impact type as in CPC outlooks may achieve this in the future.

Finally, and perhaps most importantly, 73% of core partners believed that the LIBSOs issued by WFO EWX have been accurate or very accurate. In order to evaluate the true accuracy of LIBSOs, WFO EWX has developed preliminary impact-based verification indices for severe weather, flooding, and fire weather, all of which verified the forecasts made during fall 2015. A full description of this deterministic verification approach for categorical, tercile-based LIBSO forecasts with examples is given in Dickinson *et al.* (2018). Overall, LIBSOs issued since fall 2015 have performed 36% better than climatology (with a range of 25-50% for each impact) based on Heidke Skill Scores. Therefore, it appears that the LIBSOs issued by WFO EWX are quantifying above, near, or below normal impacts in a way that matches both public perception and “reality,” something which may be critical for building trust among core partners so that they may take preparedness actions based on the LIBSOs. In addition to refining the existing verification process, future work will also focus on expanding LIBSOs to other CWAs and developing a more objective process for issuing LIBSOs using ENSO, antecedent conditions, and other predictors like CPC’s seasonal outlooks and other climate teleconnections.

*Acknowledgements.* The authors thank Jason Runyen and Bob Fogarty (WFO EWX) for completing some of the local studies highlighted in this paper. Two climate courses attended by the first author that were led by Marina Timofeyeva-Livezey (NOAA/NWS Climate Services Division), Barb Mayes-Boustead (WDTB), and others helped provide motivation for this work. Conversations with several CPC forecasters and NOAA contractors have also improved this work.

## References

- Allen, J. T., M. K. Tippett, and A. H. Sobel, 2015: Influence of the El Niño/Southern Oscillation on tornado and hail frequency in the United States. *Nat. Geosci.*, **8**, 278-283.
- Ashley, S. T., and W. S. Ashley, 2008: Flood fatalities in the United States. *J. Appl. Meteor. Climatol.*, **47**, 805-818.
- Bradshaw, L. S., R. E. Burgan, J. D. Cohen, and J. E. Deeming, 1983: The 1978 National Fire Danger Rating System: Technical documentation. USDA Forest Service, Intermountain Forest and Range Experiment Station, Ogden, UT 84401, General Technical Report INT-169, 44 pp, [https://www.fs.fed.us/rm/pubs\\_int/int\\_gtr169.pdf](https://www.fs.fed.us/rm/pubs_int/int_gtr169.pdf)
- Carbin, G. W., M. K. Tippett, S. P. Lillo, and H. E. Brooks, 2016: Visualizing long-range severe thunderstorm environment guidance from CFSv2. *Bull. Amer. Meteor. Soc.*, **97**, 1021-1031.
- Cook, A. R., L. M. Leslie, D. B. Parsons, and J. T. Schaefer, 2017: The impact of El Niño-Southern Oscillation (ENSO) on winter and early spring U.S. tornado outbreaks. *J. Appl. Meteor. Clim.*, **56**, 2455-2478.
- Dickinson, T., L. J. Hopper, Jr., M. Lenz, J. W. Zeitler, 2018: Improving impact-based seasonal outlooks for South Central Texas. *25<sup>th</sup> Conference on Probability and Statistics*, Austin, TX, Amer. Meteor. Soc., 8.6, <https://ams.confex.com/ams/98Annual/webprogram/Paper333817.html>
- Furl, C., H. Sharif, J. W. Zeitler, A. E. Hassan, and J. Joseph, 2018: Hydrometeorology of the catastrophic Blanco river flood in South Texas, May 2015. *J. Hydrology: Regional Studies*, **15**, 90-104.
- Goddard, L., and M. P. Hoerling, 2006: Practices for seasonal to interannual prediction. *U. S. CLIVAR Variations*, **4**, U. S. CLIVAR Office, Washington, DC, 1-6.
- Hampshire, N. L., B. W. Williams, and B. M. Fogarty, 2017: An analysis of the record breaking April 2016 San Antonio hail storm compared to other giant hailstorms. *Major Weather Impacts of 2016*, Seattle, WA, Amer. Meteor. Soc., 3.1, <https://ams.confex.com/ams/97Annual/webprogram/Paper303219.html>
- IHS Markit, 2017: U.S. metro economies: Past and future employment levels, Transportation and the cost of congestion; population forecast. 62 pp, <http://www.usmayors.org/wp-content/uploads/2017/05/Metro-Economies-Past-and-Future-Employment-12.pdf>
- Lee, S.-K., A. T. Wittenberg, D. B. Enfield, S. J. Weaver, C. Wang, and R. Atlas, 2016: Springtime U.S. regional tornado outbreaks and their links to ENSO flavors and North Atlantic SST variability. *Environ. Res. Lett.*, **11**, 044008, doi:10.1088/1748-9326/11/4/044008.
- Lin, P., L. J. Hopper, Jr., Z.-L. Yang, M. Lenz, and J. W. Zeitler, 2018: Insights into hydrometeorological factors constraining flood prediction skill during the May and October 2015 Texas Hill Country flood events. *J. Hydromet.*, in review.
- Livezey, R. E., and M. M. Timofeyeva, 2008: The first decade of long-lead U.S. seasonal forecasts: Insights from a skill analysis. *Bull. Amer. Meteor. Soc.*, **88**, 843-854.
- Murdoch, G. P., T. T. Lindley, and C. J. Morris, 2016: A Doppler radar and conceptual analysis of a horizontal longitudinal vortex in influencing the Bastrop Complex Wildfire. *J. Operational Meteor.*, **4**, 160-169.
- Nielsen-Gammon, J., 2012: The 2011 Texas drought. *Texas Water J.*, **3**, 59-95. <https://journals.tdl.org/twj/index.php/twj/article/download/6463/6066>
- NOAA National Centers for Environmental Information (NCEI) U.S., 2018: Billion-dollar weather and climate disasters, <https://www.ncdc.noaa.gov/billions/>
- NWS, 2013: National Weather Service Weather-Ready-Nation roadmap. [http://www.weather.gov/media/wrn/nws\\_wrn\\_roadmap\\_final\\_april17.pdf](http://www.weather.gov/media/wrn/nws_wrn_roadmap_final_april17.pdf)
- O'Lenic, E. A., D. A. Unger, M. S. Halpert, and K. S. Pelman, 2008: Developments in operational long-range climate prediction at CPC. *Wea. Forecasting*, **23**, 496-515.

- 
- Peng, P., A. Kumar, M. S. Halpert, and A. G. Barnston, 2012: An analysis of CPC's operational 0.5-month lead seasonal outlooks. *Wea. Forecasting*, **27**, 898-917.
- Saha, S., and Coauthors, 2014: The NCEP Climate Forecast System, version 2. *J. Climate*, **27**, 2185-2208.
- Saharia, M., P.-E. Kirstetter, H. Vergara, J. J. Gourley, Y. Hong, and M. Giroud, 2017: Mapping flash flood severity in the United States. *J. Hydrometeor.*, **18**, 397-411.
- Texas Interagency Coordination Center (TICC), 2018: Energy Release Component (ERC) fact sheet. [https://ticc.tamu.edu/Documents/PredictiveServices/Fuels/ERC\\_fact\\_sheet.pdf](https://ticc.tamu.edu/Documents/PredictiveServices/Fuels/ERC_fact_sheet.pdf)
- Timofeyeva-Livezey, M., F. Horsfall, A. Hollingshead, J. Meyers, and L.-A. Dupigny-Giroux, 2015: NOAA Local Climate Analysis Tool (LCAT): Data, methods, and usability. *Bull. Amer. Meteor. Soc.*, **96**, 537-545.
- U.S. House of Representatives, 2017: Weather research and forecasting innovation Act of 2017. Pub. L. No. 115-25, <https://www.congress.gov/115/plaws/publ25/PLAW-115publ25.pdf>
- Weaver, J., L. C. Harkabus, J. Braun, S. Miller, R. Cox, J. Griffith, and R. J. Mazur, 2014: An overview of a demographic study of United States emergency managers. *Bull. Amer. Meteor. Soc.*, **95**, 199-203.



## Improving Impact-based Seasonal Outlooks for South Central Texas

Ty Dickinson<sup>1</sup>, Larry Hopper<sup>2</sup>, and Mark Lenz<sup>2</sup>

<sup>1</sup>*School of Meteorology, The University of Oklahoma*

<sup>2</sup>*NOAA/NWS Austin/San Antonio Weather Forecast Office*

### 1. Introduction

“Is this an above normal year?” Forecasters and broadcast meteorologists get questions like this on a regular basis. Although for different reasons, the answer to that question may be useful to both meteorologists and members of the public, but how does one truly answer it? Currently, the meaning of “above normal” generally lies in terms of subjective perceptions based on experiences as opposed to objective measures (temperature and precipitation being two notable exceptions). As impact-based decision support services (IDSS) for weather and climate continue to expand in the National Weather Service (NWS), one question arises immediately: “Can we accurately quantify impacts at seasonal and sub-seasonal timescales, especially for extreme weather?”

As improvements come in statistical and dynamical tools, consolidation tools used to create an objective forecast from multiple sources, and skill in forecasts driven by ENSO, the Climate Prediction Center's (CPC's) seasonal outlooks will continue to increase in skill and provide more insight to users (O'Lenic *et al.* 2008). However, proper interpretation of these outlooks is sometimes not done correctly. In addition, some users have trouble taking a national outlook and scaling it to a regional or local level. Thus, the NWS Weather Forecast Office Austin/San Antonio (WFO EWX) began delivering impact-based seasonal outlooks to their stakeholders in fall 2015. These outlooks use a blend of national outlooks (*e.g.*, CPC's seasonal outlooks, NOAA's drought outlooks, *etc.*) and local research to combine various levels of expertise into a single outlook [for more information on delivering these outlooks, see Hopper *et al.* 2018]. The Austin-San Antonio metroplex is currently one of the most rapidly growing urban areas in the United States. Current estimates have the population in this area tripling by 2050 compared to 2000. Rapid population growth combined with hydrological challenges, such as a lack of soil infiltration due to low depth to bedrock over a region with relatively complex terrain, cause the ever-increasing vulnerability to high-impact weather to become quickly apparent. National climate outlooks are currently used most in the agricultural sector and for drought planning. Haigh *et al.* (2015) found climate information to be very useful for agricultural risk management. Several studies continued this point to develop useful seasonal climate outlooks for agriculture, such as Finnessey *et al.* (2016), Klemm and McPherson (2017) and Prokopy *et al.* (2017). Climate information is also used across emergency management networks, but these networks sometimes face challenges in using complex scientific information, such as ambiguous data and unclear uncertainty (Roberts and Wernstedt 2016). The delivering of these outlooks directly to stakeholders from a WFO provides an opportunity for the scientific information being presented to be explained clearly while also building on operational capabilities by expanding the tree of national climate outlooks to various high-impact weather. Thus, the primary objective of this study is to develop impact-based verification indices for severe weather, flooding, and fire weather. These indices attempt to quantify a relatively subjective perception of which tercile a season falls into so that more objective, verification-driven forecasts may be developed in the future.

Section 2 discusses the development of an index to measure impacts from severe weather, river and flash flooding, and fire weather. Section 3 explains how the index is then used to verify forecasts made by the office. Lastly, Section 4 describes ongoing and future work to further improve this process.

### 2. Methodology: The verification index

The overarching question of this study is how does one quantify impacts, and can they be objectively measured and predicted? We attempt to design our objective metrics in such a way that it matches public

perception and “reality” for any given season as well as be a repeatable but customizable process. The first step in objective forecasts is to have a baseline climatology for this WFO’s county warning area (CWA) in South Central Texas. Baseline climatologies are created for severe weather, river and flash flooding, and fire weather; river flooding and flash flooding are combined because most river floods are also flash floods where most of the population within WFO EWX’s CWA live. These climatologies utilize “indicators”, various data to describe one aspect of the weather phenomena that, when used collectively, will fully depict the season as it pertains to the respective weather event. We call these climatologies complete with indicators as verification indices because they are initially acting to verify outlooks done by the office.

We began by defining seasons to be tested: December, January, February (DJF, hereafter referred to as winter); March, April, May (MAM, referred to as spring); June, July, August (JJA, referred to as summer); and September, October, November (SON, referred to as fall). For each index, indicators fall into one of three categories: occurrence, impacts, or meteorology/severity. These categories capture a full description of a season offering the strongest overall quantification. The basis for each index utilizes the number of reports and the number of report days for occurrence, damages and a blend of injuries and fatalities for impacts, and total CWA rainfall for meteorology/severity. Damages are adjusted to 2010 levels using the consumer price index (DOL 2017). Total CWA monthly rainfall was found using Texas Water Development Board quadrangles (TWDB 2017). These quadrangles divide Texas into a 1° latitude by 1° longitude grid. Any quadrangle that contained more than 75% of the CWA was considered in the analysis. An average of each quadrangle’s seasonal value then was used as total CWA rainfall. Additional indicators, like a blend of fatalities and injuries that is discussed in Section 2.1, were then added to each index to hone in on specifics from each hazard.

Our verification indices are modeled after the CPC’s nonparametric tercile approach. Each indicator in the index is ranked, where 1 is the greatest number (i.e., the most number of reports/most damages) and  $n$  is the smallest number where  $n$  is the number of years in the climatology. Total CWA rainfall in the fire weather index is the only exception (smallest rainfall value given 1, largest given 30) since lower rainfall totals are more indicative of enhanced fire weather. In the case of a tie, all tied values are assigned the rank that is equal to the midpoint of the unadjusted ranks. Then, we take the sum of all indicator ranks across a year and find the rank of this sum. The final rank analysis thus weights all indicators equally throughout the index (see Table 1 for a simplistic example of this process). The final rank analysis is done so that the smallest sum is given the top rank. The upper third ranks are deemed above normal, middle third are near normal, and bottom third are below normal. To check the internal consistency of our indices, a statistical measure called Cronbach’s Alpha was used (Cronbach 1951). Cronbach’s Alpha is a number from 0 to 1.0 where 1.0 represents perfect internal consistency. Commonly accepted rules to describe Cronbach’s Alpha values are: 0.90 and above is excellent, 0.80 to 0.90 is good, 0.70 to 0.80 is acceptable, and anything below 0.70 should be questioned. Analysis was done with every indicator in each season in each index and then by taking one indicator out; the maximum value of Cronbach’s Alpha represented the group of indicators that were the most consistent and thus used as the final index.

**Table 1** An example of how ranking works in the verification index using only two indicators. Note that a low sum is given a higher rank as low sums indicate more significant indicator values.

Year	Reports	Report Days	Report Rank	Days Rank	Sum	Sum Rank
2006	22	6	3	3	6	3
2007	279	35	1	1	2	1
2008	8	4	4	4.5	8.5	4
2009	7	4	5	4.5	9.5	5
2010	25	8	2	2	4	2

### 2.1. Severe weather

Severe weather was analyzed first, and the storm reports were collected from the National Center for Environmental Information’s Storm Events Database (NCEI 1999). Our 1981-2010 climatology includes storm reports for severe thunderstorm wind, severe hail, tornadoes, and lightning. We kept all penny-size hail reports and above ( $> 0.75$  in) because this was the severe criteria for virtually the entire climatology prior to it

increasing to quarter size ( $> 1$  in) in January 2010. Although lightning is not considered in making a thunderstorm severe, if it was listed as a storm report it means that there was either a fatality, injury, or damage figure associated with it, which by definition is an impact. Lightning reports were not added to the Storm Events Database until 1996 under NWS Directive 10-1605 so all Storm Data Publications prior to 1996 were read and appropriate additions were made.

Initially, fatalities and injuries were two separate indicators. Upon looking at the data, it was seen that there were a significant number of zeros for fatalities, especially in the winter. This presents a problem in statistical analysis (although certainly not in societal analysis) because all the zeros would share a common rank. As a result, there was not much differentiation between any given year when looking at the fatalities (and injuries) ranks alone. As a result, we define a blend of fatalities and injuries to capture both impacts while also providing differentiation among years. This blend ranks fatalities but uses injuries to break tied ranks in fatalities. This provided a solution that allowed the impacts of a fatality to have more weight than an injury and still accounted for both fatalities and injuries because the range and variability of fatalities was not large.

To design an index specific for severe weather, we added the following indicators into the index: total tornado path length (occurrence) and maxima of tornado width, hail diameter, and non-tornadic wind magnitude (meteorology/severity). Cronbach's Alpha analysis showed spring was the least consistent, but still good at about 0.80 for all indicators, and winter was the most consistent at about 0.87. However, it was found that by removing total CWA rainfall from the index, the Cronbach's Alpha value increased. Since it is expected that increasing the number of items in the analysis would increase the Cronbach's Alpha value (Cortina 1993), total CWA rainfall was making the index less internally consistent. From a meteorological standpoint, this makes sense since severe weather impacts, more often, come with discrete storm modes as opposed to a widespread rainfall event.

## *2.2 River and flash flooding*

Like severe weather, storm reports were collected from NCEI's Storm Events Database. However, the database only has reports from 1996 forward, again due to NWS Directive 10-1605. In order to expand our climatology to 30 years, Storm Data Publications and archived E-5 reports were thoroughly investigated for reports of flooding impacts. Although it may not have been perfect, since our index uses ranks, and not the raw data for each indicator, it is not so much the actual values as much as where it falls in comparison to the other years. It is almost certain that highly unusual years would become evident in the final ranks.

In addition to the foundational indicators, we added the number of times river gages went above moderate flood stage (occurrence) and maximum one- and two-day rainfalls (meteorology/severity) to the index. 52 river gages located on major rivers throughout the CWA were selected. All instances of a river gage going over its moderate flood stage threshold were recorded and then split into the seasons of each year. The collective total among all river gages for a single season was used as the indicator. In determining maxima in rainfall, 54 COOP stations were used. COOP stations were selected to cover all counties in the CWA, with several in larger population areas. The overall maximum for both one day and two days at these 54 stations given in xmACIS2 were used as the indicators. Cronbach's Alpha analysis showed the index was very good, as three out of four seasons were above 0.9; spring was the exception and had a Cronbach's Alpha of 0.85.

## *2.3 Fire weather*

Fire weather was the last hazard we investigated. We were able to obtain an extensive dataset of all fires, including prescribed burns from the Texas State Fire Marshal's Office spanning from 1982-present. Any prescribed burn that did not have acres burned entered was discarded from the dataset. After analysis, it was noticed that there were zero acres burned for every fire entered from 1982 through 1999. Therefore, we were forced to use a 15-year climatology of 2000-2014.

Three indicators were added to the fire weather index: total acres burned (impacts), average maximum temperature (meteorology/severity), and a blend of frontal passages and a Keetch-Brynum Drought Index analysis (meteorology/severity; see Table 2 for a summary of all indicators used for the various indices).

Average maximum temperature was calculated using climate division data gathered from NOAA's Local Climate Analysis Tool (Timofeyeva-Livezey *et al.* 2015); about 45.5% of the CWA lays within climate division 6 and about 54.5% of the CWA lays within climate division 7. Each climate division's average maximum temperature was multiplied by the respective decimal to determine a spatially-weighted average. This is a process that can be done to determine total CWA rainfall if other datasets are not available. Cronbach's Alpha values for this index were excellent. Like total CWA rainfall in the severe weather index, total damages were found to be making the fire weather index less internally consistent possibly due to inconsistencies in reporting monetary impacts caused by fires, so it was removed.

**Table 2** A summary of all indices and the indicators that comprise them. Total CWA rainfall was taken out of the severe weather index and total adjusted damages was removed from the fire weather index due to having poor statistical relationships in their respective indices. This was shown through Cronbach's Alpha values increasing when the indicator was removed.

Weather Hazard	Occurrence	Impacts	Meteorology/Severity
Severe Weather	Number of storm reports	Fatalities/Injuries Blend	Maximum tornado width
	Number of report days	Damages	Maximum hail diameter
	Total tornado path length		Maximum non-tornadic wind magnitude
River and Flash Flooding	Number of storm reports	Fatalities/Injuries Blend	Total CWA rainfall
	Number of report days	Damages	Maximum 1-day rainfall
	Frequency of river gages above moderate flood stage		Maximum 2-day rainfall
Fire Weather	Number of fire reports	Fatalities/Injuries Blend	Total CWA rainfall
	Number of report days	Total acres burned	Average maximum temperature
			KBDI/Frontal passages blend

### 3. Verification of South Central Texas climate outlooks

Figure 1 displays the plot made after analysis using the verification index for severe weather. Although all 4 seasons are plotted on the same graph, comparisons between one season and another is dangerous. For example, a below normal year in the spring, the season that is climatologically most active for severe weather, tended to have about 20 to 30 severe reports while in the other seasons a below normal year could have less than 5. A better interpretation of the sum of any given year is how it compares to other sums relative to the season of interest. The top overall sum of 223 corresponds to fall 2001; that season saw 56 severe reports and 39 injuries due to severe weather. Meanwhile, the lowest sum for a top rank corresponds to spring 1997 which is the year of the deadly Jarrell EF/F5 tornado. Spring 1997 had a total of 140 severe reports and 28 fatalities. Obviously, these two seasons are much different in their associated impacts, displaying how the same process can lead to varied results depending on the timeframe that is being analyzed. This is useful because it can quickly point out highly anomalous seasons relative to the season's climatology. Finally, the

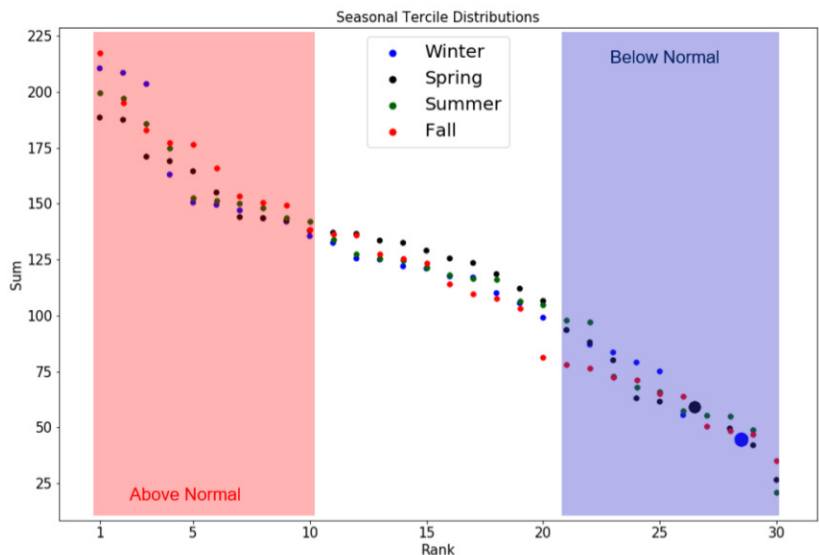


**Fig. 1** A plot displaying the distribution the distribution of years in the severe weather climatology. A larger dot means more than one year was tied for a final rank. The y-axis is the sum of the indicators and is reversed so that a larger sum correlates with above normal impacts.



meteorological forcings driving a season can vary yet still verify as the same tercile. In other words, a more active weather pattern may not necessarily lead to more impacts than a season with one single large event. While spring 1997 was largely driven by one large event, the second overall spring rank was 2007, a year where several moderate severe weather days aggregated to verify as above normal. This is a positive result since verification of above normal impacts can come from multiple types of seasons.

Figure 2 depicts the river and flash flooding analysis plot. The overall distribution is similar to severe weather with less change of slope for the near normal points. Although the summertime is the season with the most flooding reports, spring and fall have relatively high climatological percentages of reports. For this reason, the distribution is more linear than the one for severe weather but not nearly as linear as the fire weather plot shown in Fig. 3 discussed below). For river and flash flooding, the top six above normal years clearly separate themselves and is a major motivation for delivering impact-based outlooks. This CWA has over half of Texas's flooding deaths since 1996 and as the Austin/San Antonio metroplex continues to expand the potential for significant river and flash flooding will also grow.

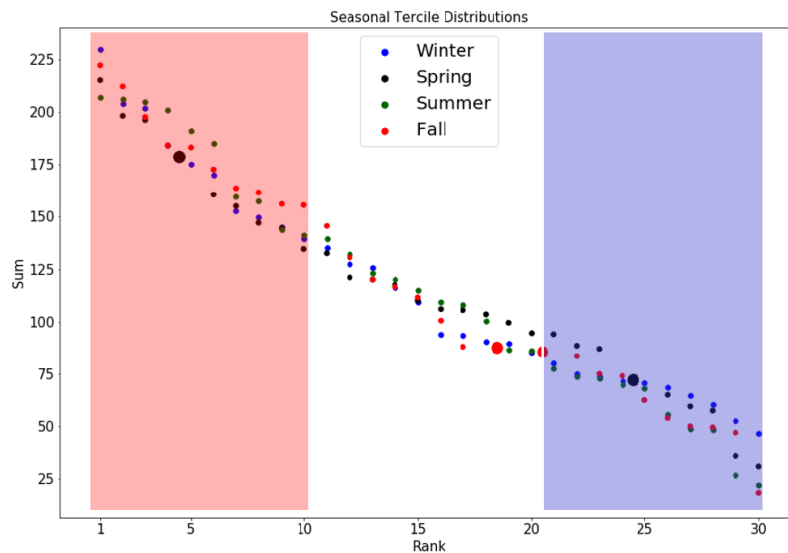


**Fig. 2** As in Fig. 1, but for river and flash flooding.

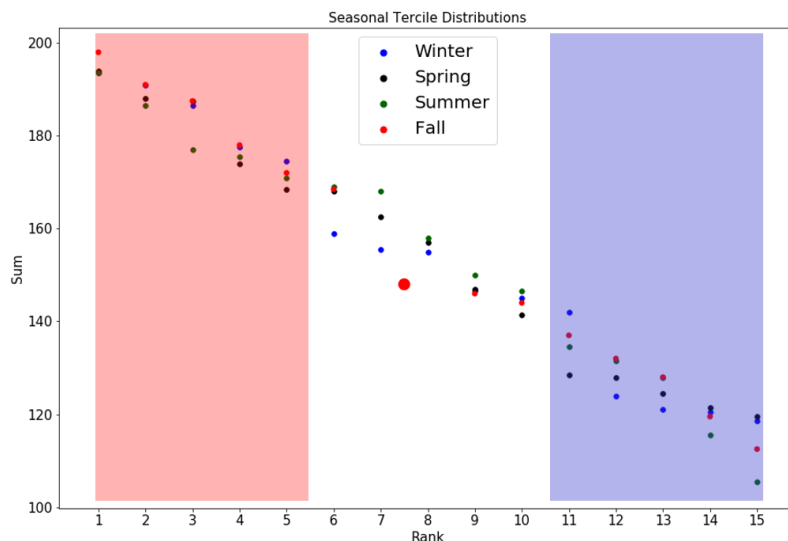


**Fig. 3** As in Fig. 1, but for fire weather.

Figure 3 shows the results of the fire weather analysis. This plot is virtually linear, most likely owing to the climatology being 15 years as opposed to 30 years and that the occurrence of fire reports is virtually uniform across all four seasons. However, interseasonal comparisons should be avoided because the meteorological and agricultural mechanisms enhancing fire weather threats have a seasonal variability component. The large dot in the middle of the plot represents two years that ended having the same final rank. This point displays the need for a 30-year climatology; in one year, the first half of the season was very dry and hot which enhanced fire potential while the second half of the season was the opposite: wetter and cooler than normal. The other year comprising that single dot was one where fewer acres burned and the entire season had moderate fire risk. Hence, there is less discrimination between years in this index, especially in the near normal range. Fine tuning the indicators and expanding to a longer climatology as more data becomes available will act to make this index much better moving forward.

Now that there is a baseline climatology, objective verification techniques can be undertaken to verify outlooks already issued by the WFO. The verification scheme developed using the indices outlined above can be broken down into 7 steps (Table 3 is another depiction of the process):

**Table 3** A depiction of the verification process for severe weather. For example, fall 2015 had 19 severe reports. The closest value in the severe weather index was 18 in 1997. Fall 2015 was then assigned the 1997 rank of 9. The index score is the sum of all ranks (*e.g.*, 75), the closest value is again found, and given that rank (in this case, is 6)

Fall Season	Reports	Report Days	Fatalities Injuries	Tornado Track	Adjusted Damages	Largest Hail Size	High Wind	Widest Tornado
<b>2015</b>	19	6	0	18.6 mi.	\$2.07M	1.0 in.	71 mph	440 yd.
<b>Rank</b>	9th	9th	20th	3rd	6th	20th	5th	3rd
<b>Value (Year)</b>	18 (1997)	6 (3 times)	0 (21 times)	26 mi. (2004)	\$1.75M (2000)	1.0 in. (1994)	70 mph (3 times)	400 yd. (2004)

- 1) Collect observed values for each indicator of an index;
- 2) For any given indicator (*e.g.*, number of reports), find the closest value within the index to the observed value;
- 3) Assign the rank for the indicator of the season being verified as the same rank assigned to the value identified in step 2;
- 4) Repeat steps 2 and 3 for each indicator in the index;
- 5) Sum all the indicator ranks;
- 6) Find the closest sum value from the index to the result found in step 5;
- 7) The final rank of the season being verified is then assigned the same rank as the year with the closest sum value (*i.e.*, the sum value found in step 6).

**Table 4** A summary of forecasts issued by WFO Austin/San Antonio and the season's corresponding verification using our indices. Severe weather hit 6 of 9 forecasts while river and flash flooding and fire weather hit 3 out of 6.

Season	Severe Weather		River and Flash Flooding		Fire Weather	
	Forecast	Verification	Forecast	Verification	Forecast	Verification
<b>Fall 2015</b>	Slight Above	Above (6)	Above	Above (3)	Near Normal	Near (6)
<b>Winter 2016</b>	Above	Near (12)	Slight Above	Below (21)	Below	Below (11)
<b>Spring 2016</b>	Slight Above	Above (6)	Slight Above	Above (3)	Near Normal	Below (15)
<b>Summer 2016</b>	Slight Above	Below (26)	Slight Above	Above (8)	Slight Below	Below (11)
<b>Fall 2016</b>	Slight Below	Below (26)	Below	Near (13)	Slight Below	Near (6)
<b>Winter 2017</b>	Slight Below	Above (3)	Slight Below	Near (11)	Slight Below	Near (8)
<b>Spring 2017</b>	Slight Above	Above (6)				
<b>Summer 2017</b>	Near Normal	Near (11)				
<b>Fall 2017</b>	Slight Below	Below (27)				

This verification scheme has been done to date completely for 21 forecasts made between fall 2015 to fall 2017 for severe weather (9 seasons) and fall 2015 to winter 2016-17 for river and flash flooding and 6 fire weather (6 seasons each) (shown in Table 4). Six out of nine severe weather forecasts hit the correct tercile and three out of six forecasts hit for both river and flash flooding and fire weather. Skill in these seasonal forecasts was found using Heidke Skill Scores (HSS; Heidke 1926). The formula for a HSS is

$$HSS = \frac{C - (\frac{1}{3} * T)}{\frac{2}{3} * T}$$

where C is the number of correct forecasts and T is the number of forecasts being scored. Using this formula, HSS's were found to be 0.50 for severe weather and 0.25 for both river and flash flooding and fire weather. A HSS for climatology is 0 since it is assumed one out of every three climatology forecasts is correct. Therefore, WFO EWX's skill is 50% better than climatology for severe weather and 25% better than climatology for river and flash flooding and fire weather for forecasts made since fall 2015.

#### 4. Conclusions and next steps

Overall, objective verification indices that capture impacts can be created and are meaningful to both meteorologists and the public. Impacts are captured from a quantitative aggregation of various data describing the season quantitatively. Each indicator is weighted equally in the ranking process that produces a single number that sorts years within each season by their impacts. These ranks may then be sorted into terciles, much like CPC's temperature and precipitation outlooks. The indices presented here are baseline indices that will be improved as operational capabilities and our understanding of quantifying impacts also are improved. In addition, these indices are used to verify the forecasts made by the office. Currently, the office has shown to have skill in combining national outlooks and local expertise to produce a forecast tailored to a CWA's stakeholders.

There are currently several areas of work still being explored to improve this process. For example, streamflow is being considered as an additional indicator to the river and flash flooding index. In addition, some measure of fuel moisture, such as fuel release component, looks to replace the KBDI blend in the fire weather index. Lastly, using the PRISM dataset to more accurately quantify total rainfall is being explored. Winter weather is an additional index being designed with guidance from WFO Detroit. The overarching process has been shown to have successes thus far and has also been designed in a repeatable but customizable way so that indices can be tailored to specific regional nuances.

*Acknowledgements.* We would like to acknowledge John Nielsen-Gammon (TAMU), Bob Rose (LCRA), Scott Breit (TFS), Carolyn Pursley (Texas State Fire Marshal's Office), Michael Churma (NWS), Jenna Meyers (NWS), Cameron Homeyer (OU), and Jason Furtado (OU) for their contributions in designing the index, retrieving data, and objective forecasting ideas currently being tested. This project has been supported by NOAA's Ernest F. Hollings scholarship and the University of Oklahoma School of Meteorology's James Bruce Morehead Award for Undergraduate Research in Weather and Climate.

#### References

- Cortina, J. M., 1993: What is coefficient alpha? An examination of theory and applications. *Journal of Applied Psychology*, **78**, 98-104, <http://dx.doi.org/10.1037/0021-9010.78.1.98>.
- Cronbach, L. J., 1951: Coefficient alpha and the internal structure of tests. *Psychometrika*, **16**, 297-334, <https://doi.org/10.1007/BF02310555>.
- Department of Labor Bureau of Labor Statistics, 2017: Consumer price index. Accessed June 2017, <https://www.bls.gov/cpi/>
- Finnessey, T., M. Hayes, J. Lukas, and M. Svoboda, 2016: Using climate information for drought planning. *Climate Research*, **70**, 251-263.
- Haigh, T., E. Takle, J. Andresen, M. Widhalm, J. S. Carlton, and J. Angel, 2015: Mapping the decision points and climate information use of agricultural producers across the U.S. *Corn Belt. Climate Risk Management*, **7**, 20-30, <https://doi.org/10.1016/j.crm.2015.01.004>.
- Heidke, P., 1926: Berechnung des Erfolges und der Gute der Windstarkevorhersagen inm Sutrnmwungsdienst (Measures of success and goodness of wind force forecasts by the gale-warning service). *Georg. Ann.*, **8**, 301-349.
- Hopper, L. J., T. Dickinson, and J. W. Zeitler, 2018: Delivering impact-based seasonal outlooks for South-Central Texas. *Special Symposium on Impact-Based Decision Support Services*, Austin, TX, Amer. Meteor. Soc., 1.5A, <https://ams.confex.com/ams/98Annual/webprogram/Paper329900.html>.

- 
- Klemm, T., and R. A. McPherson, 20162017: The development of seasonal climate forecasting for agricultural producers. *Agricultural and Forest Meteorology*, **232**, 384-399, <https://doi.org/10.1016/j.agrformet.2016.09.005>
- NOAA/NCEI, 1999: Storm Events Database, Version 3.0 (updated monthly). National Center for Environmental Information. Subset used: December 1980 – February 2017, accessed June 2017, <https://www.ncdc.noaa.gov/stormevents/>
- O’Lenic, E. A., D. A. Unger, M. S. Halpert, and K. S. Pelman, 2008: Developments in operational long-range climate prediction at CPC. *Wea. Forecasting*, **23**, 496-515, <https://doi.org/10.1175/2007WAF2007042.1>.
- Prokopy, L. S., J. S. Carlton, T. Haigh, M. C. Lemos, A. S. Mase, and M. Widhalm, 2017: Useful to useable: Developing useable climate science for agriculture. *Climate Risk Management*, **15**, 1-7, <https://doi.org/10.1016/j.crm.2016.10.004>.
- Roberts, P. S., and K. Wernstedt, , 2016: Using climate forecasts across a state’s emergency management network. *Natural Hazards Review*, **17**, [https://doi.org/10.1061/\(ASCE\)NH.1527-6996.0000222](https://doi.org/10.1061/(ASCE)NH.1527-6996.0000222)
- Texas Water Development Board, 2017: Precipitation and Lake Evaporation. Accessed June 2017, <http://www.twdb.texas.gov/surfacewater/conditions/evaporation/>
- Timofeyeva-Livezey, M., F. Horsfall, A. Hollingshead, J. Meyers, and L. A. Dupigny-Giroux, 2015: NOAA Local Climate Analysis Tool (LCAT): Data, methods, and usability. *Bull. Amer. Meteor. Soc.*, **96**, 537-545.

## Forecasting Long-term Water Supply Using Stochastic Methods with Trend Consideration: A Study on Lake Meredith in the Canadian River Basin in Texas

John Zhu and Nelun Fernando  
*Texas Water Development Board, Austin, Texas*

### 1. Introduction

How much water supply can come from a certain reservoir in 2020, 2030, 2040, 2050 and 2060? This is a key question that must be answered for the water planning process in Texas. Currently, the state's water planning rules request regional planning groups to use the firm yield computed by the Texas Commission of Environmental Quality (TCEQ) updated Water Availability Model (WAM) Run3 (full permit diversion and no return flow) as available supply, plus consideration of future sedimentation effects which would reduce water supply. WAM is the official water accounting model used for water rights permitting, regulation, and water planning purposes in Texas. The WAM uses the Water Right Analysis Package (WRAP) developed by Texas A&M University (Wurbs 2015). WRAP simulates management of water resources of river basin(s) under a priority-based water allocation system with river basin hydrology represented by sequences of naturalized stream flows and reservoir net evaporation rate at pertinent locations. Naturalized flows are sequences of monthly flows representing natural hydrology and are typically developed by adjusting historical gauged streamflow data to remove the impacts of reservoir construction, water use, and other human activities. Currently, most of TCEQ's WAMs use hydrologic input from 1940s to 1990s. That means the firm yield computed by such a model is only applicable for the period from 1940s to 1990s. One effort now is to extend the input hydrologic data to recent years to include 2011, which is the worst one year drought in the observational record going back to 1895. Using an extended hydrology reveals potentially critical issues with respect to water availability. For example, some river basins have decreasing streamflow and some reservoirs have had lower storage in the past decade (*i.e.*, Lake Meredith since 2000) and some have even run dry (*i.e.*, O.C. Fisher Lake in 2013). The firm yields from reservoirs decrease with the extended hydrologic input. This is an indication that the firm yield values used presently are probably not applicable for the future because future hydrological conditions will differ from present hydrology.

In this study we investigate the potential of using stochastic hydrological forecasting with an incorporation of observed long-term trends in streamflow. The Monte Carlo method and the best trend line through regression are employed to generate a synthetic hydrology input for the future period (2020 through 2069), which is the time horizon needed in water resource planning. A constraint for limiting the number of wet and dry years that can cluster together is also incorporated in the process for generating the synthetic hydrology to maintain the observed patterns of wet and dry year clustering. In this study, we take Lake Meredith in the Canadian River basin (Fig. 1) as an example, because a clear downward trend has been observed at the Amarillo gauge, which is located upstream of Lake Meredith on the Canadian River. Finally,

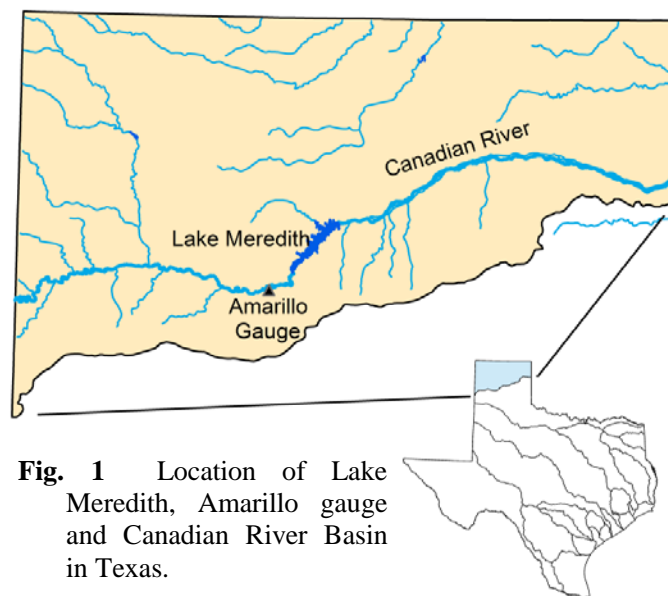


**Fig. 1** Location of Lake Meredith, Amarillo gauge and Canadian River Basin in Texas.



we forecast the available water supply for Lake Meredith over the next 50 year time horizon (*i.e.* for 2020, 2030, 2040, 2050, and 2060) at various given confidence intervals or certain criterion, such as 65-percent and 85-percent exceedance probabilities.

## 2. Methodology

As stated above, the existing WAM model is only applicable to the existing hydrologic condition from 1940s to 1990s, because the future hydrologic condition is not as the same as existing conditions. Therefore, for that specific future time (up to 2060 or beyond), we must extend the hydrologic input and the simulation period to a future time (up to 2060 or beyond), if we are to use the WAM model to compute firm yield from reservoir. In this case, the future naturalized streamflow, which is generated by precipitation, has a random nature. Therefore, the Monte Carlo method is applied to generate a synthetic hydrology. However, trend in the existing hydrology should also be considered if there is a clear trend, especially a non-linear trend. Moreover, we must consider the maximum length of continued dry or wet period, because naturally a dry period must finally end with a wet period, and vice versa. In other word, naturalized streamflow also has a cyclical nature (*i.e.* not pure random process). This factor affects reservoir firm yield, which is determined for drought conditions. If we inadvertently generate an extremely long dry period through the random selection process, an unrealistically lower firm yield would be generated. Therefore, a constraint of maximum dry period and maximum wet period is introduced in our random selection process, based on the available historical record. As an example in this study, future firm yields from Lake Meredith in the Canadian River Basin are simulated by TCEQ's WAM Model for the Canadian River Basin (Espey Consultants, Inc. 2002). The model has been updated by extending its hydrologic input data from 51 years (1948-1998) to 65 years (1948-2012) to obtain a better representation of the hydrology in the Canadian River Basin. The recent drought (2011-2013) event is included in this extended hydrology. Extending the hydrology also enables us to increase the population available for random sampling. The inflow to Lake Meredith is represented by the adjusted gauge flow (*i.e.* naturalized) at the U.S. Geological Survey gauge at Amarillo. Adjusted gauge flow refers to accounting for, and removing, diversions above the gauge.

Stochastic models, which are often known as time series models have been used in scientific, economic and engineering applications for the analysis of time series data (Barndorff-Nielsen *et al.* 1998; Srikanthan and McMahon 2000; U.S. Bureau of Reclamation 2003). Time series modeling techniques have been shown to provide a systematic empirical method for simulating and forecasting the behavior of uncertain hydrologic systems and for quantifying the expected accuracy of the forecasts (Machiwal and Jha 2006). If there is a systematic linear trend in seasonal inflow, this could be incorporated in the simulated time series (Ward *et al.* 2012). Streamflow at the Amarillo gauge has a non-linear recession trend. We, therefore, propose a new methodology for generating the synthetic hydrology that incorporates the non-linear trend. Steps for generating the synthetic streamflow and modifying the model for simulation are discussed below:

1. Analyze existing annual naturalized flows to see if there is an obvious trend. If there is a trend, make the best fit trend line and its formulation. In this case, we found the best fit (highest R-square value) curve is exponential (Fig. 2).
2. Find out the maximum length (year) of high flow and maximum length (year) of low flow by computing exceedance probability below 25-percent and above 75-percent, respectively (Fig. 3). These maximum lengths will be used in the synthetic process by random selection as a constraint to maintain the cyclic nature of naturalized flows. If the selected year exceeds the maximum limit,

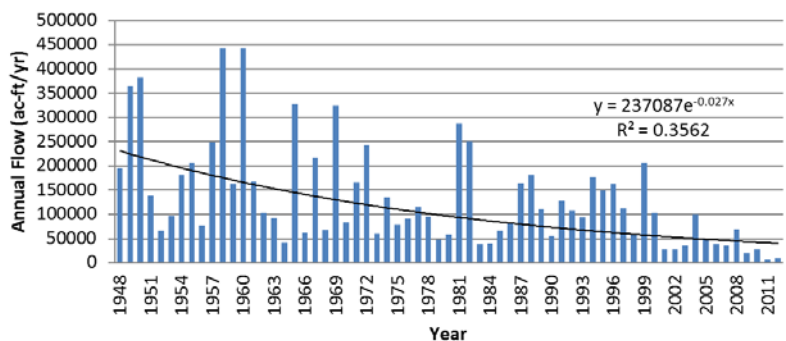


Fig. 2 Existing annual naturalized flows and its best fitted trend line at the Amarillo gauge.

it would be skipped and a year of different type will be selected to construct the synthetic hydrologic sequence. In this case, the maximum length for a clustering wet period is 3 years and 4 years for dry period (Fig. 3).

3. Select a year randomly from the existing naturalized flow to construct year by year the future flows till 2069 by following the trend line (or value of the slope for those years). This task is done using the following methodology:

- 3a. Randomly select a year ( $t_1$ ) from the existing naturalized flow ( $Q_{t_1}$ ) and compute the naturalized flow ( $Q_{t_2}$ ) for a future year ( $t_2$ ) (Fig. 4) by the formulation:

$$Q_{t_2} = (V_{t_2} / V_{t_1}) * Q_{t_1}$$

where  $V_{t_1}$  and  $V_{t_2}$  are the value of trend line at year  $t_1$  and  $t_2$ , respectively.

- 3b. Repeat step 3a for next future year until all flows for the future years (up to 2069) are done.

- 3c. If the maximum length of 4-year dry period defined in step 2 is exceeded at step 3b, the 5th dry year is skipped until a different type (wet or neutral) of year's hydrology occurs. This will guarantee that the constructed hydrology does not exceed the known maximum length of drought. This step is important because too many years drought clustering together would be unrealistic and would lead to extreme low firm yield.

- 3d. To preserve the trend in the existing streamflow, the newly constructed synthetic dataset should be adjusted to ensure that the existing trend is maintained exactly. The original trend line may be altered a little bit (less than 1%) in the above random process. This adjustment is done by comparing the difference between the existing and new trend line for the period from the beginning year (*i.e.*, 2013) to the last year (2069) of new flows year by year. Then the differences are distributed to the month flows proportionally based on the flow of each month in the entire calendar year. After applying the differences, the original regression equation is preserved.

4. Repeat step 3 to make a series of 1000 natural hydrology input datasets. The decision to use 1000 input datasets is based on another study on the reliability of reservoir firm yield, which indicates that 500 datasets are sufficient for a convergence of firm yield mean value (Yang *et al.* 2017). Figure 5 shows the distribution of these 1000 simulated firm yields, which reveals a normal distribution.
5. Modify the model input file for the sediment condition at 2020, 2030, 2040, 2050 and 2060. Sedimentation in reservoir reduces its capacity and affects storage volume and gives lower firm yield. We use an elevational sedimentation rate, derived from volumetric surveys undertaken by the Texas Water Development Board in 1965 and 1995 (1,330 acre-feet per year or 0.15 percent of 1965 capacity), to construct the projected capacities and elevation-area-capacity rating curves of above planning decades for Lake Meredith (Zhu *et al.* 2018).

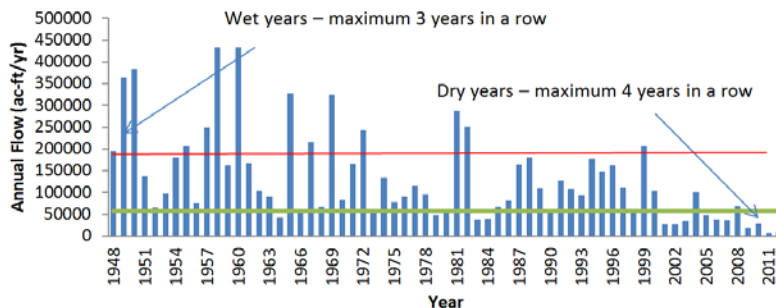


**Fig. 3** Identify wet and dry pattern from existing flows.

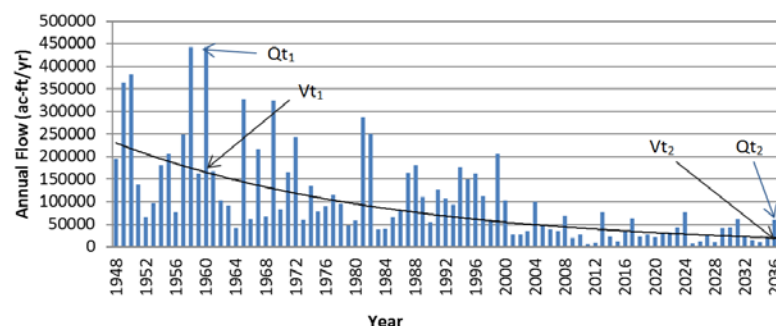


**Fig. 4** Construct flow at future time ( $t_2$ ) by randomly selecting existing time ( $t_1$ ) and by using the above formulation.

6. Run the modified model of 2020, 2030, 2040, 2050 and 2060 by using the newly constructed 1000 hydrologic dataset for the simulation periods, respectively. For each decade, 1000 firm yields are computed for Lake Meredith.
7. Analyze statistical properties of the computed 1000 firm yield results at each simulated decade (*i.e.*, 2040; Fig. 5). Results indicate that firm yields are normally distributed, so mean, median and standard deviation are derived per normal distribution. The exceedance probability of the computed 1000 firm yield results for each simulated decade is plotted too (Fig. 6).
8. Evaluate available water supply for each decade simulated by selecting the best criteria, such as an exceedance probability, a certain percentile, or confidence interval. In this experimental study, we selected Confidence Intervals, 99-percent, 95-percent, 90-percent, and 80-percent to examine the magnitude of the simulated firm yields for all decades designed.

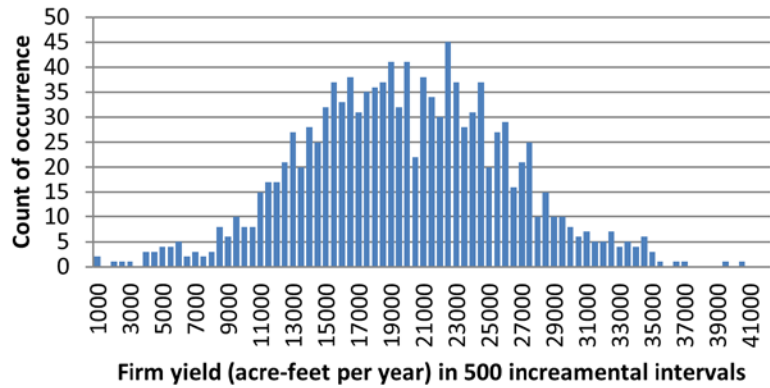


Fig. 5 Distribution of firm yields for result of simulation for 2040.

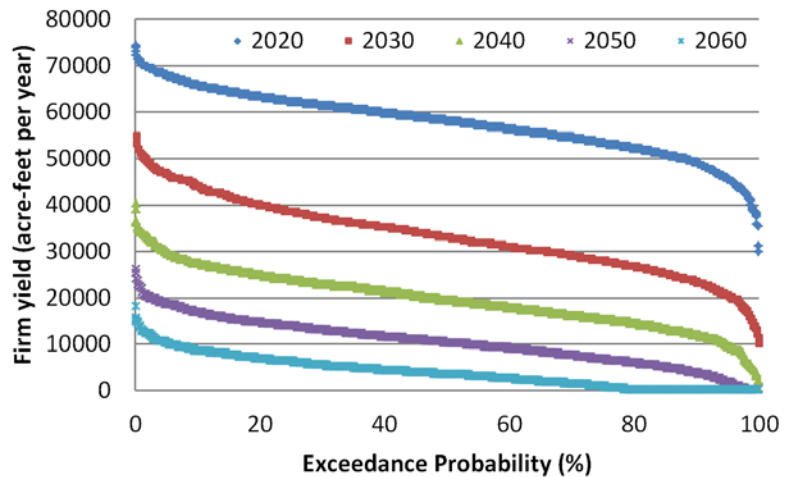


Fig. 6 Exceedance probability of firm yield for simulations for 2020, 2030, 2040, 2050, and 2060.

### 3. Preliminary results for Lake Meredith in Canadian River Basin

Results for Lake Meredith indicate that firm yield in the future decreases as the simulation period increases. The original TCEQ Canadian WAM (1948-1998) firm yield for Lake Meredith is 79,970 acre-feet per year at exceedance probability of 65-percent. The firm yield for 2010 (period of simulation is from 1948 to 2010) is 75,280 acre-feet per year (also bears 65-percent exceedance probability). If one does not want to change the current exceedance probability (65-percent), the simulated firm yield is approximately 55,390, 30,280, 17,040, 8,350, and 1,970 acre-feet per year for 2020, 2030, 2040, 2050, and 2060, respectively. Alternatively, at 85-percent exceedance probability, simulated firm yield is approximately 50,780, 25,180, 13,170, 5,040, and zero (0) acre-feet per year for 2020, 2030, 2040, 2050, and 2060, respectively.

Exceedance probability of firm yields in all simulated decades (2020, 2030, ..., 2060) are plotted in Figure 6. Results indicate that firm yield declines from 2020 to 2060. For planning purposes, a planner could set a certain exceedance probability limit as a standard (criterion) for selecting the firm yield. As indicated in Figure 6, a higher exceedance probability would lead to a lower firm yield and a cautious approach (*i.e.* avoiding over-allocation of available water supply) for water allocation in the future. However, one should avoid selecting too high an exceedance probability (meaning extremely lower firm yield) because it would result in unrealistically low water supply projections for the future. This could lead to unmet water demands in the future resulting in adverse socio-economic impacts. It could also result in water loss to evaporation if the reservoir water is not allocated for beneficial use during the non-drought periods.

A planner can also select a certain Confidence Interval for determining the future firm yield. A confidence interval is the probability that a value will fall between an upper and lower bound of a probability distribution. The lower bound is of interest to the designer or planner interested in adopting a cautious approach to water planning. For example, at the 99-percent Confidence Interval, the lower bound of firm yield is 57,051, 32,748, 19,109, 9,966, and 3,683 acre-feet per year for 2020, 2030, 2040, 2050, and 2060, respectively (Fig. 7). These are greater than the above mentioned firm yields at 65-percent and 85-percent exceedance probabilities. For some decades, simulated firm yields become larger with decreased confidence interval. For instance, at 99-percent Confidence Interval, firm yield is 57,051 acre-feet per year for 2020, while at 80-percent Confidence Interval, firm yield is 57,301 acre-feet per year for 2020. Table 1 provides some typical Confidence Intervals and their associated firm yields.

In this particular study, it appears that exceedance probability around 80-90 percent is a reasonable selection of future firm yield, because the slope drops sharply on curves of firm yield vs. exceedance probability in Fig. 6 above 90 percent exceedance probability, meaning the occurrence is poor (probability of occurrence is low). If we pick exceedance probability at a higher percent (*i.e.* 99 percent), it would lead to a lower firm yield picked which may be never occurring. If we pick a lower exceedance probability, it means higher firm yield but it would cause over allocation and unmet shortage in the future. In this particular case, it appears that firm yields at around 85 percent exceedance probability is safe enough for planning purpose (green line in Fig. 7). Confidence Interval is another criterion that can be used in this type of stochastic study. The higher Confidence Interval means higher probability for the corresponding firm yield in this stochastic forecasting. A normal distribution with known mean and standard deviation of simulated firm yield is tested in this study. It appears firm yield does not change significantly from mean value with increased Confidence Intervals (Table 1).

#### 4. Conclusion and recommendation

As an experimental study, we combine a stochastic approach (Monte Carlo method) and the incorporation of trend to forecast firm yield for the 2020, 2030, 2040, 2050, and 2060 planning decades for Lake Meredith in Canadian River Basin. A constraint (limit of dry and wet periods) for maintaining the cyclic nature of natural hydrology is also incorporated in the synthetic processes. Simulated results indicate that firm yields will decline significantly in future decades from 2020 to 2060. This can be a good reference for water resource planning. It appears that, with a sufficient population for sampling and proper consideration for

**Table 1** Selected confidence intervals and their associated firm yield for decades from 2020 to 2060.

Key criterion		Firm yield (acre-feet per year) at given year				
		2020	2030	2040	2050	2060
Mean		57,551	33,338	19,569	10,336	3,943
Standard deviation		6,715	7,868	6,192	4,994	3,414
Median		58,105	33,145	19,475	10,315	3,520
Lower bound of given Confidence Interval (percent)	99	57,051	32,748	19,109	9,966	3,683
	95	57,171	32,888	19,219	10,056	3,753
	90	57,231	32,958	19,269	10,096	3,783
	80	57,301	33,048	19,339	10,146	3,813

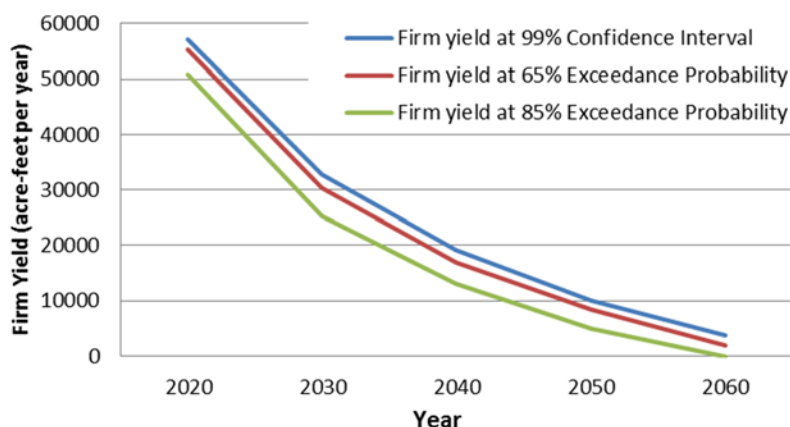


**Fig. 7** Simulated firm yields for decades 2020 through 2060 at 99-percent Confidence Interval, 65-percent Exceedance Probability and 85-percent Exceedance Probability.



future trends, simulated firm yields reveal a clear statistical distribution for planners to determine future projected water supply.

Based on this study, we believe that the 2016 Regional Water Plan for the Panhandle Region (Freese and Nichols, Inc. 2016) can be improved in future planning cycles. The 2016 Plan gave a constant (static) estimated firm yield (37,505 acre-feet per year), safe yield (32,928 acre-feet per year), and zero available supply from 2020 to 2060. Safe yield is safer than firm yield because the 2016 Plan assumed a longer drought than the drought of record. Lake Meredith is an important source of water supply for 11 cities, including Amarillo and Lubbock in the Texas Panhandle. Drought in recent years had significantly affected the storage in this reservoir and drawn attention to water supply issues in the region. It forced the Canadian River Municipal Water Authority to develop groundwater resources from the Ogallala Aquifer to meet their supply shortage. Therefore, earlier planning for the worst case scenario is vitally important to overcome potential future shortages. This study demonstrates a methodology that could be applied to water planning in Texas to improve the reliability of water availability estimates over the next fifty year planning horizon. The study is particularly applicable to other locations in the state that have declining streamflow trends. Modifications to the methodology presented here would be needed if it is to be applied to locations that do not have declining streamflow trends in the observational record.

## References

- Barndorff-Nielsen, O.E., V. K. Gupta, V. Pérez-Abreu, and E. Waymire, Eds., 1998: *Stochastic Methods in Hydrology: Rain, Landforms and Floods*. Advanced Series on Statistical Science and Applied Probability, Vol. 7, World Scientific Publishing Co. Pte. Ltd., 207 pp.
- Espey Consultants, Inc., 2002: *Water Availability Models for the Red and Canadian River Basins*, Vol. 1 Report and Appendices A-K.
- Freese and Nichols, Inc., 2016: *Regional Water Plan for the Panhandle Water Planning Area*, Panhandle Water Planning Group Commission.
- Machiwal, D. and M. K. Jha, 2006: Time series analysis of hydrologic data for water resources planning and management: A review. *J. Hydrol. and Hydromech*, **54**, 237-257.
- Srikanthan, R. J. and T. A. McMahon, 2000: Stochastic generation of climate data: a review. Cooperative Research Centre for Catchment Hydrology, Monash University, Monash, Vic., 34 pp.
- U.S. Bureau of Reclamation, 2003: *Stochastic Modeling Methods*, Dam Safety Office, Report No. DSO-03-04, Department of Interior, 35pp, <https://www.usbr.gov/ssle/damsafety/TechDev/DSOTechDev/DSO-03-04.pdf>
- Ward, M. N., M. B. Casey, M. B. Kye, and H. K. Yasir, 2012: Reservoir performance and dynamic management under plausible assumptions of future climate over seasons to decades. *Climatic Change*, **118**, 307-320, doi:10.1007/s10584-012-0616-0
- Wurbs, R. A., 2015: *Water Rights Analysis Package (WRAP) Modeling System Reference Manual*, TR-255, 11<sup>th</sup> Edition, Texas Water Resources Institute, College Station, Texas, 405pp.
- Yang, Y., C. G. Guthrie, R. Solis, N. Fernando, and J. Zhu, 2017: Reliability of firm yield for Texas reservoirs, TWDB internal report.
- Zhu, J., Y. Yang, H. Holmquist, and N. Leber, 2018: Projected reservoir rating curves based on sedimentation surveys and their application to water planning in Texas. *Proc. World Environmental and Water Resources Congress 2018*, Minneapolis, MN, accepted.

## Tracking Progress on NOAA's MAPP-CTB Projects: Accelerating Transition of Research Advances into Improved Operational Capabilities

Jiayu Zhou<sup>1</sup> and David DeWitt<sup>2</sup>

<sup>1</sup>Climate Mission, Office of Science and Technology Integration, NOAA/NWS Headquarters

<sup>2</sup>Climate Prediction Center, NOAA/NWS/NCEP

### 1. Introduction

NOAA's operational climate monitoring and prediction products provide the public with critical information about environmental conditions for better preparedness and improved resiliency. NOAA's Modeling, Analysis, Predictions and Projections - Climate Test Bed (MAPP-CTB) projects support transition of research advances from external community to National Centers for Environmental Prediction (NCEP) to accelerate the improvement of operational climate monitoring and predictions (Fig. 1). Three focus areas are 1) testing the performance of model components and schemes of methodologies, 2) testing experimental prediction methodologies and products, and 3) testing a multi-model subseasonal climate prediction system via model selection, system optimization and products evaluation. By tracking progresses on twenty-three MAPP-CTB projects, this presentation assesses the Transition Readiness Level (TRL) via measurements of benchmarks and deliverables following NOAA Administrative Order 216-105B (NOAA 2016), meanwhile highlights major achievements to date beyond the development phase (TRL > 5).

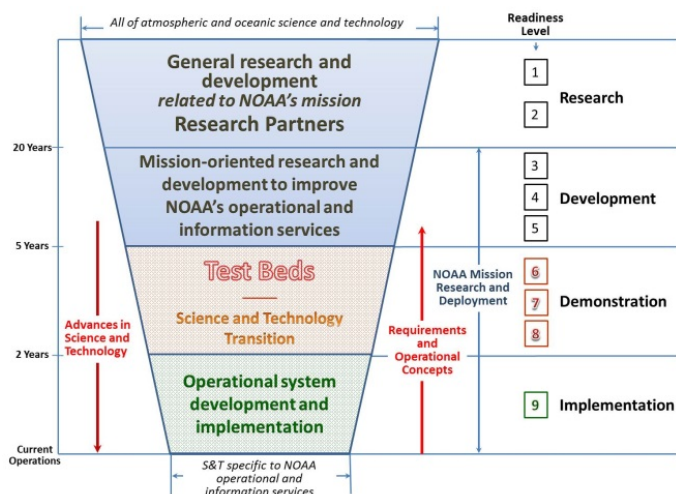


**Fig. 1** NOAA research and development funnel. (MacDonald *et al.* 2006)

By tracking progresses on twenty-three MAPP-CTB projects, this presentation assesses the Transition Readiness Level (TRL) via measurements of benchmarks and deliverables following NOAA Administrative Order 216-105B (NOAA 2016), meanwhile highlights major achievements to date beyond the development phase (TRL > 5).

### 2. Performance of model components and schemes of methodologies

*Targets:*

- Model components critical to subseasonal-to-seasonal (S2S) prediction
- Representation of predictability sources
- Parameterization of subgrid scale dynamic-thermodynamic processes
- Data assimilation

*Projects status:*

Model Components and Schemes	Research Developer	Operation Beneficiary	TRL
1. Flash lake model	USU	CFS	6
2. Community Noah-MPv2 LSM	NCAR	CFS	7
3. NASA GMAO's physically-based cloud/aerosol packages	SUNY	GFS, CFS	6
4. Cloud and boundary layer processes	UW, JPL	GSF, CFS	7
5. Turbulence and cloud processes	UU	GSF, CFS	6
6. Land Information System	NASA	NLDAS	5

7. MOM6/SIS2 Hybrid-GODAS (eddy permitting)	UMD	GODAS	5
8. Coupled wave-Ocean System	GFDL	CFS, NGGPS	5
9. LETKF assimilation for sea ice analysis and forecasting	UMD	CFS, NGGPS	5

*Progress reports:*

Project 1 Flash lake (Flake) model (PI: J. Jin)

- The offline Flake model is improved to better simulate lake ice.
- The lake ice simulations are significantly improved in the coupled CFS-Flake model for the Great Lakes.
- The near-surface air temperature for winter and early spring is better predicted with different forecast leads (Fig. 2).

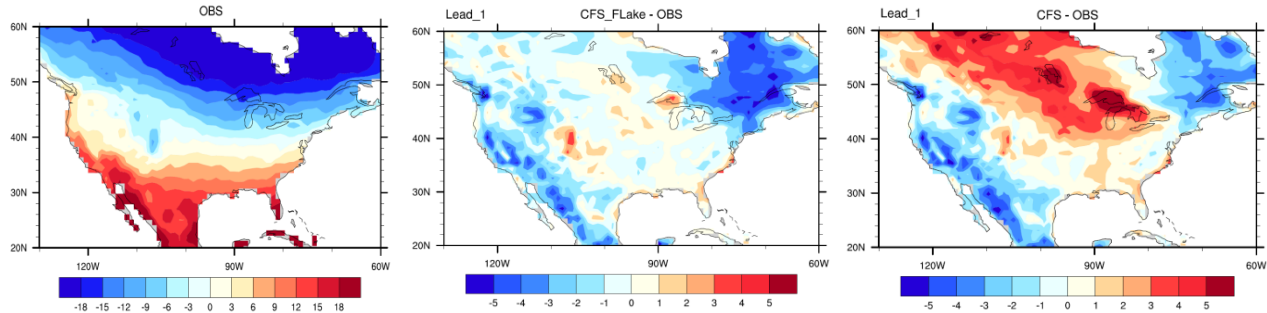


**Fig. 2** One-month-lead two meter height temperature ensemble forecasts over North America averaged for JFM 2014. The left panel is for observation. The rest two panels are for the differences of forecast by CFS-Flake (middle) and CFS (right) minus observation, respectively.

Project 2 Community Noah-MP (Multiple Parameterization) version 2 land surface model (LSM) (PI: F. Chen)

- CFS land-surface modeling system is enhanced with new global land-use and land-cover (LULC) and soil texture data. Consistent with recent community efforts to improve the specification of surface characteristics.
- Preliminary CFS reforecast results show encouraging signs of positive impact of using Noah-MP with ground-water and dynamic vegetation parameterizations on CFS prediction skills in precipitation and surface temperature (Fig. 3).

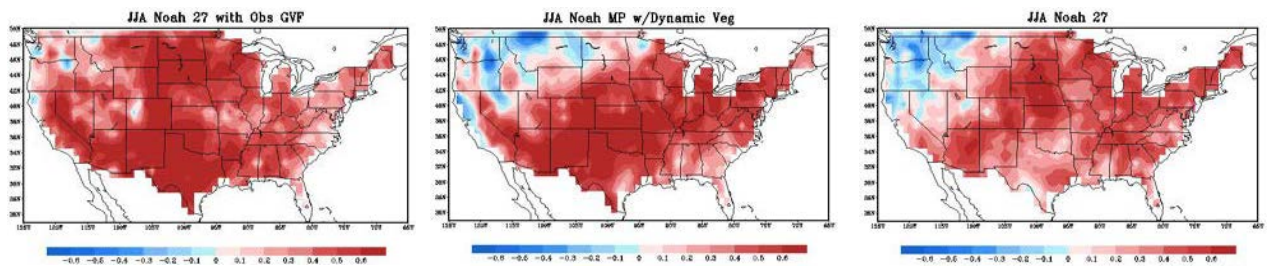


**Fig. 3** Anomaly correlation skill of averaged JJA 2-m temperature over CONUS from CFS experiments of using satellite-based GVF in Noah (left) and Noah-MP with dynamic vegetation (middle), comparing with CFS control (right).

Project 3 NASA Global Modeling and Assimilation Office (GMAO)'s physically-based cloud/aerosol packages (PI: S. Lu)

- NOAA Environmental Modeling System (NEMS) Global Forecast System (GFS) physics suite is upgraded. GMAO's physically-based aerosol and cloud microphysics package (Modal Aerosol Model (MAM) aerosol scheme; Morrison-Gottelman (MG) cloud microphysics; and cloud

condensation nuclei in cloud (CCN/IN) activation) are implemented, tested and evaluated in NEMS GFS (Fig. 4).

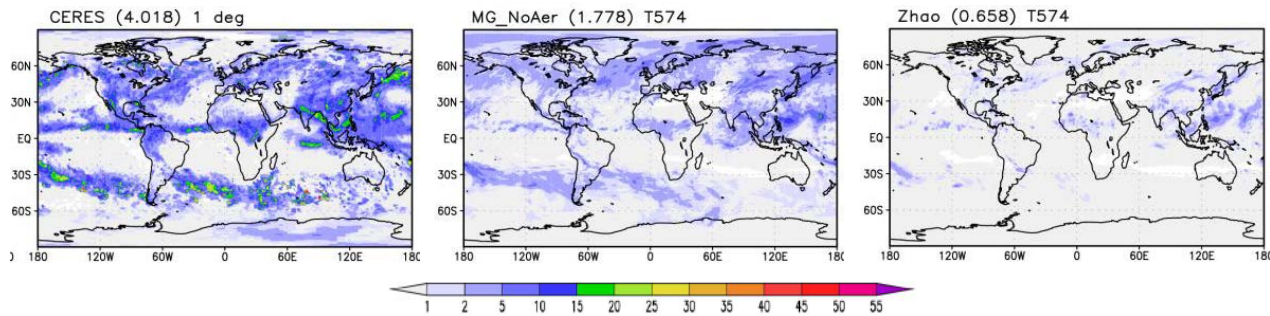


**Fig. 4** High-level cloud optical depth from NEMS GFS runs (Clouds and the Earth's Radiant Energy System (CERES) estimates (left), MG\_NoAER (middle), and CTRL (right),) averaged for Aug 10-17, 2016.

**Project 4** Cloud and boundary layer processes (Lead PI: C. S. Bretherton)

- Further development of moist eddy diffusion-mass flux (EDMF) scheme implemented in GFS and port to the Finite-Volume on a Cubed-Sphere Dynamical Core (FV3) model almost complete.
- Further tuning of Thompson microphysics scheme implemented in GFS, which now improves CONUS precipitation skill scores compared to the operational model (Fig. 5). Ported to FV3.

**Project 5** Turbulence and cloud processes (Lead PI: S.K. Krueger)

- To improve the prediction of the high-level tropical cloud fraction, which is too large in the SHOC (Simplified Higher-Order Closure) test runs with the GFS, SHOC was modified to include two new prognostic equations for variances of total water and static energy; meanwhile the source terms for total water variance were diagnosed from a Giga LES, and a simplified representation of the impact of detrainment of total water on the variance developed.
- Algorithms were developed that efficiently sample the distribution of cloud condensate diagnosed by SHOC for radiative transfer calculations. The algorithms have been tested against a time series of SHOC parameters fit to tropical deep convection (giga-large-eddy simulation (Giga-LES) simulations using high resolution (100-m horizontal grid size) and large domain (200 km by 200 km). (Fig. 6).

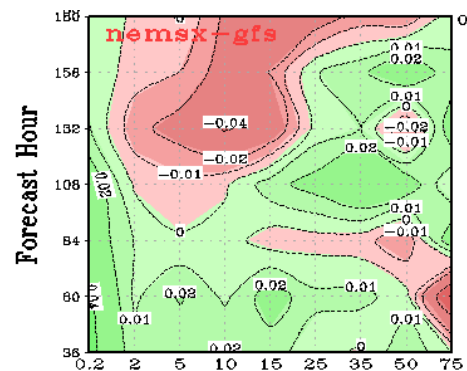


**Fig. 5** Modified Thompson cloud microphysics improves GFS precipitation skill over CONUS, as measured by the equitable threat score (ETS). The horizontal axis is precipitation in mm/day. The green regions show improvement. For almost all precipitation intensities at forecast leads up to 72 hours, the ETS is improved by about 5%.

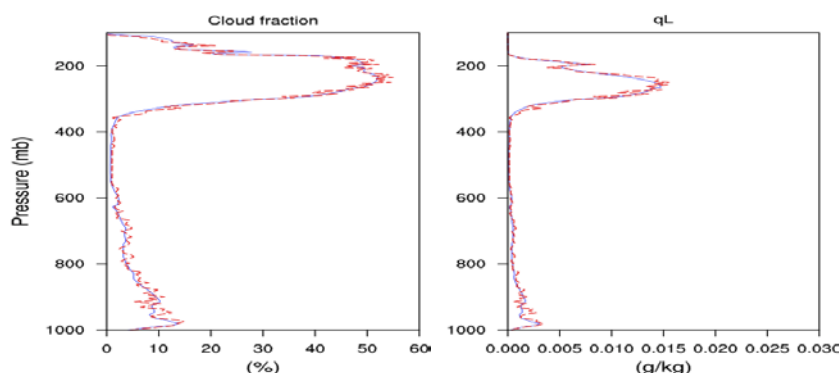


**Fig. 6** The figure shows domain-mean profiles of cloud fraction (left panel) and cloud liquid water content (right panel) obtained directly from the simulation (blue), and as reproduced by Monte Carlo methods (red) using 250 samples. The instantaneous errors are a few percent in cloud fraction and a few mg/kg in cloud water content.



- The closure for updraft fraction for multiple updraft types was tested by using a large-eddy simulation of deep convection in a large domain.

### 3. Experimental prediction methodologies and products

*Targets:*

- Prediction of extreme events
- New tools and ideas
- Products for End-user needs

*Projects status:*

Monitoring and Prediction Methodologies	Research Developer	Operation Beneficiary	TRL
10. CFS-based severe weather forecast tools	CU	CPC	7
11. Week 3 & 4 T and P forecast products	UCSD	CPC	8
12. Flash drought monitoring processes	UCLA	CPC in real-time	7
13. Subseasonal Excessive Heat Outlook System for global tropics and subtropics	UMD/ESSIC	CPC	6
14. Water sector applications of S2S climate products	NCAR	CPC	5
15. Calibration, bridging and merging (CBaM) for S2S prediction	CPC	CPC	5
16. Application of seasonal climate forecast to wildland fire management in Alaska	UAF	CPC, NWS/AR	5

*Progress reports:*

Project 10 CFS-based severe weather forecast tools (PI: M.K. Tippett)

- Assessment of skill of monthly forecasts for NOAA regions (Fig. 7).
- Case studies examining the relation between forecast consistency for notable events.
- Upward trends in number of tornado reports per outbreak.

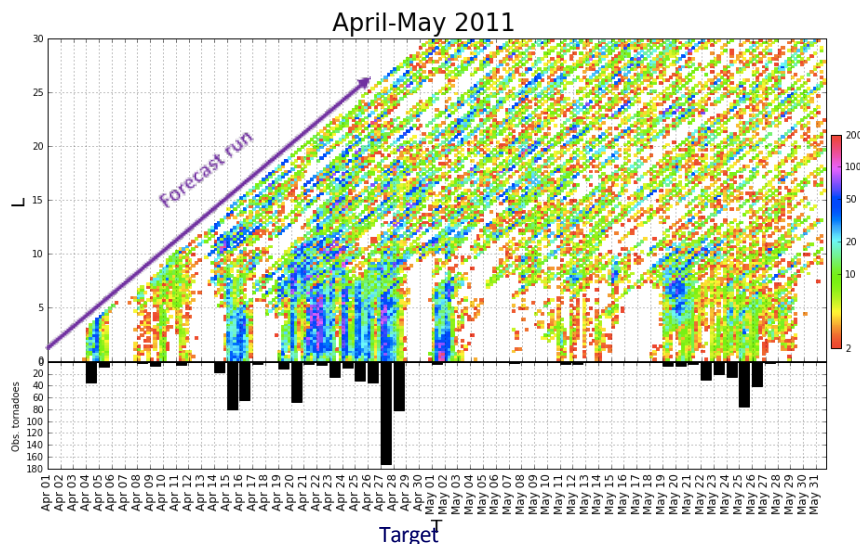


**Fig. 7** CFSv2 forecasts (colors) of daily Tornado Environment Index (TEI) summed over the US at varying lead during the period April-May 2011 when historic and deadly tornado outbreaks occurred. Bar plot shows the number of tornadoes reported on the corresponding day. It shows good indications of active/inactive periods at around the 10-day lead and fairly accurate timing around the 5-day lead mark.

Project 11 Week 3 & 4 T and P forecast products (Lead PI: S.-P. Xie)

- Continued monitoring and demonstration of skill of the MJO/ENSO statistical models in CPC's Experimental Week 3-4 temperature and precipitation outlooks (Fig. 8).



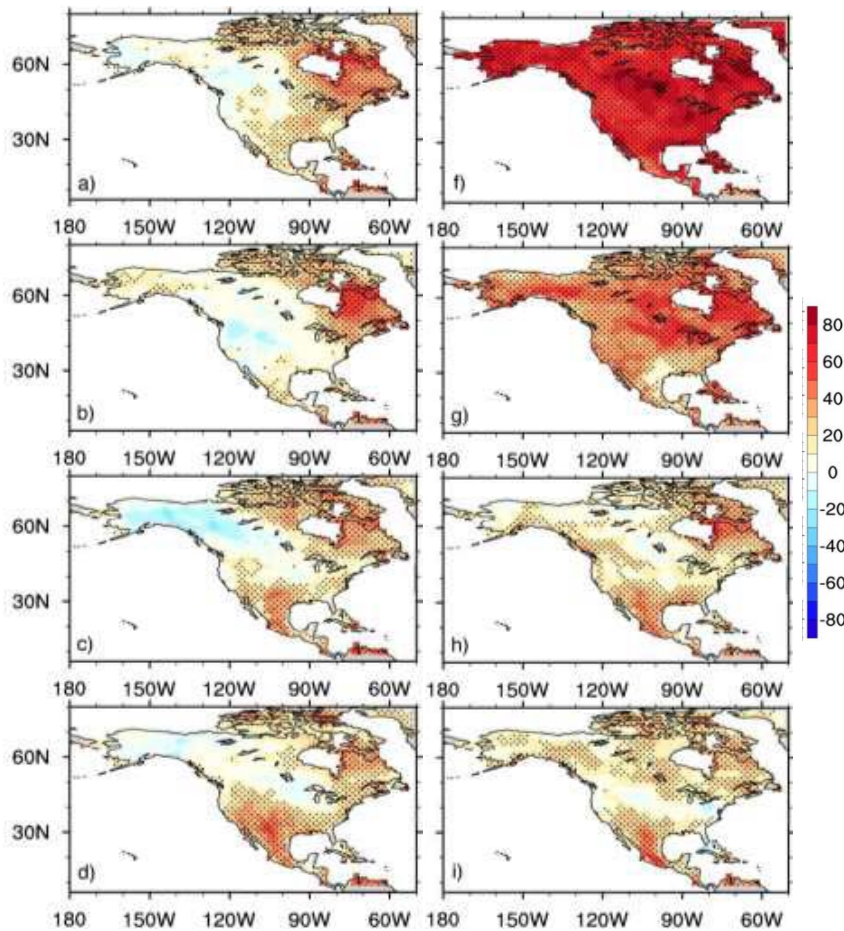
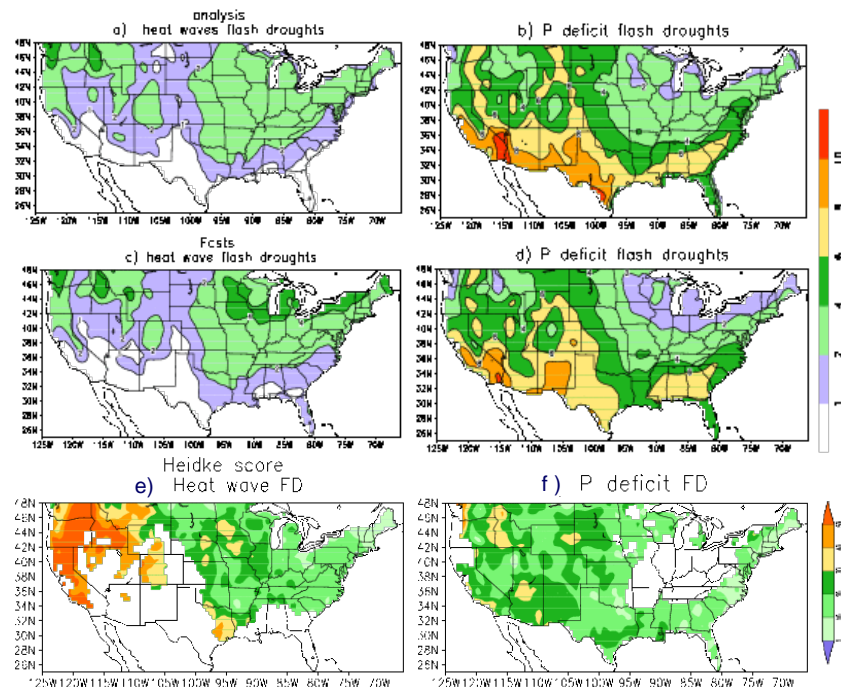


**Fig. 8** To examine the role of atmospheric initialization, two versions of initialization are compared using GFDL FLOR model. FLOR-v1 primarily captures the forcing from the ocean surface, whereas FLOR-v2 includes the additional contribution from realistic atmospheric initial conditions (AICs). The figure on left shows Heidke skill scores (HSSs) of wintertime (DJF) weekly ensemble mean T2m hindcasts of 50th percentile exceedance from FLOR-v1 (a-d) and FLOR-v2 (f-i) at lead times of 1 through 4 weeks. It reveals that the forecast skill of T2m increases dramatically for the first two weeks over the majority of North America from FLOR-v1 to FLOR-v2, and FLOR-v2 also performs noticeably better at week 3, indicating that accurate AICs are important for week 3-4 forecasts over North America.

**Project 12** Flash drought monitoring processes (PI: D.P. Lettenmaier)

- Evaluated the ability of the CFSv2 seasonal forecasts to capture the number of flash droughts of both types (Fig. 9).

**Fig. 9** The ability of the CFSv2 seasonal forecasts to capture the number of flash droughts has been evaluated. The figure shows the frequency of occurrence (%) of pentads under (a) heat wave flash droughts from analysis, (b) P deficit flash drought from analysis, (c) and (d) same as (a) and (b), but from CFSv2 seasonal forecasts, starting from 1 April, 1 May, 5 June and 5 July pooled together for the period from 1982-2010, (e) and (f) are corresponding Heidke skill scores. An experimental real-time flash drought monitor is provided on the CPC website.



- Produced daily ET and total soil moisture fields by forcing the VIC model with CPC precipitation and temperature analyses.
- Now provide an experimental real-time flash drought monitor on the CPC website;

**Project 13** Subseasonal Excessive Heat Outlook System for global tropics and subtropics (PI: A. Vintzileos)

- Developed a quasi-operational real-time version of Global Subseasonal Excessive Heat Outlook System (G-SEHOS) and conducted a reforecast, which is diagnosed to show the need for a generalization of the definition of extreme heat events.
- The generalized definition in principle of (1) describing adequately tipping points in human physiology that lead to heat disease, (2) being general enough to be applicable in both extra-tropical, subtropical and tropical areas, (3) having a relation with mortality, and (4) being predictable in subseasonal-to-seasonal lead times was tested (Fig. 10) and refined using direct observations from Meteorological Terminal Aviation Routine Weather Report (METAR).
- Compared excessive heat events (EHE) intensity differences for METAR and Reanalysis data, and calculated quantile mappings between METAR observations and reanalysis products.

**Heat wave intensity versus mortality for ORD and PHX (1975-2010)**

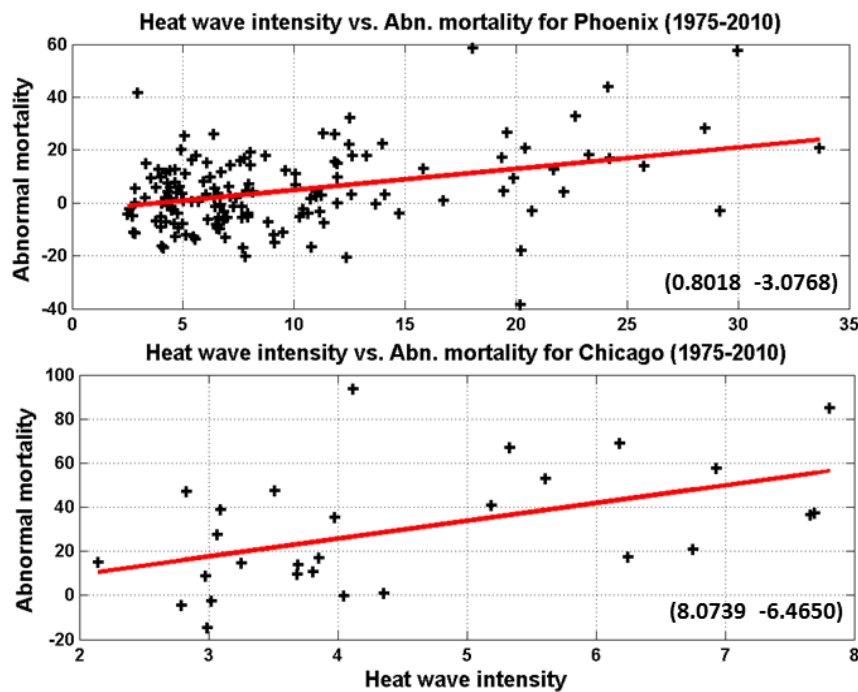


**Fig. 10** In order to extend existing operational SEHOS to the entire globe, a new definition of EHE was introduced. The functionality of this new definition has been tested against a list of documented EHE. The figure shows scatter plots of the intensity of EHE and abnormal mortality for Phoenix-PHX (humid type) and Chicago-ORD (dry type). Red lines show the linear regression between intensity of EHE and abnormal mortality. For low EHE intensity, mortality is not correlated with EHE; however, as the intensity of the EHE increases, there is a clear increase of abnormal mortality.

#### 4. Multi-Model Subseasonal Climate Prediction System

*Targets:*

- Optimization of model design
- Robust MME forecast system

*Projects status:*

Multi-Model System	Research Developer	Operation Beneficiary	TRL
17. Diagnosis of subseasonal NMME forecasts on skill, predictability, & multi-model combinations	GMU	CPC	6
18. NCEP GEFS for monthly forecasts	EMC	CPC	6
19. Operational NMME probabilistic seasonal forecast products improvement	IRI	CPC	9

20. Real-time MME subseasonal forecast system	UM-RSMAS	NMME	5
21. NASA GEOS-5 system	NASA, USRA	NMME	5
22. CCSM4 subseasonal prediction	UM-RSMAS	NMME	5
23. Navy's Earth System Model S2S prediction	NRL	NMME	5

### Progress reports:

**Project 17** Diagnosis of subseasonal NMME forecasts on skill, predictability, & multi-model combinations (PI: T. Delsole)

- Demonstration of forecast skill of temperature and precipitation over the contiguous United States on the 3-4 week timescale (Fig. 11). These results provide a scientific basis for predictability on these timescales.
- Formalization of a rigorous significance test for serially correlated daily data.
- A new method for determining the ensemble size and initialization frequency of the lagged ensemble that minimizes the MSE. The method can identify the optimal lagged ensemble without having to actually run that particular forecast configuration.
- Identification of the optimal lagged ensemble for subseasonal forecasts of the MJO and seasonal forecasts of ENSO in CFSv2.

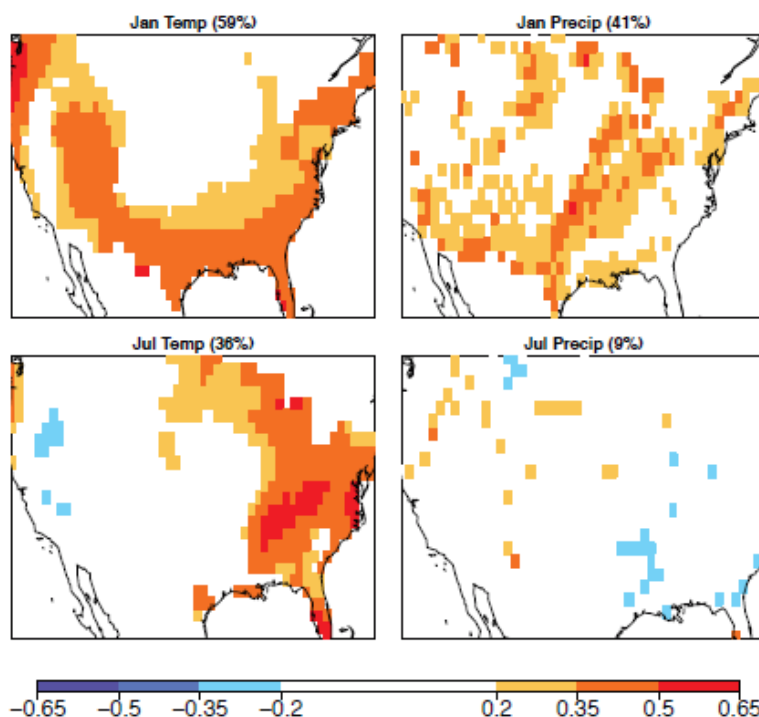


**Fig. 11** Correlation skill of week 3-4 temperature (left) and precipitation (right) CFSv2 hindcasts over CONUS during January (top) and July (bottom), 1999-2010 (12 years). The hindcasts are based on a 4-day lagged ensemble (comprising 16 members drawn from 4x daily hindcasts). Values that are statistically insignificant at the 5% level (according to the permutation test) are masked out. The percentage area with significant correlation skill (positive and negative) is indicated in the title of each panel.

### Project 18 NCEP GEFS for monthly forecasts (PI: Y. Zhu)

- Investigation of the configuration for MGEFS through 4 suites of experiments during a 2-yr experiment period. (Fig. 12).
- Finished an 18-yr reforecast with a high-resolution (34km for 0-8 days and 52km for 8-35 day) model and 11 member ensemble, every other 7 days.

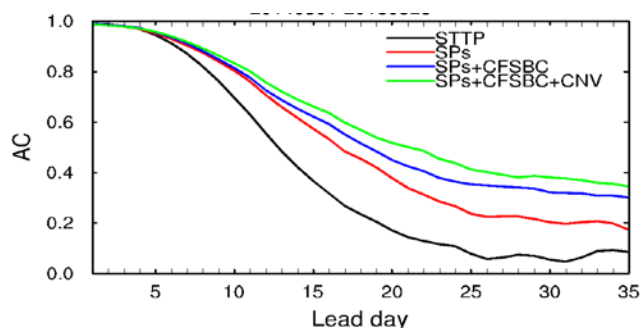


**Fig. 12** NCEP MGEFS MJO forecast skills in terms of bi-variant correlation of the Wheeler-Hendon RMM indices for four different experiments during the period of May 2014 to May 2016. A significant improvement in MJO forecast skill (from 12.5 days to 22 days) is carried out after applying the new stochastic physics perturbation (SPs), updated SST (CFSBC) and new convective schemes (CNV).



- Readiness of a real-time MGEFS version with the identical configuration as reforecast but larger ensemble size (21 members).

#### Project 19 Operational NMME probabilistic seasonal forecast products improvement (PI: A Barnston)

- At IRI, systematic errors in individual coupled model forecast spatial patterns were corrected, resulting in skill improvements in specific regions and seasons. Overall improvements are quite limited, however. On the other hand, improvements at a local (not pattern) level are substantial for both precipitation and temperature. The CCA was therefore found to be useful for an unintended purpose, as local corrections can be done using simpler methods than CCA. Another unexpected finding was that applying the CCA to the entire globe as a single region produced equal or better results (Fig. 13) than applying it to individual regions and merging the corrected forecasts into a global forecast.

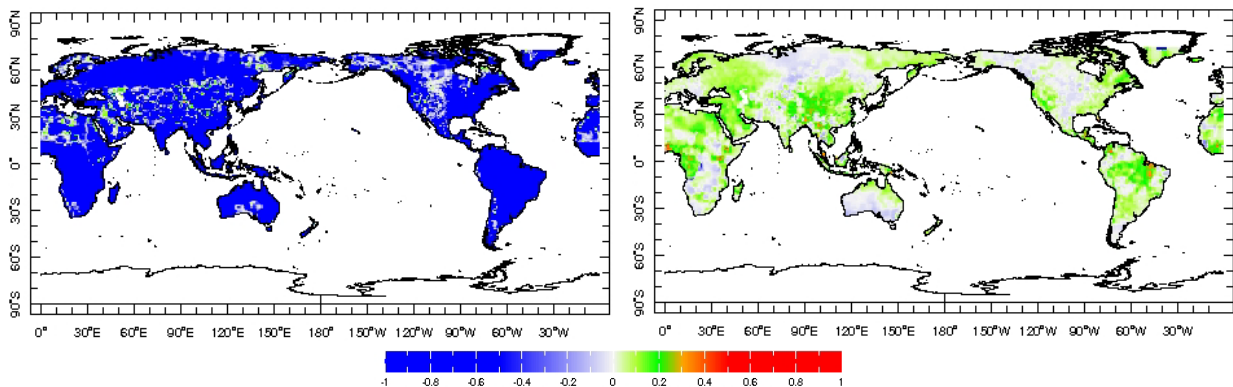


**Fig. 13** Geographic distribution of root mean squared error skill score (RMSESS) over the globe as a single region, for temperature forecasts by the NCEP-CFSv2 model for January-March made in early December. The left panel shows the original skill, and the right panel the skill following the CCA correction. The RMSESS is in terms of standardized anomalies with respect to the observed mean and standard deviation.

#### Project 20 Real-time MME subseasonal forecast system (PI: B. Kirtman)

- Production of re-forecasts by modeling groups
- Re-forecasts being posted at IRI
- Coordination with CPC in preparation for real-time forecasts in July
- Website (Fig. 14)

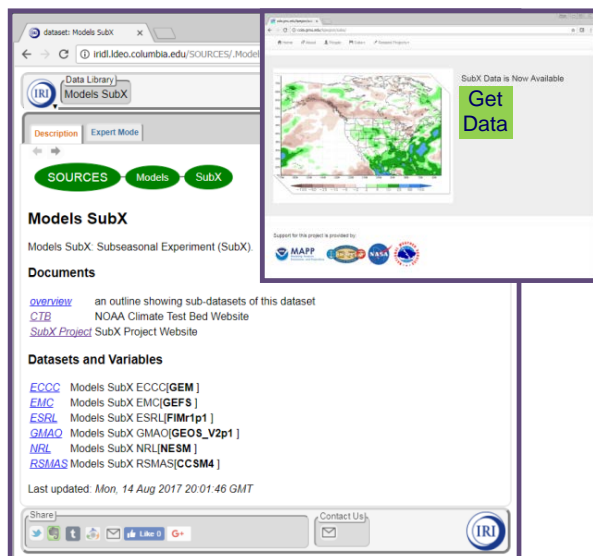


**Fig. 14** A website has been created to provide public information about the Subseasonal Experiment (SubX) project, datasets, models, and research activities. (<http://cola.gmu.edu/kpegion/subx/>) Each modeling group is producing re-forecasts following the SubX protocol. The re-forecasts are being made available to the research community on the IRI data server. The IRI continues to update the NMME monthly archive in the IRI Data Library in real time every month as new output files are made available by the contributing forecast centers. It also assists users of the NMME archive who send requests for help in accessing the data.

## 5. Remarks

The creditability of seasonal-to-subseasonal climate service relies heavily on the prediction skill, which

currently is limited in forecast operation, and the researches on the topic present many challenges (as appeared in the Project 19 research). NWS sincerely invites partners in the research community to work together on the strongholds to meet the legislative act for S2S forecasting innovation passed recently (U.S. 115<sup>th</sup> Congress 2017). As the skill improvement brought about by the advancement of existing dynamical models and statistical tools has been approaching bottleneck, shifting research paradigm in approach to think outside of the box to foster innovation stimulated from rapid developing science areas, such as machine deep learning (Jones 2017), system experimental design (Zhou and DeWitt 2016) *et al.*, needs much attention and encouragement for their potential helpfulness to make breakthrough.

## References

- MacDonald, A., E., R. Fulton, M. Kenny, S. Murawski, P. Ortner, A. M. Powell, A. Sen, and L. Uccellini, 2006: Research location in NOAA: physical and social sciences. 72 pp. [ftp://ftp.oar.noaa.gov/SAB/sab/members/2006/07\\_meeting/PSTT\\_Final\\_Report.pdf](ftp://ftp.oar.noaa.gov/SAB/sab/members/2006/07_meeting/PSTT_Final_Report.pdf)
- Jones, N., 2017: How machine learning could help to improve climate forecasts. *Nature News*, **548**, 379-380.
- NOAA, 2016: NOAA Administrative Order (NAO) 216-105B: Policy on research and development transitions. 11pp. [http://www.corporateservices.noaa.gov/ames/administrative\\_orders/chapter\\_216/NAO%20216-105B%20UNSEC%20Signed.pdf](http://www.corporateservices.noaa.gov/ames/administrative_orders/chapter_216/NAO%20216-105B%20UNSEC%20Signed.pdf)
- U.S. 115<sup>th</sup> Congress, 2017: Weather Research and Forecasting Innovation Act of 2017. Pub. L. 115-25. 131 Stat. 91-128. Apr. 18, 2017. <https://www.congress.gov/115/plaws/publ25/PLAW-115publ25.pdf>
- Zhou, J. and D. DeWitt, 2016: Integration of systems engineering into weather-climate model optimization. *Climate Prediction S&T Digest, NWS Science and Technology Infusion Climate Bulletin Supplement*, 41st NOAA Climate Diagnostics and Prediction Workshop, Orono, ME, DOC/ NOAA, 39-42, doi:10.7289/V5JS9NH0.



# 4. HIGH LATITUDE VARIABILITY

42<sup>nd</sup> NOAA Annual Climate Diagnostics and  
Prediction Workshop

23-26 October 2017, Norman, Oklahoma



## Diagnosing Extremes and Trends of Seasonal Temperatures in Alaska

John E. Walsh and Brian Brettschneider

*Alaska Center for Climate Assessment and Policy  
University of Alaska, Fairbank, AK*

### 1. Introduction

Recent changes in the Arctic's climate have been large and widely reported (AMAP, 2011; IPCC, 2013). These changes span multiple components of the climate system: sea ice, snow cover, glaciers and the Greenland Ice Sheet, and permafrost. Changes in these various components are consistent with atmospheric warming, which has also been well documented, especially during the past few years when the Arctic has set new records for winter and annual temperatures (Richter-Menge and Mathis, 2017). The present paper represents a step towards the attribution of this warming by evaluating the contribution of changes in atmospheric circulation in a region (Alaska) for which the warming of recent decades is typical of the Arctic.

Figure 1 shows the post-1950 Arctic warming in map form for the winter season (December-February) and at the annual (January-December) time scale. Alaska's annual mean warming, which is slightly more than 2°C since 1950, is typical of most of the Arctic (Fig. 1a). The Arctic's warming is greater than most of the rest of the Northern Hemisphere, a manifestation of the well-known Arctic amplification (*e.g.*, Pithan and Mauritsen, 2014). However, the Arctic's winter warming (Fig. 1b) shows a spatially more complex pattern, with a maximum over Alaska, northwestern Canada and the Beaufort Sea. The greater spatial complexity of the winter pattern is consistent with a greater role of the atmospheric circulation in advecting into a region air that is warmer or colder than its climatological mean.

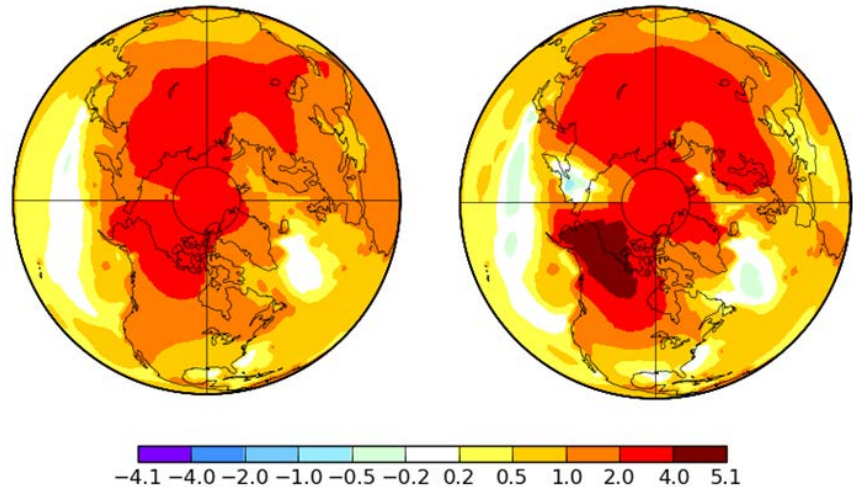


**Fig. 1** Surface air temperature change (°C) from 1950 to 2017 based on least-squares linear fit to annual (left) and winter (Dec.-Feb.) (right) temperatures. Source: NASA Goddard Institute for Space Studies, <https://data.giss.nasa.gov/gistemp/maps/>

Internal variability is readily apparent in the annual temperatures at the regional scale. Figure 2 shows time series of the annual and winter (December-February) statewide average temperatures for Alaska for the 1950-2017 period. While positive trends are apparent in both time series, interannual and multiyear variations are large, and in some cases the year-to-year variations are larger than the overall trend for the 68-year period. The 68-year changes based on least-squares fits to the time series in Fig. 2 are 2.1°C for the annual values and 4.1°C for the winter values. The corresponding trend-derived changes for the other seasons (not shown) are 2.2°C for spring, 1.3°C for summer and 0.8°C for autumn, indicating that the warming has been largest in winter and smallest in autumn.

The final two years of the winter time series in Fig. 2b provide support for the premise that the atmospheric circulation is a key factor in interannual temperature variations over Alaska. The statewide average temperatures for December-February ending in 2016 and 2017 were -9.8°C and -14.7°C, respectively. These temperatures

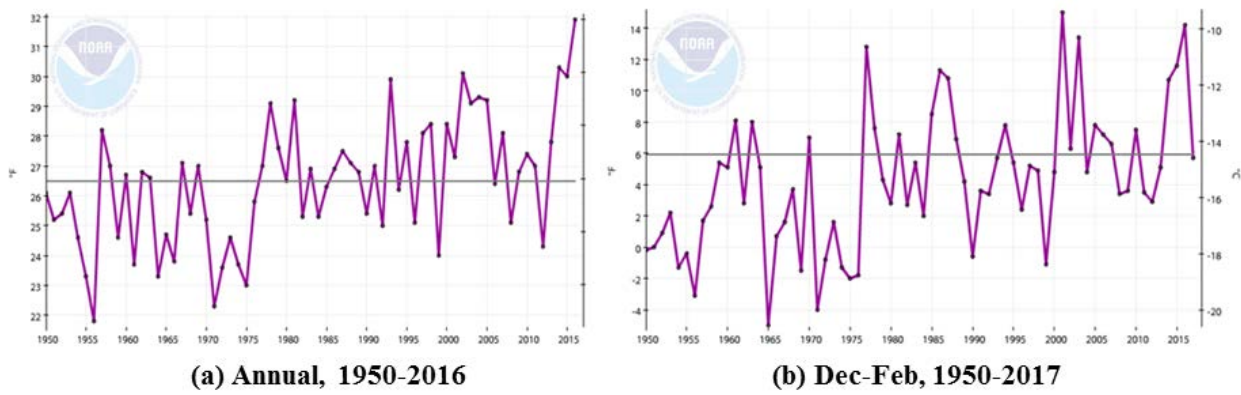


**Fig. 2** Time series of Alaska statewide temperature for 1950-2016/17 for (a) the full calendar year and (b) winter. Temperature scales for °F and °C are shown on the left and right ordinate axes, respectively. Source: National Centers for Environmental Information, <https://www.ncdc.noaa.gov/cag/>

represent departures of  $+4.7^{\circ}\text{C}$  and  $-0.2^{\circ}\text{C}$  from the mean for the 1980-2010 reference period. The difference of approximately  $5^{\circ}\text{C}$  in the 3-month mean temperatures is consistent with the sea level pressure anomalies for the same three-month periods. Figure 3 shows that the 2015-2016 winter was characterized by negative pressure anomalies of more than 12 hPa in the Aleutian region, corresponding to an unusually deep Aleutian low with anomalous northward airflow and warm advection into mainland Alaska. By contrast, the winter of 2016-17 had positive sea level pressure anomalies of more than 10 hPa in the Aleutians, with even larger anomalies to the south, contributing to the eastward advection into much of Alaska. The sensitivity of Alaskan temperatures to near-surface atmospheric circulation, illustrated by the temperature and sea level pressure anomalies of these two recent winters, leads to the hypothesis that much of the trend of winter (and annual) temperatures over Alaska during recent decades is attributable to variations of the atmospheric circulation.

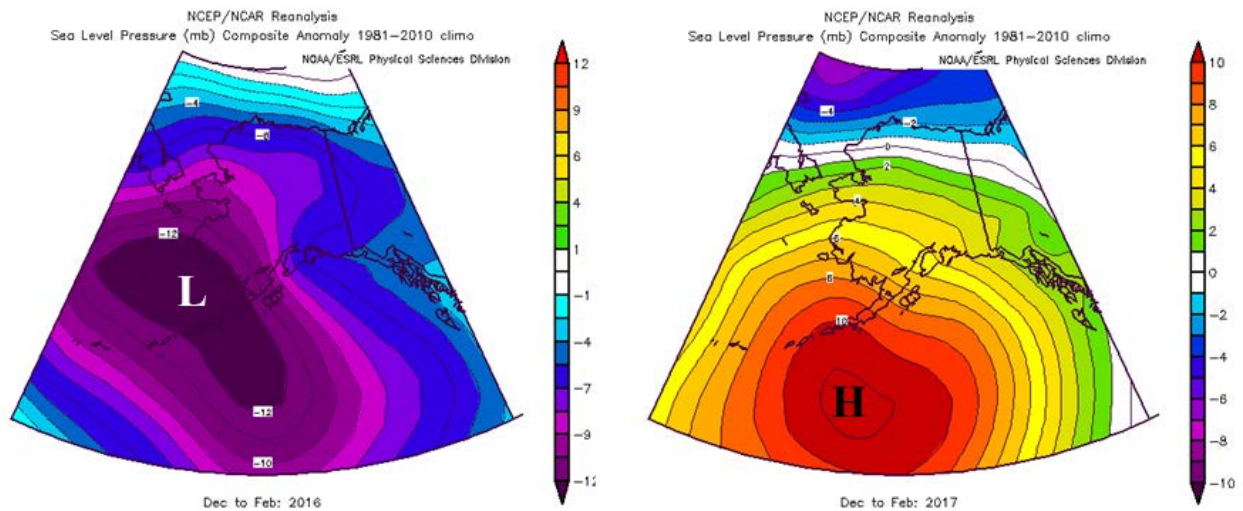


**Fig. 3** Departures from climatological mean (1981-2010) mean sea level pressure (hPa) for December-February of 2015-16 (left) and 2016-17 (right). Contour interval (2 hPa) and color bar are the same for both panels.

## 2. Methodology

Our diagnostic evaluation of the contribution of the atmospheric circulation to the recent warming of Alaska is based on an analog methodology. The analog methodology was illustrated for a single year by Walsh *et al.* (2017), who showed that winds accounted for a substantial portion of the anomalous warmth of the 2015-16 winter and spring (October-April). The approach consists of a comparison of a particular year's sea level pressure (SLP) field over the Alaska region with the SLP fields of all other years in the 1949-2017 period, the selection of the five years with the closest match of SLP fields, and the construction of an analog-

derived temperature by averaging the temperatures of the five best analog years. Guided by the results in the previous study, we base our analog-year selection on the spatial pattern correlation over the Alaska domain bounded by 50°N, 75°N, 180°W and 130°W, SLP as the analog selection variable, and the five best analogs for each year. We perform the analog selection for the statewide temperatures of each season (winter, Dec-Feb; spring, Mar-May; summer, Jun-Aug; autumn, Sep-Nov), although our emphasis will be on the winter season.

We denote the portion of a seasonal temperature anomaly unexplained by the atmospheric circulation as the “excess warmth”, which is also referred to in the literature as the “dynamically adjusted temperature anomaly” (*e.g.*, Deser *et al.* 2014). The “excess warmth” can be attributable to (1) local effects that aggregate systematically in a statewide average, (2) anomalous surface states (anomalies of ocean temperature, sea ice, snow cover), or (3) external forcing such as the effects of increasing greenhouse gas concentrations. A clean separation of the second and third potential attribution sources is not possible from the observational data because increasing greenhouse gas forcing can result in changes in ocean temperature, sea ice and/or snow cover, thereby augmenting direct radiative effects on air temperature. The direct radiative effects of increasing greenhouse gas concentrations may be further partitioned into increased downwelling radiation from anthropogenic sources (CO<sub>2</sub>, CH<sub>4</sub>, *etc.*) and from water vapor, as atmospheric warming is expected to be accompanied by an increase of specific humidity (Serreze *et al.*, 2012; Cullather *et al.*, 2016). However, if the temperature anomaly unexplained by the atmospheric circulation shows a systematic warming over time, then one can point to a trend of “excess warmth” that is consistent with the direct and indirect effects of increasing greenhouse gas concentrations.

### 3. Results

The “excess warmth” will be negative if the actual temperature is colder than the mean value of the five best circulation analog years, and it will be positive if the actual temperature is warmer than the analog-derived value. Figure 4 shows the excess warmth as a function of season and subperiod (quartile) of the 68-year period of record. In all seasons except autumn, the excess warmth increases monotonically from the earliest to the most recent 17-year quartile. In all seasons except autumn, it is negative in the first two quartiles and positive in the two most recent quartiles. Even in autumn, the most recent quartile has the most positive value of excess warmth. The increase from the first to the final quartile ranges from 1.2°C in autumn to 3.0°C in winter, with an annual mean increase of 1.5°C. As an indication of the sensitivity to the metric used in analog selection, we note that the winter-season increase of excess warmth is 3.0°C when analogs selection is based on the spatial pattern correlation, while it is 4.1°C when based on the root-mean-square difference of the gridded pressures.

Least-squares linear fits to the time series of excess warmth for each season enable estimates of changes from 1949/50 to 2016/17. These changes are shown in Fig. 5, together with the corresponding total changes in temperature (trends including the circulation-driven component) and the percentages of the total trend that

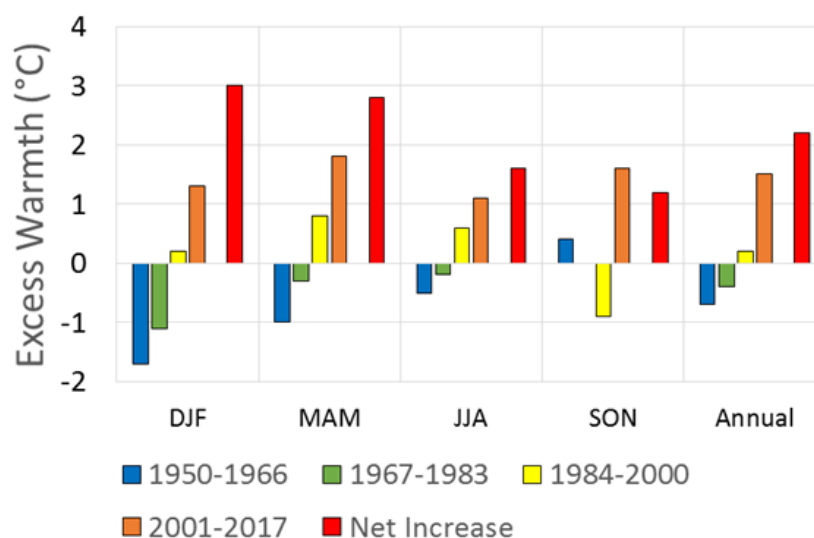


**Fig. 4** Excess warmth (°C) by season and quartile (17-year period), from earliest (blue) to most recent (orange). Negative values indicate that actual temperature was cooler than the analog-derived, positive values indicate actual temperature was warmer than analog-derived. Also shown (red bars) are the total changes in excess warmth from the first to the last quartile.



the excess warmth represents in each season. During winter the linear-trend increase of excess warmth is approximately  $2.1^{\circ}\text{C}$ , which is 51% of the total linear-trend-derived change of  $4.2^{\circ}\text{C}$ . During autumn, the  $0.5^{\circ}\text{C}$  increase of excess warmth represents 64% of the total warming. During spring and summer, essentially all the total increase of temperature is “excess warmth”, as there is essentially no trend in the circulation-derived component of the temperatures. Alternatively, one may say that the atmospheric circulation has not made a detectable contribution to changes of temperature over Alaska during spring and summer, while it has made a substantial contribution in winter and autumn. If the values for the four seasons are averaged into annual values, the increase of excess warmth is  $1.5^{\circ}\text{C}$ , which is approximately 75% of the overall

$2.1^{\circ}\text{C}$  increase of annual mean temperature from 1949 to 2017. However, it should be emphasized that this percentage has a strong seasonal variation, with winter and autumn being the seasons in which the atmospheric circulation has been a major contributor (49% in winter, 36% in autumn) to the overall temperature trend.

#### 4. Conclusion

The results show that (1) the atmospheric circulation explains a substantial portion of the winter and autumn variability and trends of temperature over Alaska, and (2) the portion of the temperature variations unexplained by the atmospheric circulation exhibits a systematic trend in all seasons over the 1949–2017 period. The “excess warmth” (the portion of the temperature variations unexplained by the circulation) accounts for about  $1.5^{\circ}\text{C}$  of the total  $2.1^{\circ}\text{C}$  warming of the annual mean temperature since 1949. This contribution is largest ( $2.1^{\circ}\text{C}$ ) in winter and spring, the two seasons in which the observed warming has been largest, and it compares favorably with the model-simulated warming attributable to increased greenhouse gas forcing.

As noted in Section 2, the approach used in this study cannot distinguish the direct radiative effect of increasing GHG concentrations from the effects of varying surface conditions (ocean temperatures, sea ice, snow cover), for which changes may be driven at least in part by increasing GHG concentrations. Nor can the analog methodology address the possibility that GHG forcing may be contributing to changes in the atmospheric circulation, although there is an emerging consensus that systematic changes of the atmospheric circulation in middle and high latitudes are presently obscured by internal variability (Shepherd, 2014; Screen *et al.*, 2014; Overland, 2016). Variations in the atmospheric circulation, in turn, play a role in the cloud cover, which can affect surface air temperatures in all seasons. Controlled model experiments are required to sort out the effects of these various components of anthropogenic forcing. However, the results reported here do point to the importance of the atmospheric circulation in explaining the recent warming of Alaska during winter and autumn.

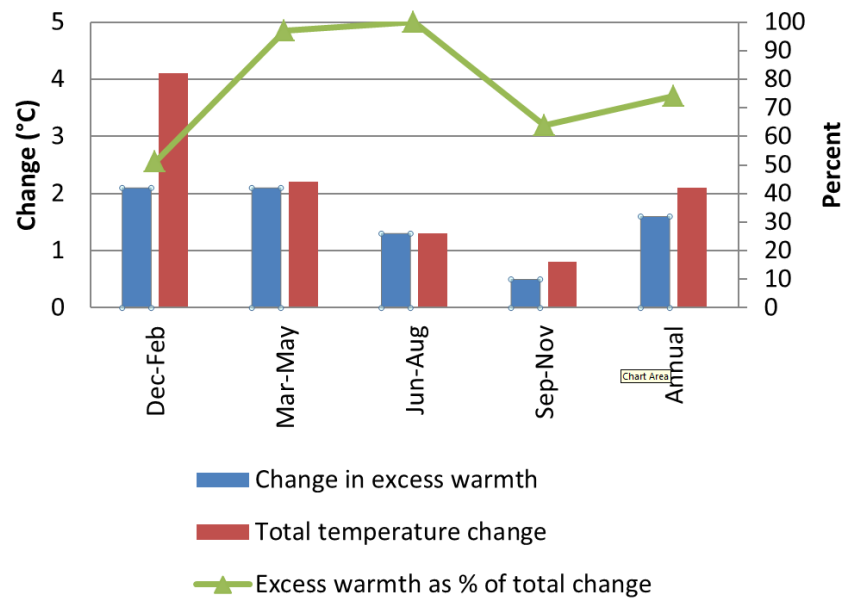


**Fig. 5** Change in excess warmth by season based on least-squares linear fit to yearly values, 1949/50 through 2016/17 (blue bars). Also shown are total changes of temperature (red bars) and change in excess warmth as a percentage of the total change of temperature (green line). The latter is the same as the ratio of the trends.



*Acknowledgements.* This study was funded by NOAA's Climate Program Office, Grant NA15OAR4310169.

## References

- AMAP, 2011: Snow, Water, Ice and Permafrost in the Arctic: Climate Change and the Cryosphere. Arctic Monitoring and Assessment Programme (AMAP), Oslo, Norway, xii+538 pp.
- Cullather, R. L., Y.-K. Lim, L. N. Boisvert, L. Brucker, J. N. Lee, and S. M. J. Nowicki, 2016: Analysis of the warmest Arctic winter, 2015-2016. *Geophys. Res. Lett.*, **43**, 10,808-10,816, DOI: 10.1002/2016GL071228.
- Deser, C., A. S. Phillips, M. A. Alexander and B. V. Smoliak, 2014: Projecting North American climate over the next 50 years: uncertainty due to internal variability. *J. Climate*, **27**, 2271–2296.
- IPCC, 2013: *Climate change 2013: The physical science basis. Contribution of Working Group I to the Fifth Assessment Report of the Intergovernmental Panel on Climate Change*. Stocker, T. F., D. Qin, G.-K. Plattner, M. Tignor, S. K. Allen, J. Boschung, A. Nauels, Y. Xia, V. Bex and P. M. Midgley (eds.), Cambridge University Press, Cambridge, U. K. 1535 pp.
- Overland, J. E., 2016: A difficult Arctic science issue: Midlatitude weather linkages. *Polar Science*, **10**, 210-216.
- Pithan, F., and T. Mauritsen, 2014: Arctic amplification dominated by temperature feedbacks in contemporary climate models. *Nature Geoscience*, **7**, 181-184.
- Richter-Menge, J., and J. T. Mathis, 2017: The Arctic. In State of the Climate in 2016, *Bull. Amer. Meteor. Soc.*, **98**, Special Suppl., S129-S154.
- Screen, J. A., C. Deser, I. Simmonds, and R. Tomas, 2014: Atmospheric impacts of Arctic sea ice loss, 1979-2009: separating forced change from internal variability. *Clim. Dyn.*, **43**, 333-344.
- Serreze, M. C., A. P. Barrett, and J. Stroeve, 2012: Recent changes in tropospheric water vapor over the Arctic as assessed from radiosondes and atmospheric reanalyses. *J. Geophys. Res.*, **117**, D10104, doi:10.1029/2011JD017421.
- Shepherd, T. G., 2014: Atmospheric circulation as a source of uncertainty in climate change projections. *Nature Geoscience*, **7**, 703-708, doi: 10.1038/ngeo2253.
- Walsh, J. E., P. A. Bieniek, B. Brettschneider, E. S. Euskirchen, R. Lader and R. L. Thoman, 2017: The exceptionally warm winter of 2015-16 in Alaska. *J. Climate*, **30**, 2069-2088.

## Atmosphere-Sea Ice Coupling Processes in Observations and CMIP5

Qinghua Ding<sup>1</sup>, Michelle L'Heureux<sup>2</sup>, Kirstin Harnos<sup>2</sup>, Nathaniel Johnson<sup>3</sup> and Mitch Bushuk<sup>2</sup>

<sup>1</sup>Department of Geography, Earth Research Institute, University of California, Santa Barbara, CA

<sup>2</sup>Climate Prediction Center, NCEP/NWS/NOAA, College Park, MD

<sup>3</sup>Geophysical Fluid Dynamics Laboratory, OAR/NOAA, Princeton, NJ

### 1. Introduction

In this study, we aim to understand the influence of the summertime circulation on Arctic sea ice melt in September and find an important circulation mode with a single cell over Greenland that explains a substantial fraction of sea ice September variability at interannual and decadal time scales. This circulation feature is highly correlated with other key variables affecting the sea ice energy balance, such as vertical velocity and air temperature in the entire troposphere, cloudiness in the lower boundary layer and downwelling longwave radiation at the surface.

### 2. Hypothesis of mechanism

The mechanism behind these connections is hypothesized as follows: anomalous high pressure causes strong downdrafts in the Arctic and thus adiabatically warms the atmosphere above the sea ice. At the same time, increases in moisture advection and cloudiness are driven by the anomalous anticyclonic circulation pattern centered over Greenland. This combination of a warmer, cloudier, and more humid atmosphere increases downward longwave radiation and leads to increases in sea ice melt. We suggest that the observed circulation trend over the past 40 years resembles this mode and therefore explains as much as 60% of the recent sea ice decline in September.

### 3. Assessment of anthropogenic contributions

To assess anthropogenic contributions to this circulation trend, we examine an ensemble mean of 26 CMIP5 runs and 30 members of NCAR Large Ensemble Community Project (LENS) runs under anthropogenic forcing since 1979. We find that the observed circulation change around Greenland results from a combination of a hemispherical uniform increase in geopotential height due to anthropogenic forcing and a strong regional barotropic increase from the surface to the upper troposphere centered over Greenland (Fig. 1). Figure 2 shows the height-latitude JJA zonal mean geopotential

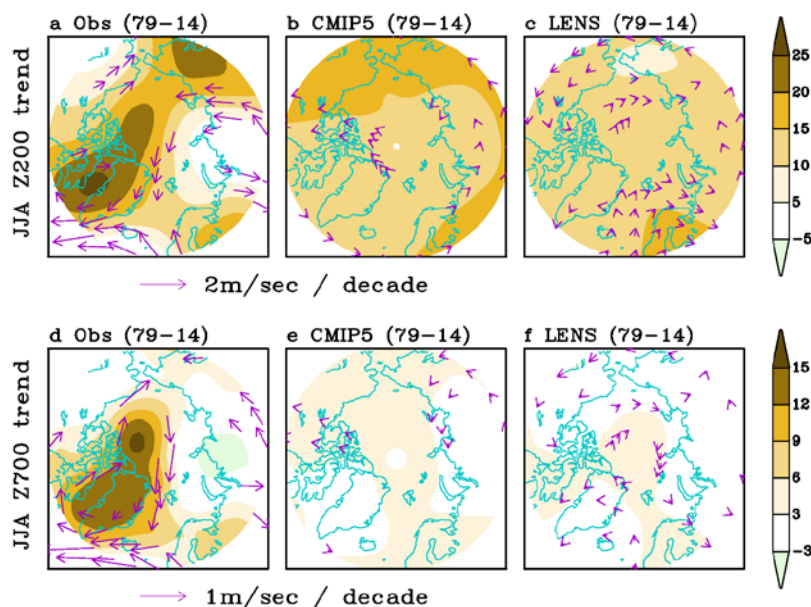


**Fig. 1** Observed (reanalysis) and model estimated radiative forced trends in upper and lower tropospheric geopotential height and winds. Linear trends of summer (JJA) geopotential height (m per decade) and zonal and meridional winds at 200hPa (upper panels) and 700hPa (lower panels) for the period 1979–2014 from a) and d) ERA-Interim, b) and e) the 26-model ensemble mean from the CMIP5 project, and c) and f) the 30-member ensemble mean from the LENS project.

height, temperature and specific humidity trends from ERA-Interim and ensemble means of LENS and CMIP5. The models exhibit different vertical structures from the observations, implying different underlying mechanisms associated with Arctic warming in the models and real world. The anthropogenically forced trend pattern is characterized by a uniform rise of heights everywhere in the Arctic with the larger rise in the upper troposphere. The observation features an obvious barotropic structure that favors the increase of height in the deep Arctic and adiabatic warming increasing towards the surface. The circulation change in the Arctic with a strong barotropic structure is not readily explained by anthropogenic forcing and sea ice feedbacks in summertime (Figs. 1 and 2).

#### 4. Examination of causality

We then use two sets of experiments to examine the direction of causality in the linkage between circulation and sea ice. The first set uses the ECHAM5 atmospheric general circulation model (GCM) coupled with a simple thermodynamic sea ice–ocean model. By nudging the model's wind pattern to observations (reanalysis), we found that the model reproduces patterns of observed changes in temperature, vertical velocity, longwave radiation fields, and a subsequent decline in sea ice. From this set, we conclude that the circulation plays a leading role in modulating the thermodynamic state of the Arctic atmosphere. The second set quantifies the contribution of summer (JJA) circulation changes to sea ice loss in September. We employ a sea ice–ocean model that features sea ice dynamics and ice–ocean interactions but is driven by prescribed atmospheric forcing fields. In the control run, we use observed surface atmospheric forcing from ERA-Interim and reproduce well the observed sea ice decline from 1979 to 2014. In the experiment, we remove any part in the forcing field that is linearly related to the circulation change over Greenland and then use the residual forcing fields to force the ocean–sea ice model again. We find that forcing due to the circulation change over Greenland explains 60% of sea ice decline in September.

To our knowledge, these numerical experiments are for the first time demonstrating the connection between circulation variability and sea ice loss.

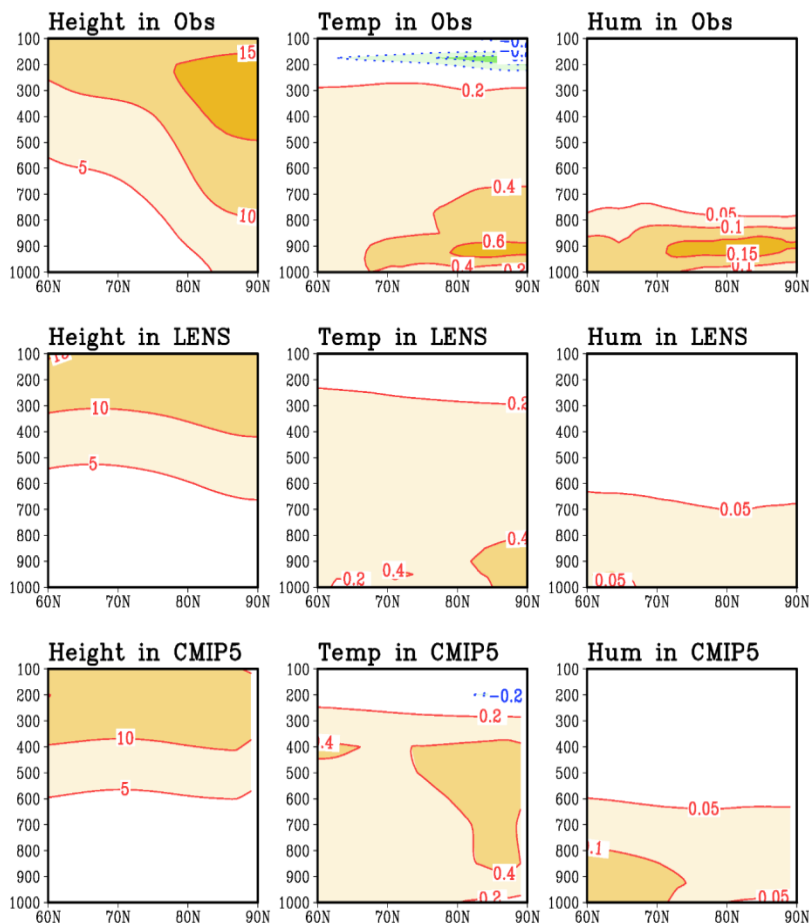


**Fig. 2** Linear trends of JJA zonal mean height (unit: m/decade), temperature (C/decade) and specific humidity (g/kg/decade) in the period 1979-2014 from ERA-Interim (upper panels) and the ensemble mean of 26 members of CMIP5 historical runs (middle panels) and 30 members of LENS historical runs (lower panels).

## Searching for Arctic Temperature Trends and Extremes from Original Station Records

Taneil Uttal

*Physical Science Division, NOAA Earth Systems Research Laboratory, Boulder, Colorado*

### 1. Introduction

Over the last decade since the International Polar Year (IPY) NOAA has led development of the International Arctic Systems for Observing the Atmosphere (IASOA) consortium (Uttal *et al.* 2016 and [www.iasoa.org](http://www.iasoa.org)). The IASOA (Fig. 1) consortium has resulted in a voluntary, international partnering of Observatories operated by institutions and agencies of the 8 Arctic countries. The mission is to create networked observing practices, long-term data sets and groups of specialists to further understand and monitor the evolution and process of Arctic weather, climate and linkages to the rest of the planet. The data at the IASOA observatories is uniquely Arctic and represents a part of the planet where the diurnal cycle has significant variance over the year ranging from the extremes of 24 hours of night, 24 hours of day and long periods with mixed astronomical, nautical and civil twilight. While this sun-earth geometry is of course a well known fact for the polar regions, the resulting need for choosing averaging periods that are representative of the annual cycles of solar irradiance at Arctic sites is often overlooked, and the use of more globally representative seasonal averaging periods can obscure and distort detection of even the simple analysis of temperature trends.

### 2. Data

Most of the IASOA Observatories are collocated with weather stations, which have unusually long records especially for the Arctic region. In this study, the Tiksi Observatory in the Russian Arctic is highlighted by a detailed digitized historical records (referred to hereafter as AARI) starting in 1936 that was compiled by the Russian Arctic and Antarctic Research Institute from original detailed handwritten records. These are used to assess the Global Historical Climate Network Daily (GHCND) data for Tiksi that is available from NOAA/NCEI and described by Menne *et al.* (2012). In the following sections, (1) a comparison is made of the digitized historical AARI and NCEI daily temperature minimum and maximum ( $T_{\min}$  and  $T_{\max}$ ), (2) it is shown that Arctic seasons need to be defined as “cold”, “warm” and “transitional” based on temperature clustering, (3) temperature trends are analyzed based on resulting definitions of the Tiksi specific Arctic seasons and as a function of the length of the data record, and (4) a preliminary assessment is made to identify decadal changes in the occurrence of extreme temperature events in Tiksi.

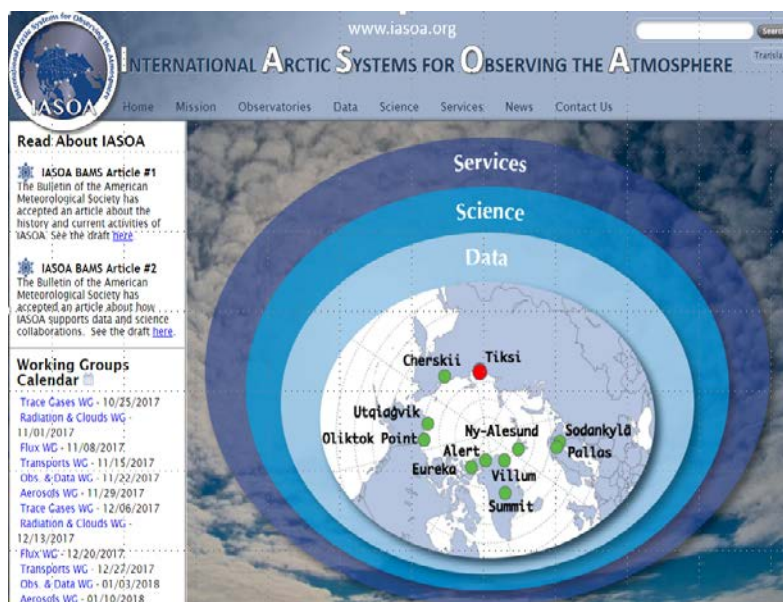


**Fig. 1** Screenshot of the Home Page of the International Arctic Systems for Observing the Atmosphere (IASOA) web site ([www.iasoa.org](http://www.iasoa.org)). The Tiksi Station in the Russian Arctic is highlighted as the focus of this surface temperature study.



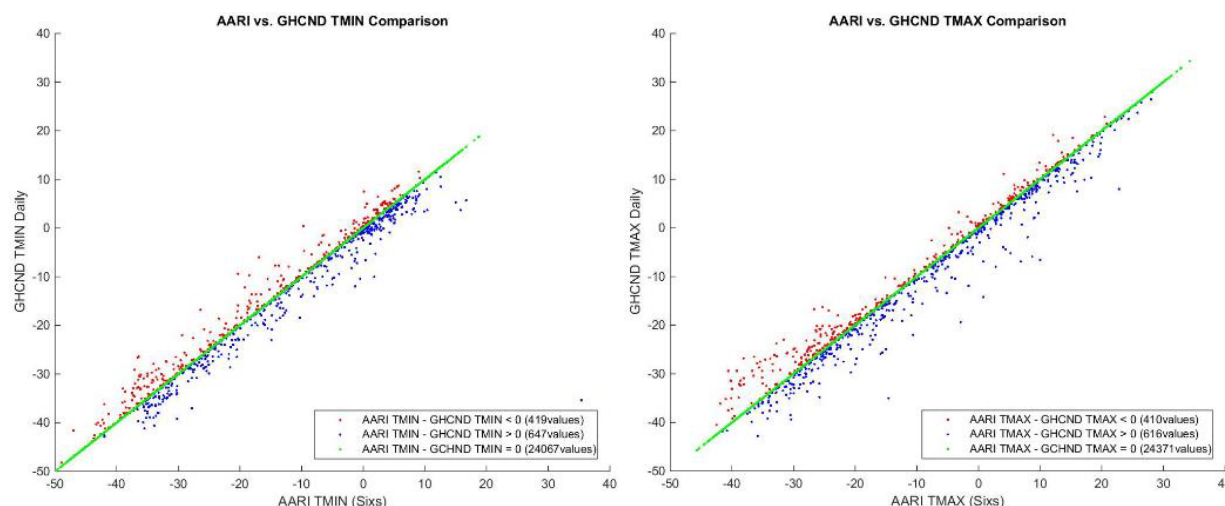


**Fig. 2** Comparisons of AARI and GHCND for  $T_{\min}$  (left) and  $T_{\max}$  (right) over the period 1936-2014.

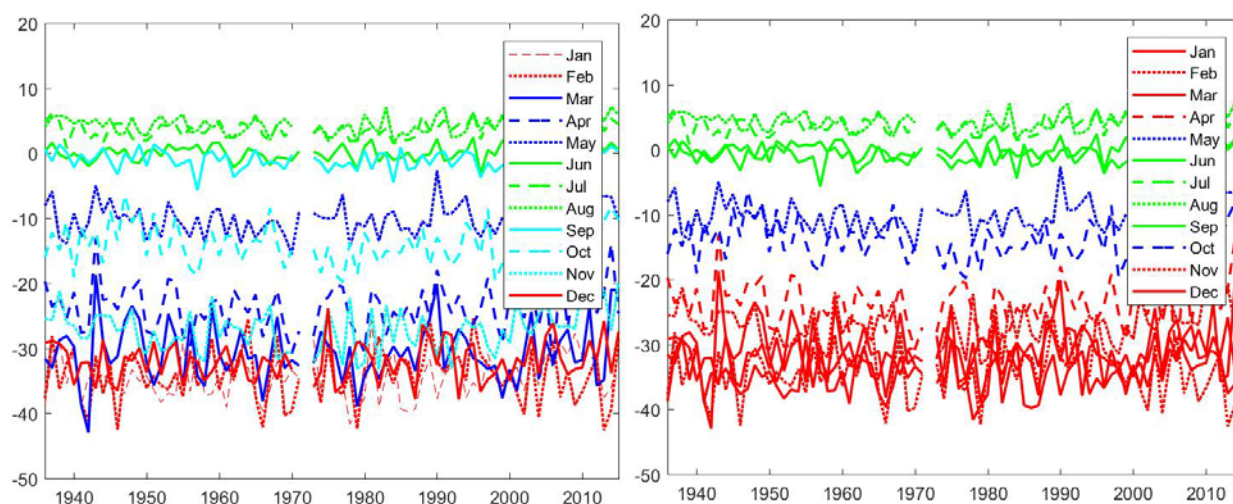


**Fig. 3** AARI and GHCND for  $T_{\min}$  (left) and  $T_{\max}$  (right) over the period 1936-2014. Months are color coded green (JJA (left) and JJAS (right)), red (DJF (left) and NDJFMA (right)), blue (MAM (left) and M (right)) and turquoise (SON (left) and O (right)).

### 3. Comparison of the historical and NCEI daily temperature minima and maxima ( $T_{\min}$ and $T_{\max}$ ) at the Tiksi Station

Temperature records in Tiksi started in 1934 with reported measurements at 00Z, 06Z, 12Z, 18Z and 21Z. Additional reported measurements were added at 03Z, 09Z, and 15Z from 1965. Daily minima and maxima temperatures were separately recorded throughout the measurement period with six's thermometers that are designed to record highest/lowest temperature until reset (after each 24 hour reporting period). Figure 2 shows comparison of AARI and GHCND for daily  $T_{\min}$  and  $T_{\max}$ .

Despite the apparent visual scatter, daily values are identical ( $TAARI - TGHCND = 0$ ) for 95.76% and 95.96% of the time for  $T_{\min}$  and  $T_{\max}$  respectively. Preliminary analysis suggests that the small percentage of time ( $\sim 4\%$ ), when sometimes large discrepancies occurred, is when the GHCND data set substituted a minimum and maximum temperature value from 3 hourly measurements; these have been shown to have exceedingly poor correspondence with actual daily minimum and maximum temperatures. Based on these results it was determined that the GHCND data are reliable for determining multi-decadal temperature trends and extremes and are used in the following sections.



#### 4. Arctic seasonality

Figure 3 shows monthly average temperatures at Tiksi from 1936 to 2014 from GHCND data illustrating how monthly temperatures at this high latitude (71.596°N) site naturally cluster into a warm season, a cold season and 2 shorter transition seasons. Based on this clustering the Tiksi seasons are partitioned as 'warm' defined as June-July-August-September (JJAS), 'cold' defined as November-December-January-February-March-April (NDJFMA), 'cold-to-warm' transition as May (M) and 'warm-to-cold' transition as October (O).

#### 5. Tiksi accumulating temperature trends

In Fig. 5 accumulating trends and monthly averages are shown for both JJA-DJF and JJAS-NDJFMA seasons. Accumulating trends (°C/year) are a function of the length of the record over which the trend is calculated. Figure 4 illustrates how accumulating trends are calculated; the trend °C/decade for a start time of 1940 to 2014 (blue line in lower figure) is near 0°C/year. The trend in °C/decade for a start time of 1980 to 2014 is 0.125°C/decade, the trend for a start time of 1998 to 2014 is 0.27 0°C/year. Therefore the top panels in Fig. 5 shows the how the trend changes as data is utilized from further and further back in the record; this is an alternative to straight line regressions through different sections of a time-series which is a more standard practice. Figure 5 indicates that the rate of warming is small when calculated from the beginning of the record; this is largely due to the fact the 1940s were a decade of notable Arctic warming, a phenomena that is still poorly understood (Yamanouchi 2011). It is also noted that for the Arctic cold season, the sign as well as the magnitude of the trend can change depending on whether or not DJF or ONDMFM is used to subset the data. This is especially true for trends calculated with start dates in the 1970s and later. For the Arctic warm season JJA/JJAS, it is not unexpected that there are

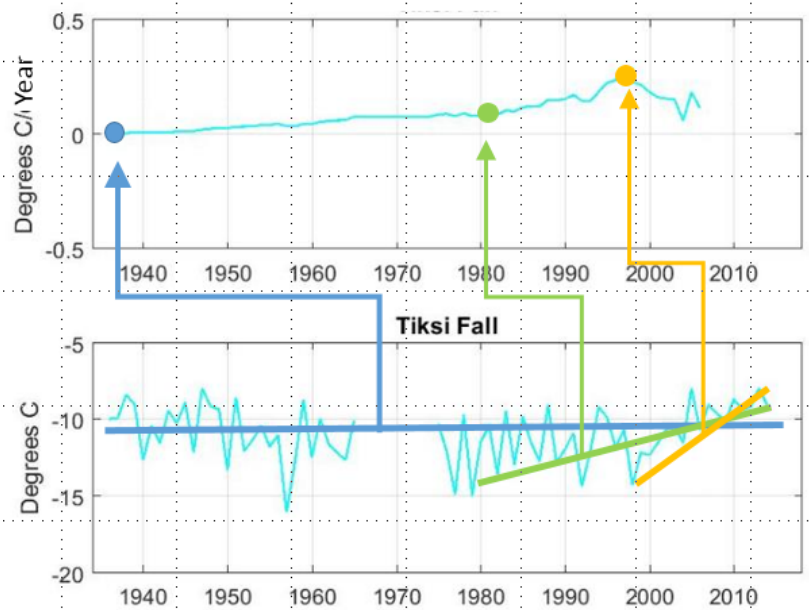


**Fig. 4** Illustration of how trends 'accumulate' as the start time over which the trend is calculated varies. Note: Trend calculation stops 10 years before end of record which in this example is 2004-2014.

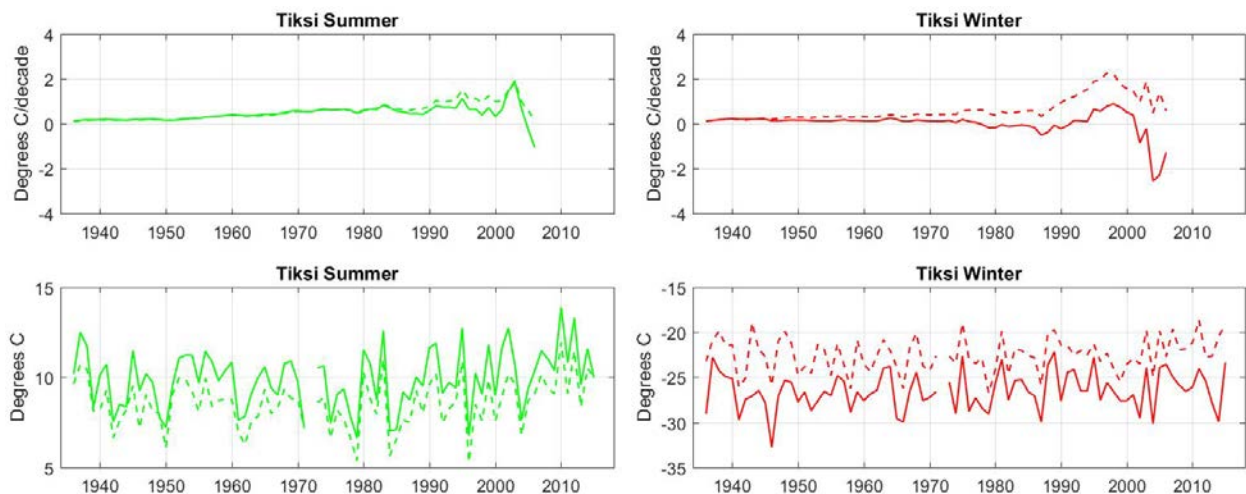


**Fig. 5** The accumulating trend (top panels) and the monthly mean temperatures (bottom panels) for Tiksi summer/warm season (left) and Tiksi winter/cold season (right). Solid lines are for summer (JJA) and winter (NDJ) periods and dashed lines are for warm (JJAS) and cold (ONDJFM) periods.

only small changes in the trends as the Arctic is a state of melt that stabilizes surface air temperature.

## 6. Tiksi extreme temperature events

The occurrence of temperature events exceeding the 95th and 99th percentiles was assessed. For the 95th percentile events and between the 1960s and the 2000s (last full decade) there was a fairly monotonic increase from 65 to 98 events/decade. However, it should be noted that in the 1940s and 1950s there were 115 and 90 extreme warm events respectively at the Tiksi station.

## 7. Conclusions

This article calls attention to the long-term detailed Arctic station data that is available through IASOA which is useful for model assessment and improvement, especially for the recent decades when the station meteorological data is accompanied with intensive measurements of process variables such as surface energy budget terms and clouds. It is also demonstrated that trend analysis should be based on periods defined by the latitude dependent seasonal forcing of the sun; otherwise true trends can be obscured and or misinterpreted. Finally, it is concluded that Arctic change must be assessed in the context of longer time records covering mid-century warming to fully understand the current processes and significance of what is currently considered to be the “new Arctic” system.

## References

- Menne, M. J., I. Durre, R. S. Vose, B. E. Gleason, and T. G. Houston, 2012: An overview of the Global Historical Climatology Network - daily database. *J. Atmos. Oceanic Technol.*, **29**, 897–910, <https://doi.org/10.1175/JTECH-D-11-00103.1>
- Yamanouchi, T., 2011: Early 20th century warming in the Arctic: A review, *Polar Science*, **5**, 53-71, [doi.org/10.1016/j.polar.2010.10.002](https://doi.org/10.1016/j.polar.2010.10.002)
- Uttal, T., S. Starkweather, J. R. Drummond, T. Vihma, A. P. Makshtas, L. S. Darby, J. F. Burkhart, C. J. Cox, L. N. Schmeisser, T. Haiden, M. Maturilli, M. D. Shupe, G. De Boer, A. Saha, A. A. Grachev, S. M. Crepinsek, L. Bruhwiler, B. Goodison, B. McArthur, V. P. Walden, E. J. Dlugokencky, P. O. Persson, G. Lesins, T. Laurila, J. A. Ogren, R. Stone, C. N. Long, S. Sharma, A. Massling, D. D. Turner, D. M. Stanitski, E. Asmi, M. Aurela, H. Skov, K. Eleftheriadis, A. Virkkula, A. Platt, E. J. Førland, Y. Iijima, I. E. Nielsen, M. H. Bergin, L. Candlish, N. S. Zimov, S. A. Zimov, N. T. O'Neill, P. F. Fogal, R. Kivi, E. A. Konopleva-Akish, J. Verlinde, V. Y. Kustov, B. Vasel, V. M. Ivakhov, Y. Viisanen, and J. M. Intrieri, 2016: International Arctic Systems for Observing the Atmosphere: An International Polar Year legacy consortium. *Bull. Amer. Meteor. Soc.*, **97**, 1033–1056, <https://doi.org/10.1175/BAMS-D-14-00145.1>

## New Pathway of Tropical Influences on Arctic Subseasonal Warming Events in the Troposphere

Yen-Heng Lin<sup>1</sup> and S.-Y. Simon Wang<sup>1,2</sup>

<sup>1</sup>Department of Plants, Soils and Climate, Utah State University, Logan, UT

<sup>2</sup>Utah Climate Center, Utah State University, Logan, UT, USA

### 1. Introduction

Midlatitude weather extremes are highly correlated to the variations of Arctic and tropical circulations. High-amplitude fluctuations of the jet streams result in heat exchange between the Arctic and midlatitude regions, creating a feedback mechanism between subseasonal Arctic warming and stagnation of midlatitude atmospheric waves. In a companion study (Wang *et al.* 2017), we show a rapid tropospheric warming (RTW) process as illustrated in Fig. 1 during the 2015-2016 winter, depicted by the polar cap height (PCH) variation and Arctic Oscillation (AO). The RTW case from late December to early January induces negative AO but does not feature any stratospheric warming or precursor, hence distinguishing it from the sudden stratospheric warming (SSW) case that subsequently occurs during March and April. The documented increase in the frequency of RTW has been linked to increased weather extremes (Fig. 2; Wang *et al.* 2017). Previous research links subseasonal Arctic warming events to tropical convective activities in the Pacific region (Jahnson and Feldstein 2010; Lee *et al.* 2011). Further evidence presented in this study suggests that this tropical link to increased RTW cases has strengthened in recent decades.

### 2. Data and methods

Daily reanalysis data of the National Centers for Environmental Prediction (NCEP)/Department of Energy Reanalysis II (R2) is used for atmospheric circulation analysis. For boundary heat forcing of sea surface temperature (SST), we utilize monthly anomalies of the NOAA Extended Reconstructed Sea Surface Temperature version 5 (ERSSTv5). Arctic rapid tropospheric warming (RTW) events are defined following Wang *et al.* (2017). This is when the polar cap height variation has a persistently positive anomaly (*i.e.* the geopotential height anomaly is larger than 1.5 standard deviation) in the troposphere, and the stratosphere remains negative to neutral. Based on this definition, 31 RTW events are identified from 1979 to 2015 winter (November-March) and are consequently synthesized into a composite. The composite of RTW events is created using the transition of RTW events evenly divided into 7 phases, from the highest status of AO (Phase 1) to the lowest status of AO (Phase 7). Phases 2-6 are defined as the transit phases. A more detailed

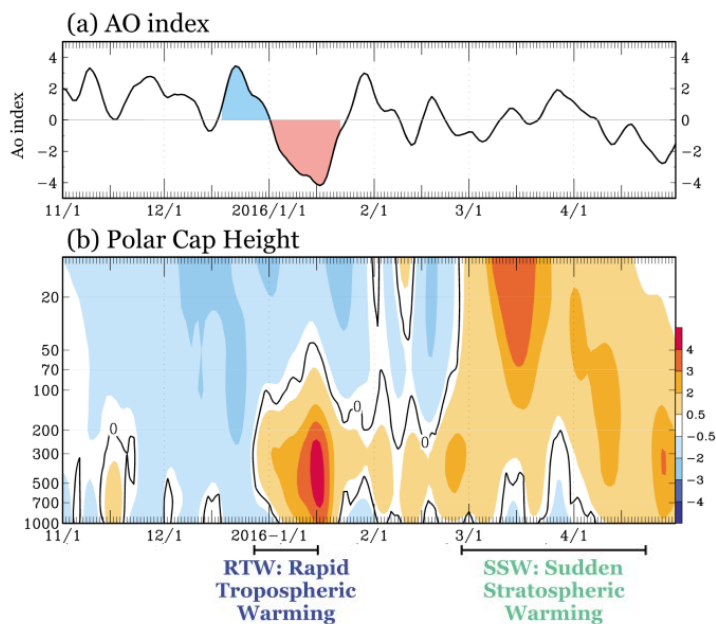


**Fig. 1** (a) Daily Arctic Oscillation index from 1 November to 30 April with 5 day moving average; the shaded period indicates the rapid tropospheric warming (RTW) case. (b) Time-height cross section of daily polar cap height (PCH) over Arctic region (north of 65°N) with 5 day moving average using NCEP reanalysis 2 data. (Wang *et al.*, 2017; Fig. 1a, b)

description of these methods is found in Wang *et al.* (2017).

### 3. Analysis results

To examine the circulation changes associated with the increase in RTW cases in the past decade, we show the average 250-hPa velocity potential (VP250) in the transit phases of RTW cases in two eras. First, the earlier era is from 1979 to 1987 with 12 RTW cases, and the recent era is from 1998 to 2015 with 19 RTW cases (Figs. 3a and 3b). The results reveal deep convections (upper-troposphere divergence) in the Pacific in both eras. However, the difference between the two reveals an eastward shift of the deep convection to the eastern Pacific as shown in Fig. 3c. A similar difference is seen in the linear trend of VP250 in winter since 1979 (Fig. 3d).

The changes in deep convection of RTW events lead to the next analysis of investigating the decadal variations of the wintertime VP250 which is shown in Fig. 4. The variations reveal an increase in divergence anomaly (Fig. 4a) in the eastern tropical Pacific in the last two decades. The central Pacific region also exhibits a divergent anomaly during the same period. This change is further elucidated by the variance of wintertime VP250 (Fig. 4b), which shows higher VP250 variances in the central and eastern tropical Pacific in the recent era. Moreover, Fig. 4c shows the frequency anomalies of the strong VP250 divergence (VP250 is less than -1.5 standard deviation) in winter. The results echo the changes of mean value and variance that the tropical Pacific in the recent era has more active convections than the early era.

Lee *et al.* (2011) indicates that the intraseasonal tropical convective precipitation can affect the Arctic warming. To examine how the increase in the tropical deep convection is relevant to the increased frequency of RTW in the recent era, we further conduct the wave activity flux (WAF) (Takaya and Nakamura 2001) analysis on the composite of RTW cases in the early era (12 cases) and recent era (19 cases) to depict the change of tropical deep-convection forcing

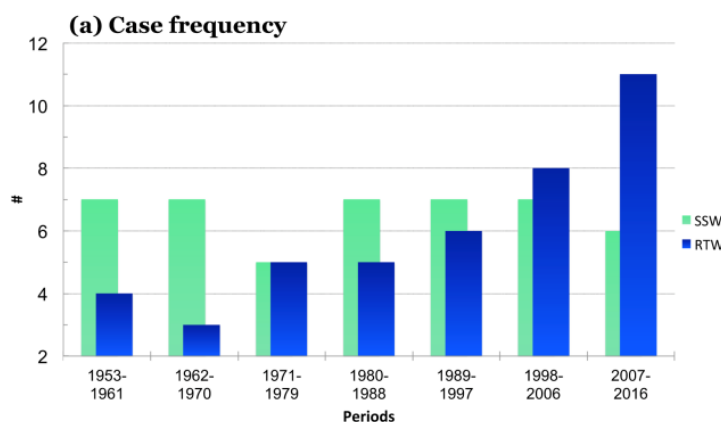


**Fig. 2** The case frequencies of RTW (blue) and SSW (light green) cases plotted at every 9 years during the November–March period. (Wang *et al.* 2017; Fig. 4a)

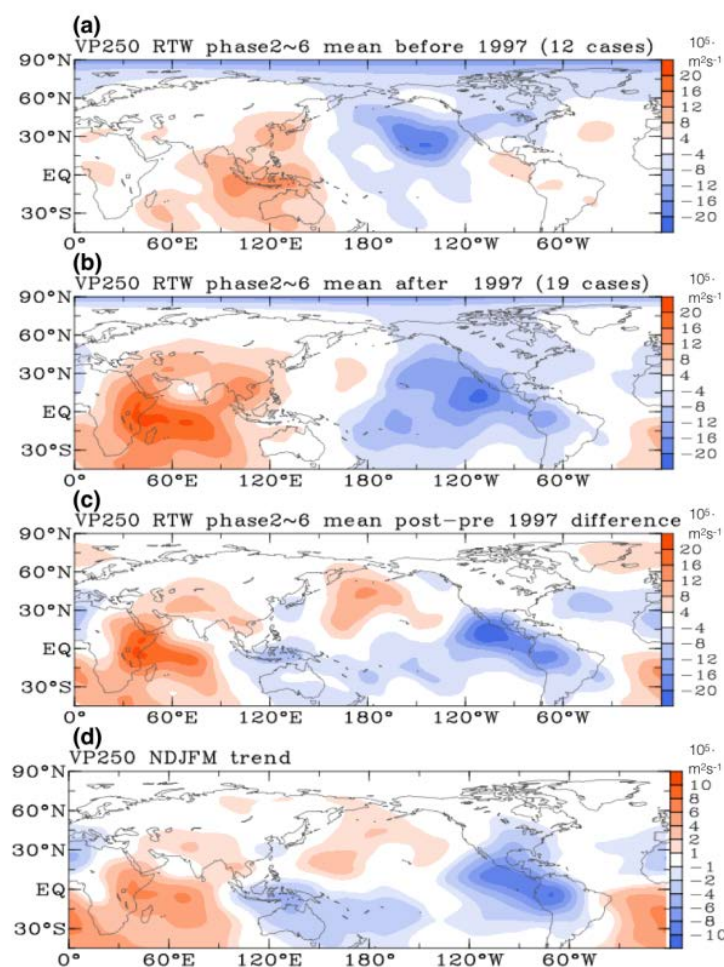


**Fig. 3** (a) The 12 cases composite of the averaged 250-hPa velocity potential (VP250) during the RTW transit phases from 1979 to 1997. (b) the same as (a), but for the 19 cases from 1998 to 2016. (c) the difference between recent two decades (b) and previous two decades (a) of the composite of RTW VP250. (d) The linear trend of VP250 in winter after 1979.



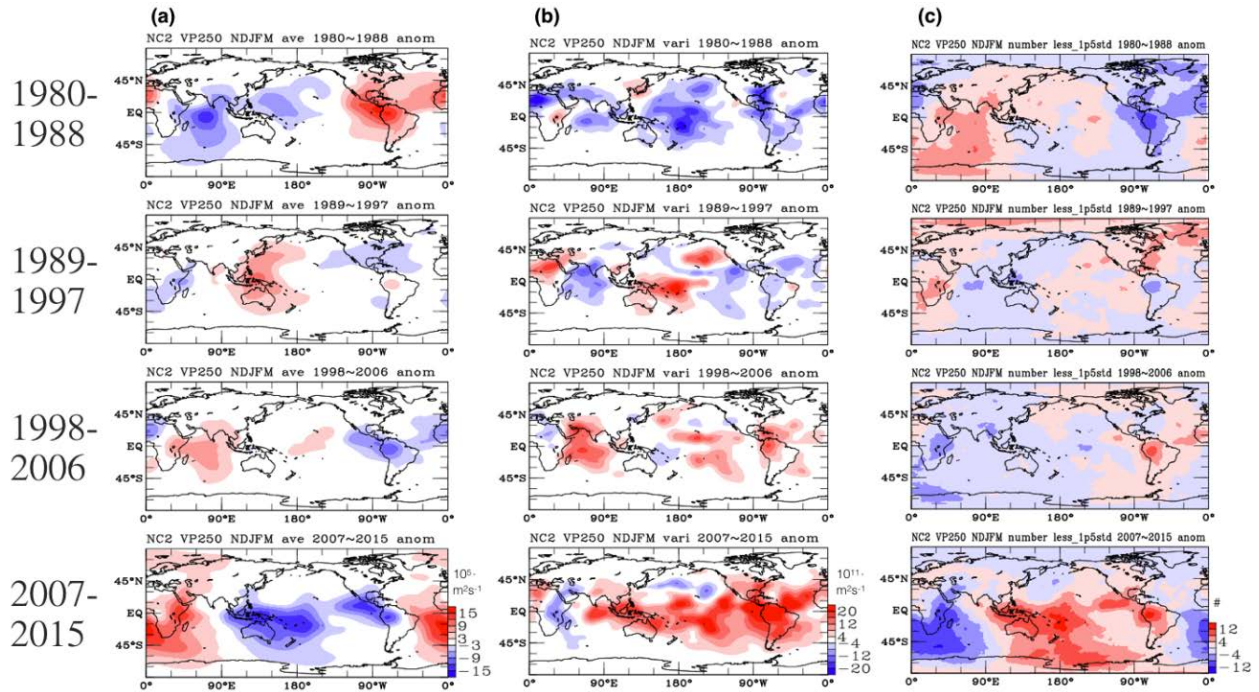


**Fig. 4** The 9-year average of (a) wintertime (November-March) 250-hPa velocity potential (VP250) anomaly, (b) wintertime VP250 variance anomaly, and (c) the frequency of VP250 anomaly that is less than -1.5 standard deviation in winter.

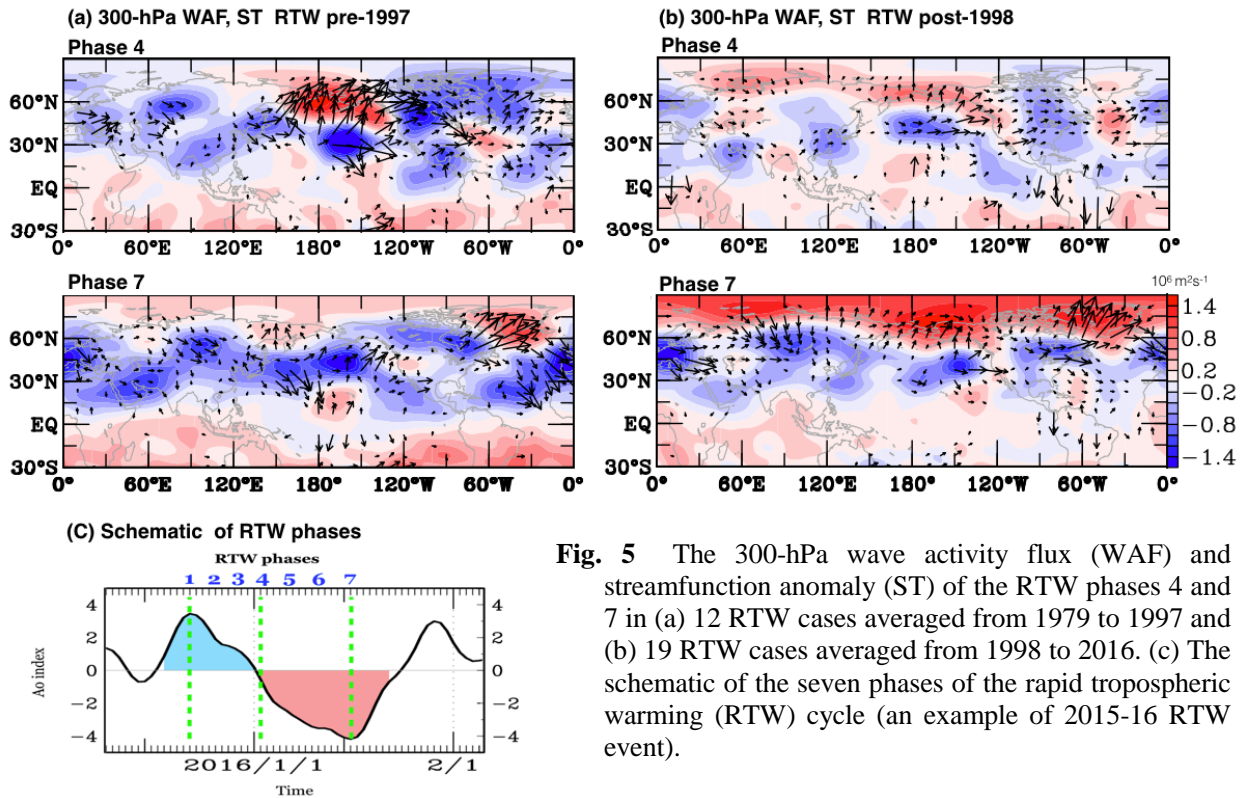


**Fig. 5** The 300-hPa wave activity flux (WAF) and streamfunction anomaly (ST) of the RTW phases 4 and 7 in (a) 12 RTW cases averaged from 1979 to 1997 and (b) 19 RTW cases averaged from 1998 to 2016. (c) The schematic of the seven phases of the rapid tropospheric warming (RTW) cycle (an example of 2015-16 RTW event).

and its impact pathway, which is shown in Fig. 5. In the recent era, the 300-hPa WAF (Fig. 5b) reveals a northeastward wave train generated from the Eastern Pacific. This wave train forms a high-pressure anomaly in the southwest U.S., a low-pressure anomaly in the eastern U.S., and a high-pressure anomaly in the



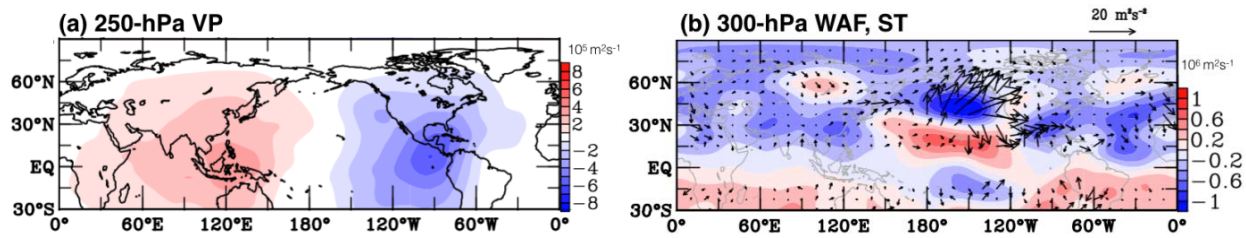


**Fig. 6** The composite analysis of 132 stronger convection (250-hPa velocity potential anomaly  $< -1.5$  standard deviation) days in the eastern tropical Pacific ( $240^{\circ}\text{E}$ – $285^{\circ}\text{E}$ ,  $10^{\circ}\text{S}$ – $20^{\circ}\text{N}$ ) from 1979 to 2015 winter in (a) 250-hPa velocity potential and (b) 300-hPa wave activity flux and streamfunction.

northern Atlantic from phase 4, where AO is shifting from positive to negative (Fig. 5c). This feature is not discernable in the early era (Fig. 5a). This wave train combines with the Pacific Northern American (PNA) teleconnection pattern from the central Pacific to induce high-amplitude wavy jet streams and cause high-pressure (warming) anomalies in Alaska and the Greenland regions.

To further evaluate the impact of deep convection in the eastern tropical Pacific, we construct the composite of upper-troposphere VP and WAF when the VP<sub>250</sub> anomaly index is less than  $-1.5$  standard deviation (Fig. 6). The result shows a similar PNA teleconnection pattern and a wave train over the U.S., which is consistent with previous modeling studies (Hoskins and Ambrizzi 1981; Branstator 2014).

#### 4. Conclusion

The upshot of these analyses is the following. The recent increase in the frequency of subseasonal Arctic rapid tropospheric warming events is associated with the increase in variations of tropical deep convection in the central and eastern tropical Pacific. The active tropical convection induces higher chances of teleconnection patterns to influence the midlatitude and the Arctic circulations, resulting in more weather extremes and more RTW events in the boreal winter. Moreover, the impact pathway from the eastern tropical Pacific to the U.S. and to the Northern Atlantic becomes more important to influence northern hemisphere circulations because of the increase in the frequency of the deep convections in the eastern tropical Pacific in recent decades.

Further studies will be focused on the combined influences of the deep convections in different areas of Pacific to have better prediction of Arctic tropospheric warming case and extreme weather event and be focused on investigating the mechanisms of inducing more deep convection in the eastern tropical Pacific in recent decade.

#### References

- Branstator, G., 2014: Long-lived response of the midlatitude circulation and storm tracks to pulses of tropical heating. *J. Climate*, **27**, 8809–8826, doi:<https://doi.org/10.1175/JCLI-D-14-00312.1>.
- Hoskins B. J., and D. J. Karoly, 1981: The steady linear response of a spherical atmosphere to thermal and orographic forcing. *J. Atmos. Sci.*, **38**, 1179–1196.
- Johnson, N. C., and S. B. Feldstein, 2010: The continuum of North Pacific sea level pressure patterns: Intraseasonal, interannual, and interdecadal variability. *J. Climate*, **23**, 851–867.
- Lee, S., T. Gong, N. Johnson, S. B. Feldstein, and D. Pollard, 2011: On the possible link between tropical convection and the Northern Hemisphere Arctic surface air temperature change between 1958 and 2001. *J. of Climate*, **25**, 4350–4367.
- Takaya, K., and H. Nakamura, 2001: A formulation of a phase-independent wave-activity flux for stationary and migratory quasigeostrophic eddies on a zonally varying basic flow. *J. Atmos. Sci.*, **58**, 608–627.
- Wang, S.-Y., Y.-H. Lin, M.-Y. Lee, J.-H. Yoon, J. D.D. Meyer, and P. J. Rasch, 2017: Accelerated increase in the Arctic tropospheric warming events surpassing stratospheric warming events during winter. *Geophys. Res. Lett.*, **44**, 3806–3815, doi: 10.1002/2017GL073012.

## **Influence of the Stratosphere on MJO-AO Teleconnections in the Subseasonal to Seasonal (S2S) Models**

Laura M. Ciasto<sup>1,2</sup>, Michelle L'Heureux<sup>1</sup>, Kirstin J. Harnos<sup>1,2</sup>, and Jason C. Furtado<sup>3</sup>

<sup>1</sup>*Climate Prediction Center, NOAA/NWS/NCEP, College Park, MD*

<sup>2</sup>*Innovim, LLC, Greenbelt, MD*

<sup>3</sup>*School of Meteorology, University of Oklahoma, Norman, OK*

### **1. Introduction**

There is increasing evidence that the Madden Julian Oscillation (MJO), the leading mode of intraseasonal variability in the tropics, may be a source of predictability for the extratropical Northern Hemisphere (NH) atmospheric circulation during the boreal winter. Several studies have linked variability in the MJO to the leading modes of Northern Hemisphere (NH) atmospheric variability including the North Atlantic Oscillation (NAO; Cassou 2008) and the Arctic Oscillation (AO; L'Heureux and Higgins 2008). Of particular interest is the extent to which the extratropical stratospheric circulation has a modulating influence on these MJO-AO teleconnections, which, in turn, influence temperature and precipitation over North America. This study examines the observed boreal winter relationships between the MJO and the AO during different phases of the stratospheric polar vortex and then evaluates how well these relationships are captured in subseasonal to seasonal prediction models.

### **2. Data and methods**

The analysis focuses on the extended boreal winter (November- March) for the period 1979-2016. Daily MJO indices, obtained from the Bureau of Meteorology (BOM), are based off the method of Wheeler and Hendon (2004). MJO events are identified using the primary requirement that the amplitude of the leading two Real-time Multivariate MJO (RMM) series  $[(RMM1^2 + RMM2^2)^{1/2}]$  exceeds 1. The daily AO index is obtained from the NOAA/CPC website ([http://www.cpc.ncep.noaa.gov/products/precip/CWlink/daily\\_ao\\_index/ao.shtml](http://www.cpc.ncep.noaa.gov/products/precip/CWlink/daily_ao_index/ao.shtml)) and is calculated by projecting the ERA-Interim (Dee *et al.* 2011) daily  $z_{1000}$  anomalies onto the leading Empirical Orthogonal Function (EOF) of monthly  $z_{1000}$  anomalies over the region 20°N-90°N. The stratospheric polar vortex (SPV) is calculated the same way but for  $z_{050}$  height anomalies.

Reforecast data are used from prediction models that are part of the World Weather Research Program (WWRP)/ World Climate Research Program (WCRP) Subseasonal to Seasonal (S2S) Project database (Vitart *et al.* 2017). The analysis uses models from BOM, ECMWF, and NCEP. The simulated AO index is calculated for each model by projecting the leading EOF of observed  $z_{1000}$  height anomalies onto the simulated  $z_{1000}$  height anomalies for each forecast lead. Doing so ensures that the models are all showing how the same pattern evolves in time. The same method is used to calculate the SPV using  $z_{050}$  height anomalies. The simulated RMM indices are calculated using the method outlined in Vitart (2017) and are obtained from the S2S website (<http://s2sprediction.net/>).

### **3. Relationships between the MJO, AO and the SPV**

Figure 1 shows the observed frequency of the AO events as a function of MJO phase. When the considering all states of the SPV (top left), the AO strongly favors the positive sign in MJO phases 2-5 and the negative sign in phases 7-8, consistent with L'Heureux and Higgins (2008). However, when the SPV is anomalously strong, ( $SPV > 0.5$ , top right), the AO favors the positive polarity regardless of MJO phase. Conversely, the AO remains negative for all MJO phases when the SPV is anomalously weak ( $SPV < -0.5$ , bottom right). In the absence of strongly positive or negative polar vortex anomalies (*i.e.*, neutral conditions,

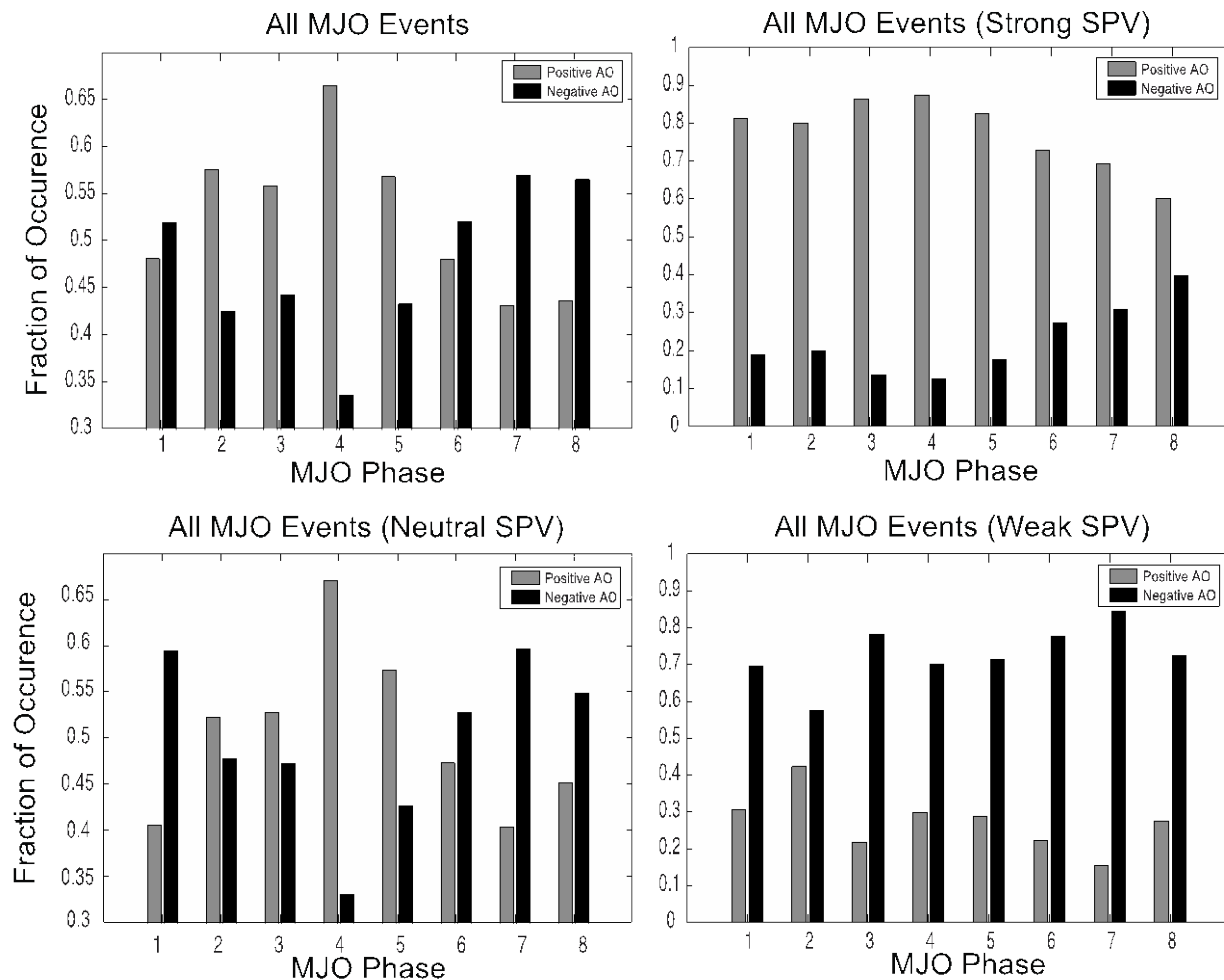


**Fig. 1** Fraction of MJO days (as a function of phase) when the November-March AO is in the (grey bars) positive or (black bars) negative phase and the SPV is (top left) any amplitude, (top right) anomalously strong, (bottom right) anomalously weak, and (bottom left) neutral.

bottom left), the same relationships emerge as when all phases of the SPV are considered. These results suggest that the overall MJO-AO relationship in Fig. 1 primarily reflects a tropospheric link.

Figure 2 shows similar analysis using the three aforementioned S2S models and focuses on the MJO-AO relationship when all states of the SPV are considered. Note that the models each have distinct combinations of forecast periods and forecast frequencies, sampling different subsets of the observational period. Consequently, the models results are compared to observations that have been subsampled to match each those forecast periods/frequencies. The discussion highlights the relationships at MJO phases 4 and 7, which have been shown to be linked to the positive and negative phases of the AO, respectively.

Relative to the observations, ECMWF overestimates the fraction of positive AO days during phase 4 of the MJO. However, during phase 7, ECMWF is able to capture the high occurrence of negative AO days. The opposite is true in the NCEP S2S model in which the positive AO relationship with phase 4 of the MJO is well-simulated, but the negative AO relationship with phase 7 is overestimated. The best representation of the observations is evident in the BOM with the positive AO relationship slightly overestimated and the negative relationship in Phase 7 well-captured. Because these MJO-AO relationships in Fig. 2 are analyzed at lead 0, it is expected that these relationships would be well-captured in the models. While the anomaly correlations of the simulated winter AO demonstrate high skill at lead 0 ( $r > 0.95$ ; not shown), the anomaly correlations of the MJO amplitude are considerably lower ( $r < 0.8$ ; not shown), which may have an impact on the ability to capture MJO-AO relationships.

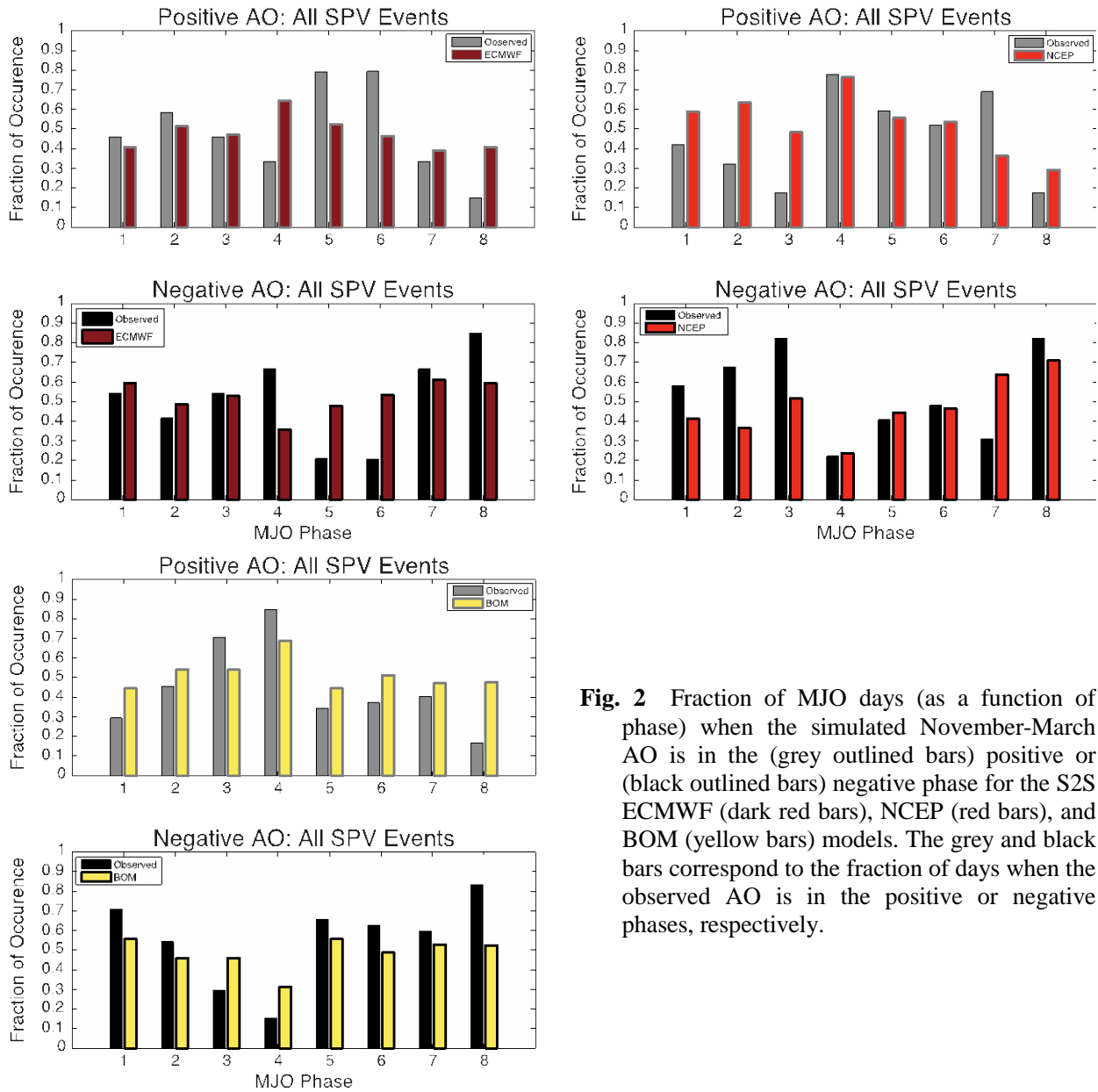


**Fig. 2** Fraction of MJO days (as a function of phase) when the simulated November-March AO is in the (grey outlined bars) positive or (black outlined bars) negative phase for the S2S ECMWF (dark red bars), NCEP (red bars), and BOM (yellow bars) models. The grey and black bars correspond to the fraction of days when the observed AO is in the positive or negative phases, respectively.

#### 4. Future work

The results of this analysis suggest that models have difficulty reproducing the boreal winter MJO-AO relationships. Because the tropospheric MJO-AO relationship is poorly captured in some of the models, the evaluation of the modulating effect of the stratosphere in the models could be further complicated. A possible explanation is that the inability to capture the MJO-AO relationship might be related to the MJO, which are not as well reproduced in the models as the AO. Future work will further examine how the representation of the MJO in the models influences the overall MJO-AO relationship. This analysis will also be extended to the other models in the S2S database.

*Acknowledgements.* This work is supported by NOAA/CPO MAPP program.

#### References

Cassou, C., 2008: Intraseasonal interaction between the Madden-Julian Oscillation and the North Atlantic Oscillation. *Nature*, **455**, 523-527.



- Dee, D. P., and Coauthors, 2011: The ERA-Interim reanalysis: Configuration and performance of the data assimilation system. *Quart. J. Roy. Meteor. Soc.*, **137**, 553–597.
- L'Heureux, M. L., and R. W. Higgins, 2008: Boreal winter links between the Madden–Julian Oscillation and the Arctic Oscillation. *J. Climate*, **21**, 3040–3050.
- Vitart F., and co-authors, 2017: The sub-seasonal to seasonal prediction (S2S) project database. *Bull. Am. Meteorol. Soc.*, **98**, 163–176.
- Vitart, F., 2017: Madden-Julian Oscillation prediction and teleconnections in the S2S database. *Quart. J. Roy. Meteor. Soc.*, **143**, 2210–2220.
- Wheeler, M., and H. Hendon, 2004: An all-season real-time multivariate MJO index: Development of an index for monitoring and prediction. *Mon. Wea. Rev.*, **132**, 1917–1932.

## Prediction of Seasonal Arctic Sea Ice Extent Using the NMME

Kirstin J. Harnos<sup>1,2</sup>, Michelle L'Heureux<sup>1</sup>, Qin Zhang<sup>1</sup>, and Qinghua Ding<sup>3</sup>

<sup>1</sup>Climate Prediction Center, NOAA/NWS/NCEP, College Park, MD

<sup>2</sup>Innovim, LLC, Greenbelt, MD

<sup>3</sup>University of California, Santa Barbara, CA

### 1. Introduction

Arctic sea ice decline is a well-documented topic with many studies outlining the September minimum as decreasing by more than 10% per decade since satellite observations began in 1979. Within the past few decades, the rate of decline has been shown to be increasing significantly due to both thinning ice and longer melt seasons. When it comes to prediction of the Arctic sea ice extent (SIE), there is potential for skillful predictions mainly attributed to individual modeling system's ability to predict the long-term trend (Sigmond *et al.* 2013; Wang *et al.* 2013; Chevallier *et al.* 2013; Holland *et al.* 2011; *etc.*).

SIE prediction skill has been assessed by a variety of dynamical, statistical, and heuristic models. For other variables, it has been shown that predictions using the ensemble means from different models tend to outperform any individual system (Merryfield *et al.* 2013; Stroeve *et al.* 2014). The North American Multi-Model Ensemble (NMME) takes advantage of the multi-model approach by utilizing a multi-agency team to collect and organize global model data on a somewhat uniform spatial and temporal scale. This study seeks to expand on previous multi-platform studies by utilizing output from five NMME models to determine the skill in predicting Arctic SIE based on the long term trend and year-to-year (Y2Y) variability.

### 2. Data

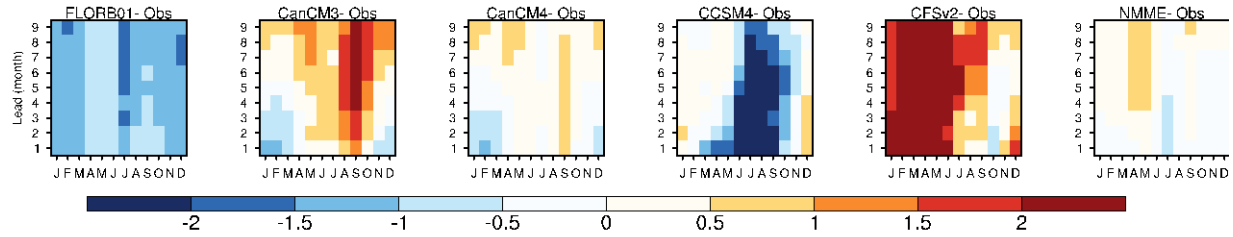
There are 5 models that currently provide sea ice predictions to the NMME archive. Each hindcast simulation is initialized and allowed to run for either 12 months (CanCM3, CanCM4, FLORB-01, and CCSM4) or 9 months (CFSv2). To maintain consistency for all models and in creating an NMME average, all of the models are evaluated during the 1982-2011 time period, which represents the time when all 5 models have results and for a 9 month forecast extent. Observations derived from NASA Bootstrap version of the National Snow Ice Data Center and NASA GSFC sea ice concentration data are utilized in order to calculate the skill metrics.

### 3. Summary of results

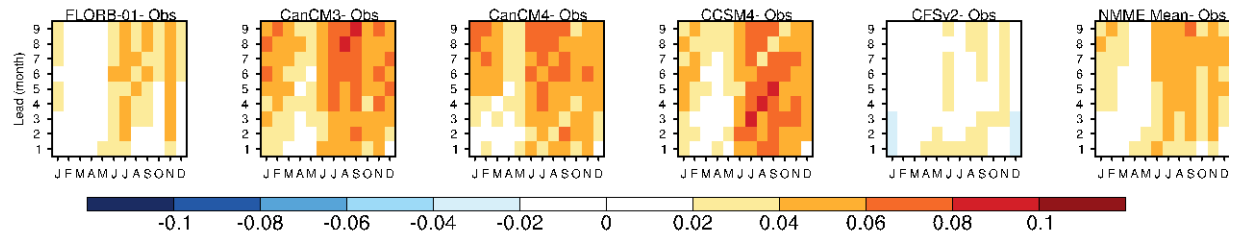
Figure 1 shows the model bias for (a) total SIE and (b) Y2Y SIE. Overall, the NMME predictions of total SIE have less error than the individual predictions. In contrast, the Y2Y difference evaluates SIE prediction irrespective of the long-term trend. For all individual models and the NMME, the Y2Y differences show a generally positive bias, meaning that from one year to the next, the models tend to predict more SIE than observed. While the Y2Y values are not providing information on the long-term trend, this result implies the models are not capturing the magnitude of the loss of SIE from one year to the next. The NMME Y2Y bias shows improvement over CanCM3, CanCM4, and CCSM4, with CFSv2 and FLORB-01 having overall the best Y2Y prediction.

To further quantify prediction skill, Figure 1 also shows the anomaly correlation coefficient (ACC) values for the (c) total SIE and (d) Y2Y SIE. One primary feature across all models is the smaller ACC in Y2Y variability compared to the prediction of total SIE. For both total and Y2Y SIE, the NMME predictions result in generally higher ACC compared to the individual. The higher ACC with NMME is evident for predictions of Y2Y variability, especially for lead times greater than 3 months. The NMME also noticeably improves upon CanCM3, CanCM4, and CCSM4 for predictions of total SIE. Overall, relative to the skill of individual

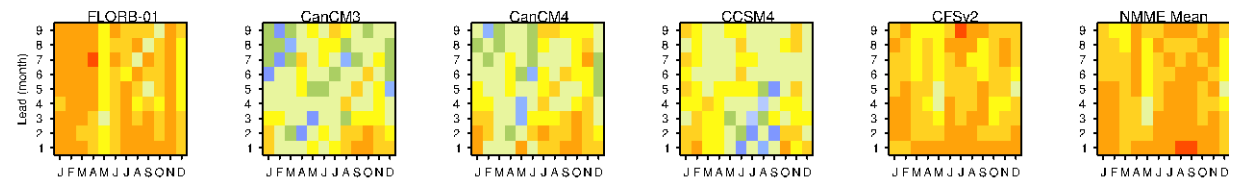
## (a) Total SIE



## (b) Y2Y SIE



## (c) Total ACC



## (d) Y2Y ACC

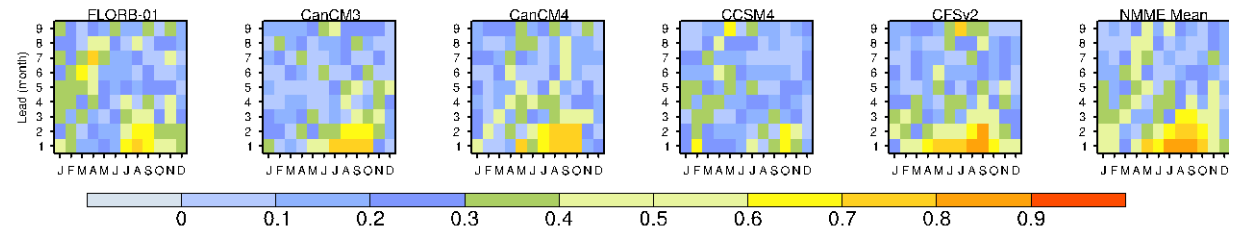


**Fig. 1** Model bias (model minus observations) including the NMME for (a) Total SIE [ $106 \text{ km}^2$ ], (b) the Y2Y SIE [ $106 \text{ km}^2$ ], (c) Total ACC, and (d) Y2Y ACC.

models, the NMME offers the most bias reduction for predictions of total SIE, and the correlations are highest for the prediction of Y2Y SIE.

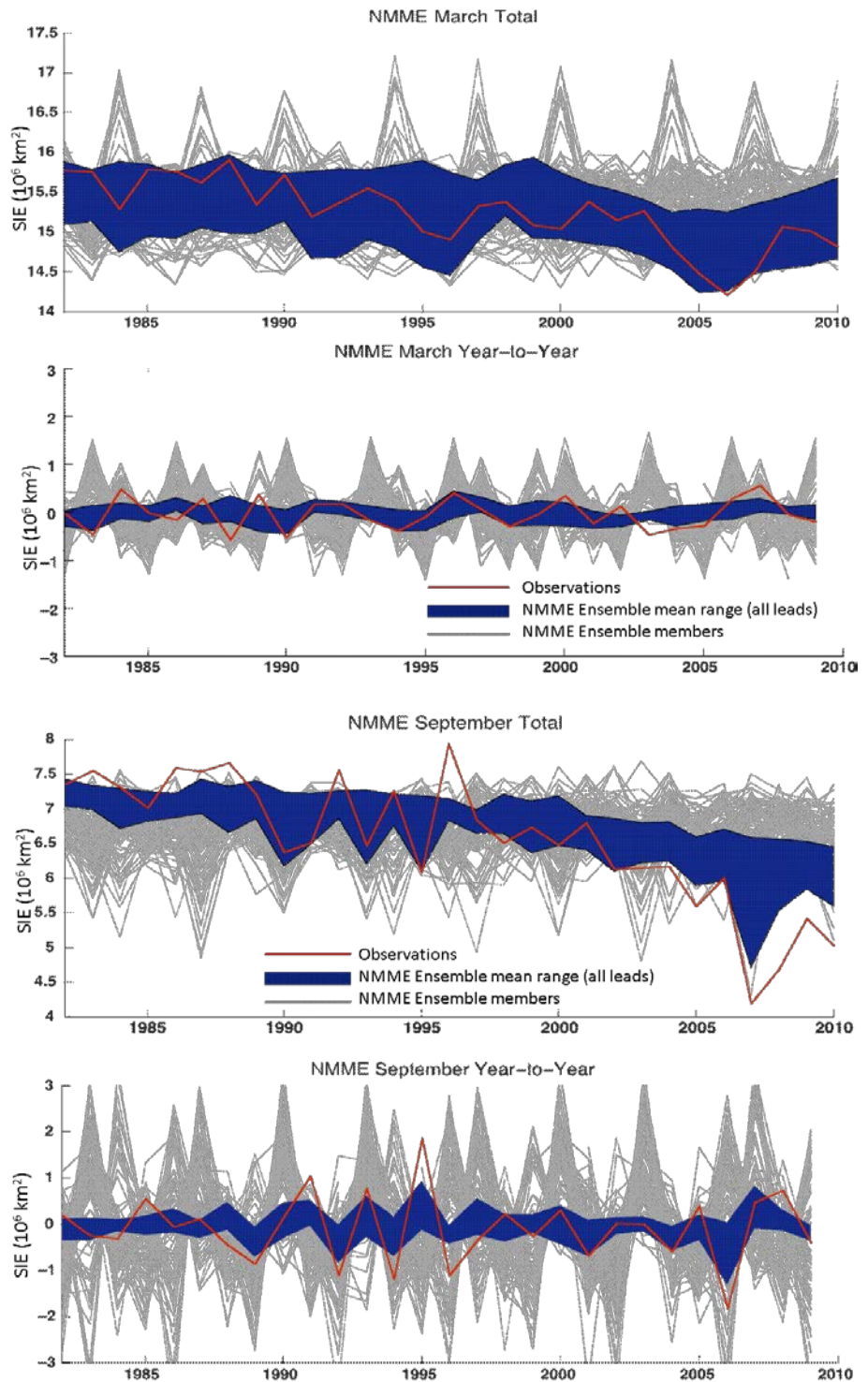
### 3. NMME SIE time series

Figure 2 compares the total and Y2Y SIE observational data (red) to the range of ensemble means (blue) and all members (grey) from NMME for 1982–2010. All forecast lead times are shown leading up to the March or September target month. The biases seen in Figure 1 are also reflected within this analysis, except now it is easier to view the evolution of the model forecasts as the SIE changes over time. For predictions of March total SIE, the observations largely fall within the spread of the NMME. The observations also largely lie within the spread of predictions for March Y2Y SIE. However, for the Y2Y SIE predictions, the variance of the individual members is clearly larger than the observed variability across the NMME.

In contrast to March, predictions for September total SIE show that there are periods of time when the observations clearly lie outside of the spread of the model predictions. This is particularly true in the years following the large sea ice melt in 2007, when the NMME underestimated the degree of sea ice loss. Only during the recent period did the spread of forecasts from these models contain the observed September SIE.

As for the March total SIE, the NMME predictions of September SIE appears to encompass the observed variability more often than any individual model. For the September Y2Y SIE, the observations largely lie within the spread of the model forecasts with the exception of the more extreme Y2Y years. But even in those instances, it appears the variance of the Y2Y individual members largely captures the variance of the observational data.

Both the total and Y2Y time series in Figure 2 are smoothed using a 10-year running mean and presented versus model ACC and RMSE values. These scatterplots (Figure 3) show the skill for the 9 forecast lead times with respect to the total or Y2Y SIE. The associated 10-year period is indicated by the color shading, with reds (blues) indicating later (earlier) periods. Over these running 10-year periods, the ACC values in both September and March do not show any clear tendency over time. The RMSE tells a different story especially during September when the RMSE values are considerably larger during the more recent decades than the ones prior. The RMSE for Y2Y SIE does not show the same temporal trend, with the larger errors inclusive of decades with the largest Y2Y departures shown in Figure 2. Because Y2Y changes are independent of the longer-term trends, this suggests that errors in the prediction of the total SIE are increasing over time because the NMME is not adequately capturing the trend or variability in recent years. In contrast, March does not show the same clear trend over time, and in general, the amplitude of RMSE for both total and Y2Y SIE is smaller in March compared to September, likely due to smaller trends and year-to-



**Fig. 2** Time series for NMME SIE in March (top two panels) and September (bottom two panels) for total (upper) and Y2Y (lower) SIE with observations (red line), the range of ensemble means at all lead times (blue shading), and individual ensemble members (grey lines).

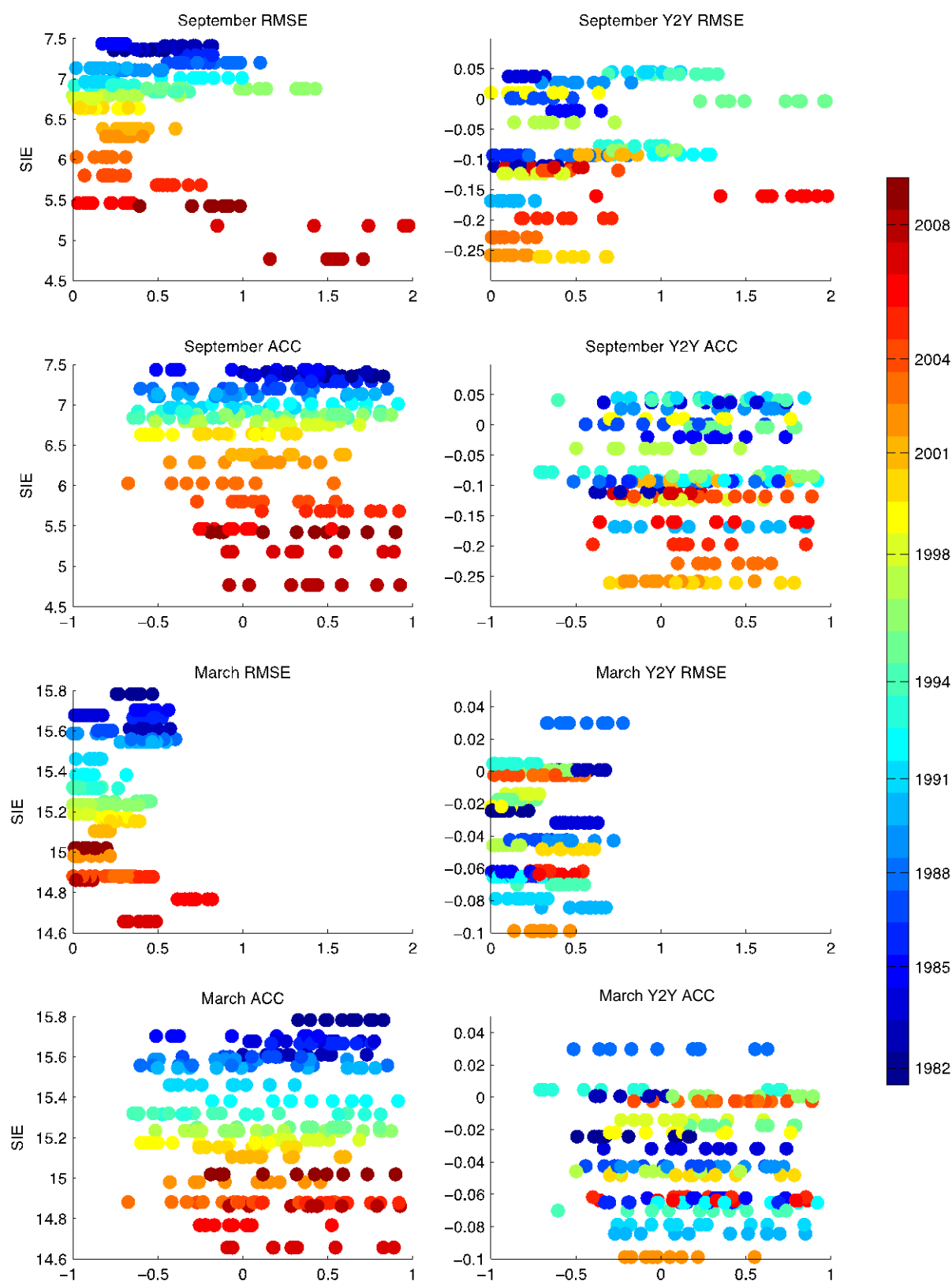


**Fig. 3** Scatterplots of September (top two panels) and March (bottom two panels) root-mean-square error (RMSE; upper) and ACC (lower) versus total SIE (left) and Y2Y (right) with years indicated by the colors.



year variability during a month when the SIE is typically maximized.

#### 4. Discussion

The NMME approach provides the most gain over individual models through decreased bias for predictions of total SIE and increased correlations of Y2Y SIE variability. There is a tendency for all models and the NMME to over-predict Y2Y SIE from one year to the next. The struggle of the models to predict the following year SIE change, along with the increasingly larger errors for September SIE predictions in recent decades, suggest that prediction of the trend remains a fundamental challenge for most coupled modeling systems. Regardless, it is clear that the average of multiple models generally exceeds the skill of any one modeling system, so the NMME demonstrates value for the prediction of Arctic SIE.

#### References

- Chevallier, M., D. Salas-Melia, A. Voldoire, and M. Deque, 2013: Seasonal forecasts of the Pan-Arctic sea ice extent using a GCM-based seasonal prediction system. *J. Climate*, **26**, 6092–6104, doi:10.1175/JCLI-D-12-00612.1.
- Holland, M. M., D. A. Bailey, and S. Vavrus, 2011: Inherent sea ice predictability in the rapidly changing Arctic environment of the Community Climate System Model, version 3. *Clim. Dyn.*, **36**, 1239–1253, doi:10.1007/s00382-010-0792-4.
- Merryfield, W. J., W.-S. Lee, W. Wang, M. Chen, and A. Kumar, 2013: Multi-system seasonal predictions of Arctic sea ice. *Geophys. Res. Lett.*, **40**, 1551–1556, doi:10.1002/grl.50317
- Sigmond, M., J. C. Fyfe, G. M. Flato, V. V. Kharin, and W. J. Merryfield, 2013: Seasonal forecast skill of Arctic sea ice area in dynamical forecast system. *Geophys. Res. Lett.*, **40**, 529–534, doi:10.1002/grl.50129.
- Stroeve, J., L. C. Hamilton, C. M. Bitz, and E. Blanchard-Wrigglesworth, 2014: Predicting September sea ice: Ensemble skill of the SEARCH Sea Ice Outlook 2008–2013. *Geophys. Res. Lett.*, **41**, 2411–2418, doi:10.1002/2014GL059388.
- Wang, W., M. Chen, and A. Kumar, 2013: Seasonal prediction of Arctic sea ice extent from a coupled dynamical forecast system. *Mon. Wea. Rev.*, **141**, 1375–1394, doi:10.1175/MWR-D-12-00051.1

## Multi-week Prediction Skill Assessment of Arctic Sea Ice Variability in the CFSv2

Yanyun Liu<sup>1,2</sup>, Wanqiu Wang<sup>1</sup> and Arun Kumar<sup>1</sup>

<sup>1</sup>Climate Prediction Center, NOAA/NWS/NCEP, College Park, MD

<sup>2</sup>Innovim, LLC, Greenbelt, MD

### 1. Introduction

Recently, National Oceanic and Atmospheric Administration has initiated activities to improve skill of forecasts in weeks 3-4 time-range to extend weather forecast capability beyond the conventional range of 10-15 days. While Arctic sea ice forecast at seasonal time scales has received considerable attention (Bushuk *et al.* 2017), very limited work has been done on shorter time scales. In this study, a fully coupled atmosphere-ocean model is used to evaluate forecast skill of weekly mean sea ice from week 1 to week 6 for Arctic regions using the NCEP's Climate Forecast System version 2 (CFSv2). This is the first effort to diagnose and assess multi-week Arctic sea ice prediction skill from a coupled atmosphere-ocean model.

### 2. The forecast model, data and processing method

The retrospective forecast data analyzed in this study is from the fully coupled CFSv2 model (Saha *et al.*, 2014). Raw forecast data include output from four 45-day forecast runs from 0000, 0600, 1200, 1800 UTC each day. This study focuses on the analysis of weekly-mean anomalies from CFSv2 for 0-week to 5-week lead. For each forecast starting day, the following steps are taken to produce weekly average of ensemble mean forecast: (1) forecast runs from latest three days were used to form a lagged ensemble of 12 runs; (2) daily average of 12-run ensemble mean is computed for 42 target days; (3) non-overlapping 7-day weekly average is calculated from daily ensemble mean for 0-week lead (day 1 to day 7 average) to 5-week lead (day 36-day 42 average). The forecast data of ensemble-mean weekly average is then rearranged according to lead time and target (or verification) week.

For the assessment of the CFSv2 performance, the sea ice concentration (SIC) data from National Snow and Ice Data Center (NSIDC) (Cavalieri *et al.*, 1996; Fetterer *et al.*, 2002) during 2000–2015 is used. To facilitate the calculation, and for a consistent comparison, the corresponding observational data are rearranged following the CFSv2 forecast structure to form the weekly average of SIC for each target verification week starting from each calendar day between 2000–2015 both for NASA Team and NASA Bootstrap algorithms.

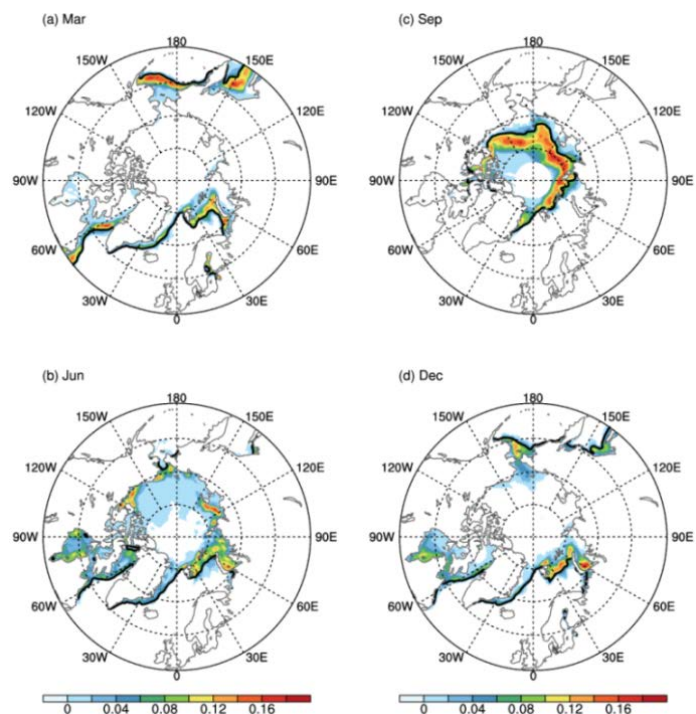


**Fig. 1** (a) Total variance of Arctic SIC for 4 target months of (a) March, (b) June, (c) September and (d) December during 2000–2015, obtained from NSIDC observations. The black lines represent the 15% concentration contour in the NSIDC observations, which is usually used to define the sea ice edge.

The average of SIC using NASA Team and NASA Bootstrap algorithms is then calculated and used for verification.

For both forecast and observation, a 16-year (2000–2015) average of 7-day mean SIC is calculated for each starting date from Jan 1<sup>st</sup> to Dec 31<sup>st</sup> ( $d=1-365$ ); for forecast, calculation is done for each lead time (L0–L5). The climatology for each starting date ( $d$ ) is defined as the 31-day ( $d-15$  to  $d+15$ ) running mean of the resulting 16-year average and is denoted as  $F_c(d, L)$  for the forecast and  $O_c(d)$  for the observation.

Three types of anomalies are calculated: total anomaly, interannual anomaly, and submonthly anomaly. The total anomaly is calculated as the deviation of total weekly-mean values of SIC from the climatology. The interannual anomaly is defined as the monthly mean of the total anomaly. The submonthly anomaly is the deviation of the total anomaly from the interannual anomaly. The interannual anomaly is further divided into two components, the trend interannual anomaly and detrended interannual anomaly.

### 3. Results

Figure 1 shows the spatial pattern of total weekly anomaly variance of NSIDC Arctic SIC anomaly for 4 target months (March, June, September and December) during 2000–2015. Large variance is generally located near the sea ice edge indicated by the 15% SIC black contours. The Arctic SIC shows relatively high variability in different Arctic regions during different months: Bering Sea and Sea of Okhotsk during March; Chukchi, Kara and Barents Seas during June, Beaufort, East Siberian and Laptev seas during September; Barents Sea during December.

For a quantitative comparison, Table 1 lists the contributions of different components, including the trend interannual, detrended interannual, and submonthly variability, to the observed total SIC variance averaged over Arctic regions ( $50^{\circ}\text{N}$ – $90^{\circ}\text{N}$ ) for 4 target months (March, June, September and December). As shown in Table 1, the Arctic SIC shows the largest (smallest) variability in September (December). The total SIC variability is dominated by detrended interannual variability, which accounts for more than 60% of the total variance. The contribution of submonthly

**Table 1** Total variance and its components (including trend, detrended interannual and submonthly variability) for 4 target months (March, June, September and December). Values are area-weighted averages from  $50^{\circ}\text{N}$ – $90^{\circ}\text{N}$ .

NSIDC SIC	Mar	Jun	Sep	Dec
<b>variance (<math>\times 10^3</math>)</b>				
<b>Total</b>	9.024	13.788	23.686	8.859
<b>Trend</b>	1.226 (13.6%)	1.447 (10.5%)	4.567 (19.3%)	0.827 (9.3%)
<b>Interannual</b>	5.788 (64.1%)	9.506 (68.9%)	16.156 (68.2%)	5.428 (61.3%)
<b>Intraseasonal</b>	2.011 (22.3%)	2.835 (20.6%)	2.963 (12.5%)	2.604 (29.4%)

interannual anomaly is further divided into two components, the trend interannual anomaly and detrended interannual anomaly.

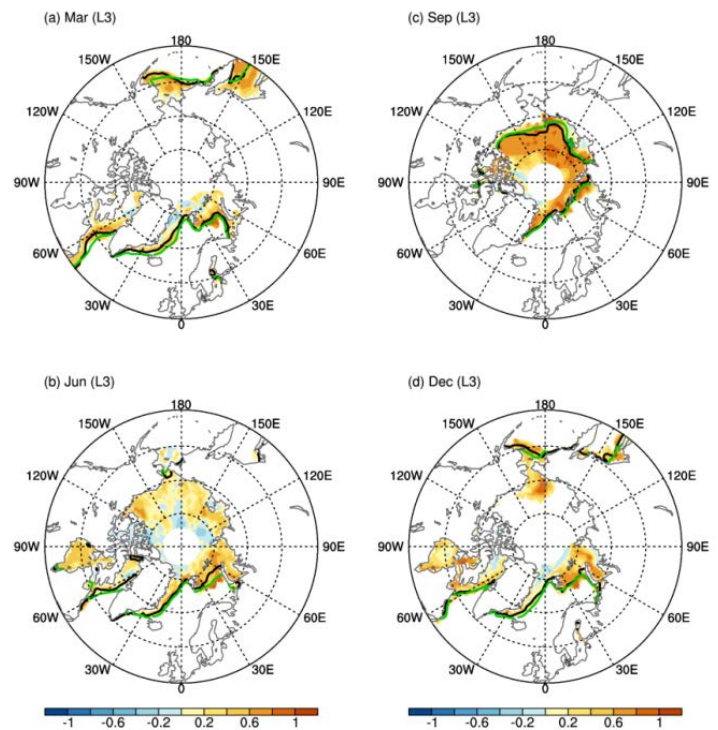


**Fig. 2** Anomaly Correlation Coefficient (ACC) between CFSv2 forecast and observations for total SIC anomalies at L3 for 4 target months of (a) March, (b) June, (c) September and (d) December.

anomalies accounts for about 20% of the total variance in March/June, 12.5% in September and 29.4% in December. Submonthly variance is 2-3 times as strong as the trend variance for March, June and December except for September in which submonthly variance is weaker than the trend variance.

Multi-week sea ice prediction skill for pan Arctic as well as individual Arctic regions is analyzed. CFSv2 captures general features of the Arctic sea ice variability, with the largest bias in marginal ice zone region.

Figure 2 shows the spatial Anomaly Correlation Coefficient (ACC) of total and interannual SIC anomalies between CFSv2 week-4 forecast and observations. The CFSv2 shows good skill at L3. The Arctic Ocean shows the highest prediction skill during September, particularly in the regions of Chukchi Sea, Beaufort Sea and East Siberian Sea where the ACC is above 0.6. The results demonstrate the multi-week prediction skill is dominated by the prediction of interannual variability although predictions of both interannual and submonthly anomalies contribute to the prediction skill.

The utility of a forecast greatly depends on the geographic characteristics of the forecast skill. Regional SIC forecast skill is especially important to the stakeholders. The ACC decreases with lead time and is region and season dependent. The ACC is relatively high for Kara and Barents Sea for all seasons. During March, the ACC is higher in Bering Sea, Sea of Okhotsk/Japan and Gulf of St. Lawrence. During June, the ACC is higher in Greenland Sea and Hudson Bay. During September, the ACC is higher in Greenland Sea, Arctic Ocean and Canadian Archipelago. During December, higher prediction skill is found in Bering Sea, Hudson Bay and Sea of Okhotsk/Japan.

Spatial and seasonal variations of the forecast ACC (anomaly correlation coefficient) skill show that the sea ice at a specific location is most predictable when this location is near the marginal zone having large sea ice variance (Figs. 1 and 2). This means that for each location there exist months for which the prediction skill is higher than the adjacent months. The skill in the month of maximum ACC (MMA) represents the best performance of the forecast system. Distribution of the maximum ACC skill among the months of melt season (April to September) at L3 is plotted in Fig. 3a with corresponding month when the maximum ACC skill is realized is shown in Fig. 3b with values 4-9 for April-September. Overall, the maximum ACC during the melt season progressively moves from south to north (Fig. 3b) with the mean sea ice concentration in the MMA increasing with latitude (Fig. 3c). The spatial distribution of maximum ACC shows a relationship with the distribution of the variance (Fig. 3d), that is, areas of larger variance corresponds to larger values of ACC. Taking 0.5 as a useful level of ACC for skillful prediction, predictability of weekly mean sea ice concentration near marginal zones is about 5-6 weeks. Prediction skill for Northern Hemisphere sea ice extent (SIE) is above 0.6 for the entire 6 target weeks and is strongly affected by interannual variability.

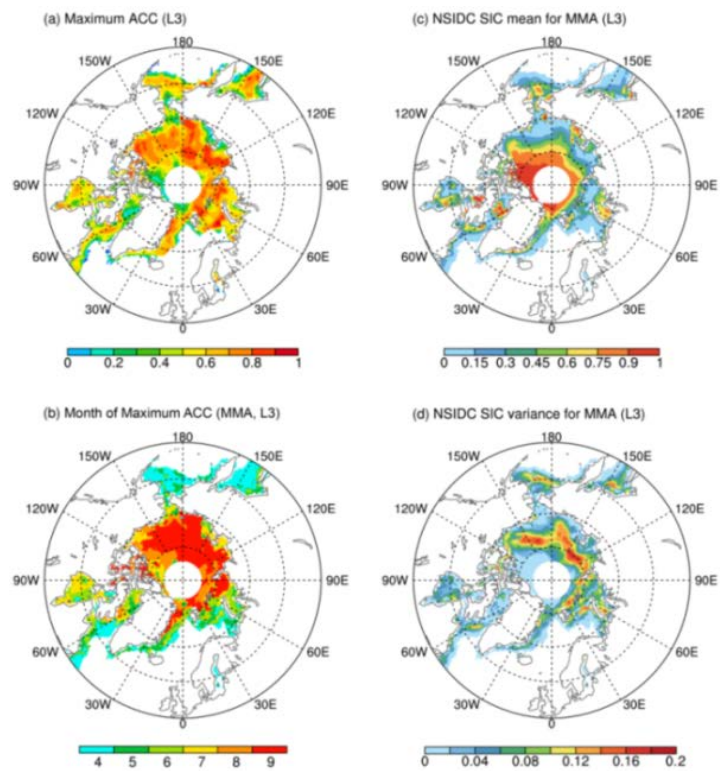


**Fig. 3** Statistics for melt season (April to September) for 3-week lead time (L3). (a) Maximum monthly mean anomaly correlation coefficient (ACC) from April to September, (b) Month of maximum monthly mean ACC (MMA), (c) NSIDC SIC mean for MMA, and (d) NSIDC SIC variance for MMA.

#### 4. Summary and discussion

This study examines Arctic sea ice weekly-mean variability and multi-week prediction skill in the CFSv2. While many studies on seasonal sea ice predictions have been published, this study appears to be the first effort to analyze sea ice prediction skill at multi-week lead time using a dynamical forecast system. The assessment in this study is based on the output from the operational NCEP CFSv2, whose configuration is not optimal and the seasonal sea ice prediction can be improved with an improved initial sea ice thickness (Collow *et al.*, 2015). In addition, while we have analyzed the contributions of sea ice variations and their prediction from trend interannual, detrended interannual, and submonthly variabilities, it will be useful to determine how these variations are contained in the initial conditions and how the memory of the components (*e.g.* sea ice, ocean, and atmosphere) of the forecast system affect the subsequent sea ice evolution. Understanding the impact of the initialization of each component will also provide guidance as to where the critical effort in improving the initialization of the forecast system should be made.

#### References

- Bushuk, M., R. Msadek, M. Winton, G. A. Vecchi, R. Gudgel, A. Rosati, and X. Yang, 2017: Skillful regional prediction of Arctic sea ice on seasonal timescales, *Geophys. Res. Lett.*, **44**, 4953–4964, doi:10.1002/2017GL073155.
- Cavalieri D. J., C. Parkinson, P. Gloersen, H. J. Zwally, 1996: Sea Ice Concentrations from Nimbus-7 SMMR and DMSP SSM/I-SSMIS Passive Microwave Data. National Snow and Ice Data Center: Boulder, CO; <http://nsidc.org/data/nsidc-0051.html>
- Collow, T. W., W. Wang, A. Kumar, and J. Zhang, 2015: Improving Arctic sea ice prediction using PIOMAS initial sea ice thickness in a coupled ocean–atmosphere model, *Mon. Wea. Rev.*, **143**, 4618–4630.
- Fetterer F., K. Knowles, W. Meier, and M. Savoie, 2002: Sea Ice Index. National Snow and Ice Data Center: Boulder, CO.
- Saha, S., and Coauthors, 2014: The NCEP Climate Forecast System version 2. *J. Climate*, **27**, 2185–2208, doi: 10.1175/JCLI-D-12-00823.1.





# 5. DROUGHT AND PLUVIAL EVENTS

42<sup>nd</sup> NOAA Annual Climate Diagnostics and  
Prediction Workshop

23-26 October 2017, Norman, Oklahoma



## Subseasonal Prediction of Warm Season Drought in North America

Hailan Wang<sup>1,2</sup>, Yehui Chang<sup>1,3</sup>, Siegfried D. Schubert<sup>1,2</sup> and Randal D. Koster<sup>1</sup>

<sup>1</sup>Global Modeling and Assimilation Office, NASA/GSFC, Greenbelt, MD

<sup>2</sup>Science Systems and Applications, Inc., Lanham, MD

<sup>3</sup>Morgan State University, Baltimore, MD

### 1. Introduction

The subseasonal prediction of warm season drought in North America remains a great challenge. The prediction skill of North American drought during warm season, the drought development in particular, in current operational drought forecast system is rather limited. This study attempts to explore potential sources of predictability for subseasonal development of warm season drought over North America by focusing on the role of leading modes of subseasonal atmospheric circulation variability. These leading modes are often present in the form of stationary Rossby waves, and have been shown to be crucial in the development of many recent short-term warm season climate extremes over North America (Schubert *et al.* 2011).

### 2. The physical processes by which stationary Rossby waves lead to subseasonal drought development

The physical processes through which stationary Rossby waves affect drought development over North America was investigated by performing a case study of the 20 May – 15 June 1988 stationary Rossby wave event (Wang *et al.* 2017). During this event (Fig. 1), severe dry conditions developed quickly over central North America upon the arrival of stationary Rossby waves, leading to the severe 1988 North American drought. Using the NASA GEOS-5 Atmospheric General Circulation Model (AGCM) and a data assimilation

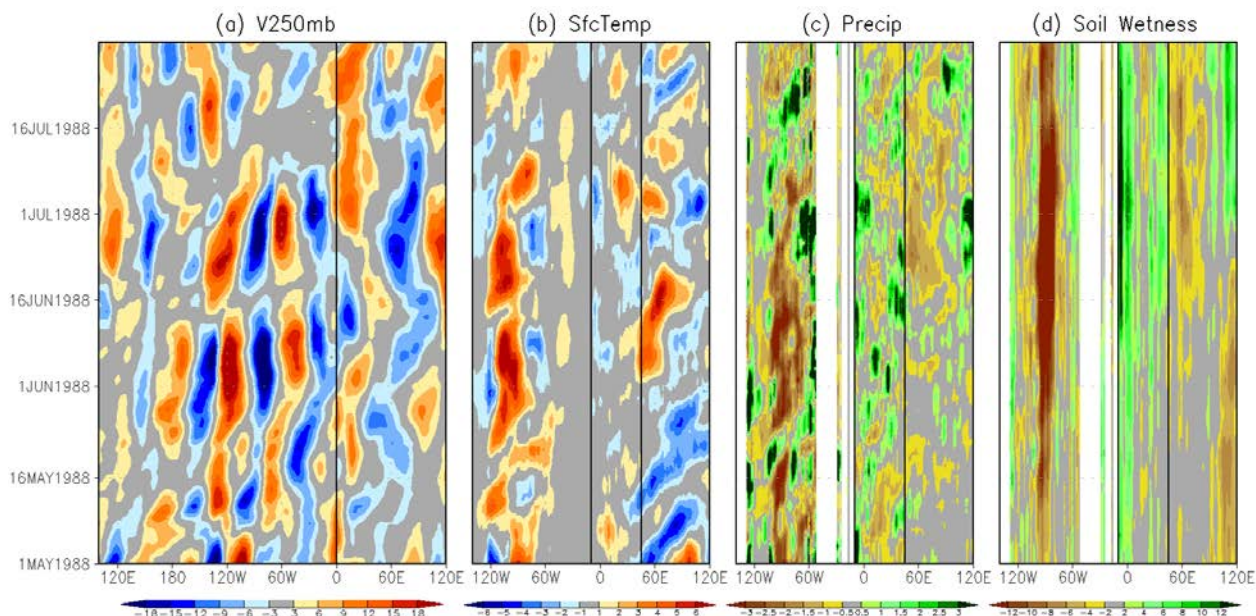
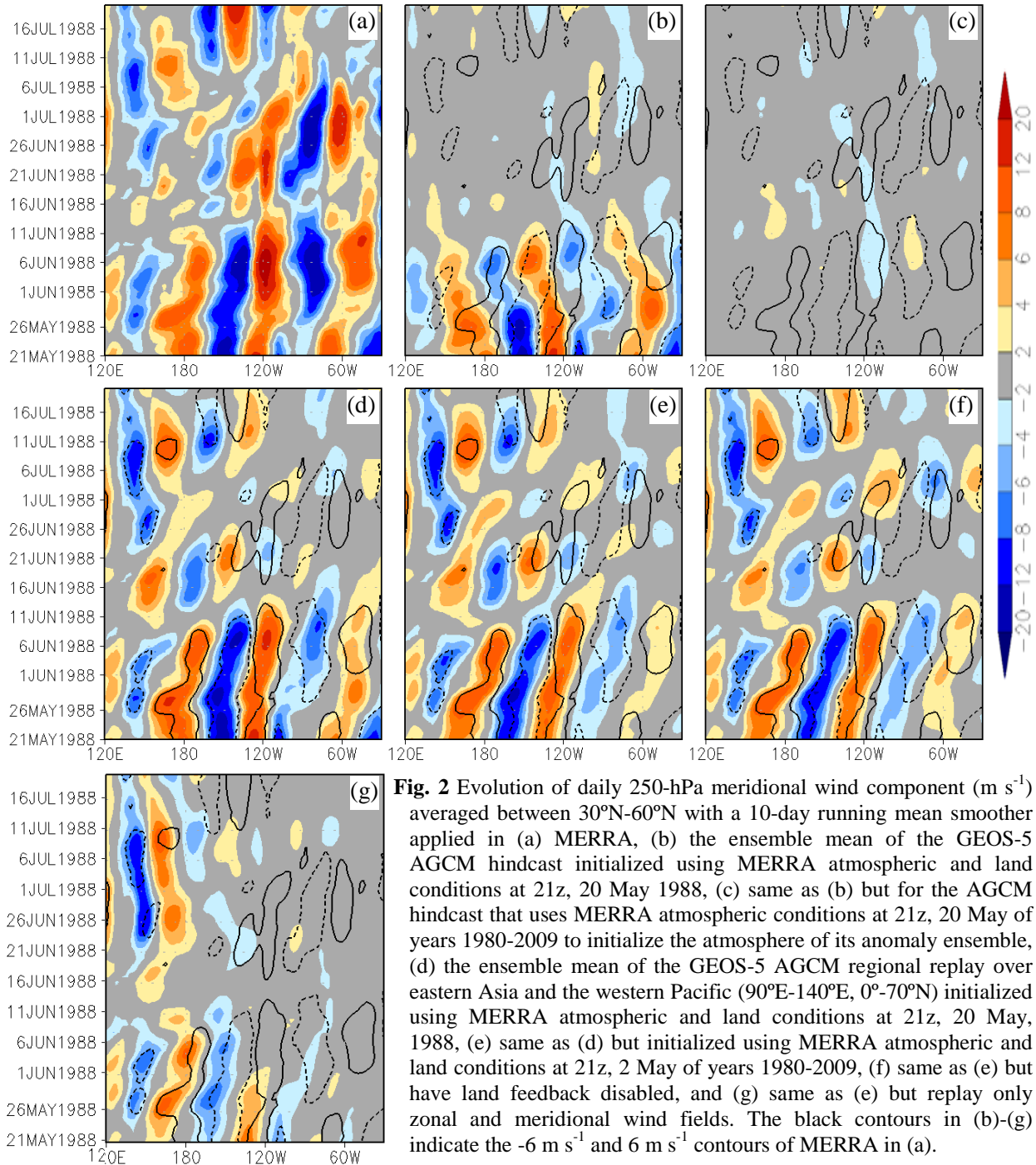


**Fig. 1** Evolution of (a) MERRA daily 250-hPa meridional wind ( $\text{m s}^{-1}$ ) averaged between  $40^{\circ}\text{N}$ - $60^{\circ}\text{N}$  west of  $0^{\circ}$  and  $50^{\circ}\text{N}$ - $70^{\circ}\text{N}$  east of  $0^{\circ}$ , with a 10-day running mean smoother applied, (b) MERRA daily surface temperature anomalies (K), (c) MERRA-Land daily precipitation anomalies ( $\text{mm day}^{-1}$ ), and (d) MERRA-Land daily surface soil wetness anomalies (%), averaged between  $30^{\circ}\text{N}$ - $50^{\circ}\text{N}$  west of  $10^{\circ}\text{W}$ , between  $35^{\circ}\text{N}$ - $55^{\circ}\text{N}$  for  $10^{\circ}\text{W}$ - $45^{\circ}\text{E}$ , and between  $50^{\circ}\text{N}$ - $70^{\circ}\text{N}$  east of  $45^{\circ}\text{E}$ , with a 5-day running mean smoother applied, during the period 1 May – 31 July 1998.

technology called “replay”<sup>1</sup>, we designed a series of AGCM hindcast experiments to isolate the contributions to this event from: (i) the atmosphere and land initial conditions in late May 1988, (ii) the observed stationary wave sources over the western Pacific, (iii) the correct model simulation of mean jet stream over the North Pacific, and (iv) soil moisture feedback over North America.

The results show the crucial importance of the strong mean jet stream over the North Pacific for guiding and constraining wave energy propagation path and speed and thereby providing a potential source of predictability. For the 20 May – 15 June 1988 stationary Rossby wave event investigated here (Fig. 2), the



<sup>1</sup> In the replay approach, the model atmosphere is constrained either fully or in part using existing reanalysis data; any subset of variables in any region of the world can be used.

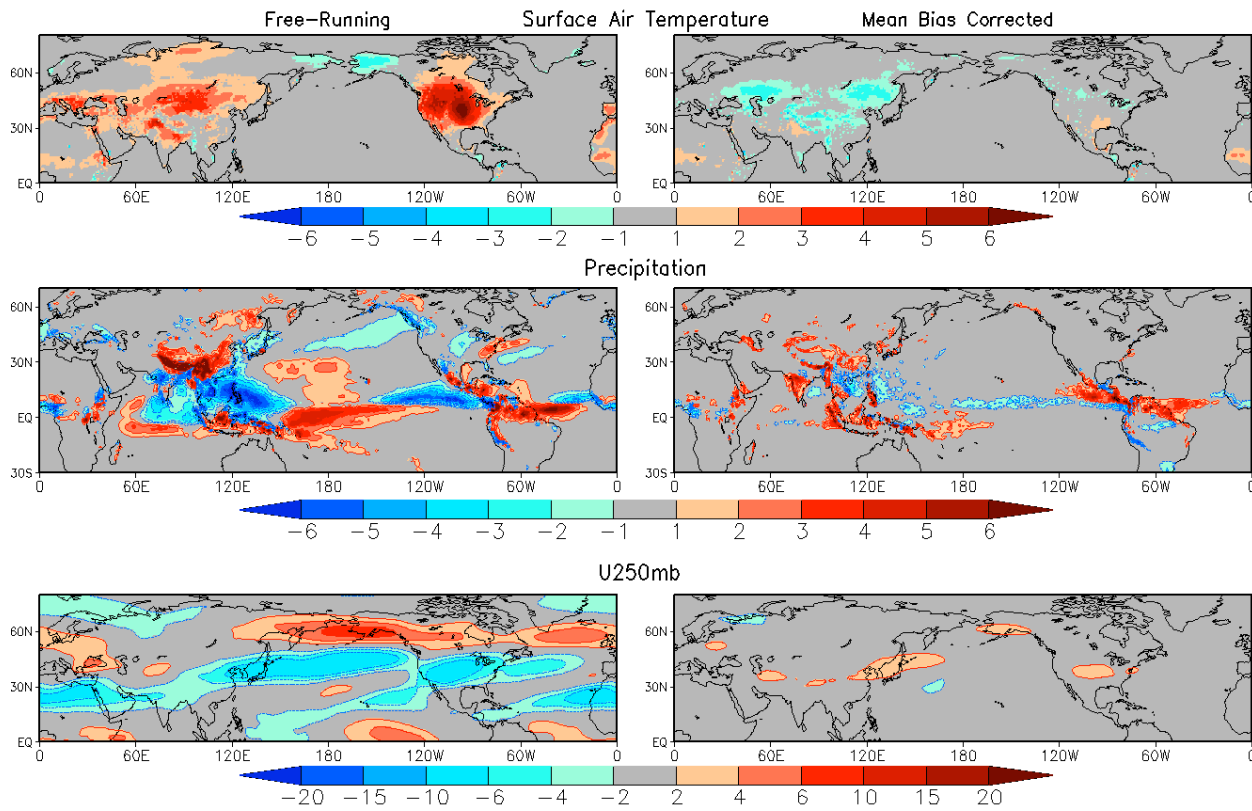


**Fig. 3** Mean model bias in precipitation (mm/day), surface air temperature (K) and zonal wind at 250mb (m/s) in the GEOS-5 free-running AGCM (left panels) and the GEOS-5 AGCM that has mean bias corrected (right panels), during JJA. The AMIP simulations over 1980-2014 are used to obtain the AGCM climatology. MERRA2 is used for model validation.

free-running model hindcast skill (Fig. 2b) is limited to only about one week, beyond which the hindcasted waves show westward retrograde displacement instead of remaining quasi-stationary as in the observations (Fig. 2a), due to the considerably weaker mean model jet over the North Pacific than the observed (Fig. 3 bottom left panel). With the mostly corrected (through regional replay of all basic model variables to MERRA over East Asia and western Pacific) North Pacific mean jet (Fig. 2d, 2e), our results show that convective anomalies over the western Pacific do produce a predilection for sustained upper-level high anomalies over central North America about one to two weeks later. Such high anomalies subsequently lead to strong local precipitation deficits, soil dryness and surface warming, and thereby to severe drought conditions there (not shown). When the north Pacific mean jet bias is only partially corrected (through regional replay of only zonal and meridional winds to MERRA over East Asia and western Pacific) (Fig. 2g), the waves show slower eastward energy propagation across the north Pacific, and the subsequent circulation anomalies over North America not only show a rather weak magnitude but also are in the wrong locations. The soil moisture feedback is found to be unimportant during the event.

Since it usually takes about two weeks for the wave energy to propagate across the North Pacific to reach North America, these waves can potentially serve as a source of subseasonal forecast skill in these downstream locations. To access this skill, however, it would be critically important for a forecast model to correctly simulate the mean Northern Hemisphere (NH) jet streams, not only their location and shape but also their magnitude, in order to allow the correct simulation of wave propagation (path and speed) across the northern oceans. The forecast model also needs to be able to predict sources of the stationary Rossby waves.

### 3. NASA GEOS-5 model bias correction

The standard GEOS-5 AGCM, like many other current models, provides weak and disoriented NH jet streams, and displays considerable biases in tropical convection and surface temperature (Fig. 3, left panels).



These biases limit the use of free-running GEOS-5 GCM for simulation and prediction of stationary Rossby waves and their effect over North America. In order to correct the GEOS-5 AGCM bias, we have applied 6-hourly climatological (1980-2015) Incremental Analysis Updates (IAU) tendencies from MERRA-2 to model basic state variables in a free-running GEOS-5 AGCM. By doing so, we are able to successfully (though artificially) correct much of the model bias. Substantial improvements are seen in model simulation of mean climate (Fig. 3) as well as weather and climate variability across many time scales.

Using a similar IAU-based approach, we have recently developed a bias-corrected NASA GEOS-5 coupled forecast system. Here a coupled replay was first performed, in which the model atmosphere is constrained to be close to MERRA-2 while letting the model ocean freely evolve. The mean atmospheric bias in the GEOS-5 coupled model was then corrected by applying the 6-hourly climatological IAU corrections from the coupled replay (1980-2014). The bias correction approach has been shown to successfully remove much of the coupled model bias in SST, precipitation and large-scale atmospheric circulation.

#### 4. Model prediction of stationary Rossby waves and the impact of model bias

Using the standard GEOS-5 AGCM and the mean bias corrected GEOS-5 AGCM, we have performed two suites of comprehensive daily hindcasts for warm seasons of 18 years (1988, 1998, 2000-2015). A comparison of these two suites of hindcasts over North America shows that the bias correction leads to considerable skill improvement for the prediction of atmospheric circulation and surface air temperature but only marginal improvement for precipitation (Fig. 4). An examination of individual drought events, such as the 2012 Great Plains flash drought, shows that the bias correction can improve the forecast skill by up to 9

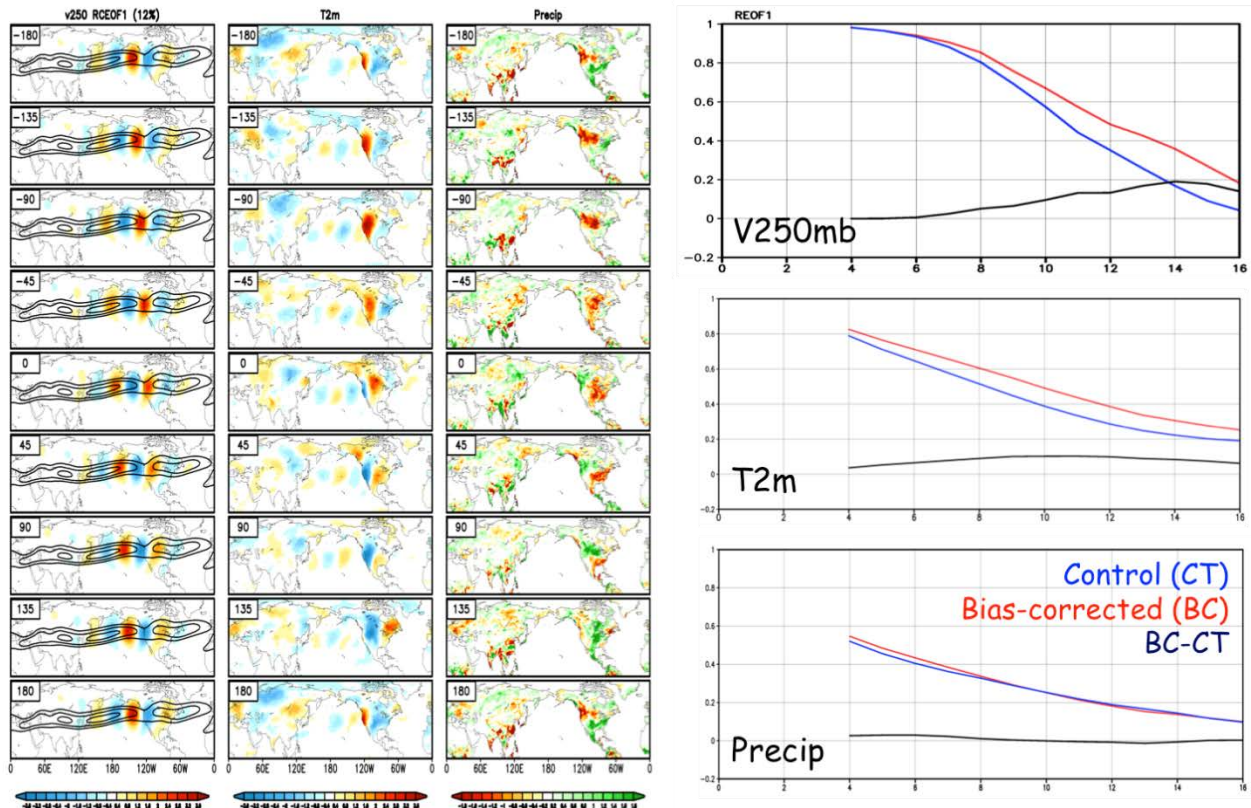


**Fig. 4** Left panel: the first rotated complex EOF (12%) of MERRA-2 daily 250mb meridional wind (V250mb) in the NH during warm season; second panel from left: composites of MERRA-2 surface air temperature anomalies when the first rotated PC is above one standard deviation; third panel from left: same as the second left panel but for NCEP CPC precipitation composites. Right panels: the forecasting skills of V250mb (top), surface air temperature (middle) and precipitation (bottom) as a function of lead days in standard GEOS-5 AGCM (blue line), the bias corrected GEOS-5 AGCM (red line), and their differences (black line).

days (not shown). Currently, the impact of the bias correction in the GEOS-5 coupled forecast system on the subseasonal prediction of warm season drought over North America is under investigation.

## 5. Summary

This study investigates the physical processes by which stationary Rossby waves lead to subseasonal development of drought conditions over North America. It is found that stationary Rossby waves can serve as a potential source of predictability for subseasonal development of North American droughts. In order to properly represent the effect of stationary Rossby waves and exploit this source of predictability, a forecast model needs to be able to predict the source of the waves, and provides a correct simulation of the NH jet streams (location, shape, magnitude). Since the NASA GEOS-5 model, like many other current models, display considerable bias during boreal summer, an objective approach has been developed to correct much of the model bias, which subsequently improves the prediction skill of the stationary Rossby waves and their impact over North America.

*Acknowledgement.* This work has been supported by the NOAA Climate Program Office Modeling, Analysis, Prediction, and Projections (MAPP) program (NA14OAR4310221).

## References

- Schubert, S., H. Wang, and M. Suarez, 2011: Warm season subseasonal variability and climate extremes in the Northern Hemisphere: the role of stationary Rossby waves. *J. Climate*, MERRA special issue, 4773-4792, doi: 10.1175/JCLI-D-10-05035.1.
- Wang H., S. Schubert, R. Koster 2017. North American drought and links to northern Eurasia: The role of stationary Rossby waves. Chapter 12, *Climate Extremes: Patterns and Mechanisms*, S. Wang *et al.* Eds., AGU Wiley Geophysical Monograph Series. ISBN-13: 978-1119067849.

## Diagnosing Extreme Drought Characteristics Across the Globe

Ehsan Najafi<sup>1, 2, 3</sup>, Indrani Pal<sup>1, 2, 3</sup>, and Reza M. Khanbilvardi<sup>1, 2, 3</sup>

<sup>1</sup>*Department of Civil Engineering, City University of New York (City College), New York*

<sup>2</sup>*Center for Water Resources and Environmental Research (City Water Center),  
City University of New York (City College), New York*

<sup>3</sup>*NOAA-Cooperative Remote Sensing Science and Technology Center (NOAA-CREST),  
City University of New York, New York*

### 1. Introduction

Droughts are one of the world's most widespread climatic disasters having significant adverse impacts on every water-dependent sector and the economy. There is now higher confidence that extreme drought risk has been changing across the globe and will increase in the future with climate change. However, global extreme drought characteristics and their connections to regional as well as large scale climate have not been fully explored. In this study, considering extreme drought magnitudes and timing in every land region of the globe over the past several decades, we try to address the following research questions: 1- How have the annual extreme drought magnitudes changed across the globe? 2- What is the spatial distribution of extreme droughts in each continent? 3- Are there any joint dependencies between extreme droughts across the globe? Our preliminary analyses suggest that many parts of the world have experienced similar patterns in terms of extreme droughts.

### 2. Methodology and data

We implemented Palmer Drought Severity Index (PDSI) dataset from 1950 to 2014, as a popular drought indicator to diagnose its extreme characteristics. This index not only integrates precipitation and temperature but is also highly correlated with soil moisture content (Dai *et al.* 2004). PDSI has been successfully applied to quantify the severity of droughts across different climates (Wells *et al.* 2004). It ranges from about -10 (dry) to +10 (wet) with values below -3 representing severe to extreme drought. Gridded monthly self-calibrated PDSI, at 2.5-degree resolution, provided by NOAA/OAR/ESRL Physical Sciences Division (PSD) (<http://www.esrl.noaa.gov/psd/>), Boulder, Colorado, is used here.

Extracting relevant information hidden in the complex spatial-temporal drought data set is complicated. To identify spatial patterns, most famous statistical methods are based on the concept of intra- and intercluster variances (like the k-means algorithm) (Bernard *et al.* 2013). In terms of drought, clustering of extreme drought has been lacking. In order to cluster the extreme drought, we used PAM Algorithm along with F-madogram (Bernard *et al.* 2013). F-madogram measures the pairwise dependence between variable time series and can be used as distance matrix in the PAM clustering algorithm. The approach we used here, combines the PAM algorithm with the F-madogram and creates a simple clustering algorithm for maxima. This method generates clusters around the representative grid cells (medoids). In order to use this approach, we consider the minimum annual PDSI of each grid cell.

### 3. Results

Figure 1 (a) shows the significant trend of monthly PDSI data from 1950 to 2014. The slopes were computed based on the seasonal Kendall Trend Test considering the Serial Dependence. Approximately, longitudinally and latitudinally, we see that grids with negative slope outnumber the positive ones, which means in general, drought has become more severe during the last several decades. The African continent, eastern China, eastern Australia, western Canada, parts of Russia and Brazil have experienced more severe droughts. The US, western part of Australia and west of China, got generally less severe. Dipole patterns in

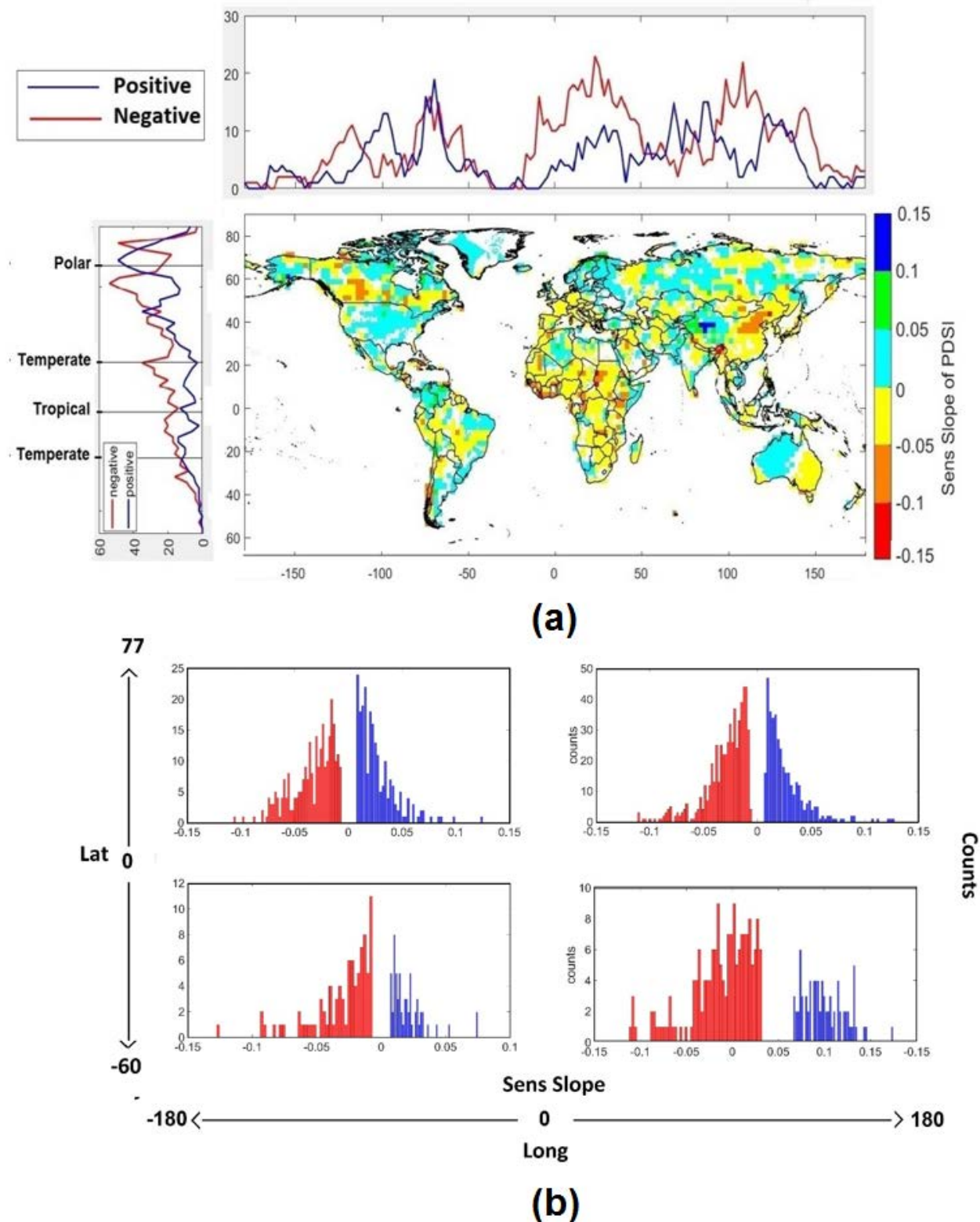


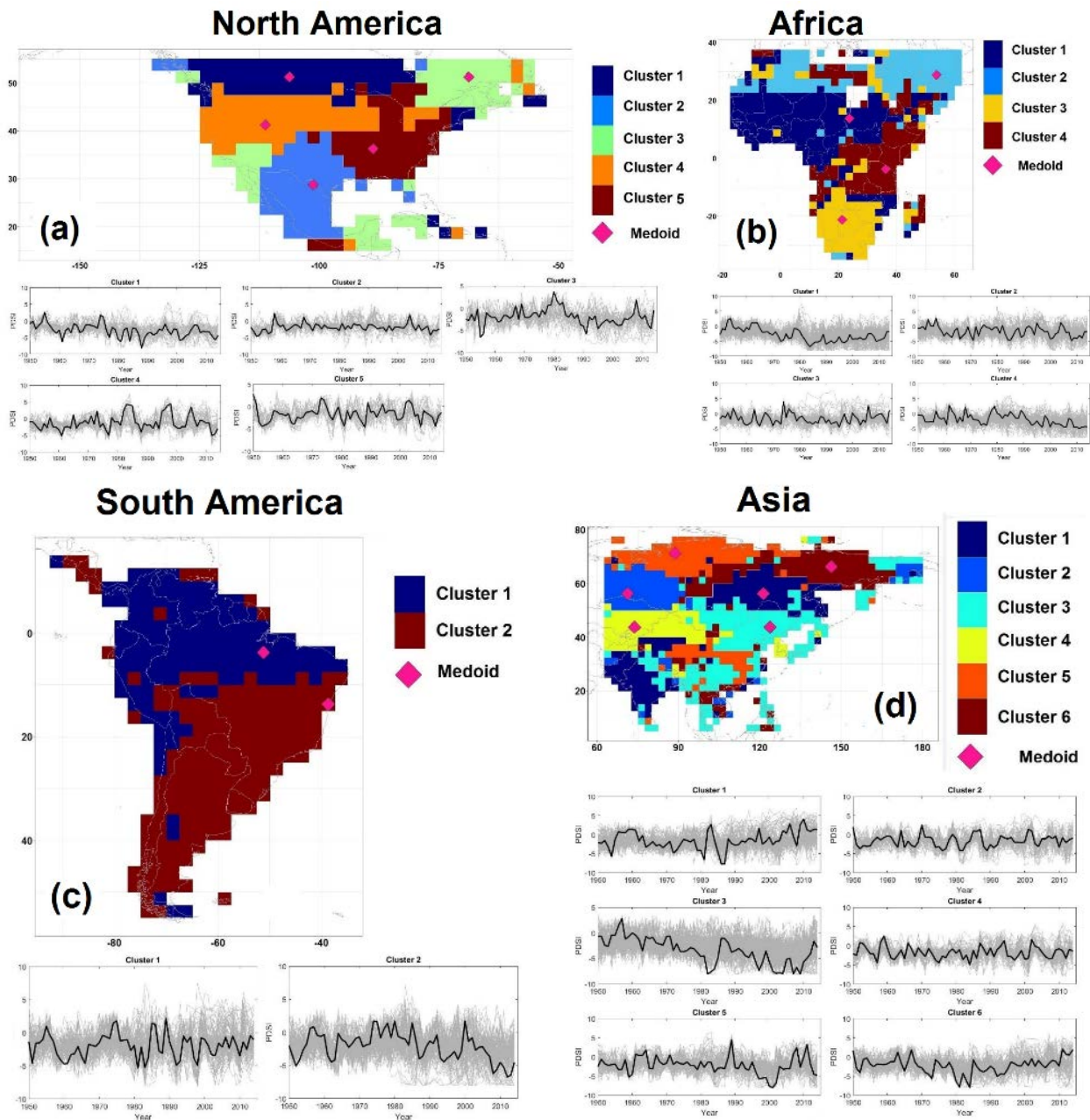
**Fig. 1** (a) Trends (Sen's Slope) of Monthly PDSI from 1950 to 2014 (95% significance), and (b) slope distribution of monthly PDSI from 1950-2014 in four regions of the globe.

Australia and China are remarkable. One of the important features of this graph is that Africa has experienced more severe droughts through time during the last several decades. Using these maps, we will see that many of the continental clusters are categorized in the same location based on these trends. The slope distribution of



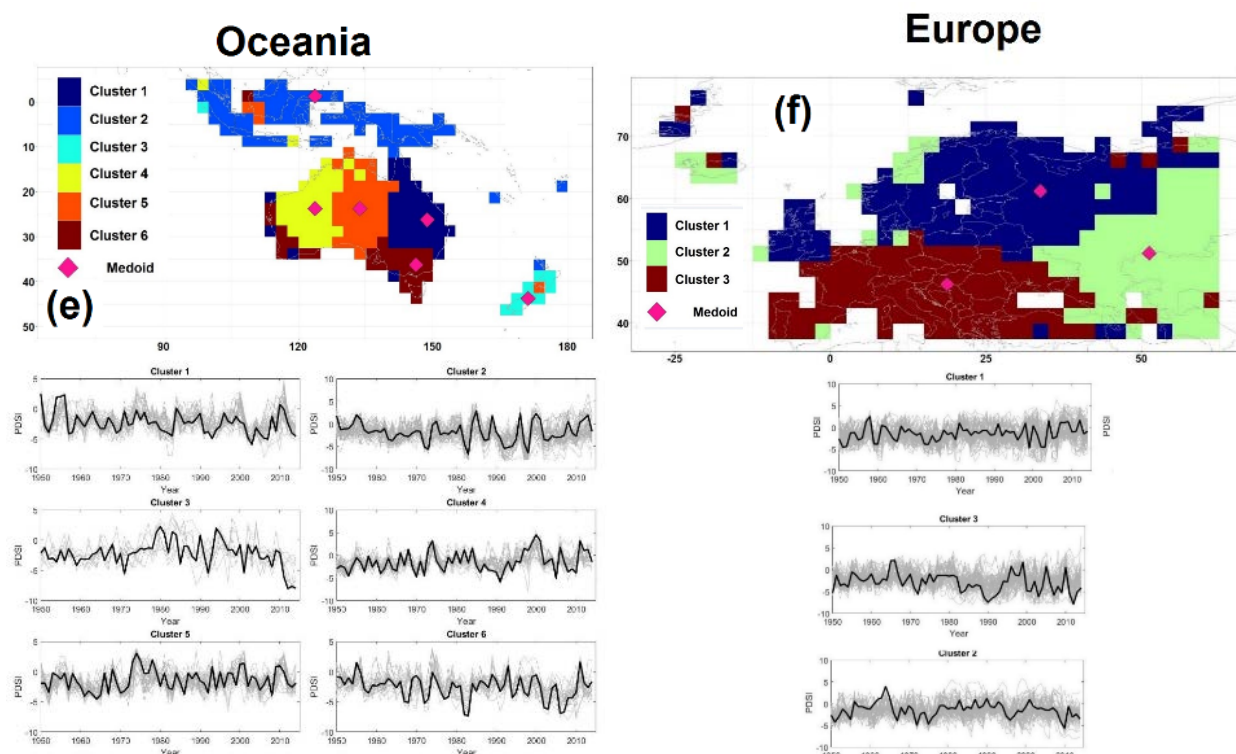
monthly and minimum annual PDSI in both latitude and longitude directions are shown in Figure 1 (b). It shows the slope distribution acquired from the previous step in 4 regions of the world. In general, the number of grids with negative slope outnumbers the positive ones.

Figure 2 represents the result of clustering for 6 continents. The number of clusters was defined based on the Silhouette Coefficient (SC) (Rousseeuw 1987). The medoids -that are the representative of each cluster- are shown by a pink diamond in each cluster and the PDSI trend of each cluster is shown under each continent's map. The trends of medoids are highlighted by a thick black color. In North America, the best number of clusters was found as 5. Clusters 2, 4 and 5 cover US and Mexico. Based on the trends of the medoids, it is clear that they are a good representative of each cluster. Interestingly South America is divided



**Fig. 2** The clusters of the annual extreme droughts over a) North America, b) Africa, c) South America, d) Asia, e) Oceania, and f) Europe from 1950 to 2014. In each map, medoids are shown by pink diamonds. The graphs depict the time series of PDSI for each cluster. The time series of the medoids are highlighted.





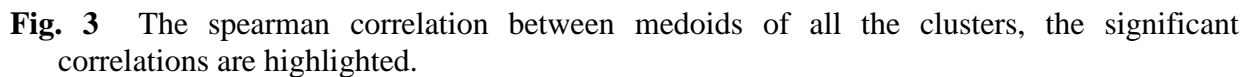
**Fig. 2 (con't.)**

into just two clusters in north and south and Europe and Africa are divided into 3 and 4 clusters respectively. In Asia, we found 6 clusters. Among all the continents, Asia contains the noisiest clusters, especially in the south (for example see the Cluster 3). This issue has been reflected in the time series of the medoids too. Based on Koppen climate classifications, there are many types of climatic regions in Asia and this might be one of the explanations of these noisy clusters. Unlike Asia, Oceania is very well classified. Australia is covered with 4 clusters; however, the cluster number 6 is a little noisy. New Zealand and South Eastern Asian countries are all in one cluster.

Figure 3 presents the Spearman correlation between the medoids of all the clusters. The significant correlations are highlighted. The largest positive correlation belongs to cluster 3 of Asia and cluster 1 of Africa (0.58) and the largest negative correlation can be seen between cluster 3 of Oceania and cluster 6 of Asia (-0.5). In addition to these intercontinental correlations, there are significant correlations between clusters of each continent. For example, clusters 1 and 2 in Africa positively and clusters 1 and 3 in Europe negatively are correlated. The next step of this study will be examining the association between these clusters and climatic patterns such as sea surface temperature (SST). It should be noted that many problems are associated with some degrees of uncertainty, in these situations, the decision maker tries to find a solution that performs relatively well across uncertainties (Najafi *et al.* 2018; Afshar and Najafi 2014; Najafi and Afshar 2013; Armal *et al.* 2018). In the future, we will recognize and consider the uncertainties associated with the clustering as well as uncertainties between clusters and explanatory factors such as SST.

## References

- Afshar, A., and E. Najafi, 2014: Consequence management of chemical intrusion in water distribution networks under inexact scenarios. *J. Hydroinform.*, **16**, 178–188, DOI: 10.2166/hydro.2013.125
- Armal, S., N. Devineni, and R. Khanbilvardi, 2018: Trends in extreme rainfall frequency in the contiguous United States: Attribution to climate change and climate variability modes. *J. Climate*, **31**, 369–385, <https://doi.org/10.1175/JCLI-D-17-0106.1>
- Bernard, E., P. Naveau, M. Vrac, and O. Mestre, 2013: Clustering of maxima: Spatial dependencies among heavy rainfall in France. *J. Climate*, **26**, 7929–7937, <https://doi.org/10.1175/JCLI-D-12-00836.1>



- Dai, A., K. E. Trenberth, and T. Qian, 2004: A global dataset of palmer drought severity index for 1870–2002: Relationship with soil moisture and effects of surface warming, *J. Hydrometeorol.*, **5**, 1117–1130.
- Najafi, E., and A. Afshar, 2013: Consequences management of chemical intrusions in urban water distribution networks using the ant colony optimization algorithm. *J. Water & Wastewater*, 82–94.
- , N. Devineni, R. M. Khanbilvardi, and F. Kogan, 2018: Understanding the changes in global crop yields through changes in climate and technology. *Earth's Future*, Accepted Author Manuscript. doi:10.1002/2017EF000690
- Rousseeuw, P., 1987: Silhouettes: A graphical aid to the inter-pretation and validation of cluster analysis. *J. Comput. Appl. Math.*, **20**, 53–65.
- Wells, N., S. Goddard, and M. J. Hayes, 2004: A self-calibrating palmer drought severity index. *J. Climate*, **17**, 2335–2351.

## Future Projections of U.S. Drought and Pluvial Event Characteristics

Elinor R Martin

*School of Meteorology, and South Central Climate Science Center  
The University of Oklahoma, Norman, OK*

### 1. Introduction

Drought and pluvial events have large socio-economic impact in the U.S. and around the world. In order to increase resilience to these events, it is necessary to understand how these dry and wet periods will change in the future. Much prior work has focused on drought, and results show increasing drought frequency and intensity, especially in subtropical regions (*e.g.* Cook *et al.*, 2014, Touma *et al.* 2015, Dai and Zhao 2016, Hunt 2011). However, there has been much less focus on how extended wet periods, or pluvial events will change in the future and how these changes relate to the overall precipitation trends. While we expect the most intense rain events to increase (*e.g.* O'Gorman and Schneider 2009), it is not known if this will be true for pluvial events, like the May 2015 heavy rainfall event in Oklahoma and Texas. Although there are numerous definitions of droughts, this study uses a meteorological definition that only considers precipitation. This study will determine how future precipitation trends manifest in terms of frequency, severity, and duration of both droughts and pluvials.

### 2. Data and methodology

Observations of precipitation from two monthly datasets are used; Climate Research Unit (CRU) TS v3.23 precipitation at 0.5° resolution from 1901-2014 and Global Precipitation Climatology Center (GPCC) v7 precipitation at 1° resolution from 1901-2015. Historical and future projection (scenario Representative Concentration Pathway (RCP) 8.5) experiments are used from 24 Coupled Model Intercomparison Project Phase 5 (CMIP5) models (Taylor *et al.* 2012). Changes in future characteristics are established using differences between 2080-2100 RCP8.5 output and 1980-2000 historical output. All model data are regridded bilinearly to a common 2° horizontal resolution to facilitate comparison between the models and create a multi-model mean.

To identify meteorological drought and pluvial events, the 6-month standardized precipitation index (SPI) is calculated for the observations and model output (McKee *et al.*, 1993). SPI is calculated at each grid point, for the duration of the observations and the model output (1900-2100), and drought and pluvial events are defined based on two categories: moderate ( $\pm 1$ ) and severe ( $\pm 2$ ). An event is identified when the SPI exceeds the threshold, and the duration of the event is the number of months that the threshold is exceeded. As the 6-month SPI is used, the thresholds only need to be exceeded for 1-month to be identified as an event. The average SPI during an event is used as a measure of the event intensity.

### 3. Results

#### 3.1 Climatology and trends

Since 1901, both observational datasets show a wetting trend (in precipitation and SPI) across most of North America, with the exception of the Southwest. The multi-model mean of the CMIP5 historical model simulations also show a similar pattern, with a drying to wetting gradient from the southwest to northeast, as shown in numerous prior studies. In the future, the models are in good agreement that this trend will continue in the future. However, a northwest to southeast swath across the US has less agreement on the sign of the trend in the transition zone from wetting to drying. However, the variability of SPI (and precipitation) shows a very different signal. Using the 9-year running standard deviation of SPI, the two observational datasets do not agree as well, especially across Canada. A trend of increasing variability in precipitation is evident in

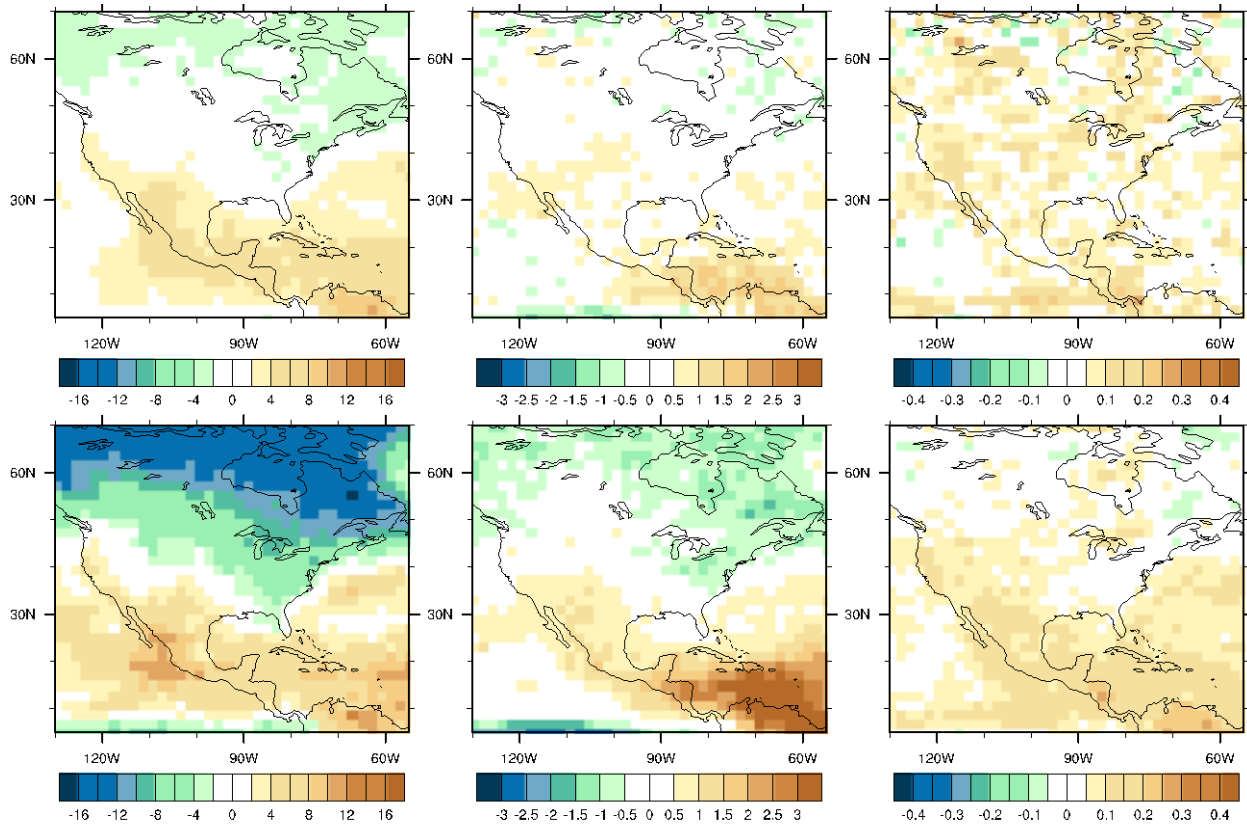


**Fig. 1** Multi-model mean change in drought event characteristics (number (left column), duration (middle column), and intensity (right column)) between 2080-2100 and 1980-2000. Top row for severe ( $SPI < -2$ ) and bottom for moderate ( $SPI < -1$ ) drought events.

much of the western and northeastern U.S. Historical CMIP5 model simulations show almost no trend in this variability, but in the future, almost all models show a strong trend of increasing variability across the entirety of North (and Central) America. This increase in variability suggests more frequent drought and pluvial events will occur in the future.

### 3.2 Future changes

The multi-model mean changes in drought and pluvial event characteristics are shown in Fig. 1 and Fig. 2, respectively. In all cases, the changes are larger in moderate events in comparison to severe events. The spatial pattern of the change in number of drought events matches well with the precipitation trends in moderate and severe drought cases. In moderate events, droughts are projected to increase in length by approximately 1 month in the southwest U.S. and over 3 months in parts of the Caribbean. Interestingly, the intensity of droughts is projected to increase across the whole North and Central America, irrespective of whether the precipitation is increasing or decreasing. Drought intensities increase up to approximately 0.2 SPI in moderate and severe drought events.

Similar results are seen in the cases of projected changes to pluvial events. Moderate and severe pluvial events are projected to increase across much of North America, especially in the north and east. As for drought events, the average intensity of pluvials is projected to increase for moderate and severe events across North America. Hence, both wet and dry events will become more intense in the future across North America.

When comparing the drought and pluvial event characteristics with precipitation trends, it is evident that there are some locations where “opposite” projections are occurring. For example, precipitation is projected to increase but drought frequency, duration, and/or intensity are also increasing. To investigate the locations where this is occurring, Fig. 3 highlights regions where drought and pluvial characteristics are in the opposite direction to the precipitation trend in the multi-model mean CMIP5 simulations. For the number of events, the

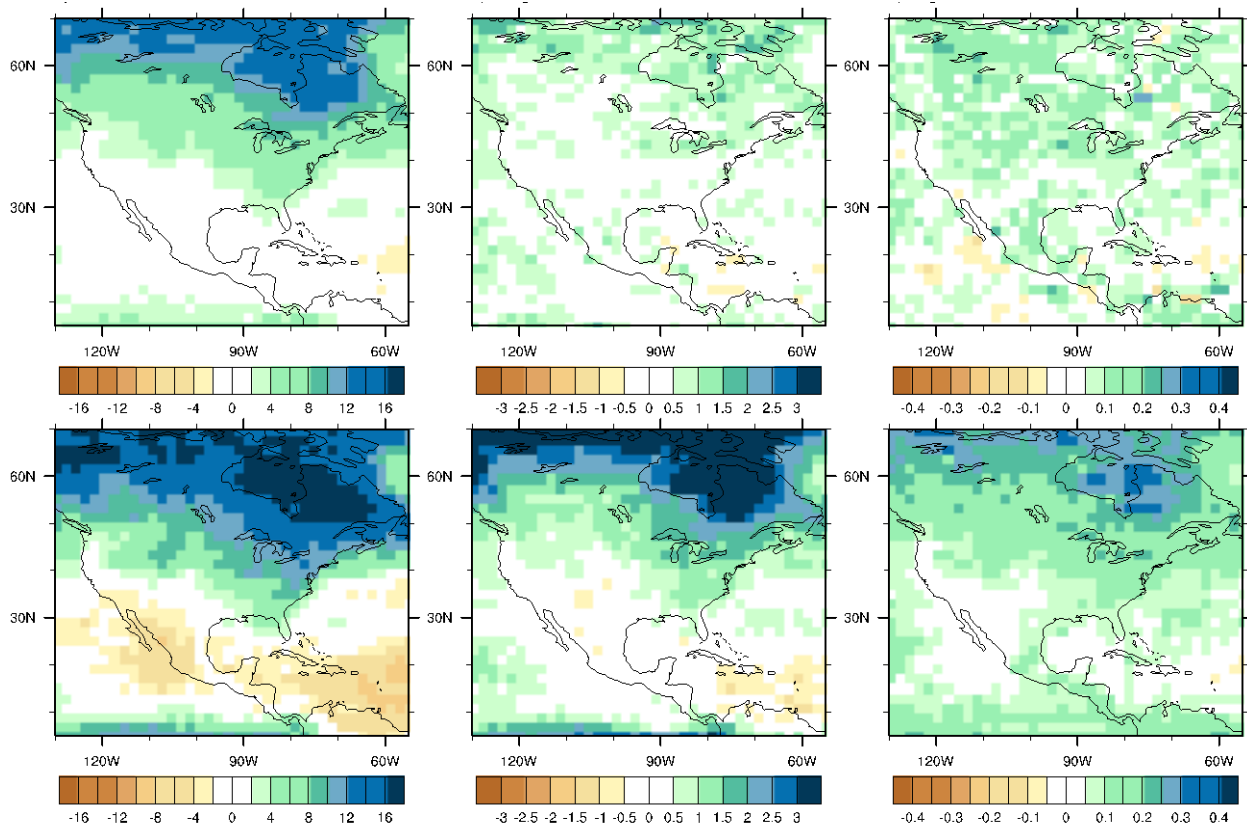


**Fig. 2** As in Figure 1 but for pluvial events characteristics.

signal is across the central U.S. in the region between increasing and decreasing precipitation trends where the model agreement on the sign of the trend is smaller. This is also the case for the duration of events, although there is some area expansion, especially in the severe category. The most spatially extensive signal is for the intensity of events. These results suggest that even in regions where precipitation is projected to increase (the north and east U.S.), severe (and moderate to some extent) drought events are projected to increase in duration and intensity (and vice versa with pluvial events in the southwest U.S. and Central America. This has important implications for planning and resilience to events.

#### 4. Summary

Precipitation trends alone do not give information about future drought and pluvial characteristics that are important for planning and impacts. Comparing two observational datasets of precipitation with simulations from the CMIP5 suite of experiments, good agreement is seen in precipitation trends in the historical period but there is less agreement (between the two observational datasets themselves and the models) in the variability. In the future, the variability in the 6-month SPI is projected to increase across the whole North America, suggesting that the characteristics of drought and pluvial events will be changing. As expected from prior studies, generally, wet regions are getting wetter with more frequent, longer lasting, stronger pluvials (and vice versa for drought events). Uniquely, this study also investigates when wet and dry events occur in regions where the precipitation trend is of the opposite sign. Especially for severe droughts/pluvials we see wetting areas with more, longer, and stronger droughts (and vice versa). There is still a need to understand the drivers, spatial variability and predictability of these events across North and Central America.

#### References

Cook, B. I., J. E. Smerdon, R. Seager, and S. Coats, 2014: Global warming and 21st century drying, *Clim. Dyn.*, **43**, 2607-2627, doi: 10.1007/s00382-014-2075-y.



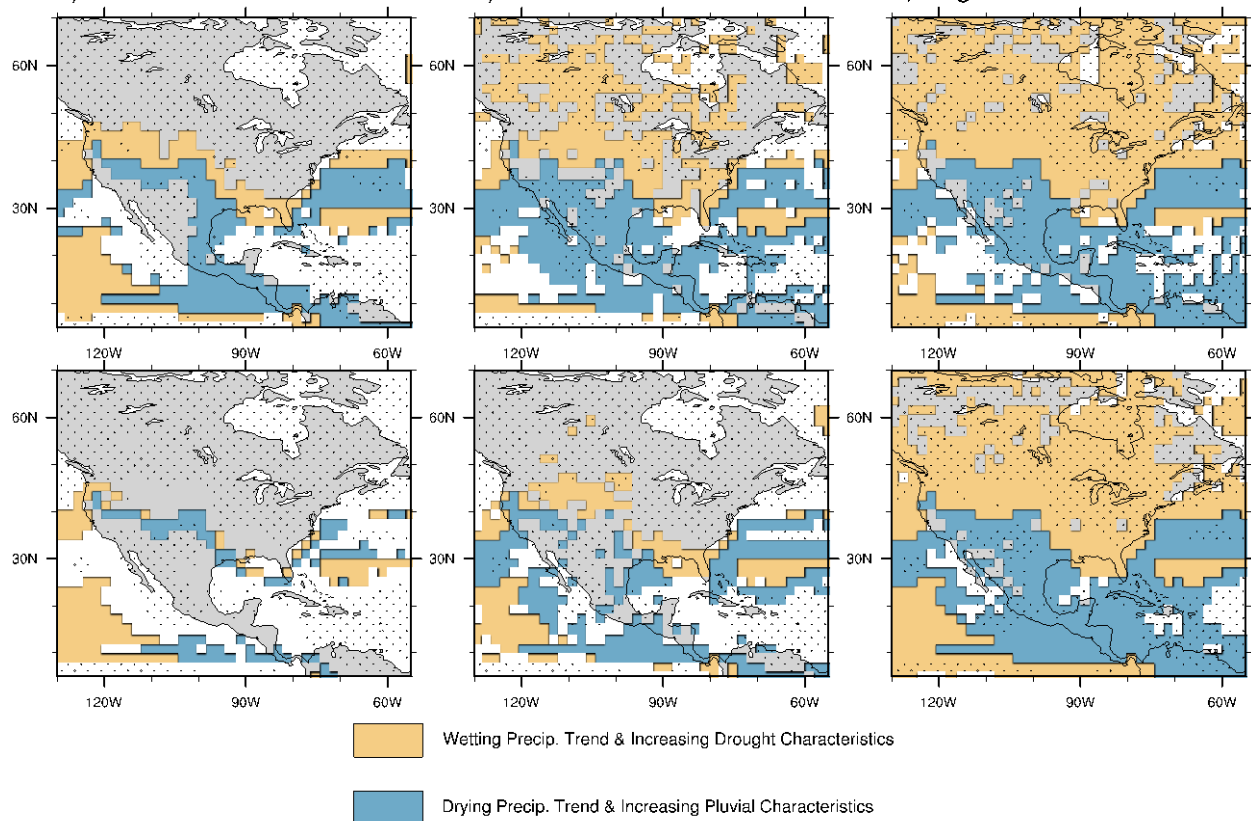


**Fig. 3** Multi-model mean locations showing increases in drought (orange) and pluvial (blue) characteristics (number (left column), duration (middle column), and intensity (right column)) when the precipitation trend is wetting and drying, respectively (*i.e.* opposite sign). Top row for severe ( $SPI < -2$ ) and bottom for moderate ( $SPI < -1$ ) drought events.

- Dai, A., and T. Zhao, 2016: Uncertainties in historical changes and future projections of drought. Part I: Estimates of historical drought changes, *Clim. Change*, doi: 10.1007/s10584-016-1705-2
- Hunt, B. G., 2011: Global characteristics of pluvial and dry multi-year episodes, with emphasis on megadroughts. *Int. J. Clim.*, **31**, 1425–1439.
- McKee, T., N. Doesken, and J. Kleist, 1993: The relationship of drought frequency and duration to time steps, in Proceedings of the 8th Conference on Applied Climatology, pp. 179–184, Anaheim, Calif, USA.
- Taylor, K. E., R. J. Stouffer, and G. A. Meehl, 2012: An overview of CMIP5 and the experiment design, *Bull. Amer. Meteor. Soc.*, **93**, 485–498.
- Touma, D., M. Ashfaq, M.A. Nayak, S-C. Kao, and N.S. Diffenbaugh 2015: A multi-model and multi-index evaluation of drought characteristics in the 21st century. *J. Hydrol.*, **526**, 196-207.
- O'Gorman, P. A., T. Schneider, 2009: The physical basis for increases in precipitation extremes in simulations of 21st-century climate change. *Proc. Nat. Aca. Sci.*, **106**, 14773-14777, doi: 10.1073/pnas.0907610106.

## Long-term Variation of US Land Surface Hydrological Extremes

Yun Fan and Huug van den Dool

Climate Prediction Center, NCEP/NWS/NOAA, College Park, MD

### 1. Introduction

Drought and flood are two opposite land surface hydrological extremes. They are frequent natural disasters and can happen anywhere. It is those severe land surface hydrological extremes that cover a large-scale space and last long term periods can bring devastating disasters to the human society and major disruption to earth's ecosystems. Therefore, one may ask questions like: Do our current land surface monitoring and modeling systems have the capability to reproduce those land surface hydrological extremes that have occurred in the past multi-decades? What are the main reasons for the major land surface hydrological extremes in the US? Hence, to better understand the attributions of those major land surface hydrological extremes and eventually to accurately predict them are important for science and protecting human society.

### 2. Methodology

Soil moisture responds to precipitation accumulation like a low-pass filter and is a significant physical variable for land surface monitoring and studies. A newly generated long-term (from 1895 to present) land surface hydrological dataset by the CPC leaky bucket land surface hydrological model (Huang *et al.* 1996),

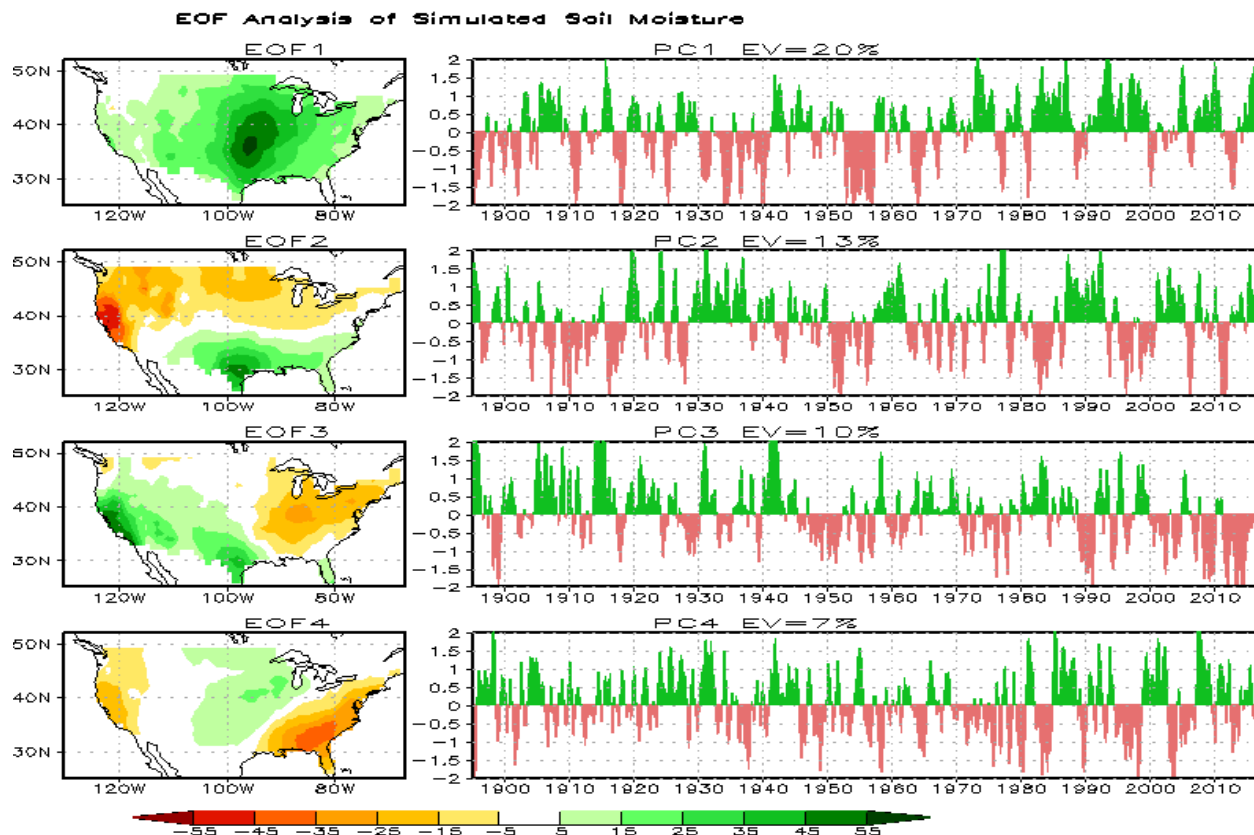


**Fig. 1** EOF analysis for simulated soil moisture for period 1895 to 2017.

which was forced with the improved National Centers for Environmental Information (NCEI) monthly observed precipitation and 2m surface air temperature (well quality controlled) over the 344 US climate divisions (Vose *et al.* 2014), was used to study land surface hydrological extremes and their variations in the US for the past 120 plus years.

The leaky bucket land surface hydrological model used here can be described as following:

$$dw/dt = P - E - R - G \quad (1)$$

where  $w$  is total soil moisture,  $P$  observed precipitation,  $E$  evaporation,  $R$  runoff, and  $G$  loss to ground due to gravity impact.

There were some concerns (McRoberts *et al.* 2011) that the variance of the early time data produced (*i.e.* 1895 - 1930) may be too low and would be “different” from the data collected in late time. Our analysis (Fig. 1 and Fig. 2) shows that the data in the early period appears quite “normal” and the major features are quite similar to those in the late period. There is no surprising found in both the observed (precipitation and 2 meter temperature) data (not shown) and simulated data.

Comparing to observed precipitation and 2 meter temperature EOF analyses (not shown), the simulated soil moisture data has less noisy with lower frequency variations. By definition, land surface soil moisture or soil water is a direct indicator for agricultural drought, *i.e.* soil water deficiency. Based on the equation (1), it is the right side  $P-E-R-G$  (recharge or discharge) dictates the direction of drought intensification or drought improvement, not just  $P$  only. This will be addressed again in latter part of this study.

### 3. Long-term variations

The preliminary results (Figs. 2, 4, 5, 7) show that the major land surface hydrological extremes occurring in the past 12 decades were well captured by simulation in terms of severity, duration, and spatial distribution,

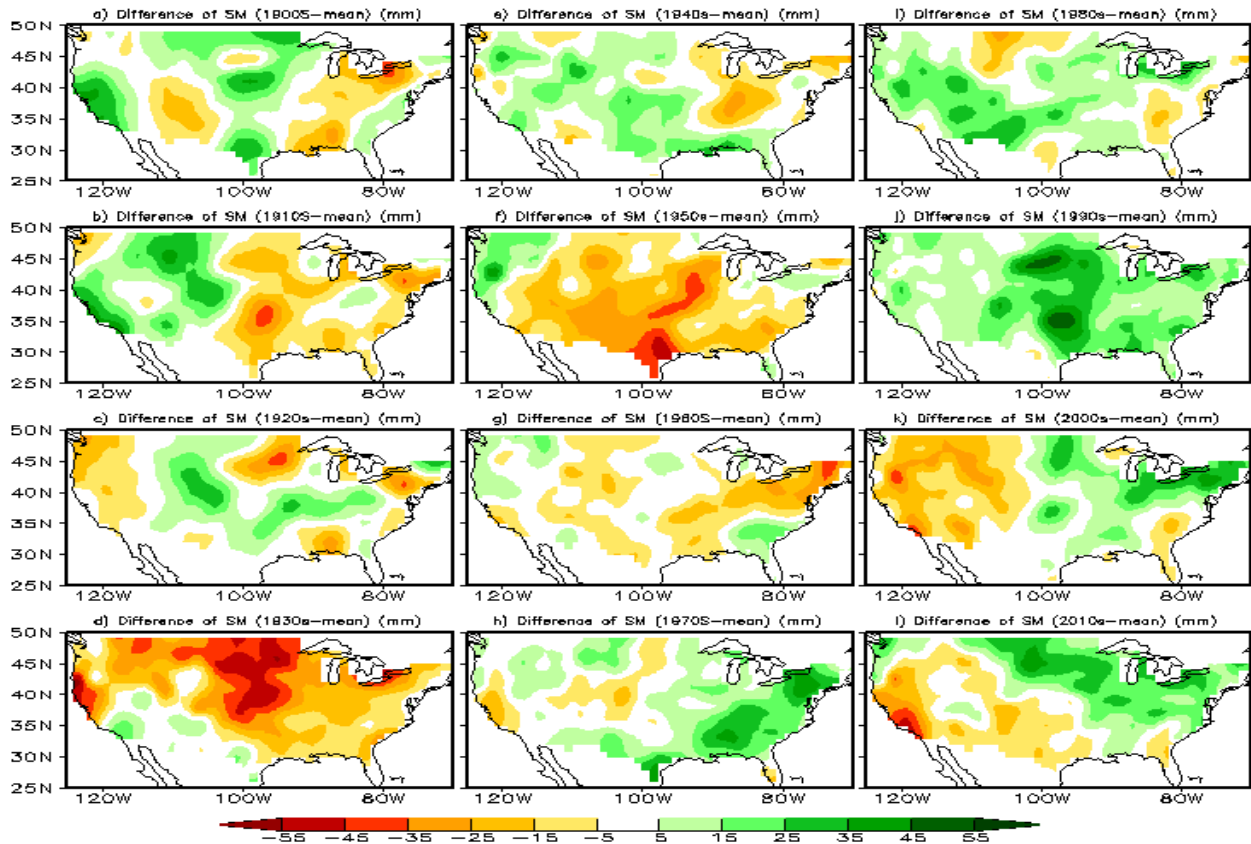


**Fig. 2** Decadal simulated land surface soil moisture anomaly variation from decade of 1900s (top left panel) to 2010s (bottom right panel).

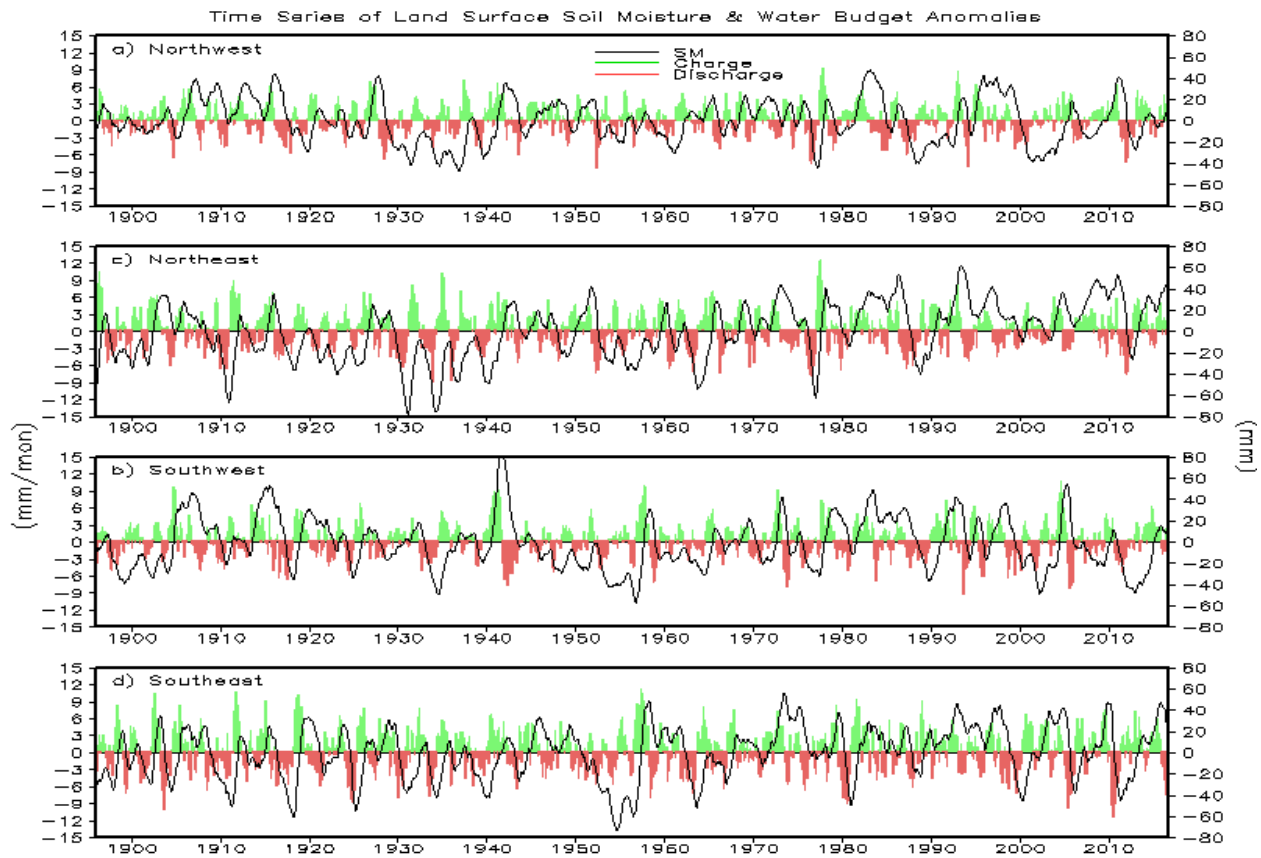


**Fig. 3** Land surface soil moisture anomalies (solid line, unit: mm) and soil water recharge/discharge (green/red shaded area, unit: mm/mon) for period of 1895-2017.

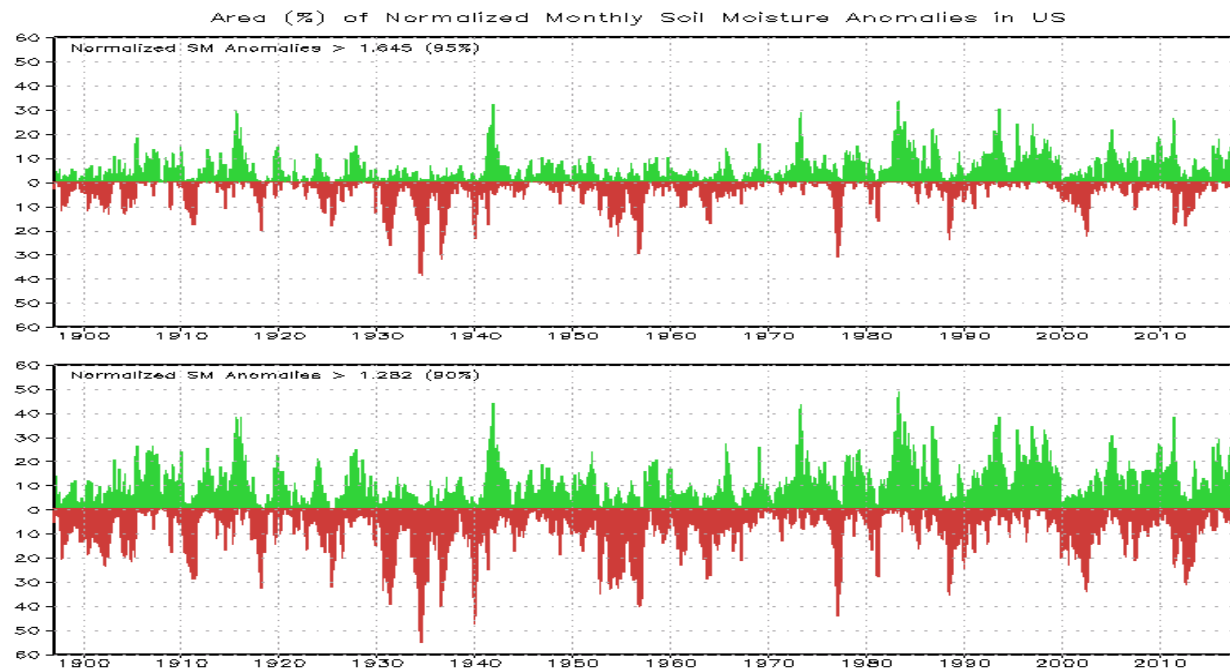


**Fig. 4** Time series of areas (%) covered by wet (green) and dry (red) extremes in period of 1895 to 2017.

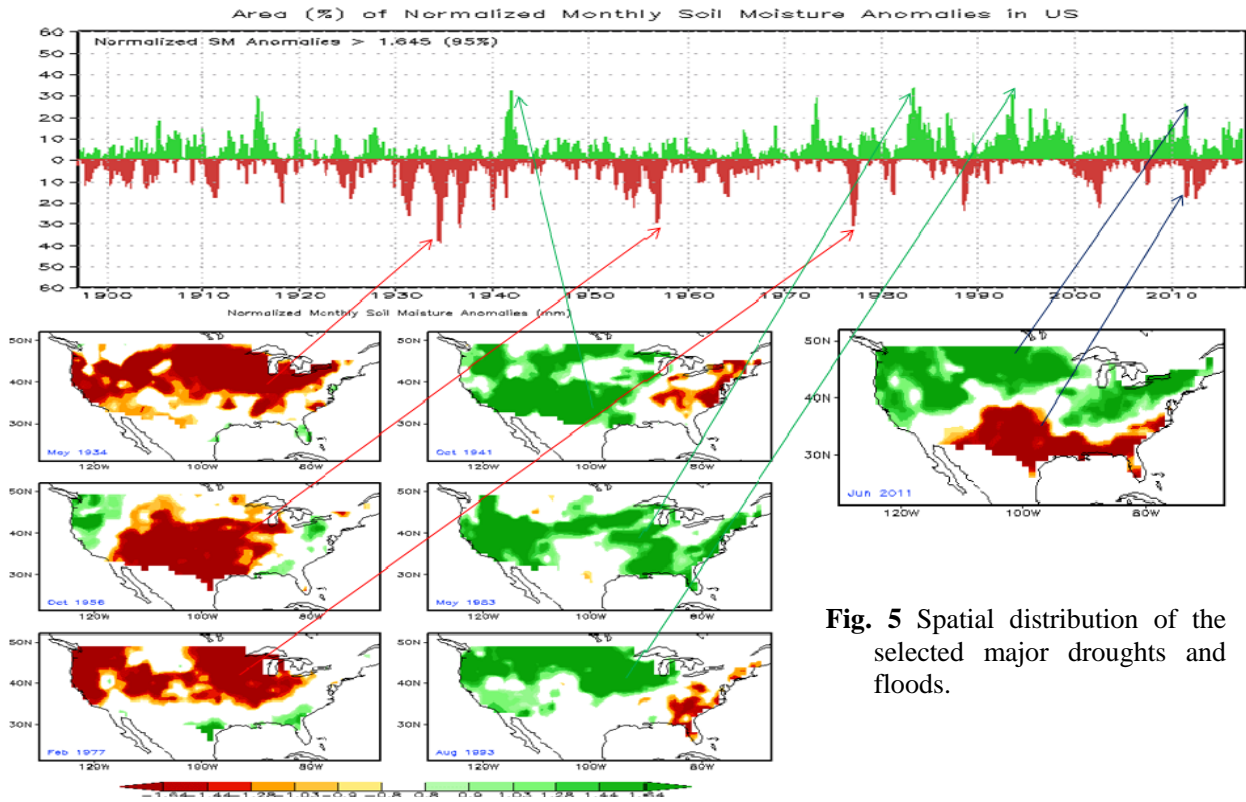


**Fig. 5** Spatial distribution of the selected major droughts and floods.

such as the decade-long major droughts (dust bowl era) in the 1930s in large parts of the US, multi-year severe droughts in the 1950s in the US (including the southern Great Plain), and big floods in the middle and northern Great Plains in 1993.

Compared to the EOF analyses of observed precipitation, observed 2 meter temperature, simulated evaporation, and runoff etc. (not shown), the variation of land surface soil moisture (Fig. 1) is largely driven by observed precipitation, but modulated clearly by other factors mentioned above. In order to explore this further, the equation (1) can be written as:

$$W(t+dt) = W(t) + \int (P - E - R - G) dt \quad (2)$$

where  $W(t+dt)$  is soil moisture at time  $t+dt$ ,  $W(t)$  is soil moisture at initial time  $t$ , and  $\int (P - E - R - G) dt$  is the integration of land surface water budget during  $dt$  period and can be viewed as land surface soil water recharge or discharge.

It is true that all kinds of droughts originate from a deficiency of precipitation or meteorological drought. However, precipitation is not the only factor to dictate the direction of land surface soil moisture (agricultural drought) variations. For example, even if it has rainfall somewhere, its soil moisture could decrease further if its evaporation is larger than the incoming precipitation. Figure 3 clearly shows that land surface soil moisture exactly goes up or down with the variation of recharge (green shaded areas) or discharge (red shaded areas). Land surface water storage change or soil moisture tendency  $W(t+dt) - W(t)$  is totally determined by land surface soil water recharge or discharge  $\int (P - E - R - G) dt$ , as it should be.

Therefore, the above results indicate that in order to predict either agricultural drought to intensify or improve more accurately, we need to predict land surface soil water recharge or discharge  $\int (P - E - R - G) dt$  more accurately.

#### 4. Dry/wet extremes in past 120+ years

There are many definitions for the hydrological extremes and different definitions focus on different aspects based on users. To some extent, some of them are somewhat arbitrary. The main interesting here is for



those severe land surface hydrological extremes which cover a large-scale spatial area and last long-term periods. These kind of extremes usually can bring devastating disasters to the human society and major disruption to earth's ecosystems. Here, a simple and objective definition for the percentage area covered by hydrological extremes is introduced as:

$$\begin{aligned} \text{Extreme Area (\%)} &= 100 \times (\text{extreme grids}) / (\text{Total grids}) \\ &= 100 \times (\sum (X - \mu)/sd) / (\text{Total Grids}) \end{aligned} \quad (3)$$

where  $\sum (X - \mu)/sd$  represents the total number of grids that the normalized soil moisture anomalies exceed certain thresholds, such as 1.9, 1.5, 1.2, 0.8 and 0.5, which mimic categories of the US official drought severity classification: D4, D3, D2, D1 and D0 (also see Fig. 7).

Figure 4 depicts time series of the simulated US wet/dry hydrological extremes for past 123 years. Many major drought and flood events are well captured, such as the famous 1930s dust bowl era, severe droughts in 1950s, and extreme floods in 1941, 1983 and 1993. The results also reveal that these major land surface hydrological extremes tend to cluster together and have relatively large-scale spatial patterns (Fig. 5). These large-scale patterns should be impacted by large-scale circulation anomalies and theoretically more predictable. It will be a nightmare for forecast if major droughts are small scale and spread everywhere.

To further understand the attributions of those major land surface hydrological extremes, the Extended Reconstructed Sea Surface Temperature (ERSST) dataset (Huang *et al.* 2014) was used to explore the origins of those major land surface hydrological extremes over the US for past 120 plus years. The results indicate that wet and dry extremes in the US tend to linearly relate to tropical SST anomalies (Fig. 6), with wet extremes more favoring positive SST anomalies in previous months, and dry extremes more favoring negative SST anomalies in previous months, especially for warm (growing) season.

Lastly, the time series of the drought percent areas over the continental US from the official US Drought Monitor (<http://droughtmonitor.unl.edu/Data/Timeseries.aspx>) was used as observation or ground truth to validate the simple and objective hydrological extreme area (%) index introduced in above.

The official US drought monitor started operation in 1999 and it provides a weekly map of the US drought conditions by multi-government agencies and universities. It is based on climatic, hydrologic, soil condition measurements and reports from various resources. Figure 7 depicts that the simple drought area index introduced here can reproduce major features of the official US drought index fairly well. The results also show the spatial distributions of corresponding droughts from the two methods are matched quite well (not shown).

## 5. Conclusion

The preliminary results show that there are significant decadal spatial-temporal variations of land surface hydrological extremes over the US, with clear long-term trend: warm trend over the western US and wet trend over the northeastern US.

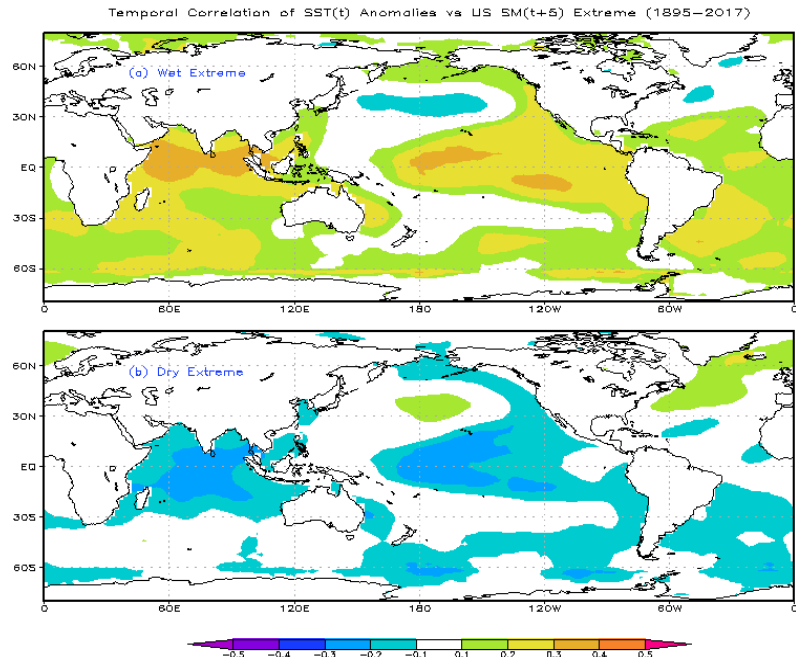


**Fig. 6** Temporal correlation of monthly US wet/dry extremes area index to previous 5 month global SST anomalies.

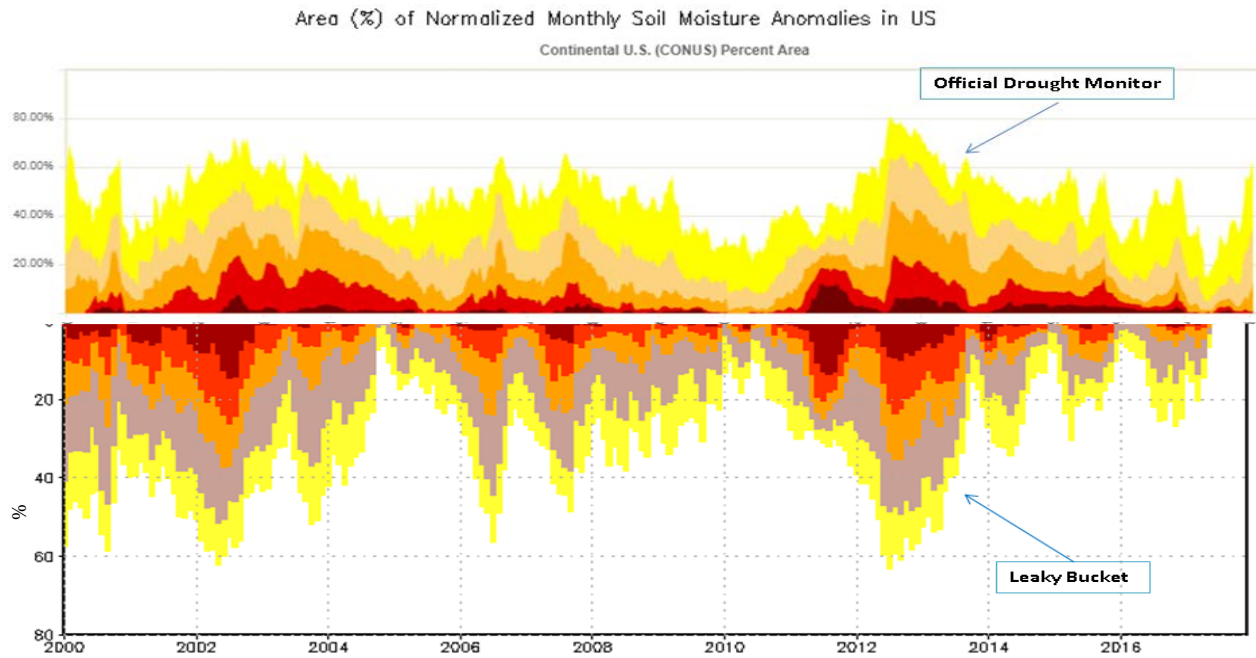


**Fig. 7** Time series of areas (%) covered by classified (D0 to D4, related yellow to dark red) droughts from the official US drought monitor (upper panel) and CPC Leaky Bucket model (lower panel) for period of 2000 to 2017.

Land surface wet/dry extremes over the US linearly response to the previous month(s) tropical cold/warm sea surface temperature anomalies, which provide a good predictor for forecasters. Usually, the major land surface hydrological extremes tend to cluster together with relatively large spatial scale and therefore they should potentially be more predictable from forecast point of view.

The results also show that land surface soil moisture variation exactly follows the variation of land surface water budget term. Therefore, in order to predict the variation of (agricultural) drought more accurately it needs to predict not only precipitation, but also every other component of the land surface water budget more accurately.

The simple and objective hydrological extreme area (%) index introduced in this study can very well reproduce the results from relatively complicated and somewhat subjective official US drought area index.

## References

- Huang, J., H. M. van den Dool, and K. P. Georgakakos, 1996: Analysis of model-calculated soil moisture over the United States (1931-1993) and applications to long-range temperature forecasts. *J. Climate*, **9**, 1350-1362.
- McRoberts, D. B., and J. W. Nielsen-Gammon, 2011: A new homogenized climate division precipitation dataset for analysis of climate variability and climate change. *J. Appl. Meteor. Climatol.*, **50**, 1187-1199, <http://dx.doi.org/10.1175/2010JAMC2626.1>
- Huang, B., V. F. Banzon, E. Freeman, J. Lawrimore, W. Liu, T. C. Peterson, T. M. Smith, P. W. Thorne, S. D. Woodruff, and H.-M. Zhang, 2014: Extended Reconstructed Sea Surface Temperature version 4 (ERSST.v4): Part I. Upgrades and intercomparisons. *J. Climate*, **28**, 911-930, doi:10.1175/JCLI-D-14-00006.1
- Vose, R. S., S. Applequist, M. Squires, I. Durre, M. J. Menne, C. N. Williams, C. Fenimore, K. Gleason, and D. Arndt, 2014: Improved historical temperature and precipitation time series for U.S. climate divisions. *J Appl. Meteor. Climatol.*, **53**, 1232-1251, <http://dx.doi.org/10.1175/JAMC-D-13-0248.1>

## Improving CPC's Handling of Long-term Temperature Trends

Stephen Baxter

Climate Prediction Center, NCEP/NWS/NOAA, College Park, MD

### 1. Introduction

It is well documented that CPC's seasonal temperature forecast skill derives largely from long-term warming trends over the United States (*e.g.* Peng *et al.* 2012). Most recently this was explored in a presentation at the 41<sup>st</sup> Climate Diagnostics and Prediction Workshop (Baxter 2017), wherein it was shown that CPC's deterministic seasonal forecast skill from 1995 to the present is not as good as a categorically warm forecast (a forecast where every grid cell is depicted as favoring temperatures in the upper tercile). Given this research result, it is imperative that CPC incorporate long-term trends as rigorously as possible and in a way that isolates long-term climatic changes from interannual and decadal variability. Indeed, analysis of climate variability on subseasonal to seasonal time scales is where CPC is uniquely adept.

Forecasting seasonal and subseasonal variability explicitly is where known skill is unclear. For example, the long-term Heidke skill score when above-normal is the favored forecast temperature category is near +30. However, the same skill score when below-normal is forecast falls all the way to +5. This, along with inspection of reliability diagrams, reveals a systemic cold bias in the official forecasts. To be sure this is counterintuitive considering that CPC outlooks do forecast above-normal temperatures more than the other two categories. It would be ideal to separate interannual and even decadal variability from long-term trends in order to better understand, and potentially improve, forecast skill related to various phenomena.

Two common forecast tools used to incorporate long-term trends are the linear trend and optimal climate normals (OCN). The latter is defined here as the running 15-year average temperature anomaly, which varies as a function of target season. OCN, as the name implies, generates forecast skill simply from the fact the base climatology used operationally (an aging 30-year fixed period) is inadequate, if one considers the point of a climatology to be providing your first-guess expectation at seasonal climate. The usefulness of an OCN forecast disappears if the base climatology is the OCN averaging period. Linear trends do not suffer from that shortcoming, but do suffer from the fact that variability other than long-term trends can easily be aliased into it, a characteristic shared by OCN as well. An alternative technique is introduced here, where the leading principal component of spatio-

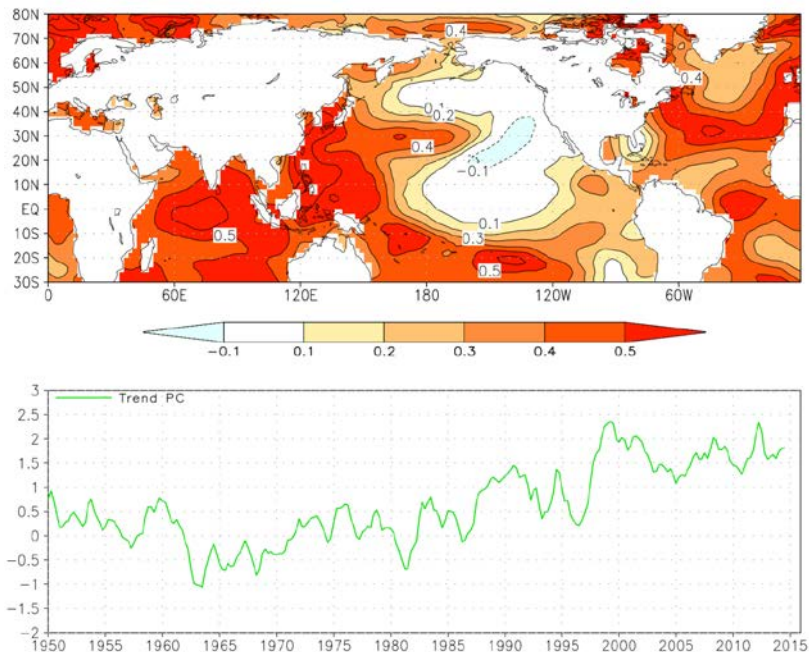


**Fig. 1** Top: Correlations of the 1<sup>st</sup> PC with ERSSTv4 data from 1950-2015. Contour interval is 0.1 with the zero contour omitted. Bottom: 1<sup>st</sup> PC is plotted from 1950-2015. A clear positive trend is notable.



temporal seasonal SST variability during the 20<sup>th</sup> century is used as the trend time series. This approach grounds the treatment of long-term trends in an important physical field within the context of other interannual and decadal variability.

## 2. Methods

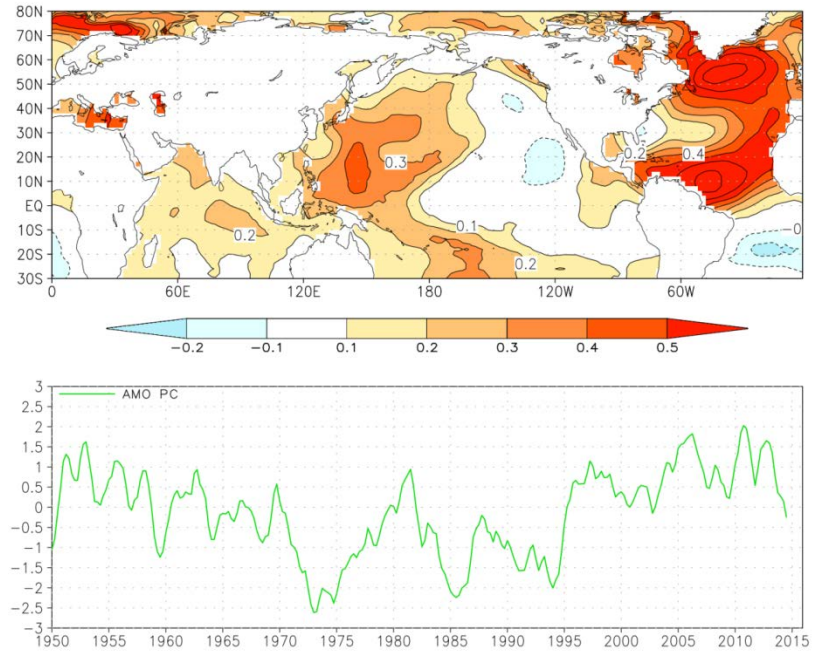
Linear trends, OCN, and regressions of the 1<sup>st</sup> PC of SST variability are used in reconstruction of seasonal temperature anomalies from 1965-2015. Temperature data is from the GHCN+CAMS dataset. The trend principal component is derived using rotated, extended EOF analysis of three-month, non-overlapping seasonal SST anomalies (Hadley SST data) from 1900-2015, following Guan and Nigam (2008). The domain of the analysis is 20oS-90oN, 0-360o. The nonstationary trend is the leading principal component, explaining 15.2% of the variance. North Atlantic decadal variability emerges as the 5<sup>th</sup> principal component; this plays some role in the low-frequency component of North American temperature anomalies.

Trends are calculated using least squares regression over the 1950-2015 period, and are used to reconstruct the seasonal temperature anomalies from 1965-2015. The PC reconstructions use a one year lag regression between the principal component and the target season. Regression analysis is performed over the 1950-2015 period, and anomalies are reconstructed for the 1965-2015 period. OCN is the average temperature anomaly over the previous 15 years for a given meteorological season, starting in 1965.

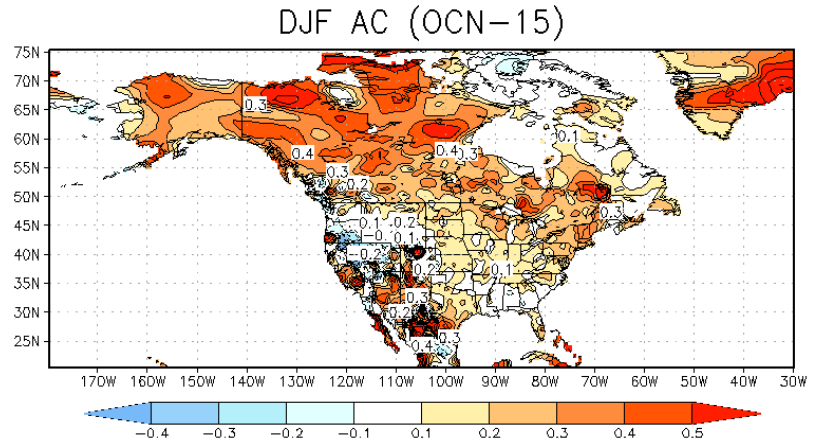
## 3. Results

Figure 1 shows correlations of the 1<sup>st</sup> PC with ERSSTv4 data over the 1950-2015 period, along with the associated time series. A clear but nonstationary trend is evident. Importantly, this trend is temporally independent of other canonical SST variability, including ENSO. Figure 2 is the same except for the 5<sup>th</sup> PC comprising Atlantic decadal variability, usually identified as the Atlantic Multidecadal Oscillation (AMO). While only the most recent 65 years are plotted in the time series, the decadal tendency is obvious.

For the sake of brevity, only meteorological winter is discussed here, though the analysis is complete for all four meteorological seasons with essentially the same results. Figure 3 shows the anomaly correlation between the OCN forecast anomalies and the observed anomalies over the 1965-2015 period. Positive



**Fig. 2** Same as Fig. 1, but for the 5<sup>th</sup> PC comprising decadal variability associated with the AMO.



**Fig. 3** Correlations between the OCN-based temperature reconstructions and observed temperature anomalies from 1965-2015 for northern winter. Contour/shading interval is 0.1 with the zero contour omitted.

correlations exist across northern North America including parts of the northern CONUS, while correlations are weak over much of the central and eastern CONUS. Anomaly correlations are notably high over much of Southwest, where temperature trends are known to be prominent. Figure 4 shows the same but for the linear trend reconstructions. Importantly, this is a largely data dependent reconstruction, so this should not be taken as forecast skill. The spatial structure is nearly identical to OCN, though the magnitude of the correlations is generally higher. The SST PC reconstruction (Fig. 5) contains nearly identical spatial structure as well, with magnitudes that are fairly close to those associated with the linear trend. Figures 6 and 7 show the difference in anomaly correlations between the analysis using the SST PC and OCN and linear trends, respectively. Here it is clear that the SST PC is better than the OCN reconstruction, but somewhat worse than the linear trend. The addition of the 5th PC (AMO) to the regression and reconstruction analysis eliminates all or most of that gap (Fig. 8).

Because of the similarity between long-term trends and the 1st PC in time, their similar correlation footprints are unsurprising. However, the SST-rooted analysis has the advantage of being able to discriminate between long-term trends and decadal variability, and does not risk any obvious ENSO aliasing. OCN by its nature does not actually yield predictive information about a nonstationary climate. This becomes obvious when one considers that the next year ought to be warmer than the previous 15 years when only considering secular climate warming.

#### 4. Conclusions

A time series corresponding to long-term trends is desirable especially when it is derived in the context of interannual and decadal variability. The use of SST in this regard is preferred given its usefulness as a slowly-varying boundary condition in seasonal climate prediction. Other physical fields could be explored in similar analyses, but the SST-rooted analysis is well-documented and physically robust.

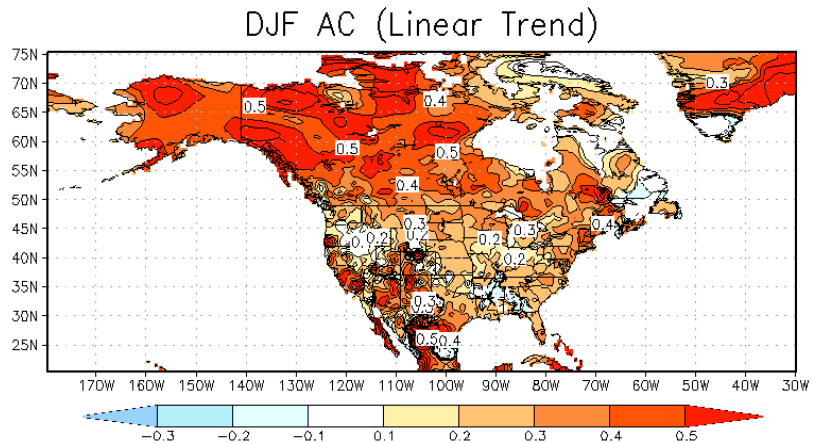


**Fig. 4** Same as Fig. 3, but for reconstructions using the linear trend.

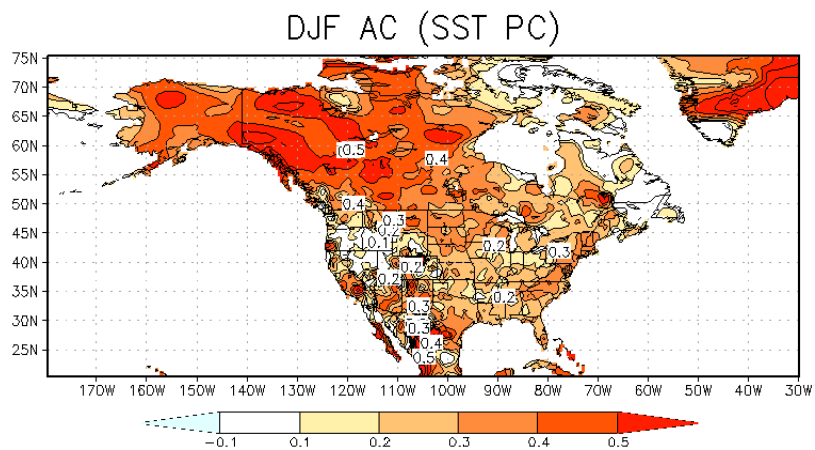


**Fig. 5** Same as Fig. 3, but for reconstructions using the 1<sup>st</sup> PC of spatio-temporal SST variability.

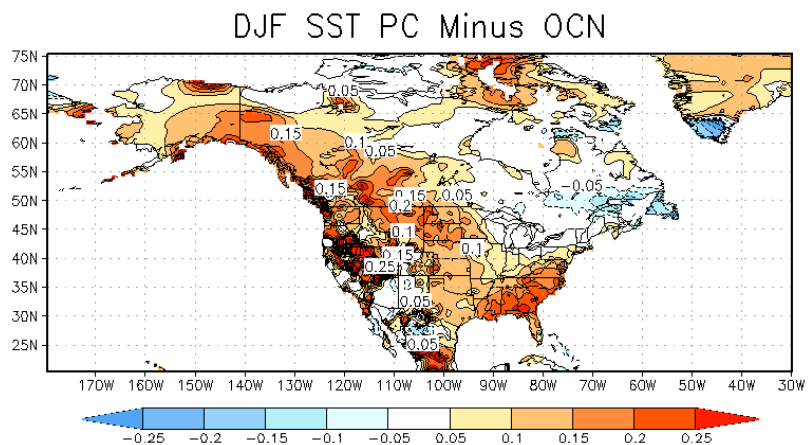


**Fig. 6** The difference between Fig. 5 and Fig. 3. Contour/shading interval is 0.05 with the zero contour omitted.



Linear removal of the 1<sup>st</sup> PC from statistical and dynamical forecast guidance can isolate interannual and decadal variability from long-term trends. In this way we can better attribute both observed and forecast climate anomalies. In light of this pilot analysis, next steps include an independent hindcast experiment and the extension to overlapping 3-month seasons. From that point forecasts of trend-based anomalies and associated probabilities can be made and used in the seasonal forecast process.

## References

- Baxter, S.: 2017. Evaluating CPC's operational seasonal temperature forecasts: Why aren't we beating a categorically warm forecast? *Climate Prediction S&T Digest, NWS Science and Technology Infusion Climate Bulletin Supplement, 41<sup>st</sup> NOAA Climate Diagnostics and Prediction Workshop*, Orono, ME, DOC/NOAA, 61-63, doi:10.7289/V5JS9NH0.
- Guan, B., and S. Nigam, 2008: Pacific sea surface temperatures in the twentieth century: An evolution-centric analysis of variability and trend. *J. Climate*, **21**, 2790–2809, doi:https://doi.org/10.1175/2007JCLI2076.1
- Peng, P., A. Kumar, M. S. Halpert, and A. Barnston, 2012: An analysis of CPC's operational 0.5 month lead seasonal outlooks. *Wea. Forecasting*, **27**, 898–917, doi:10.1175/WAF-D-11-00143.1.

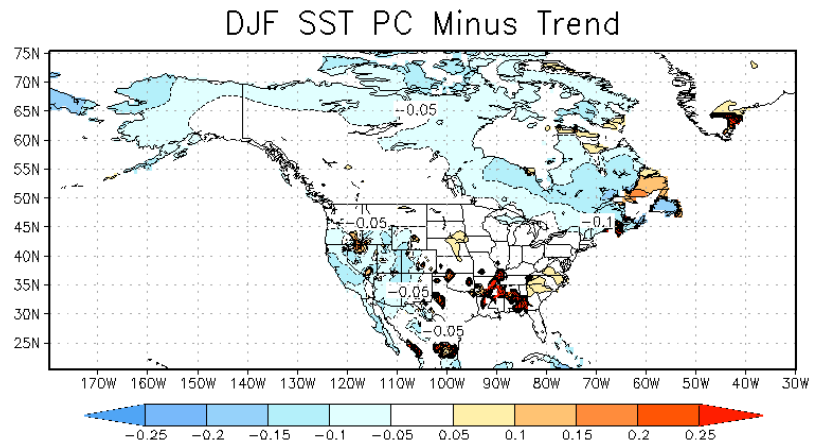


**Fig. 7** The difference between Fig. 5 and Fig. 4. Contour/shading interval is 0.05 with the zero contour omitted.

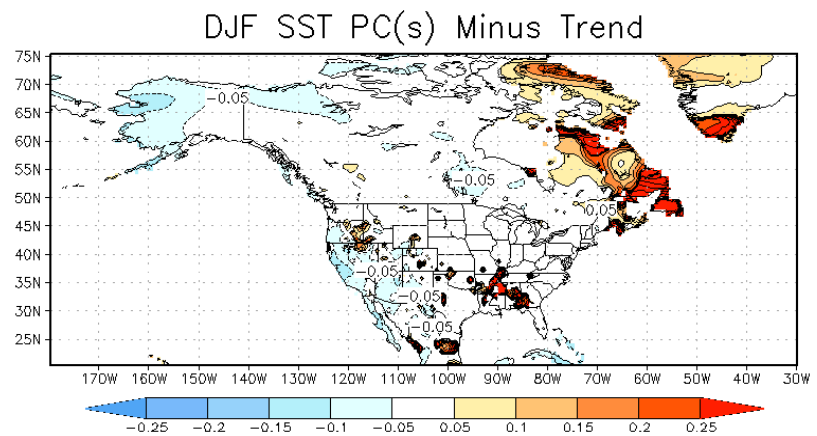


**Fig. 8** The difference between a reconstruction using the 1<sup>st</sup> and 5th PCs and Fig. 4. This shows the potential added benefit of including decadal variability.

## Drought Characteristics in Two Agro-Climatic Zones in Sub-Saharan Africa

Ayansina Ayanlade<sup>1,2</sup>, Maren Radeny<sup>2</sup>, John F. Morton<sup>3</sup>, and Tabitha Muchaba<sup>2</sup>

<sup>1</sup>Department of Geography, Obafemi Awolowo University, Ile-Ife, Nigeria

<sup>2</sup>CGIAR Research Programmed on Climate Change, Agriculture and Food Security (CCAFS),  
International Livestock Research Institute, Nairobi, Kenya

<sup>3</sup>Natural Resources Institute, University of Greenwich, Kent, United Kingdom

### 1. Introduction

The relationship between drought and loss of crops and livestock has long been known as an environmental challenge confronting agricultural production in many parts of Africa. Despite the great advancement of climate science in understanding and dealing with climate change and its impacts on the agricultural sector at the international and regional levels, awareness and the concern for the problem at local levels, especially among the rural farmers in Africa remains crucial. Most of the crops farming in Africa is rain-fed (Lobell *et al.* 2011; Ayanlade *et al.* 2017). Changing rainfall patterns will greatly affect both crop and livestock farming. In Nigeria for example, drought is not only main cause of crop loss but also leads to death of livestock in many parts of the country (Abaje *et al.* 2014; Tambo and Abdoulaye 2013). Thus, this study aims at examining the drought characteristics in two agro-climatic zones: Rainforest and Guinea savannah of Nigeria and assess the level of awareness and sensitivities of local farmers' to climate variability and change. The paper focuses on assessing the frequency and probability of prolonged dry spells over the period between 1984 and 2014, and the major coping strategies of smallholder farmers in both Rainforest and Guinea savannah agro-climatic zones of Nigeria. The study further identifies factors determining farmers' preference for selected adaptation strategies.

### 2. Methodology

The study area was divided into two agro-climatic zones: Rainforest and Guinea savannah agro-climatic zones of Nigeria. The Guinea savannah experiences precipitation of about 900-1200 mm per annum and the wet season lasts for 6 - 8 months, but much more in rainforest zone (Fig. 1). The climatic data were sourced from the archives of the Nigerian Meteorological Agency, Oshodi, Lagos over the period of 1984 to 2014. Qual-Quant research methods were used in this study. The data used were from four selected weather observatories stations; Iseyin, Shaki, Ibadan, and Osogbo. From this dataset, annual average rainfall and number of the rainy days were computed using RAINBOW software, which is designed to carry out hydro-meteorological frequency analyses and to test the homogeneity of climatic data. Questionnaires and focused group discussions were used to collect data on rural farmers' perception about the impacts of drought and their adaptation strategies used to cope during and after the extreme weather events. The study sites for household survey comprises of selected farming communities in southwestern Nigeria. The first segment of the household survey was conducted in the months of October and November of 2015, while the second segment was conducted in the months of May

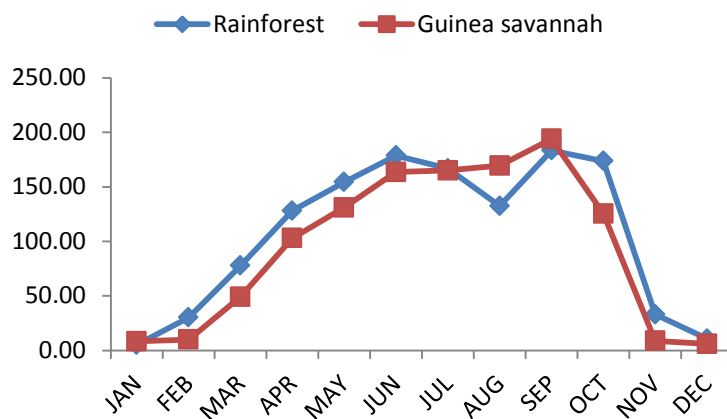


**Fig. 1** Rainfall patterns in the study area.

and June 2016. A total of 350 farmers belonged to the age group of 35-75 years were selected, using a multistage sampling method.

Drought characteristics were assessed using seasonal rainfall fluctuations and coefficient of variance (CV). The coefficient of variance statistics was calculated for rainfall amount (RA) and a number of rainy days (RD) with their T-test statistics were carried out to assess the significance of variation. Besides, the probability and the frequency of dry-spell occurrence, during the growing seasons, were estimated by considering the number of rainy days in the growing months. Any day with rainfall less than 0.3 mm was counted as a dry day.

The CV is measured as the relative variability of the rainfall amount and number of rainy days per month. It was calculated as the ratio of the standard deviation to the mean (average) for both RA and RD as in Equation 1,

$$CV = \frac{\delta_{RA/RD}}{\mu_{RA/RD}} * 100\% \quad (1)$$

where CV is the ratio of the standard deviation  $\delta_{(RA/RD)}$  to the mean  $\mu_{(RA/RD)}$  for both rainfall amount and number of rainy days. The probability and the frequency of dry spells, during the growing seasons were estimated. The probability that consecutive dry days would occur were established by considering the number of the days in the month and the total possible number of days in the growing seasons. Information about the coping strategies adopted by farmers and farmers' perception of drought was gathered through questionnaires and focus group discussions in the farming communities.

### 3. Results

The probabilities that dry spells exceed 3, 5, 10, and 15 consecutive days are much higher in the Guinea Savanna than in Rainforest zone (Fig. 2). Generally, the probabilities values of dry spells exceed the selected consecutive days are generally lower in rainforest agro-climatic zone compared to Guinea savanna agro-climatic zone. The results show a high probability that dry spells exceed 3 and 5 consecutive days during both growing seasons. In all stations, the probability that dry spells exceed 25 consecutive days is very low in all

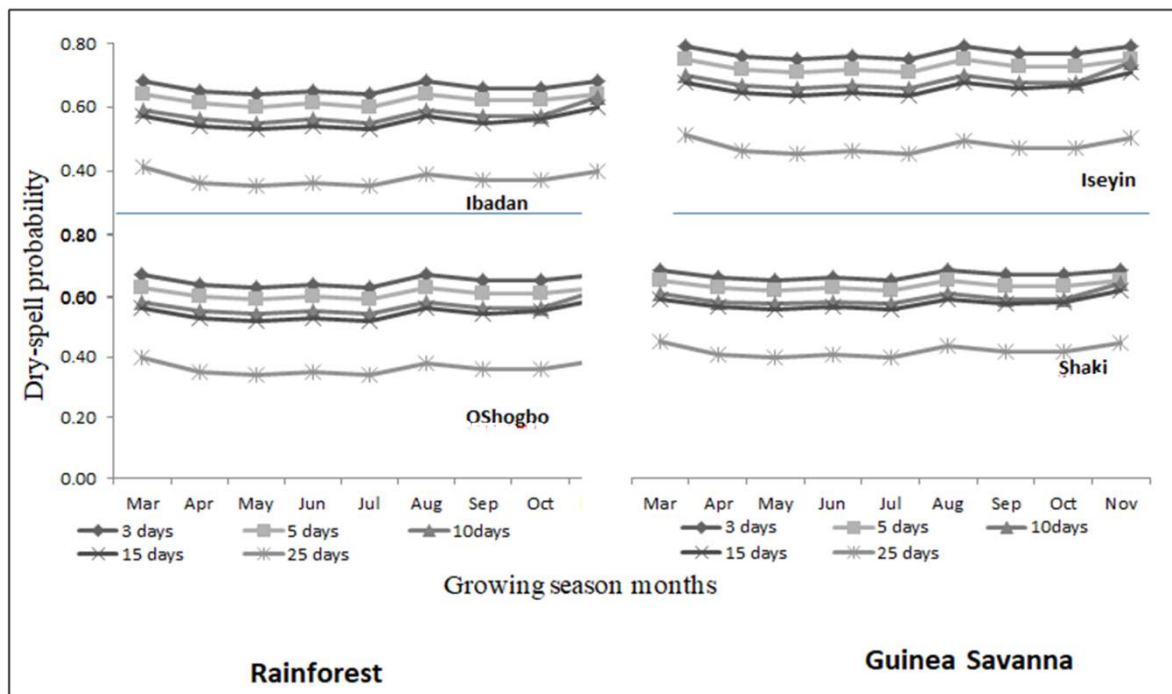


**Fig. 2** Probability of dry-spell exceeding 3, 5, 20, 15 and 25 consecutive days in growing seasons.

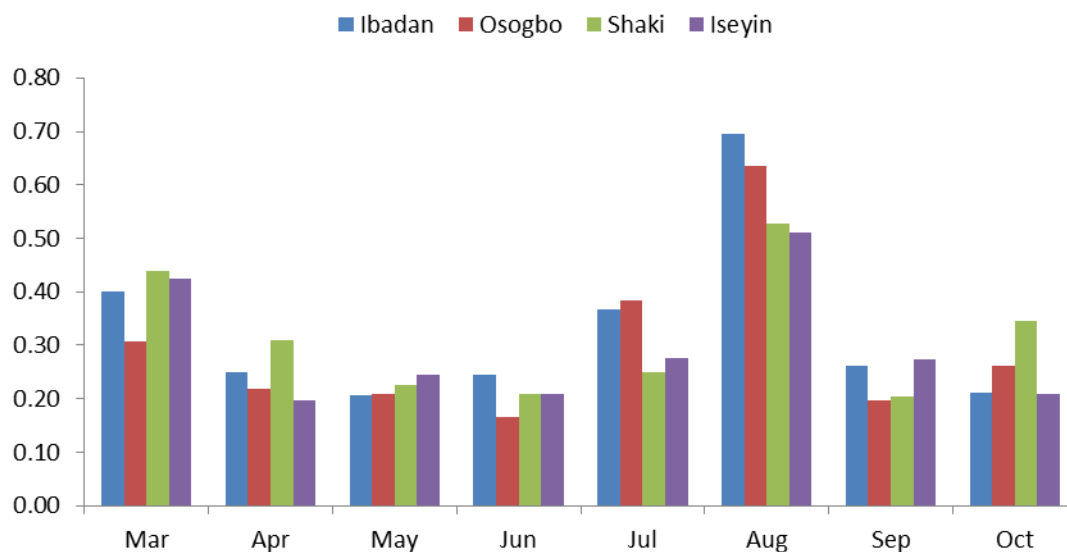


**Fig. 3** Coefficient of variation in rainy days (CV-RD) during growing seasons.

the stations with  $0.37 \leq p \leq 0.52$  (Fig. 2). These results denote that rainfall is much more reliable from the months of May till July in early growing season (EGS) but September in late growing season (LGS) for cropping.

Rainfall is much more reliable from the month of May until July with the coefficient of variance for rainy days less than 0.30, but less reliable in the months of March, August and October with CV-RD > 0.30, though CV-RD appears higher in the month of August for all the stations (Fig. 3). It is apparent that farmers' perceptions of drought fundamentally mirror climatic patterns from historical weather data. The results of the household survey show that farmers' perception of drought and extreme climate events mirror meteorological analysis. The majority of the farmers perceived that "rainfall onset, duration, and cessation have not been normal in the recent years" and they claim that "prolonged dry spell during growing seasons are now frequent in recent years". These sensitivities by farmers therefore, confirm the results from meteorological trend presented in the sections above. Though, the length of farming experiences has a significant relationship with farmers' perceptions of climate change adaptation strategies. Besides, many herders observed that "cattle health is now poor and the milk obtained from their cattle has reduced greatly, compared to several earlier centuries". In general, the "Fulani" pastoralists complained mostly about "the reduction of grazing grass and water for their cattle, though they move their cattle around for pasture".

#### 4. Summary and conclusions

This study examined drought characteristics during growing seasons in two agro-climatic zones of Nigeria and farmers perceptions of impacts and adaptation strategies. Most farmers had observed some prolonged dry spells within the months of March, April, and August, which affect their planting dates. This condition is worsened by marginally available financial resources and know-how for designing and implementing effective adaptation measures. In all the study sites, the farmers stated that "the planting dates were re-scheduled to the most suitable and favorable times for the crops to be planted". For instance, some crops are planted at the onset of rainfall, but in situations when rainfall is delayed, the planting date of the crop would be shifted to the time when the rain starts. It is apparent that farmers' perceptions of drought fundamentally mirror climatic patterns from historical weather data. However, farmers have adopted different strategies to cope with recurrent drought events in the study area. These strategies only partially compensated for the fact that agriculture would almost certainly have been better if the climate had kept constant. The facilities and equipment for adaptation should be provided at a subsidized price by the government, and that efforts should be made to develop crop varieties that can cope with the current conditions of climate change in Nigeria.

*Acknowledgements.* The authors thank the National Oceanic and Atmospheric Administration (NOAA) for financial support to present the initial draft of this paper at the 42nd Climate Diagnostics and Prediction Workshop in Norman, Oklahoma, USA. This study is part of Postdoctoral research funded by the Department for International Development (DFID) under the Climate Impact Research Capacity and Leadership Enhancement (CIRCLE) Visiting Fellowship Program. This research was hosted under CGIAR Research Program on Climate Change, Agriculture and Food Security (CCAFS), International Livestock Research Institute, Nairobi, Kenya.

## References

- Abaje, I., B. Sawa, and O. Ati, 2014: Climate variability and change, impacts and adaptation strategies in Dutsin-Ma local government area of Katsina State, Nigeria. *Journal of geography and Geology*, **6**, 103-112. doi:10.5539/jgg.v6n2p103
- Ayanlade, A., M. Radeny, and J. F. Morton, 2017: Comparing smallholder farmers' perception of climate change with meteorological data: A case study from southwestern Nigeria. *Weather and Climate Extremes*, **15**, 24-33. doi:10.1016/j.wace.2016.12.001
- Lobell, D. B., M. Bänziger, C. Magorokosho, and B. Vivek, 2011: Nonlinear heat effects on African maize as evidenced by historical yield trials. *Nature Climate Change*, **1**, 42-45. doi:10.1038/nclimate1043
- Tambo, J. A., and T. Abdoulaye, 2013: Smallholder farmers' perceptions of and adaptations to climate change in the Nigerian savanna. *Regional Environmental Change*, **13**, 375-388.



## **Probabilistic Drought Forecasts Based on the Northern American Multi-Model Ensemble (NMME)**

Li Xu<sup>1,2</sup> and Kingtse C. Mo<sup>1</sup>

<sup>1</sup>*Climate Prediction Center, NOAA/NWS/NCEP, College Park, MD*

<sup>2</sup>*Innovim, LLC, Greenbelt, MD*

### **1. Introduction**

In this study, we investigated a framework to predict drought probabilistically based on the precipitation forecast from Northern American Multi-model Ensemble (NMME). The total sixty ensemble members are selected from six NMME participated models for the study of meteorological drought forecast. The NMME precipitation forecasts are downscaled to the 0.5 degree CONUS grid and bias corrected with the Bias Corrected Spatial Disaggregation (BCSD) method. Then, the meteorological drought forecast based on the standardized precipitation index SPI6 (six months accumulation) are computed and converted to the corresponding drought categories. The grand mean (GM) index is tested to summarize the mean state of drought from the all NMME members. The probabilistic information for each drought category is measured by the concurrence at each ensemble member. The accumulated probabilities for drought categories are evaluated against observed drought events during 1982-2010 period. The results show the meteorological drought forecasts based on the NMME display robust skills over the climatological forecast at lead one to three months, indicated by both the Spearman rank correlation (Rho) and Rank Probability Skill Score (RPSS).

### **2. Challenges**

Frequent occurrences of drought in US had major societal, economical, and environmental impacts. Large differences exist in current operational drought forecasts by dynamical models, such as seen in NMME forecasts (Kirtman *et al.* 2014). The different forecasts may be able to identify a drought event, but the uncertainties are too large to classify the drought into a particular drought category Dx (x=0-4) (Mo 2008). And also, current forecast does not estimate the uncertainty thus not giving risk managers or decision makers the best or worst scenario information.

### **3. Data and methods**

We selected six representative models, i.e. CanCM3 model, CanCM4 model, GFDL\_FLOR model, NASA GEOS5 model, NOAA CFSv2 model and NCAR CCSM4 model, from the NMME historical archives. For each model we selected only 10 ensemble members which are closest to the forecast initial time (day 01 at each month). The hindcasts were run for every month from 1982 to 2010 (total 29 years), and the real-time forecasts from 2011 till recently.

The precipitation (P) forecast for lead 1-6 months are firstly downscaled to 0.5 degree CONUS grid. The downscaled P forecasts are then bias corrected by the BCSD method (Yoon *et al.* 2012) with leave-one-out cross-validation, which guarantees the target year is removed from the training pool to avoid the overfitting problem.

Six month accumulated standardized precipitation index (SPI6), as the forecast for meteorological drought with lead 1-6 months, are computed, using the corrected P forecast and the CPC unified P observations. The SPI6 forecasts from 60 ensemble members are then transferred from the normal distribution to the uniform distribution (percentile). Based on Table 1, the percentiles could be converted to the drought category Dx (x=0 to 4) defined by U.S. Drought Monitor.

**Table 1** The table used to convert drought conditions to corresponding drought categories.

Category	Drought cond.	SPI (SRI)	Percentile
D0	Anomaly Dry	-0.5 to -0.8	30% tile
D1	Moderate	-0.8 to -1.2	20% tile
D2	Severe	-1.3 to -1.5	10% tile
D3	Extreme	-1.6 to -1.9	5% tile
D4	Exceptional	-2 or less	2% tile

The sixty drought forecasts based on the percentile (uniform distribution) are averaged to the grand mean (GM) for the drought category Dx forecast. This percentile-mean method will reduce the “mean error” due to uneven distribution of SPI at “the long tail of normal distribution”, in particular for the extreme events, such as droughts. However, due to the offset effect (cancel out) of the arithmetic mean, the GM index will seriously underestimate the drought intensity (Mo and Lettenmaier 2014). We remapped the grand mean index again

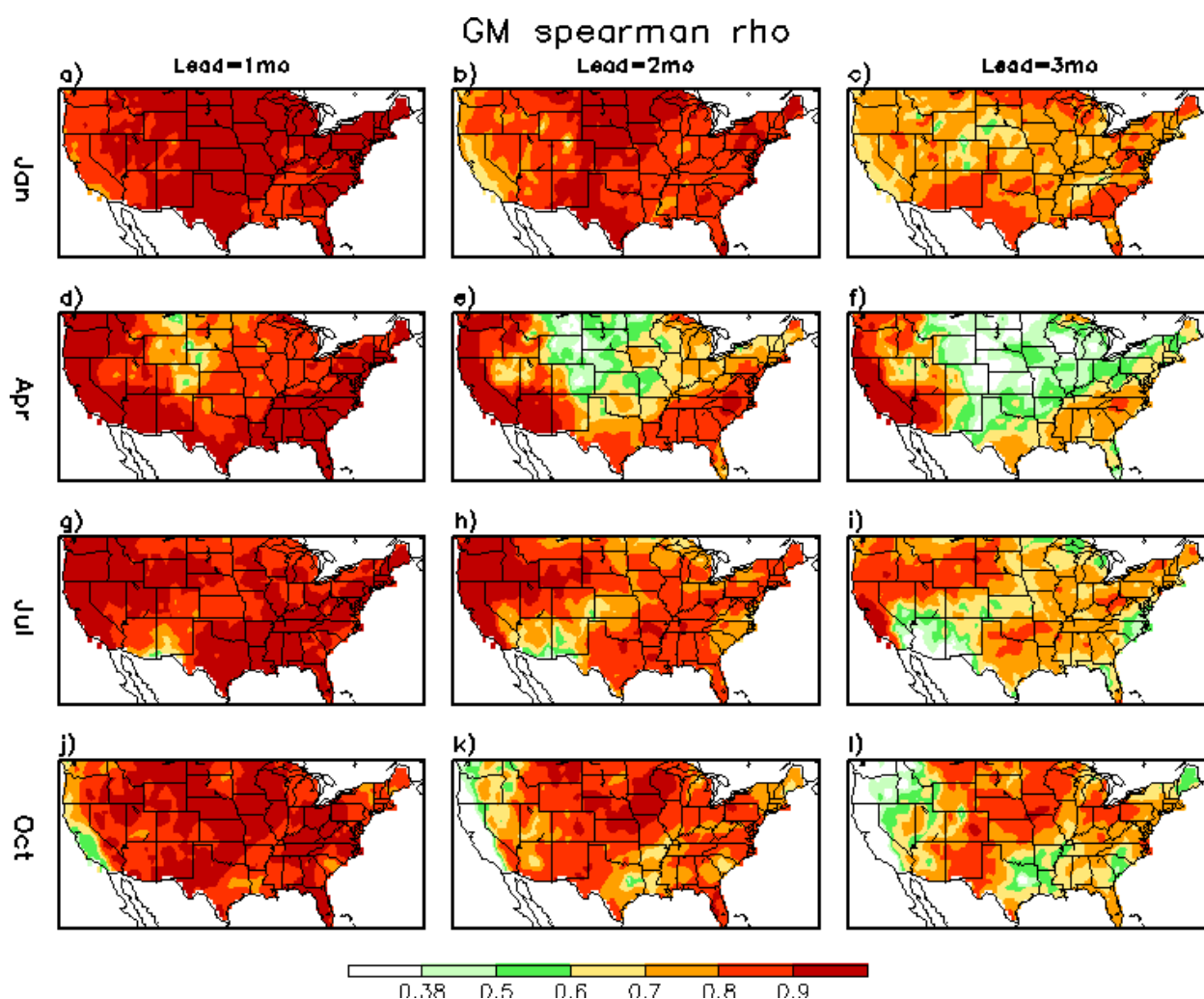


**Fig. 1** The Spearman rank correlation (rho) for the Grand Mean (GM) of drought index forecast with observation for January 01, April 01, July 01 and October 01 initial time (from top to bottom) during 1982–2010. The left, central and right columns are for the lead one, two and three months forecast, respectively.

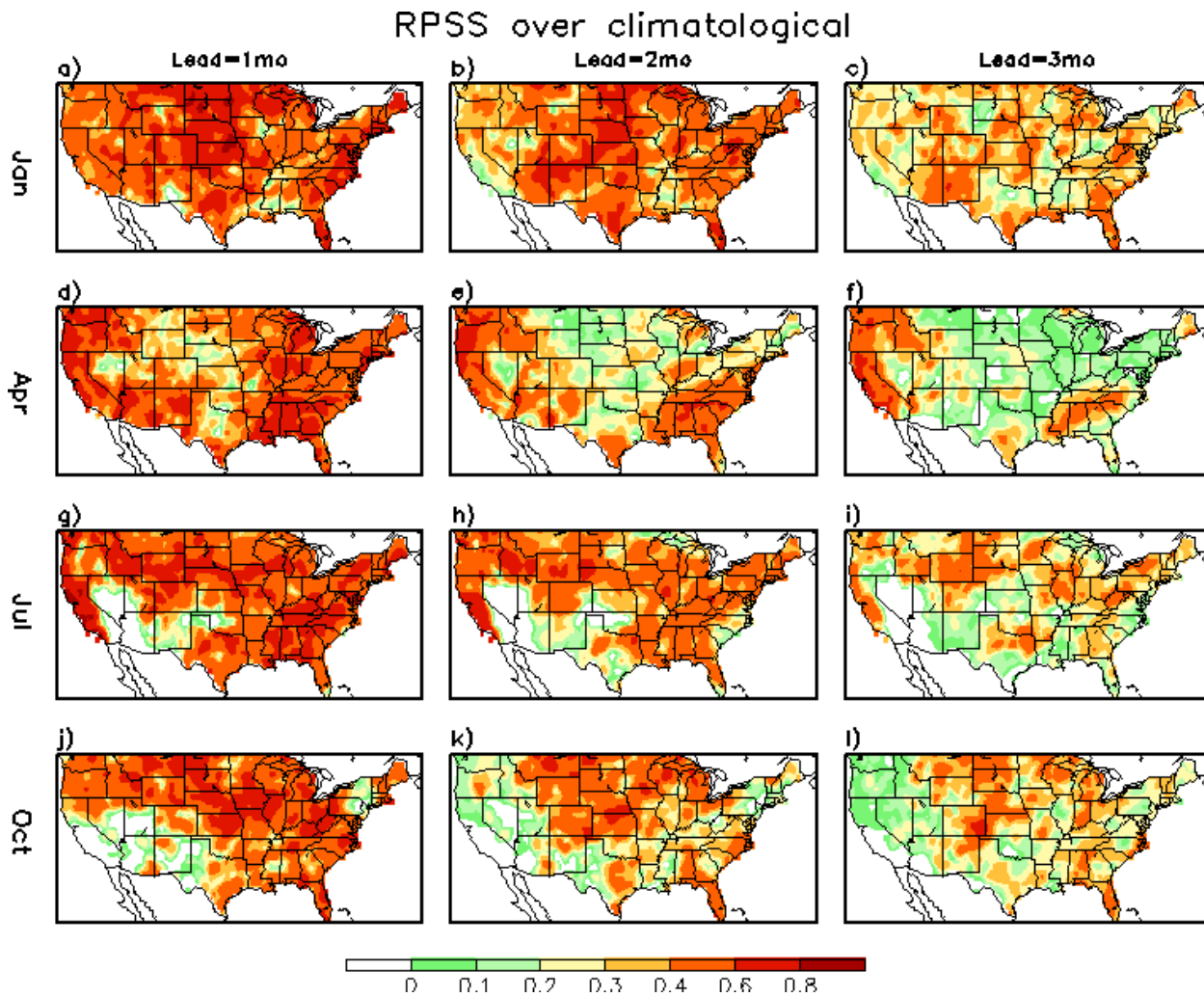


**Fig. 2** The same as Fig. 1 but for the RPSS over the climatological forecast.

to the uniform distribution based on the 29 year historical values.

The probabilistic information for each drought category  $D_x$  is measured by counting the concurrence of all sixty ensemble member. The accumulated probabilities for drought categories  $D_x$  are then evaluated against observed drought events during 1982-2010.

#### 4. Results

Observed drought events are defined by the SPI6 based on the observed rainfall from CPC unified Precipitation analyses. The rank correlation (Spearman Rho) is used to assess the GM index and Rank Probability Skill Score (RPSS) for the probabilistic forecast.

In general, the grand mean index has higher skill than individual member (figure not show). The skill of drought forecast is regional and seasonal dependent (Fig. 1). For the most regions, the rank correlation coefficients are high at lead 1-3 month, and gradually become insignificant after four months lead. The forecasts are skillful in the regimes where the initial condition dominates. Compared to the climatological forecast, the probabilistic forecasts display robust skills (Fig. 2). The skills could persist to the lead three months forecast at most US regions, but fading quickly after lead four months. The forecast skills are relative lower in spring and summer, compared with winter and fall seasons. The NMME tends to over-forecast droughts with large false alarm rate (figure not show).

---

*Acknowledgements.* This project is funded by NOAA Climate Program Office (CPO) Modeling, Analysis, Predictions, and Projections (MAPP) Program and National Integrated Drought Information System (NIDIS) grant.

## References

- Kirtman, B. P., and Coauthors, 2014: The North American Multimodel Ensemble Phase-1 seasonal-to-interannual prediction; Phase-2 toward developing intraseasonal prediction. *Bull. Amer. Meteor. Soc.*, **95**, 585-601.
- Mo, K. C., 2008: Model-based drought indices over the United States. *Journal of Hydrometeorology*, **9**, 1212-1230.
- Mo, K. C., and D. P. Lettenmaier, 2014: Objective drought classification using multiple land surface models. *Journal of Hydrometeorology*, **15**, 990-1010.
- Yoon, J.-H., K. Mo, and E. F. Wood, 2012: Dynamic-model-based seasonal prediction of meteorological drought over the contiguous United States. *Journal of Hydrometeorology*, **13**, 463-482.





# 6. SUBSEASONAL TO SEASONAL PREDICTABILITY

42<sup>nd</sup> NOAA Annual Climate Diagnostics and  
Prediction Workshop

23-26 October 2017, Norman, Oklahoma



## **An Assessment of Subseasonal Forecast Using Extended Global Ensemble Forecast System (GEFS)**

Yuejian Zhu<sup>1</sup>, Wei Li<sup>2</sup>, Eric Sinsky<sup>2</sup>, Hong Guan<sup>3</sup>, Xiaqiong Zhou<sup>2</sup>, and Dingchen Hou<sup>1</sup>

<sup>1</sup>*Environmental Modeling Center, NOAA/NWS/NCEP, College Park, Maryland*

<sup>2</sup>*IMSG at EMC, College Park, Maryland*

<sup>3</sup>*SRG at EMC, College Park, Maryland*

### **1. Introduction**

The National Oceanic and Atmospheric Administration (NOAA) is increasing its efforts to improve a numerical weather guidance for the sub-seasonal timescale. The National Centers for Environmental Prediction (NCEP) Climate Forecast System Version 2 (CFSv2; Saha *et al.* 2014) provides operational global numerical guidance at sub-seasonal and seasonal scales. Extending the NCEP Global Ensemble Forecast System (GEFS) to 35 lead days, however, enhances NCEP's subseasonal prediction capability since the GEFS has higher model resolution, a more frequent model upgrade cycle, improved stochastic physics perturbations and a larger ensemble size than the CFSv2.

In this study, four GEFS experiments (or configurations) are performed to help quantify the impacts of improved stochastic physics, boundary SST forcing and new scale-aware convective parameterization on sub-seasonal forecast skill for 500 hPa geopotential height and the Madden-Julian Oscillation (MJO). Furthermore, the impact of reforecast-based statistical post-processing on the sub-seasonal forecast skill of 2-m temperature is examined.

### **2. Methodology**

In this study, the GEFS integration is extended from 16 days to 35 days. For days 0-8 and 8-35, the GEFS has a spectral resolution of TL574 (approximately 34 km) and TL384 (approximately 52 km), respectively, with 64 hybrid vertical levels. The operational version of GEFS has 20 perturbation members and 1 control member. The initial perturbations are selected from the operational hybrid Global Data Assimilation System (GDAS) 80-member Ensemble Kalman Filter (EnKF; Whitaker *et al.* 2008, Wang *et al.* 2013).

Of all four GEFS 35-day experiments, the control experiment (CTL) uses the same configuration as the operational GEFS (Zhou *et al.* 2017) except it is extended from 16 days to 35 days. The Stochastic Total Tendency Perturbation (STTP; Hou *et al.* 2008) scheme is used to represent the model uncertainty. The SST forcing in this experiment is initialized with the Real Time Global (RTG) SST analysis and damps to an analysis climatology at a 90-d e-folding rate (Zhu *et al.* 2017).

The second experiment replaces the STTP with the Stochastic Kinetic Energy Backscatter (SKEB; Shutts 2005), Stochastically Perturbed Parameterization Tendencies (SPPT; Buizza *et al.* 1999) and Stochastic Perturbed Humidity (SHUM; Tompkins and Berner 2008) schemes, collectively known as SPs, while keeping the boundary SST forcing unchanged. The third experiment uses SPs and replaces the operational configuration of the SST forcing with a bias corrected CFSv2 predictive SST, which considers the day-to-day evolving state of the SST with respect to lead time (Zhu *et al.* 2017). This particular kind of SST forcing is known as a "two-tiered SST". The first tier means the output is from a coupled model forecast while the second tier means that SST is prescribed to an uncoupled model. The fourth experiment uses SPs, updated SST and replaces the operational convection scheme with a new scale-aware convection scheme (Han *et al.* 2017). In addition to the experiments using an uncoupled forecast system, the current stage of the fully coupled CFSv2 is also compared to these four GEFS experiments. The CFSv2 consists of 4 members, but 12 lagged members are added so that the ensemble size is more consistent with GEFS.

These four experiments are each initialized every 5 days from May 1st, 2014 to May 26th, 2016. MJO is also evaluated from these four experiments using the traditional real-time multivariate (RMM) MJO index (WH index; Wheeler and Hendon 2004; Gottschalack *et al.* 2010). The MJO skill is calculated using the bivariate anomaly correlation between the forecast and analysis RMM1 and RMM2 (Lin *et al.* 2008; Li *et al.* 2018).

Near-surface variables such as 2-m temperature are challenging to forecast on subseasonal scales, since enhancing stochastic physics, SST and convection has minimal effect on improving the performance (Zhu *et al.* 2018). Therefore, 2-m temperature needs to undergo statistical post-processing (Guan *et al.* 2018). In this study, 11-member 2-m temperature reforecast data with the same configuration as the fourth experiment from 2011 to 2015 is used to calibrate 2016. The reforecasts within this period are initialized once per week with the Global Data Assimilation System (GDAS). A climatological mean forecast error calculated from this reforecast dataset is used to calibrate 2-m temperature (Guan *et al.* 2018). A 31-day window is used and centered on each day being considered to calculate the reforecast climatology (Guan *et al.* 2015; 2018).

### 3. Results

#### 3.1 500 hPa height forecast skill

Anomaly correlation is used to measure the potential skill of the 500 hPa geopotential height. For lead week 2 over the northern hemisphere, combining SPPT, SKEB and SHUM demonstrate an increase in the potential skill (Fig. 1). Updating the bias-corrected SST and the scale-aware convection scheme further enhances the anomaly correlation. Furthermore, all four GEFS experiments perform better than the CFSv2 over the northern hemisphere. Therefore, improving the representation of the stochastic physics, SST and convection in GEFS outperforms the current stage of CFSv2.

#### 3.2 MJO forecast skill

MJO is the dominant mode in sub-seasonal variability in tropics. As such, the performance of the MJO in the forecast system is evaluated. The MJO skill over the 2-year period shows that SPs outperforms STTP

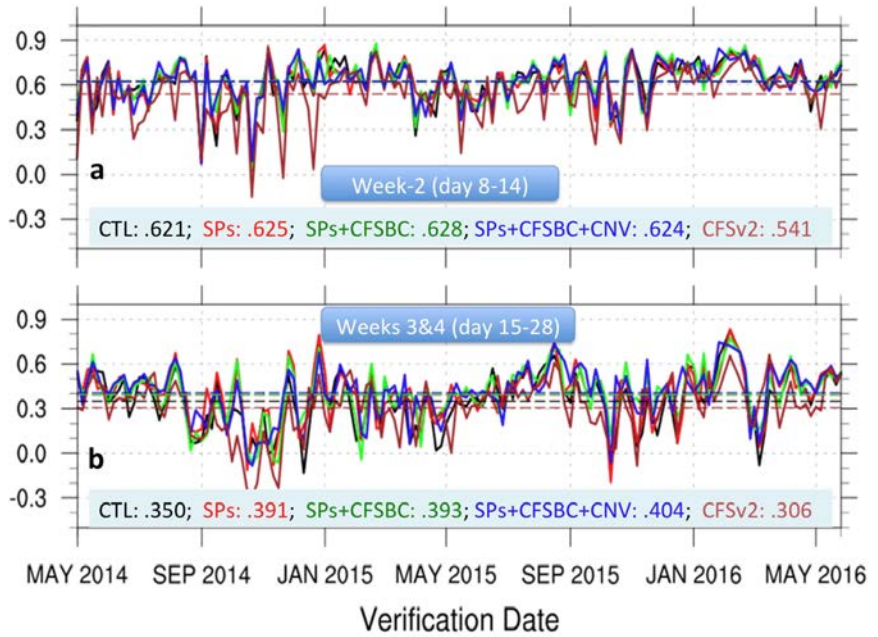


**Fig. 1** Pattern Anomaly Correlation (PAC) for Northern Hemisphere 500 hPa geopotential height for lead (a) week 2 and (b) weeks 3&4. CTL is black, SPs is red, SPs+CFSBC is green, SPs+CFSBC+CNV is blue and CFSv2 is brown with period average PAC scores for each configuration (numbers in the bottom of each plot with different color).

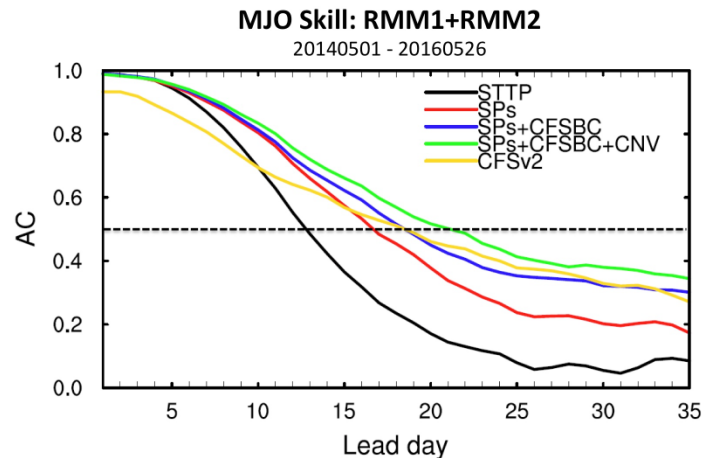


**Fig. 2** MJO forecast skill as a function of lead time for the period of May 1st, 2014 to May 26th, 2016.

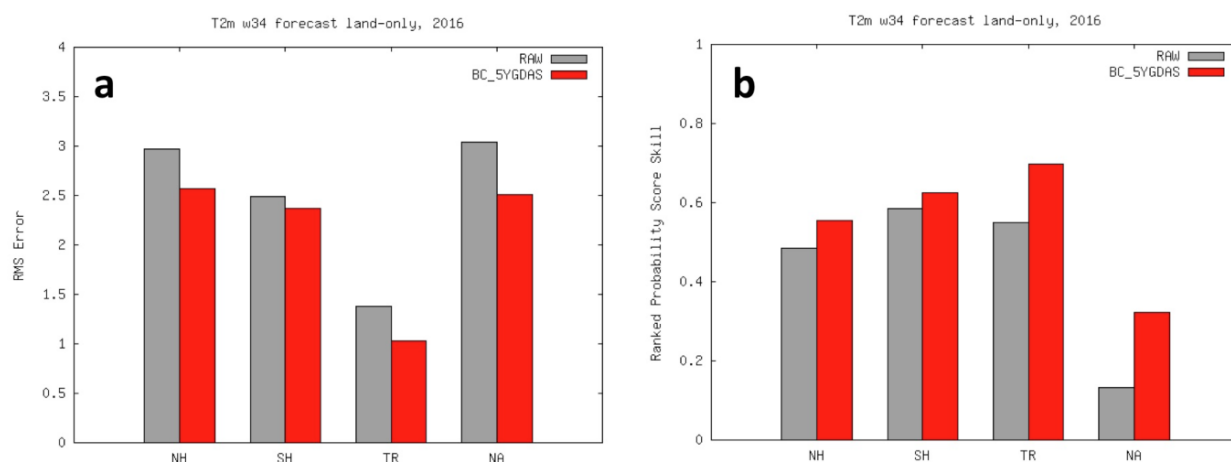


**Fig. 3** Raw (grey) and calibrated (red) regional 2-m temperature (a) RMS Error and (b) RPSS. (a,b) are averaged temporally and spatially over a 1-year period and over each region (land only) for weeks 3&4, respectively.

(CTL; Fig. 2). The CTL and SPs remain to have a skillful MJO forecast for 12.5 lead days and 16.8 lead days, respectively ( $AC \geq 50\%$ ). Adding a bias-corrected SST to SPs reaches a skill around 19 days. When combining SPs, the bias-corrected SST and the scale-aware convection, the MJO skill of SPs+CFSBC+CNV (21.5 days) exceeds the MJO skill of CFSv2 (19 days).

### 3.3 2-m temperature calibration

Calibrating the 2-m temperature using the reforecast bias method shows substantial improvement over all domains (land only) for the week 3-4 lead time (Fig. 3). The North America (land only) RMS error and RPSS (Ranked Probabilistic Skill Scores) benefit the most from the calibration. These improvements in 2-m temperature demonstrate the importance of using reforecast information for calibration.

## 4. Summary

The NCEP GEFS has been extended from 16 to 35 days to predict sub-seasonal timescales. It has been found that improving the stochastic physics perturbations, using a predictive SST and a scale-aware convection scheme substantially improves the extra-tropics forecast and MJO skill for the sub-seasonal scales, without degradation of weather forecast. The GEFS has also outperformed the CFSv2 in the extratropical and MJO skill.

Although updating the model configuration improves 500 hPa height and MJO prediction, surface variables such as 2-m temperature require statistical postprocessing in order to be significantly improved. In this study, reforecast information is used to calibrate 2-m temperature. The fourth configuration generally has the best performance, and therefore is used for the extended GEFS forecast configuration with 18 years hindcast to support the SubX project. It has been found that using the GEFS reforecast information for bias correction has greatly improved the 2-m temperature, which demonstrates the high value of using reforecast information for calibration.

**Acknowledgements.** The authors would like to thank all of helps from EMC ensemble team members, and Drs. Xingren Wu, Wanqiu Wang, Jongil Han, Xu Li and Ruiyu Sun at EMC (and CPC) for valuable discussion pertaining to the design our experiments. This study is partially supported through NWS OSTI and NOAA's Climate Program Office (CPO)'s Modeling, Analysis, Predictions, and Projections (MAPP) program.

## References

Buizza, R., M. Miller, and T. Palmer, 1999: Stochastic representation of model uncertainties in the ECMWF ensemble prediction system. *Q. J. R. Meteor. Soc.*, **125**, 2887-2908, doi: 10.1002/qj.49712556006.

- Gottschalck, J., and Coauthors, 2010: A framework for assessing operational Madden-Julian oscillation forecasts: A CLIVAR MJO working group project. *Bull. Amer. Meteor. Soc.*, **91**, 1247-1258, doi:10.1175/2010BAMS2816.1.
- Guan, H., B. Cui, and Y. Zhu, 2015: Improvement of statistical postprocessing using GEFS reforecast information. *Wea. Forecasting*, **30**, 841-854, doi: 10.1175/WAF-D-14-00126.1.
- Guan, H., Y. Zhu, E. Sinsky, W. Li, X. Zhou, D. Hou, C. Melhauser, and R. Wobus, 2018: Systematic error analysis and calibration of 2-m temperature for the NCEP GEFS reforecast of SubX Project, Submit to *Mon. Wea. Rev.* (in process).
- Han, J., W. Wang, Y. C. Kwon, S. Y. Hong, V. Tallapragada, and F. Yang, 2017: Updates in the NCEP GFS cumulus convection schemes with scale and aerosol awareness. *Wea. Forecasting*, **32**, 2005-2017, doi: 10.1175/WAF-D-17-0046.1.
- Hou, D., Z. Toth, Y. Zhu, and W. Yang, 2008: Evaluation of the impact of the stochastic perturbation schemes on global ensemble forecast. *Proc. 19th Conf. on Probability and Statistics*, New Orleans, LA, Amer. Meteor. Soc.  
[Available online at <https://ams.confex.com/ams/88Annual/webprogram/Paper134165.html>.]
- Li, W., Y. Zhu, X. Zhou, D. Hou, E. Sinsky, C. Melhauser, M. Pena, H. Guan, and R. Wobus, 2018: Evaluating the MJO forecast skill from different configurations of NCEP GEFS extended forecast. Submitted to *J. Climate* (in process).
- Lin, H., G. Brunet, and J. Derome, 2008: Forecast skill of the Madden-Julian oscillation in two Canadian atmospheric models, *Mon. Wea. Rev.*, **136**, 4130-4149.
- Saha, S., and Coauthors, 2014: The NCEP Climate Forecast System version 2. *J. Climate*, **27**, 2185-2208, doi: 10.1175/JCLI-D-12-00823.1.
- Shutts, G., 2005: A kinetic energy backscatter algorithm for use in ensemble prediction systems. *Q. J. R. Meteor. Soc.*, **131**, 3079-3102, doi: 10.1256/qj.04.106.
- Tompkins, A. M., and J. Berner, 2008: A stochastic convective approach to account for model uncertainty due to unresolved humidity variability. *J. Geophys. Res.*, **113**, D18101, doi: 10.1029/2007JD009284.
- Wang, X., D. Parrish, D. Kleist, and J. Whitaker, 2013: GSI 3DVar-based ensemble-variational hybrid data assimilation for NCEP Global Forecast System: Single-resolution experiments. *Mon. Wea. Rev.*, **141**, 4098-4117, doi: 10.1175/MWR-D-12-00141.1.
- Wheeler, M.C., and H. H. Hendon, 2004: An all-season real-time multivariate MJO index: Development of an index for monitoring and prediction. *Mon. Wea. Rev.*, **132**, 1917-1932, doi: 10.1175/1520-0493(2004)132<1917:AARMMI>2.0.CO;2.
- Whitaker, J., T. Hamill, X. Wei, Y. Song, and Z. Toth, 2008: Ensemble data assimilation with the NCEP Global Forecast System. *Mon. Wea. Rev.*, **136**, 463-482, doi: 10.1175/2007MWR2018.1.
- Zhou, X., Y. Zhu, D. Hou, Y. Luo, J. Peng, and R. Wobus, 2017: Performance of the new NCEP Global Ensemble Forecast System in a parallel experiment. *Wea. Forecasting*, **32**, 1989-2004, doi: 10.1175/WAF-D-17-0023.1
- Zhu, Y., X. Zhou, M. Pena, W. Lei, C. Melhauser, and D. Hou, 2017: Impact of sea surface temperature forcing on weeks 3 and 4 forecast skill in the NCEP Global Ensemble Forecasting System. *Wea. Forecasting*, **32**, 2159-2174, doi: 10.1175/WAF-D-17-0093.1.
- Zhu, Y., X. Zhou, W. Li, D. Hou, C. Melhauser, E. Sinsky, M. Pena, B. Fu, H. Guan, W. Kolczynski, R. Wobus, and V. Tallapragada, 2018: An assessment of subseasonal forecast skill using an extended Global Ensemble Forecast System (GEFS). Submitted to *J. Climate* (in process).



## Investigating the Potential for Seasonal Snowfall Forecasts at CPC

Stephen Baxter

*Climate Prediction Center, NCEP/NWS/NOAA, College Park, MD*

### 1. Introduction

CPC currently issues probabilistic temperature and precipitation forecasts for 3-month overlapping seasons for the upcoming 13 seasons. Seasonal snowfall forecasts are not explicitly issued, though CPC's website contains seasonal snowfall composites based on the phase of ENSO for overlapping 3-month seasons. Seasonal snowfall accumulation is an important variable over much of the CONUS; in the western U.S. snowfall is closely monitored due to its hydrological importance as well as impacts on winter tourism. Farther east there is interest in the broader impact of seasonal snowfall on economic productivity and related issues. A seasonal snowfall outlook by CPC could satisfy forecast needs for stakeholders ranging from water managers and agricultural interests to industry and the general public. A recently published data set (Kliver *et al.* 2016) provides gridded daily snowfall accumulation data from 1900 to 2009. Using the data from 1950-2009, we investigate whether seasonal snowfall accumulation might be predictable over the U.S.

### 2. Methods

Kliver *et al.* (2016) details a new gridded daily snowfall data set. We use this data at  $1^\circ \times 1^\circ$  resolution for the extended cold season spanning from October through April. (The analysis presented here was repeated using the peak winter months of December-February with little change in the results.) The October-April seasonal snowfall data is subject to a square-root correction to bring it closer to a normal distribution prior to analysis. For temperature and precipitation data we use the GHCN+CAMS data set and the gridded CPC precipitation reconstruction data set, respectively, each at the same  $1^\circ \times 1^\circ$  resolution. Sea surface temperature (SST) data is taken from the ERSSTv4 data set at  $2^\circ \times 2^\circ$  resolution.

Prediction of the seasonal snowfall can be approached in two ways: using snowfall explicitly as the predictand in

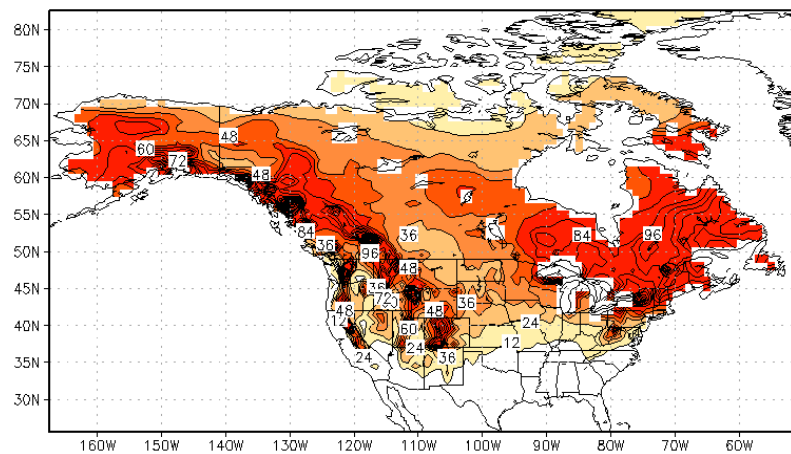


**Fig. 1** Snowfall climatology (Oct-Apr) over North America from the winter of 1950-51 to 2008-09. Contour and shading interval is 12 inches, starting at 12 inches.

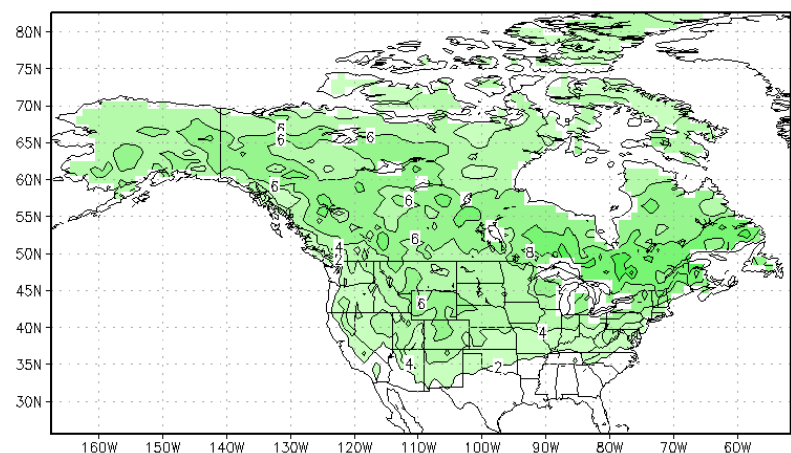


**Fig. 2** Ratio of the mean to standard deviation (Oct-Apr) in the square-root adjusted data. Contour and shading interval is 2, starting at 2. Areas where this ratio is less than 2 are masked out in subsequent figures.

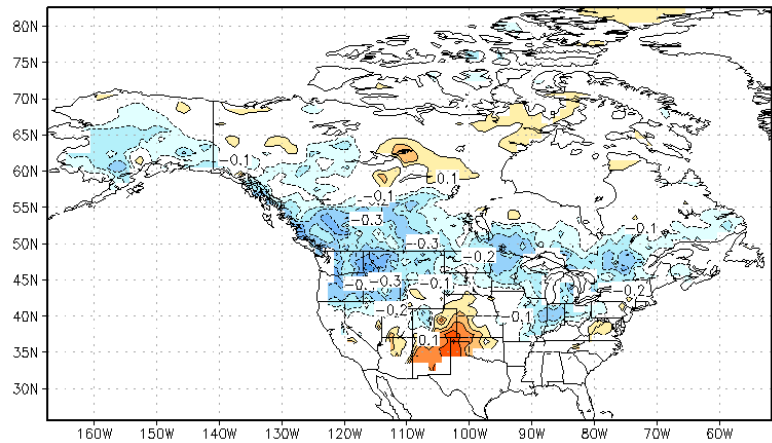
an empirical (or dynamical) forecast tool or statistically specifying seasonal snowfall using the forecast seasonal temperature and precipitation fields. Ultimately, a combination of these approaches might be pursued. In the case of the former, trends and ENSO are two predictors that we can use to explicitly predict seasonal snowfall. For trends we use a linear least-squares fit, and for ENSO we use a Niño 3.4 index calculated from the ERSST data over the 1950-2009 period. For seasonal specification, we use the temperature and precipitation data at seasonal resolution to construct point-by-point correlation maps related seasonal snowfall to temperature and precipitation, respectively.

Finally, EOF analysis of the North American seasonal snowfall anomalies is performed. The goal here is to see if the leading patterns of seasonal snowfall variability are related to known climate drivers. This will be assessed by regression the leading principal components onto time-lagged SST anomaly fields.

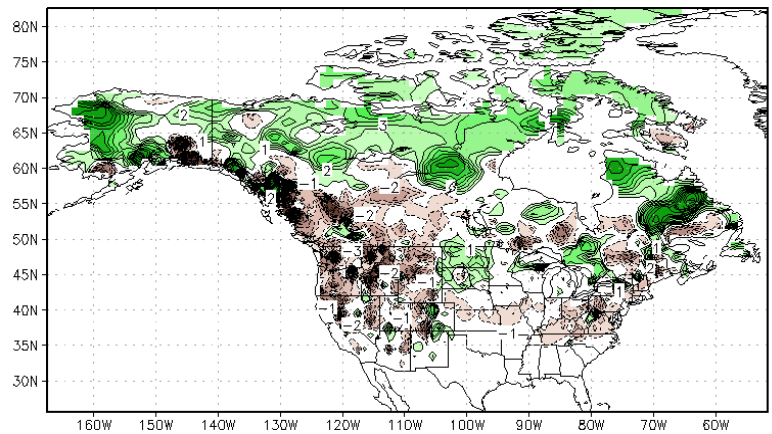
### 3. Results

Figure 1 shows the October-April climatology. The extended cold season mean snowfall values look very reasonable across North America from the gridded data set. Across parts of the West Coast and southern tier of the CONUS, the climatology is small. Using the square-root adjusted data, the ratio of the mean to the standard deviation is plotted (Fig. 2). A threshold of 2 is used here to identify areas where there is enough seasonal snowfall relative to the variance to yield a well-behaved distribution. In subsequent figures this value is used as mask to eliminate areas where seasonal snowfall forecasts may be ill-posed. This threshold, however, may be changed based on stakeholder feedback.

ENSO relationships (shown in Fig. 3) are strongest in the western U.S., with El



**Fig. 3** Linear correlation coefficient between Niño 3.4 (calculated from the ERSSTv4 dataset) and seasonal snowfall (1950-2008). Contour/shading interval is 0.1 with the zero line omitted.



**Fig. 4** Linear trend of seasonal snowfall in inches per decade (1950-2008). Contour/shading interval is 1 in/dec with the zero line omitted.

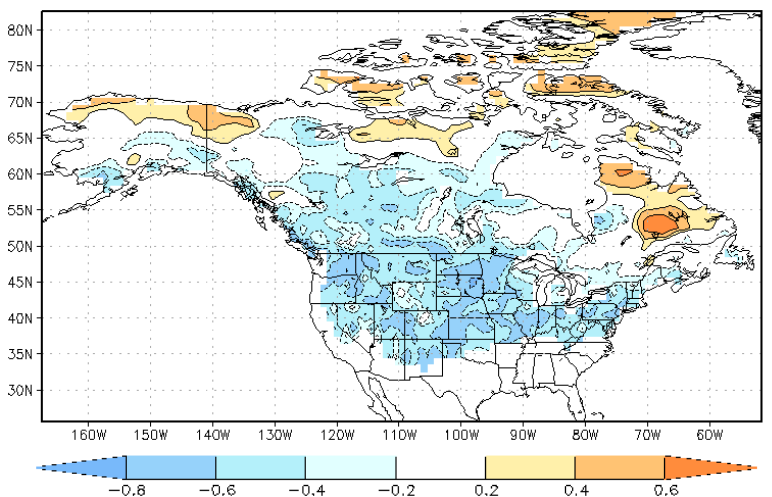


**Fig. 5** The grid-by-grid correlation between Oct-Apr seasonal snowfall and temperature (1950-2008). Contour/shading interval is 0.2 with the zero contour omitted.

Niño (La Niña) associated with below-normal (above-normal) over the interior Northwest and above-normal (below-normal) snowfall over the southern High Plains. A smaller but expected relationship is also found in the Great Lakes region, where Niño 3.4 is negatively correlated with seasonal snowfall. Somewhat unexpectedly, the relationship over the Mid-Atlantic and coastal Northeast is weak in this linear framework. Long-term, linear trends are notable across North America (Fig. 4). Negative trends are strongest over parts of the mountainous West, and to less extent parts of the Mid-Atlantic and Northeast. Positive trends are seen over much of northern tier of the continent, likely associated with increased moisture availability as a result of long-term changes in the winter climate.

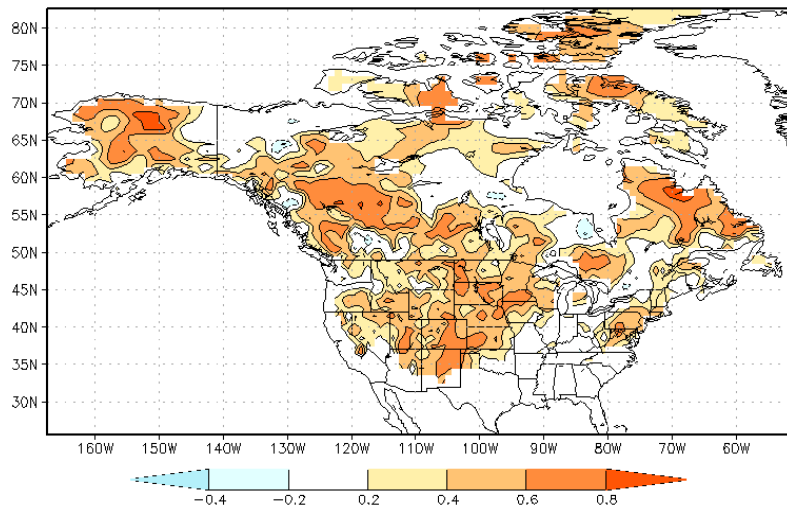


**Fig. 6** Same as Fig. 5, except for precipitation.

The temperature and precipitation correlations are quite robust, especially over the CONUS. Positive (negative) correlations exist across much of the CONUS between precipitation (temperature) and snowfall (Figs. 5 and 6). Here it is important to note that in some regions, especially the High Plains, seasonal temperature and precipitation are quite highly correlated, so these cannot be thought of as independent predictors. Nonetheless, a wetter seasonal climate is one in which there are more opportunities for snowfall accumulation; this is especially intuitive in relatively cold climates. Colder-than-average seasonal temperatures can be thought to increase the ratio of frozen to liquid precipitation by lowering the average

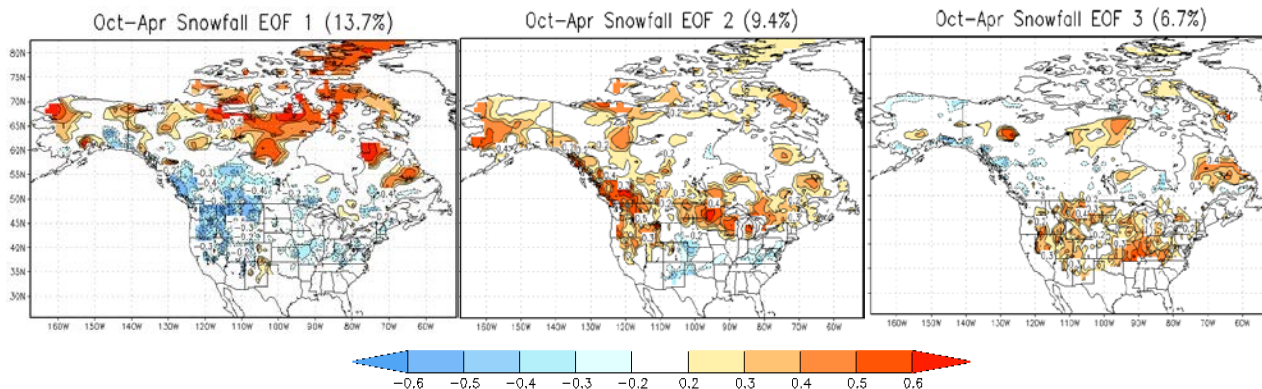


**Fig. 7** Linear correlations between the leading principal components and seasonal snowfall anomalies. Contour/shading interval is  $\pm 0.2$ .

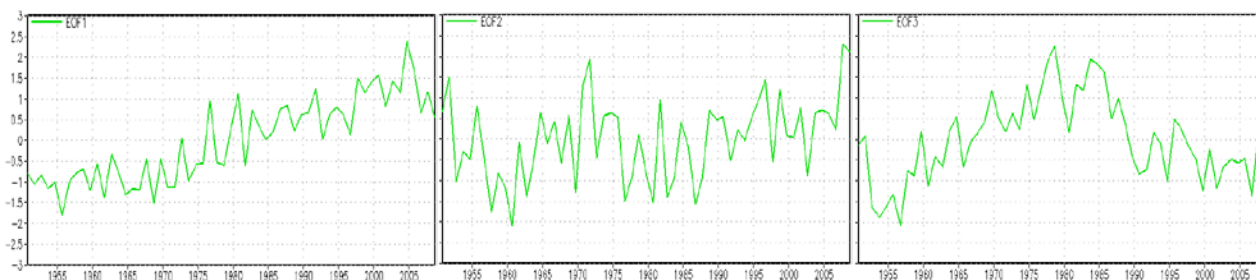


**Fig. 8** Time series of three leading principal components of seasonal snowfall variability. PCs 1, 2, and 3 most closely represent trend, ENSO, and decadal variability, respectively.

freezing level in the overlying atmospheric column. To be sure, a portion of this relationship between temperature and snowfall is based on snow cover feedbacks affecting the local radiative balance. This underscores the importance of incorporating upper-level height analysis at some point; this will allow for a clearer understanding of cause and effect between seasonal temperature, precipitation, and snowfall.

The EOF analysis reveals coherent patterns with associated time series that are consistent with known patterns of interannual to decadal variability (Figs. 7 and 8). The first three principal components are associated with long-term trends, ENSO, and decadal variability, respectively. These relationships are confirmed by regressing these time series onto the time-lagged seasonal SST anomalies (not shown here). Interestingly, PC 3 peaks in the late 1970s, a break point often seen in climate analysis from which time the modern period of climate warming has continued.

#### 4. Conclusions

Seasonal forecasts of snowfall accumulation are likely feasible based on the state of ENSO and long-term trends, statistical specification based on forecast temperature and precipitation, or both. The leading principal components of seasonal snowfall anomalies are associated with known, coherent patterns of SST variability, suggesting predictability similar to temperature and precipitation, at least in some regions. Next steps include an independent hindcast experiment to approximate prediction skill using empirical methods informed by these results, followed by assessment of dynamical model seasonal snowfall forecasts.

#### References

- Kluver, D., and Coauthors, 2016: Creation and validation of a comprehensive 1° by 1° daily gridded North American dataset for 1900–2009 snowfall. *J Atmos Ocean Technol.*, **33**, 857–871. <https://doi.org/10.1175/JTECH-D-15-0027.1>



## Improving the Stable Surface Layer in the NCEP Global Forecast System

Weizhong Zheng<sup>1,2</sup>, Michael Ek<sup>1</sup>, Kenneth Mitchell<sup>3</sup>, Helin Wei<sup>1,2</sup>, and Jesse Meng<sup>1,2</sup>

<sup>1</sup>NOAA/NCEP/Environmental Modeling Center, College Park, MD

<sup>2</sup>IMSG at NOAA/NCEP/Environmental Modeling Center, College Park, MD

<sup>3</sup>Prescient Weather Ltd, State College, PA

### ABSTRACT

The NCEP Global Forecast System (GFS) has a longstanding problem of severe cold bias in the 2-m air temperature forecasts over land in the late afternoon and nighttime during most seasons. This study examines the performance of the NCEP GFS surface layer parameterization scheme for strongly stable conditions over land in which turbulence is weak or even disappears because of high near-surface atmospheric stability. Cases of both deep snowpack and snow-free conditions are investigated with a series of five GFS experiments. The control run (CTL) uses the current GFS operational version. EXP1 tests the impact of using both the updated momentum roughness length  $z_{0M}$  and constant  $C_{zi1} = 0.8$  treatments. EXP2 applies only the updated  $z_{0M}$  treatment, EXP3 applies only the change to a constant  $C_{zi1} = 0.8$  and EXP4 applies only the Monin–Obukhov stability parameter constraint. Finally, EXP5 is performed with all three changes. The results show that decoupling and excessive near-surface cooling may appear in the late afternoon and nighttime, manifesting as a severe cold bias of the 2-m surface air temperature that persists for several hours or more (Fig.1). Concurrently, due to negligible downward heat transport from the atmosphere to the land, a warm temperature bias develops at the first model level. We test changes to the stable surface layer scheme that include introduction of a stability parameter constraint that prevents the land-atmosphere system from fully decoupling and modification to the roughness-length formulation. GFS sensitivity runs with these two changes demonstrate the ability of the proposed surface-layer changes to reduce the excessive near-surface cooling in forecasts of 2-m surface air temperature. The proposed changes prevent both the collapse of turbulence in the stable surface layer over land and the possibility of numerical instability resulting from thermal decoupling between the atmosphere and the surface. We also execute and evaluate daily GFS 7-day test forecasts with the proposed changes spanning a one-month period in winter. Our assessment reveals that the systematic deficiencies and substantial errors in GFS near-surface 2-m air

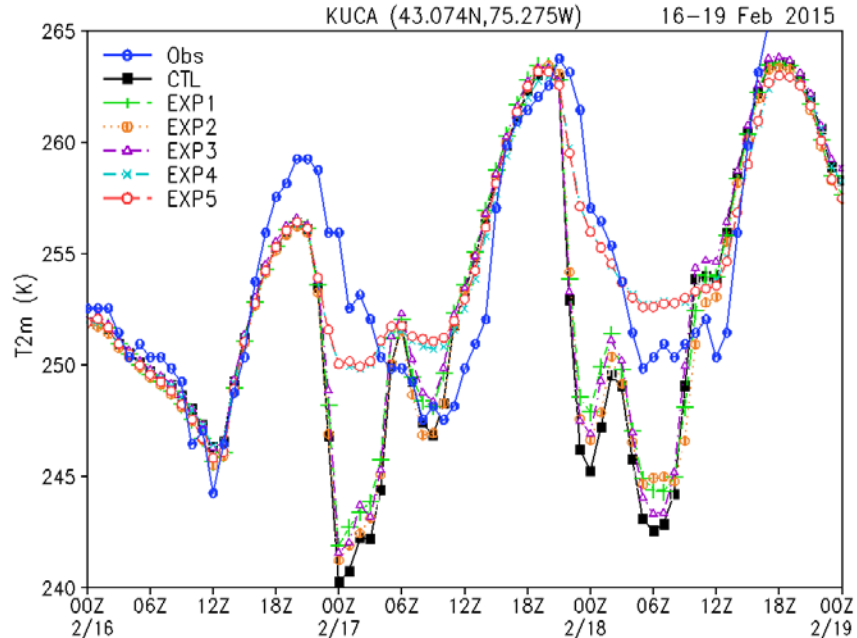


**Fig. 1** Hourly time series of 2-m air temperature (K) at Utica, NY for observations (blue), CTL (black), EXP1 (green), EXP2 (orange), EXP3 (purple), EXP4 (light blue) and EXP5 (red), during the 72-hour period of 00 UTC on 16 February to 00 UTC on 19 February, 2015.



temperature forecasts are considerably reduced, along with a notable reduction of temperature errors throughout the lower atmosphere and improvement of forecast skill scores for light and medium precipitation amounts.

The second version of the NCEP Climate Forecast System (CFSv2) made operational at NCEP in March 2011 employs the same land surface model and surface layer scheme, and similarly, has severe cold biases of 2-m air temperature, typically occurring in the late afternoon and nighttime over land or sea ice. The proposed approach of proper treatment of surface layer parameterization under very stable conditions in this study is under testing in the CFSv2. Reduction of model forecast errors thus improvement of the subseasonal to seasonal climate service are anticipated.

This work has been published in Monthly Weather Review in 2017.

## References

- Zheng W., M. Ek, K. Mitchell, H. Wei, and J. Meng, 2017: Improving the stable surface layer in the NCEP Global Forecast System. *Mon. Wea. Rev.*, **45**, 3969-3987. <https://doi.org/10.1175/MWR-D-16-0438.1>



# 7. CLIMATE DIAGNOSTICS, PREDICTION, AND ANALYSES

42<sup>nd</sup> NOAA Annual Climate Diagnostics and  
Prediction Workshop

23-26 October 2017, Norman, Oklahoma



## Changing Snowpack-streamflow Relationships in the Rio Grande Headwaters

David S. Gutzler and Shaleene B. Chavarria

*University of New Mexico*

### ABSTRACT

Surface water supplies in most areas of western North America are derived principally from snowmelt runoff from high elevation watersheds. We document the changing relationship over the past half-century between snowpack, total precipitation, and snowmelt runoff in one such watershed, the Upper Rio Grande basin (Fig. 1). Snowpack is significantly declining in this watershed, while streamflow out of the basin is also declining but proportionately much less. We diagnose these changes in terms of runoff ratios of streamflow/snowpack or streamflow/precipitation, as well as the runoff sensitivity  $d(\text{streamflow})/d(\text{snowpack})$ . We find that changes to runoff sensitivity are broadly in agreement with expectations from global climate change models, but the runoff ratio based on precipitation has not changed as much due to the increasing importance of spring season precipitation during the snow ablation season. These hydrologic changes have immediate practical consequences for seasonal streamflow forecasting, because the signal/noise ratio for such forecasts is declining rapidly as the direct correlation between snowpack (the principal source of seasonal prediction skill) and subsequent streamflow becomes smaller as snowpack declines.

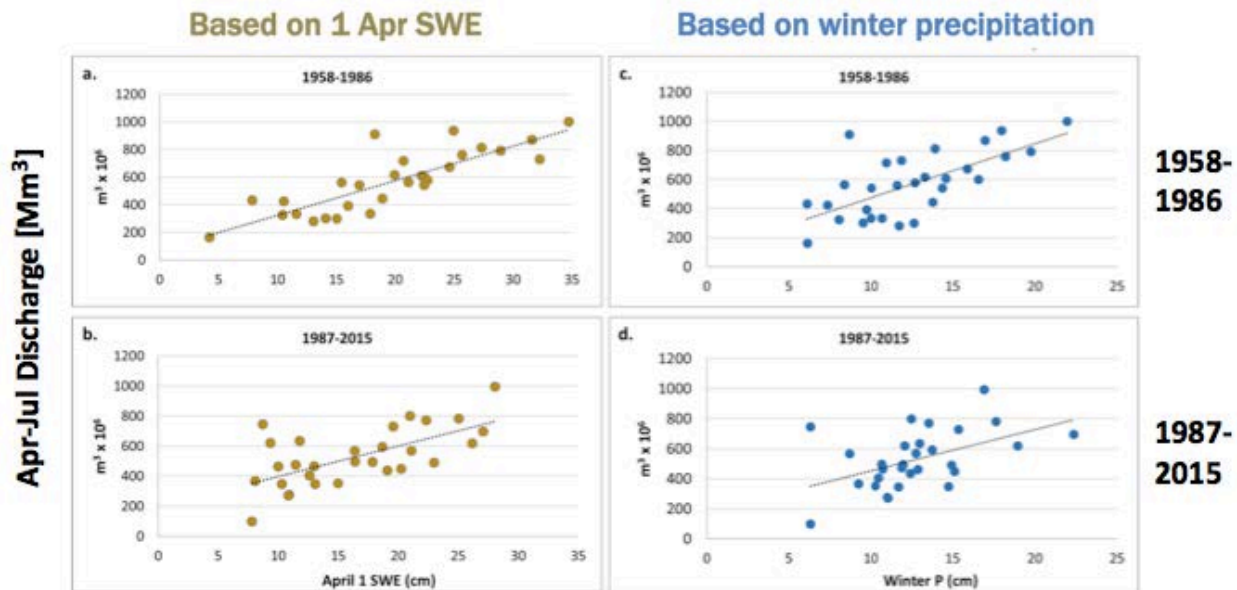


**Fig. 1** Runoff ratios of streamflow/snowpack (left column) and streamflow/winter precipitation (right column) at the Del Norte gage for 1958-1986 (top row) and 1987-2015 (bottom row). In later epoch, much worse linear fit (streamflow depends less directly on snow water equivalent (SWE) or precipitation (P)) and shallower regression slope (reduced sensitivity of streamflow to SWE or P) are found due to warmer temperatures, less snow, and more variable post-snow precipitation.

This work has been published in Journal of the American Water Resources Association in 2018.

### References

Chavarria, S. B., and D. S. Gutzler, 2018: Observed changes in climate and streamflow in the upper Rio Grande Basin. *J. Amer. Water Resour. Assoc. (JAWRA)* 1–16, <https://doi.org/10.1111/1752-1688.12640>

## Impact of High Vertical Resolution in an Oceanic General Circulation Model on Sea Surface Temperature Simulation

Ying Zhang<sup>1,2</sup>, Wanqiu Wang<sup>1</sup>, and Arun Kumar<sup>1</sup>

<sup>1</sup>Climate Prediction Center, NOAA/NWS/NCEP, College Park, MD

<sup>2</sup>ESSIC, University of Maryland, College Park, MD

### 1. Introduction

The accuracy of the sea surface temperature (SST) in the numerical models is crucial in the simulation of the Madden-Julian Oscillation (MJO) (Wang *et al.* 2015). One of major factors that impact the SST simulation in the numerical models is the vertical oceanic resolution near the surface. Studies of observations with high vertical resolution have demonstrated that the equatorial Indian Ocean is highly stratified by a strong vertical temperature gradient within the top 10 meters during a MJO field campaign in 2011-2012 winter (Ge *et al.* 2017). However, most of contemporary global coupled atmospheric-ocean models (CGCMs) have a vertical resolution of 10-m near the surface, and cannot well capture the detailed structure of vertical temperature profiles (Bernie *et al.* 2005), which is a possible reason for the degradation in the simulation and prediction of MJO.

In this study, a pair of numerical experiments is carried out using an oceanic general circulation model to investigate the influence of high vertical resolution near the surface on SST simulation. Statistical differences in SST mean state and variability due to vertical resolution in long simulations will be analyzed. The spatial and seasonal variations of these differences will also be diagnosed. The model performance during a particular MJO event is also validated with observations.

### 2. Model and experiments

The global Geophysical Fluid Dynamics Laboratory (GFDL) Modular Ocean Model version 5 (MOM5, Griffies 2012) is used in this study. The horizontal resolution is fixed at 0.5° in the zonal direction but uneven in the meridional direction: 0.25° between 10°S and 10°N, then gradually increasing from 0.25° to 0.5° between 10° and 30° in both hemisphere and staying at 0.5° poleward of 30°S and 30°N. The vertical resolution has two configurations in the upper ocean: one having 10-m vertical resolution for the upper 220 meters is called MOM5 10M version and the other having 1-m vertical resolution in the top 10 m depth is referred as MOM5 1M version. The two configurations represent the commonly used setting and a high vertical resolution setting in ocean models, respectively. Other details about model physics are described in Griffies (2012). The temperature of the top layer at 5m in the MOM5 10M and 0.5m in the MOM5 1M

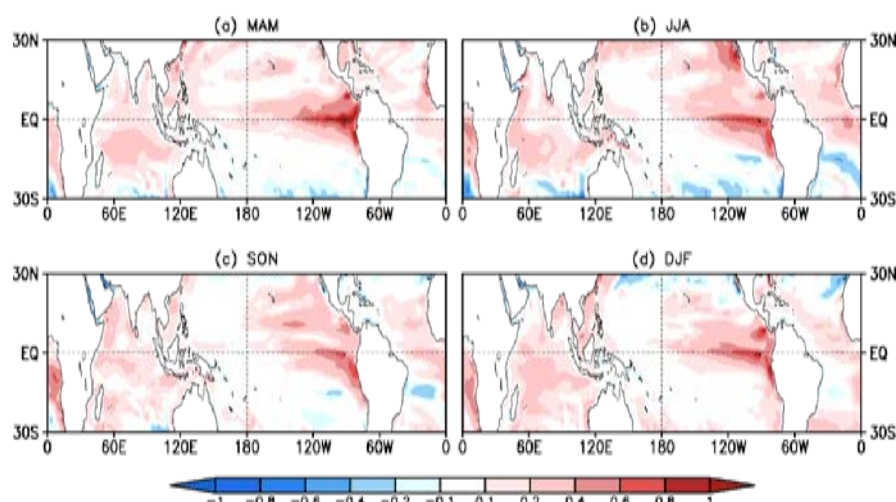


**Fig. 1** Differences in climatological simulated SSTs between MOM5 1M and 10M runs in four seasons. (a) MAM, (b) JJA, (c) SON, (d) DJF.



is considered as simulated SST as commonly defined in OGCMs.

A pair of MOM5 10M and 1M experiments is integrated from January 1<sup>st</sup>, 2006 to December 31<sup>st</sup>, 2016 with the initial fields taking from CFSR oceanic states. The atmospheric forcing fields that drive the MOM5 include downward longwave and shortwave radiation, 10m zonal and meridional winds, surface momentum fluxes and pressure, and 2m temperature and specific humidity. Ge *et al.* (2017) compared the hourly atmospheric forcing fields from the Climate Forecast System Reanalysis (CFSR, Saha 2010), the Modern-Era Retrospective analysis for Research and Applications, version 2 (MERRA2, Gelaro *et al.* 2017), and the average fields of the two reanalyses (*i.e.* the hybrid) with observations and their impacts on the simulated SST during a field campaign with strong MJO events during 2011 winter. They found that the averaged shortwave radiation of the CFSR and MERRA2 reanalyses had better agreement with observations than that from individual reanalysis and simulated SSTs driven by the hybrid dataset had less systematic bias compared to that forced by individual reanalysis. Therefore, the hourly average atmospheric forcing fields of the CFSR and MERRA2 reanalyses are used to drive MOM5 10M and 1M models in this study.

### 3. Results

#### 3.1 Difference in SST variability between MOM5 1M and 10M runs

The simulated SST variability in climatological, intraseasonal, and diurnal time scales is analyzed and compared between MOM5 10M and 1M runs over the tropical ocean. The results below are based on 10-year model outputs from Jan. 01 2007 – Dec. 31, 2016 after one-year spin up.

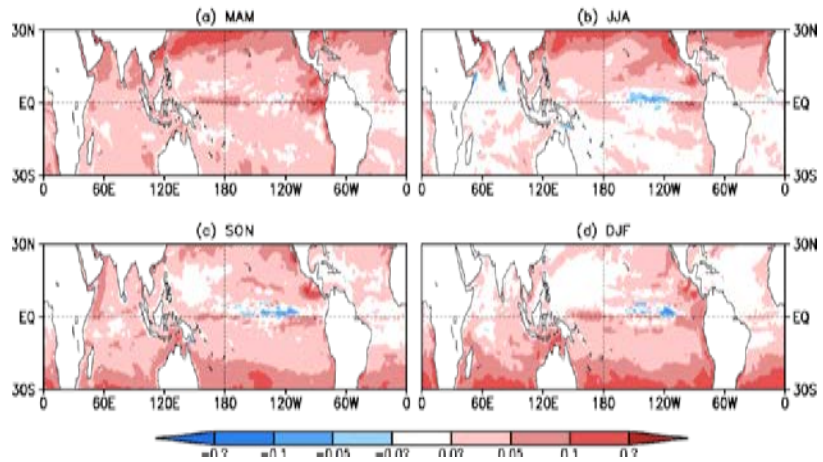


**Fig. 2** Differences in the standard deviation of simulated SST intraseasonal variations between MOM5 1M and 10M runs in four seasons. (a) MAM, (b) JJA, (c) SON, (d) DJF.

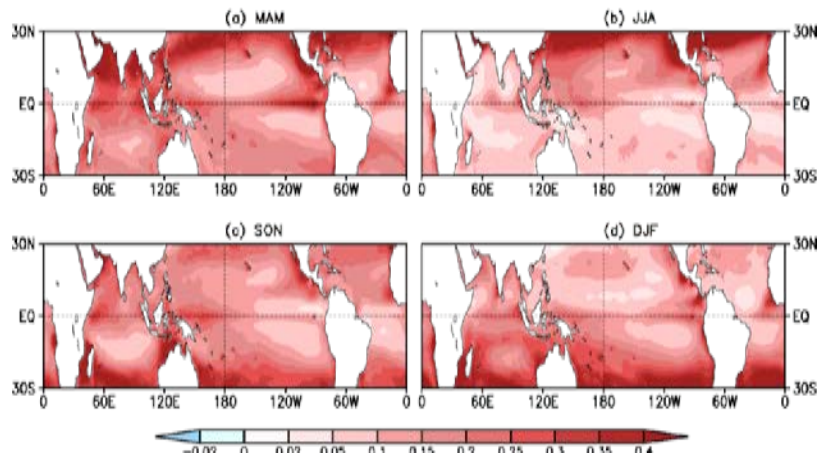


**Fig. 3** Differences in the diurnal ranges of simulated SST between MOM5 1M and 10M runs in four seasons. (a) MAM, (b) JJA, (c) SON, (d) DJF.

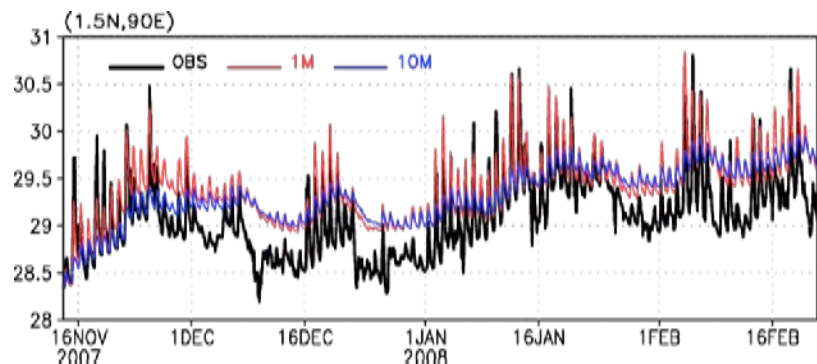


**Fig. 4** Hourly SST evolution at (1.5°N, 90°E) in a MJO event from Nov. 14, 2007 to Feb. 21, 2008 in RAMA observations (black), MOM5 1M (red) and 10M runs (blue).

MOM5 1M run produces similar SST mean states as MOM 10 run does in the western tropical Pacific in the all four seasons, but warmer SST mean states in the tropical Indian, Atlantic and the eastern Pacific Oceans in the all four seasons as shown in Fig.1.

Figure 2 illustrates the difference in standard deviation of SST intraseasonal variability between MOM5 1M and 10M runs in four seasons. Overall, MOM5 1M run has stronger intraseasonal variation than the 10M run does in nearly the entire tropical ocean during all four seasons except for some area in Indian Ocean and southern Pacific ocean during summer and northern Western Pacific Ocean during winter.

The differences in diurnal range of SST during the four seasons between MOM5 1M and 10M runs are represented in Fig. 3. MOM5 1M run has larger diurnal cycle than the 10M run does in entire tropical ocean in all four seasons. The largest difference occurs at equator and subtropics, especially in spring and winter.

### 3.2 Comparison between MOM5 runs and observations

Comparisons between model simulation and the Research Moored Array for African-Asian-Australian Monsoon Analysis and Prediction (RAMA, McPhaden *et al.* 2009) observations are done at a particular location in the equatorial Indian Ocean during a MJO event from Nov. 2007 to Feb. 2008. SST temporal evolutions of RAMA observation and MOM5 runs at that location during the MJO event are plotted in Fig. 4. MOM5 1M run exhibits stronger diurnal cycle than the 10M run does, and is closer to the observation.

The vertical temperature profiles of the observation and MOM5 results at that location (Fig. 5) also confirmed the phenomena in Fig. 4. The MOM5 1M run better represents sharp vertical temperature gradient near the surface and strong diurnal cycle in the observations than the 10M run does during the 2007 MJO event.

If separating the warming and cooling phases of the MJO event, the MOM5 1M run shows larger differences at the surface layer between the warming and cooling phases of the 2007 MJO event than the 10M run does as shown in Fig.6.

All the above results indicate the simulation of MOM5 1M run, which has high vertical resolution in the upper ocean, has stronger intraseasonal and diurnal cycle than that of the MOM5 10M run does in the tropical Indian Ocean, and is also closer to the observations.

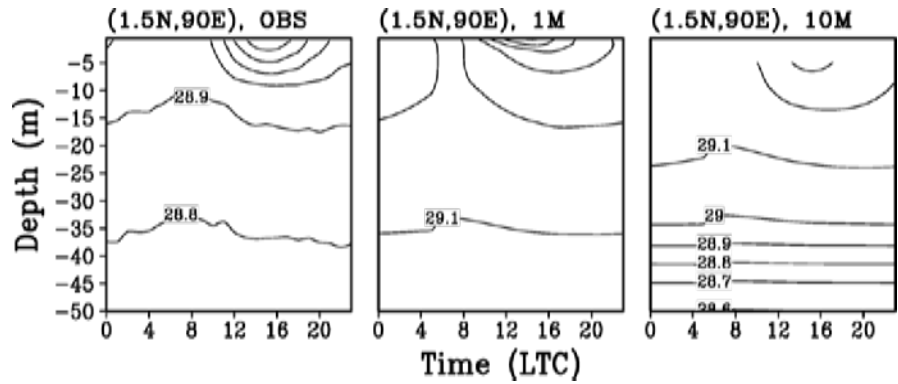


**Fig. 5** Average diurnal cycle of vertical temperature profile in the upper ocean at (1.5°N, 90°E) during the MJO event in 2007 winter from observation (left), MOM5 1M run (middle), and MOM5 10M run (right).

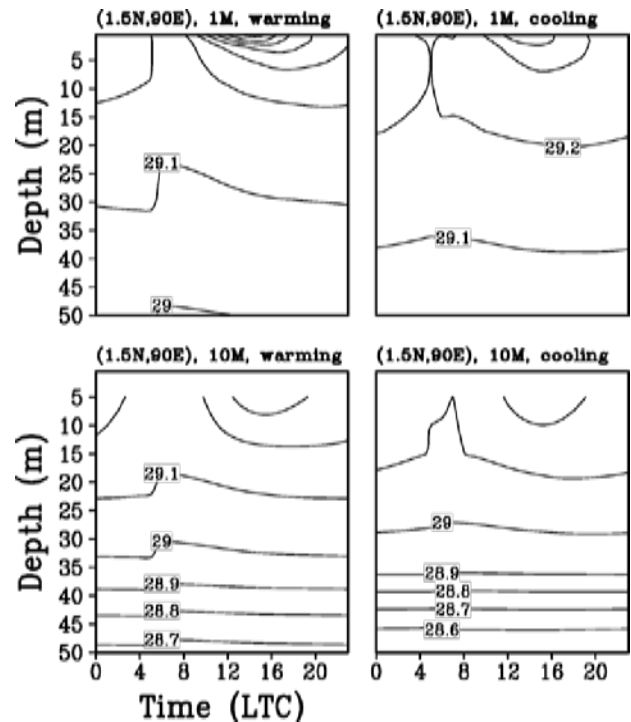


**Fig. 6** Average diurnal cycle of vertical temperature profile in the upper ocean at (1.5°N, 90°E) during warming and cooling phases of the MJO event in 2007 winter from MOM5 1M run (upper left and right) and 10M run (lower left and right).

#### 4. Discussion and conclusion

This study investigates the impact of high vertical resolution in the upper ocean in an oceanic model on the SST simulation. The comparison between the model simulations from an OGCM with high vertical resolution (1m) and those from the same OGCM with commonly used vertical resolution (10m) in the upper ocean is conducted. The model simulations are also validated with observations. The results suggest that the intraseasonal and diurnal variability of SST may be underestimated in the most CGCM with vertical resolution of 10m near the surface and this underestimation of SST simulation would affect the simulation of MJO. Therefore, high vertical resolution near the surface, such as the configuration of MOM5 1M run, is needed in SST simulation in order to potentially improve the simulation of MJO.

#### References

- Bernie, D. J., S. J. Woolnough, and J. M. Slingo, 2005: Modeling diurnal and intraseasonal variability of the ocean mixed layer. *J. Climate*, **18**, 1190-1202.
- Ge, X., W. Wang, A. Kumar, and Y. Zhang, 2017: Importance of the vertical resolution in simulating SST diurnal and intraseasonal variability in an oceanic general circulation model, *J. Climate*, **30**, 3963-3978. DOI:10.1175/JCLI-D-16-0689.1
- Gelaro, R., and Coauthors, 2017: The Modern-Era Retrospective Analysis for Research and Applications, Version 2 (MERRA-2). *J. Climate*, doi: 10.1175/JCLI-D-16-0758.1
- Griffies, S. M., 2012: Elements of the Modular Ocean Model (MOM) (2012 release): GFDL Ocean Group Tech. Rep. No. 7, NOAA/Geophysical Fluid Dynamics Laboratory, 618 + xiii pages.
- McPhaden, M. J., and Coauthors, 2009: RAMA: The Research Moored Array for African-Asia-Australian Monsoon Analysis and Prediction. *Bull. Amer. Meteor. Soc.*, **90**, 459-480, doi: 10.1175/2008BAMS2608.1
- Saha, S., Coauthors, 2010: The NCEP Climate Forecast System Reanalysis. *Bull. Amer. Meteor. Soc.*, **91**, 1015-1057, doi:10.1175/2009BAMS2871.1
- Wang, W., A. Kumar, X. Fu, and M.-P. Hung, 2015: What is the role of the sea surface temperature uncertainty in the prediction of tropical convection associated with the MJO? *Mon. Wea. Rev.*, **143**, 3156-3175. DOI: 10.1175/MWR-D-14-00385.1

## **Empirical Teleconnection-based Standards for U.S. Temperature and Precipitation Predictability at Weeks 3 and 4**

Daniel S. Harnos<sup>1</sup>, Laura M. Ciasto<sup>1,2</sup>, Nathaniel C. Johnson<sup>3,4</sup>, Michelle L. L'Heureux<sup>1</sup>,  
Cristiana Stan<sup>5</sup>, and Adam D. Allgood<sup>1</sup>

<sup>1</sup>*Climate Prediction Center, NOAA/NWS/NCEP, College Park, MD*

<sup>2</sup>*Innovim, LLC, Greenbelt, MD*

<sup>3</sup>*Geophysical Fluid Dynamics Laboratory, NOAA, Princeton, NJ*

<sup>4</sup>*Department of Atmospheric and Oceanic Sciences, Princeton University, Princeton, NJ*

<sup>5</sup>*Department of Atmospheric, Oceanic, and Earth Sciences, Center for Ocean-Land-Atmospheric Studies,  
George Mason University, Fairfax, VA*

### **1. Introduction**

The Climate Prediction Center (CPC) has been issuing probabilistic, two-class forecasts of 2-meter temperature ( $T_{2m}$ ) and precipitation ( $P$ ) for the weeks 3-4 period (days 15-28) since September 2015, effectively closing the gap between forecasts of the extended range (days 8-14) and monthly periods. The week 3-4 period has been typically thought to be one of low forecast skill, due to insufficient time for boundary conditions (*e.g.* soil moisture, sea surface temperatures) to take hold on a forecast, while dynamical guidance further suffers from substantial growth of initialization errors.

While dynamical model guidance will always play a substantial role in forecasting, statistical methods can potentially exploit signals from the initial climatic state that can uniquely inform subseasonal forecasters. For example, Riddle *et al.* (2013) and Baxter *et al.* (2014) revealed impacts of the Madden-Julian Oscillation (MJO) through subseasonal timescales on the circulation and  $T_{2m}$  of North America. Johnson *et al.* (2014) used a compositing method (detailed in next section) to support that non-linear combined influences of MJO, long-term trend, and the El Niño-Southern Oscillation (ENSO) could often produce skillful week 3-4 wintertime U.S.  $T_{2m}$  forecasts. This work seeks to quantify how the methods of statistical guidance leveraging lagged relationships with the observed initial climatic state have performed in real-time relative to dynamical model guidance during week 3-4. This statistical guidance can also serve as a benchmark for dynamical model guidance, in order to better inform subsequent model development.

### **2. Data and methodology**

Training and cross-validation data for  $T_{2m}$  (Janowiak *et al.* 1999) and  $P$  (Xie *et al.* 2010) are taken over running 3-month periods between 1982-2013 to evaluate typical lagged responses for the week 3-4 period. ENSO information is represented by the CPC Oceanic Niño Index (3-month running mean Niño 3.4 region SST anomaly) while the daily CPC Real-time Multivariate MJO (RMM; Wheeler and Hendon 2004) index characterizes the MJO state.

The first methodology to investigate Week 3-4 predictability of  $T_{2m}$  and  $P$  is the so-called “phase model” (PM) of Johnson *et al.* (2014), which closely follows traditional non-linear compositing methods. Mean and variance shifts are quantified based upon the historical week 3-4 distributions of  $T_{2m}$  and  $P$  for subsets of ENSO (El Niño, Neutral, or La Niña following typical conventions), and the MJO (one for each conventional phase and another when the MJO exhibits an amplitude  $< 1$ ), with an additional mean shift associated with decadal trends taken in a linear sense. A Gaussian probability density function (PDF) is assumed for the forecast distribution, with a fourth root transform utilized to increase normality for  $P$ , where the summed means (ENSO, MJO, and trend) and variances (ENSO and MJO) are used to develop the forecast PDF. The forecast PDF can then be compared to the climatological median values, yielding a 2-class empirical forecast.

While the former method yields differences in the forecast state, it remains imperfect as it results in possible undesirable forecast discontinuities when transitioning between climatic states (*e.g.* MJO phases 4, 5, or a weak MJO) while also failing to account for potential influences from the amplitude of the background climate state on  $T_{2m}$  and  $P$ . These shortcomings can be addressed through a multiple linear regression (MLR) framework, with predictands of  $T_{2m}$  and  $P$  and standardized predictors of: RMM1 and RMM2 for MJO, the OISSTv2 (Reynolds *et al.* 2007) 2-week mean Niño 3.4 anomaly from OISSTv2 for ENSO, and a daily index for linear long-term trend. The regression relationship is used to determine the mean shifts in the lagged (forecast)  $T_{2m}$  and  $P$  distributions based on the initial climatic state, while the climatological variance, adjusted by  $\sqrt{1-r^2}$  from cross-validation to account for overconfidence, to yield a Gaussian forecast PDF. As with the PM, the resulting distribution is evaluated with respect to climatology to yield a probabilistic forecast.

Skill evaluations utilize the Heidke Skill Score (HSS), which is the difference of the number of correct forecasts and number of forecasts to be expected to be randomly correct (50% in a two-class forecast), divided by the difference of the total number of forecasts and number of forecasts expected to be randomly correct. The HSS can range over  $\pm 100$ , with a score of 0 indicating no improvement relative to random chance while positive values indicate added value. Cross-validation is performed using a leave-one-year out methodology of leaving out one year of data and training the respective forecast model, and thereafter averaging across the full sample. The PM has been shown to be skillful previously, with skill coming from each of its predictors (*e.g.* Johnson *et al.* 2014), while the cross-validated HSS values for the MLR using various combinations of predictors during boreal winter and summer are shown in Fig. 1 and reveal a similar result.

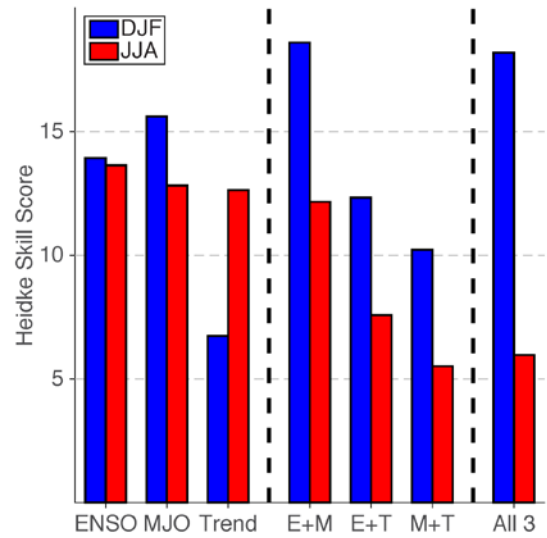


**Fig. 1** Cross-validated HSS of the MLR for T2m over the U.S. using individual and varied predictor combinations compared to the full scheme for DJF (blue) and JJA (red).

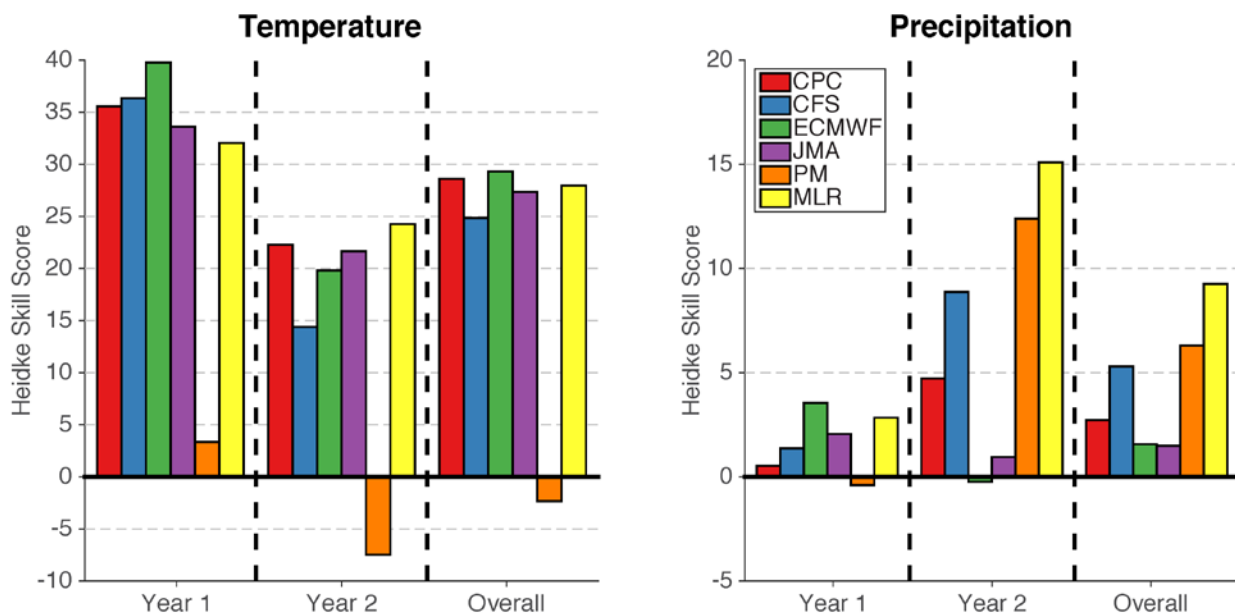


**Fig. 2** Real-time HSS averaged across the U.S. for dynamical and statistical guidance in use at CPC and the official outlooks. Note for official CPC outlooks all grid cells are used to quantify HSS, as the other guidance does not have the benefits of being able to forecast equal chances when confidence is poor.



### 3. Real-time performance

Skill metrics are presented in Fig. 2 for the PM and MLR statistical guidance along with bias-corrected dynamical model ensemble guidance from several sources (CFSv2, ECMWF, and JMA) and official CPC outlooks for the “real-time” period since CPC began issuing Week 3-4 outlooks. Each of the aforementioned guidance sources has been available to forecasters in real-time throughout this period. Results are further broken down into the first year (September 2015-August 2016) and second year (September 2016-August 2017) of service. Figure 2 reveals that all  $T_{2m}$  forecasts are skillful, with the exception of the PM. The MLR is shown to be highly competitive with dynamical models for  $T_{2m}$  forecasts, while the PM has performed relatively poorly. The poor performance of the PM in real-time for  $T_{2m}$  outlooks is largely attributed to it underrepresenting decadal trends in its forecasts relative to the MLR and other guidance, with this guidance forecasting below-normal probabilities more often than the other tools. This is also supported in subsequent results for the PM with  $P$  where it performs better given the apparent lesser importance of such trends in  $P$ . With the exception of the PM, spatial coverage of positive HSS values is widespread across the lower-48 states and Alaska for each of the guidance methods (not shown).

While  $P$  forecasts generally exhibit marginal skill overall, both statistical models outperform dynamical models in  $P$  forecasts during the real-time period. The MLR notably outperforms all other guidance for  $P$ , but the PM also outperforms each of the dynamical models. In a spatial sense, skillful forecasts for  $P$  are clustered across the West and northern tier among dynamical model guidance, while statistical guidance exhibits the broadest coverage of skillful forecasts with its best performance across the West and South (not shown).

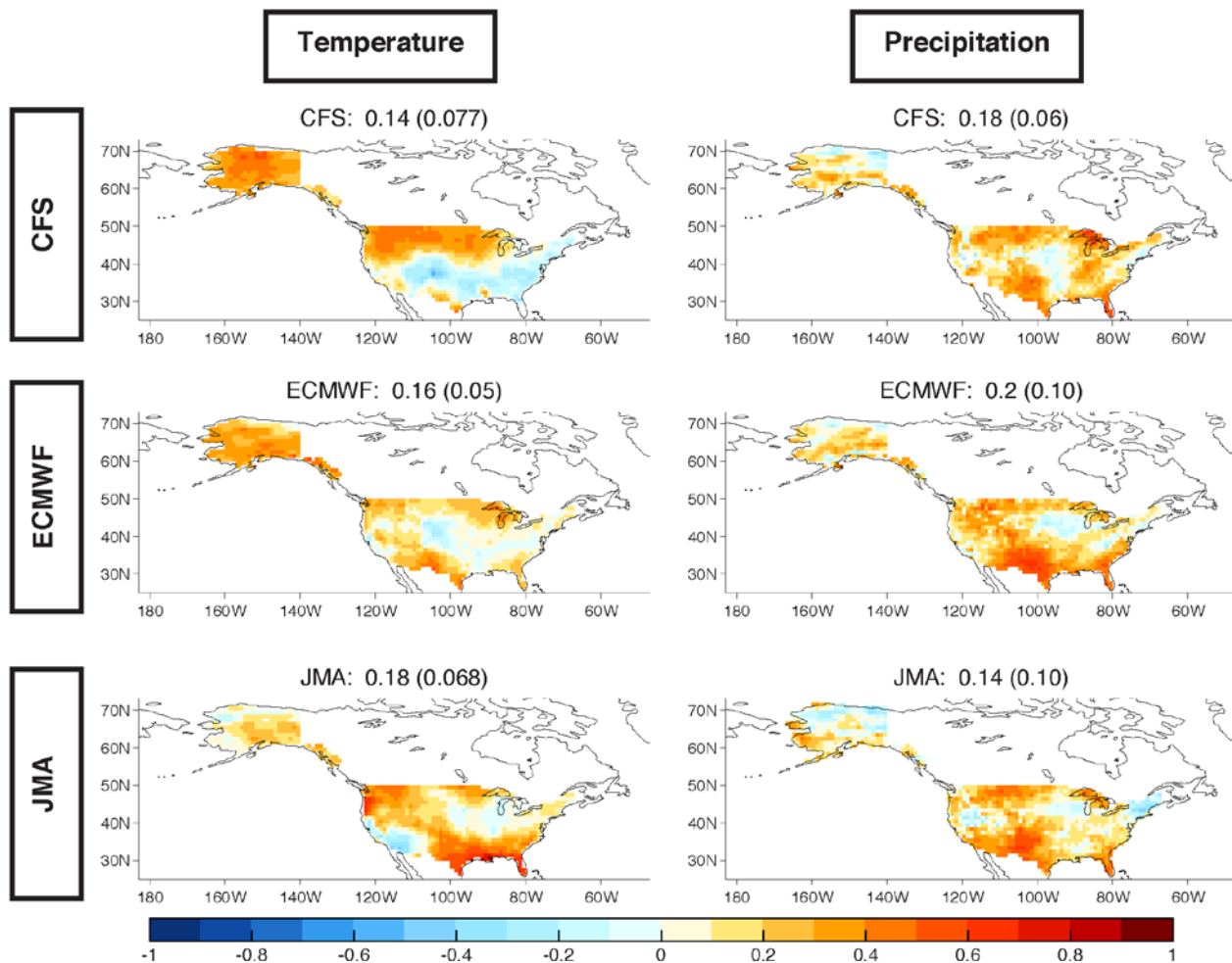


**Fig. 3** Real-time correlation of forecast probabilities from dynamical model guidance with the MLR. Domain average values are in the title, along with the explained variance in parentheses.

#### 4. Synergy between empirical and dynamical guidance

Given the apparent similarities among performance between dynamical model guidance and the MLR, it is reasonable to inquire as to what degree of overlap exists between these forecaster tools. This serves to portray regions where model guidance may be well-representing the empirical relationships from the modes utilized as predictors in the MLR, or highlighting regions where improvement in the representation of these modes would be best served for subsequent model development. To quantify the degree of overlap between the tools, correlations of forecast probabilities between the MLR and each of the three dynamical models is quantified on a grid-level scale in Fig. 3. Forecasts of  $T_{2m}$  exhibit widespread correlations  $\geq 0.5$ , with some areas  $> 0.7$ . This suggests that for this limited sample much of the forecast variance among dynamical model guidance is attributed to their proper representation of ENSO, MJO, and long-term trend. Among individual models, the JMA possesses the largest  $T_{2m}$  correlations with the MLR, likely due to it having a substantial trend component that is manifest in its repeated forecasts of above-normal temperatures (not shown). High correlations for  $T_{2m}$  in Alaska among all models are similarly attributed the importance of trends and their respective representation. High co-variability of dynamical model guidance for  $T_{2m}$  with the MLR across the northern tier of the lower-48 states is likely tied to the ENSO footprint here, while anticorrelated values in the Midwest and Ohio could be tied to poor mid-latitude responses to the MJO among dynamical models.

Compared to  $T_{2m}$ ,  $P$  forecasts are even more highly correlated among dynamical model guidance and the MLR, and over a more extensive portion of the country.  $P$  forecasts from the MLR generally explain more variance in dynamical model guidance across the West, Northern Plains through Great Lakes, and across the southern tier of the lower-48 states – each a typical “hot spot” for ENSO teleconnectivity. MJO impacts on atmospheric river activity are also likely to contribute to increased correlations in  $P$  forecasts between the MLR and dynamical guidance across the West coast and southern Alaska. The greatest  $P$  variance explained by the MLR is typically across the Southwest, where substantial drying trends have been noted in the past 30 years (not shown).

#### 5. Exploratory predictors for empirical guidance

While the MLR already exhibits substantial skill in a real-time setting, other potential modes of large-scale variability could be applied as possible predictors to further improve model skill while aiding in diagnosis of model performance. One such mode is explored here, defined as the 30-day running mean of

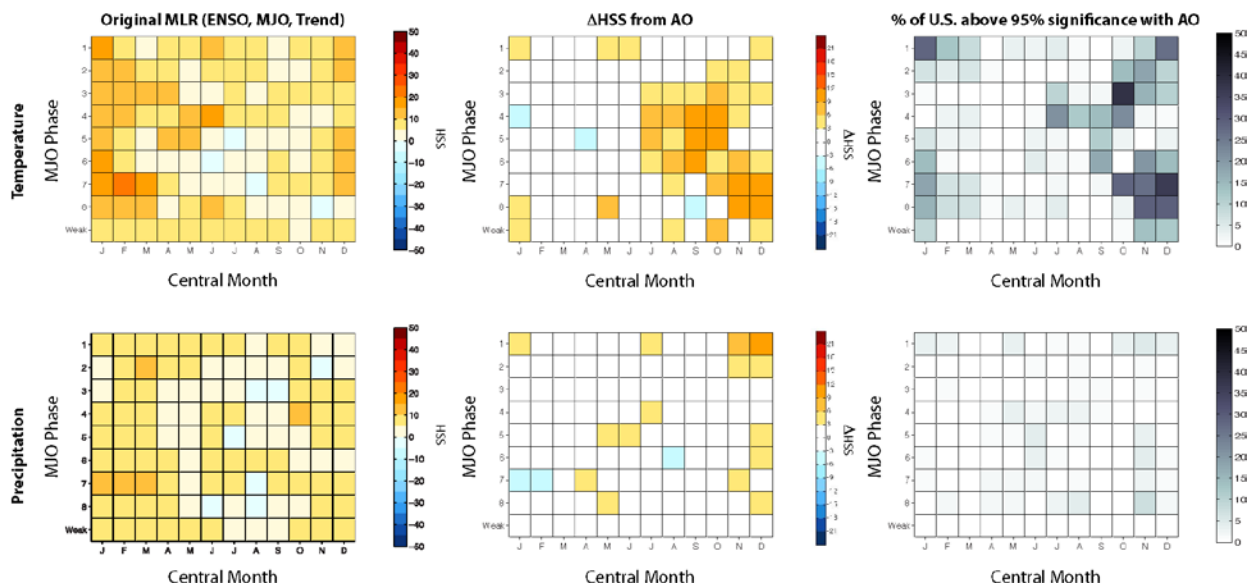


**Fig. 4** Cross-validated U.S. average HSS across all ENSO phases stratified by forecast month and MJO phase for the 3-predictor MLR (left column), change in HSS from inclusion of the CPC AO index (center column), and percentage of U.S. grid points that exceed 95% significance in the 4-predictor MLR versus the 3-predictor model based on the F-statistic.

CPC's arctic oscillation (AO) index. Figure 4 shows the impact of the AO's inclusion on the original 3-predictor MLR for both  $T_{2m}$  and  $P$ . Inclusion of the AO as a predictor during cross-validation shows substantial improvement in HSS values for  $T_{2m}$ , particularly during boreal summer through early winter. These AO impacts on  $T_{2m}$  are generally widespread and appear to be robust when compared with expected values from the F-statistic. Limited impacts are exhibited of the AO on  $P$  in terms of averaged HSS or improved spatial coverage of positive HSS values.

An example of where the AO predictor is adding value to the 3-predictor MLR is shown in Fig. 5, with the percentage of variance explained by MJO phases 6 and 7 during DJF and NDJ respectively shown for the 4-predictor model. Much of the added impacts appear to come across the eastern U.S. and Alaska, as to be expected from the centers of action in the loading pattern for this mode being situated over the Aleutians and Azores. Given that the 3-predictor MLR is already competitive or superior to dynamical model guidance in the limited real-time sample this suggests including empirical AO impacts in the statistical model may further bolster its performance. Figure 5 also suggests that with the MLR forecasts being generally anticorrelated across the eastern U.S. with the dynamical model guidance (Fig. 3), this discrepancy could be tied to the statistical framework lacking information regarding the state of the AO that could be easily rectified in this manner.

**Acknowledgements.** This project was funded by the NOAA/CPO MAPP program and NOAA NGGPS program. We appreciate the respective forecast centers for supplying their dynamical model ensemble guidance. Kyle MacRitchie and Dan Collins respectively post-processed the CFS and JMA data.

## References

- Baxter, S., S. Weaver, J. Gottschalck, and Y. Xue, 2014: Pentad evolution of wintertime impacts of the Madden-Julian Oscillation over the Contiguous United States. *J. Climate*, **27**, 7356-7367.
- Janowiak, J., G. Bell, and M. Chelliah, 1999: A gridded database of daily temperature maxima and minima for the conterminous US: 1948-1993. NCEP/CPC Atlas 6, Natl. Cent. for Environ. Predict., Camp Springs, MD.
- Johnson, N. C., D. C. Collins, S. B. Feldstein, M. L. L'Heureux, and E. E. Riddle, 2014: Skillful wintertime North American temperature forecasts out to 4 weeks based on the state of ENSO and the MJO. *Wea. Forecasting*, **29**, 23-38.

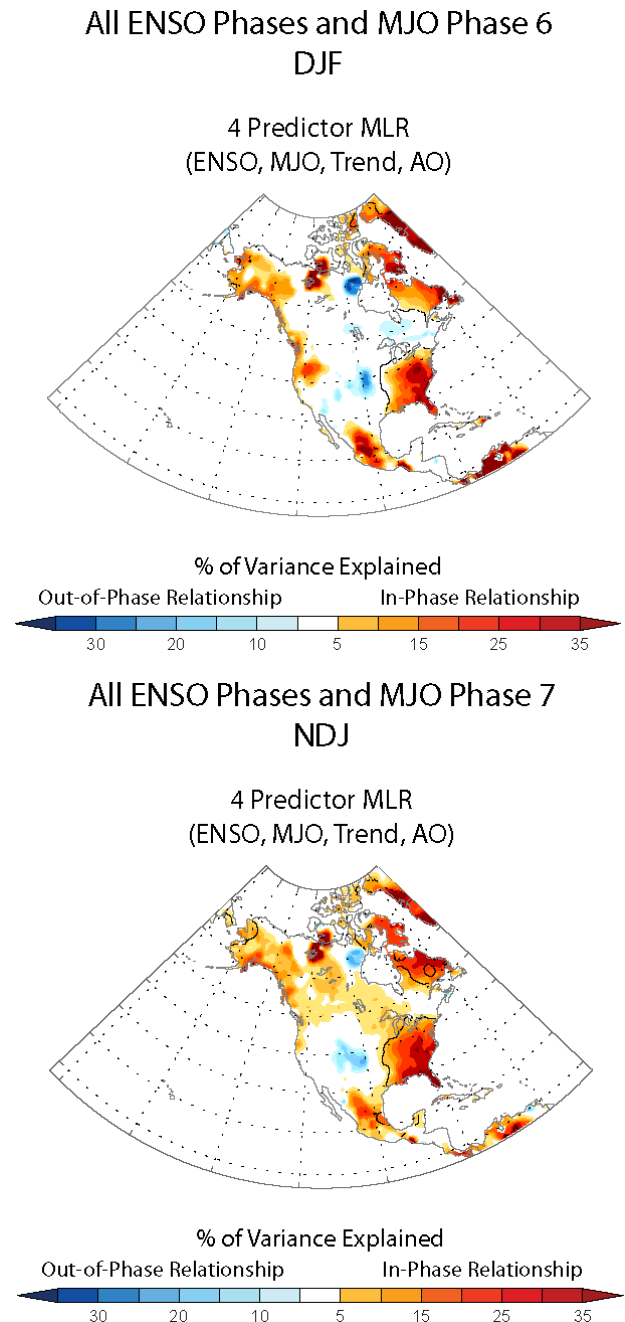


**Fig. 5** Percentage of variance explained by the 4-predictor MLR including the AO during cross-validation for selected forecast months and MJO phases. The black line denotes regions that the 4-predictor MLR significantly improves upon the 3-predictor model.

- Reynolds, R. W., T. M. Smith, C. Liu, D. B. Chelton, K. S. Casey, and M. G. Schlax, 2007: Daily high-resolution-blended analyses for sea surface temperature. *J. Climate*, **20**, 5473-5496.
- Riddle, E. E., M. B. Stoner, N. C. Johnson, M. L. L'Heureux, D. C. Collins, and S. B. Feldstein, 2013: The impact of the MJO on clusters of wintertime circulation anomalies over the North American region. *Clim. Dynamics*, **40**, 1749-1766.
- Wheeler, M. C. and H. H. Hendon, 2004: An all-season real-time multivariate MJO index: Development of an index for monitoring and prediction. *Mon. Wea. Rev.*, **132**, 1917-1932.
- Xie, P., M. Chen, and W. Shi, 2010: CPC unified gauge-based analysis of global daily precipitation. Preprints, 24<sup>th</sup> Conf. on Hydrology, Atlanta, GA, Amer. Meteor. Soc., 23A. [http://ams.confex.com/ams/90annual/techprogram/paper\\_163676.htm](http://ams.confex.com/ams/90annual/techprogram/paper_163676.htm)

## Extratropical-Tropical Interactions over Ethiopia

Endalkachew Bekele Biratu<sup>1,2</sup> and Wassila Thiaw<sup>1</sup>

<sup>1</sup>Climate Prediction Center, NCEP/NWS/NOAA

<sup>2</sup>UCAR/CPAESS

### 1. Introduction

The Belg rainfall contributes significantly to economic activities in Ethiopia, but is also characterized by high temporal and spatial variability. This study identified synoptic and subseasonal features that lead to rainfall deficits and surpluses during Ethiopian Belg season (February – May; Bekele-Biratu *et al.* 2018). In particular, the theory of tropical plume formation (Knippertz 2007) seems to hold true for Belg as tropical-extratropical interactions play a major role in modulating rainfall during this time of the year. This work also complements earlier studies on seasonal variability of Ethiopian rainfall by Habtemichael and Pedgley (1974), Camberlin and Philippon (2002), and Diro *et al.* (2011).

### 2. Data and methods

Daily rainfall data from 117 stations of the National Meteorological Service of Ethiopia is used to define dry (lower tercile) and wet Belg (upper tercile) in 1980-2010 period. The NCEP/CDAS data is used to construct composites of circulation anomalies.

### 3. Results and summary

A tripole structure in a trough/ridge pattern in the region between the Northeast Atlantic Ocean and Red Sea regions is a dominant feature that is associated with Belg rainfall variability in Ethiopia. We have identified two modes of this tripole structure. In general, rainfall deficits (surpluses) in the Belg season are associated with the anticyclone-cyclone-anticyclone (cyclone-anticyclone-cyclone) modes. The ingredients summarized below contribute to rainfall deficits over Ethiopia during the Belg season due to reduced tropical-extratropical interactions: (1) the presence of an anomalous mid-to upper-level warm anticyclone over the Red Sea; (2) the absence of a poleward moisture flux and moisture convergence across the Horn of Africa; (3) the limitation of the southward extension of the mid-to-upper-level extratropical cyclonic trough; (4) upper-level

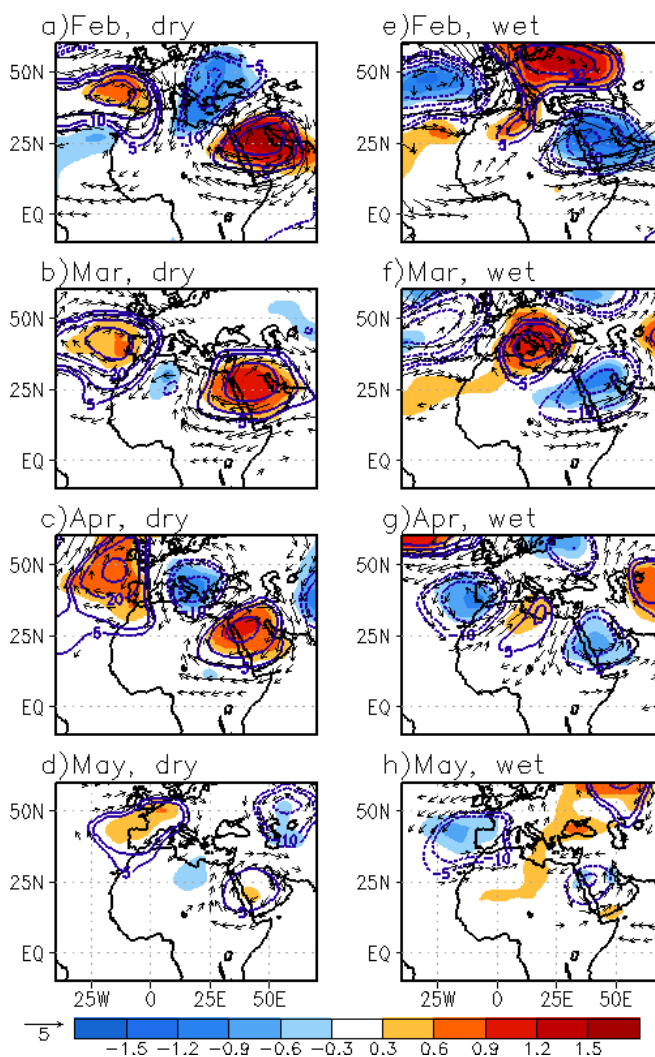


**Fig. 1** (a) - (d) Composites of daily average 500-hPa circulation anomalies for dry events: shaded temperature anomalies (K); contours are geopotential height anomalies (gpm) and vectors are wind anomalies ( $\text{m s}^{-1}$ ), significant at the 95% confidence level (student's *t*-test). (e) - (h), same as (a) - (d) except for wet events.



negative PV anomaly north of Ethiopia; and (5) the prevalence of upper-level convergence across the Horn of Africa. Moreover, the presence of an anticyclonic anomaly across the Red Sea region and the neighboring areas of the Arabian Peninsula keeps the ITCZ south of its normal position during dry Belg events (Fig. 1a-1d).

In contrast, factors that contribute to the enhancement of tropical-extratropical interactions and moisture surpluses during the Belg season include: (1) the presence of anomalous mid-to upper-level cold cyclonic trough over the Red Sea; (2) the presence of a northward moisture flux that extends deep into the Horn of Africa and the prevalence of horizontal moisture convergence over Ethiopia; (3) a southward penetration of mid- to upper-level extratropical cyclonic trough in the Red Sea region; (4) the presence of an area of anomalous upper-level positive PV anomaly cut-off north of Ethiopia; and (5) an elongated area of anomalous upper-level divergence across the Horn of Africa (Fig. 1e - 1h).

Correlation and composite analyses suggest a possible link between phases of the NAO and rainfall surpluses or deficits during the Belg season. Belg rainfall tends to be below (above) average over many parts of Eastern and southern Ethiopia during the positive (negative) phase of NAO events (Fig. 2).

The tripole pattern also plays a role in connecting NAO with circulation anomalies in the Red Sea region such that NAO induces an amplified (suppressed) Azores High in Northeast Atlantic (Diro *et al.* 2011) resulting in enhanced (weakened) Arabian High via the tripole modes. However, the regional circulation patterns and NAO belong to different scales of motion, and may not always interact with each other constructively.

## References

- Bekele-Biratu E., W. Thiaw, and D. Korecha, 2018: Subseasonal variability of the Belg Rains in Ethiopia, *Int. J. Climatol.*, DOI:10.1002/joc.5474
- Camberlin P., and N., Philippon, 2002: The East African March-May rainy season: associated atmospheric dynamics and predictability over the 1968-97 period. *J. Climate*, **15**, 1002-1019.
- Diro, G. T., D. I. F. Grimes, and E. Black, 2011: Large scale features affecting Ethiopian rainfall. *African Climate and Climate Change*, C. Williams and D. Kniveton, Eds., Springer, Dordrecht, 13-50.
- Habtemichael, A, and D. E. Pedgley, 1974: Synoptic case-study of spring rains in Eritrea. *Arch. Meteor. Geophys. Bioklimatol.*, **23**, 285-296.
- Knippertz, P., 2007: Tropical-extratropical interactions related to upper-level troughs at low latitudes. *Dyn. Atmos. Oceans*, **43**, 36-62.

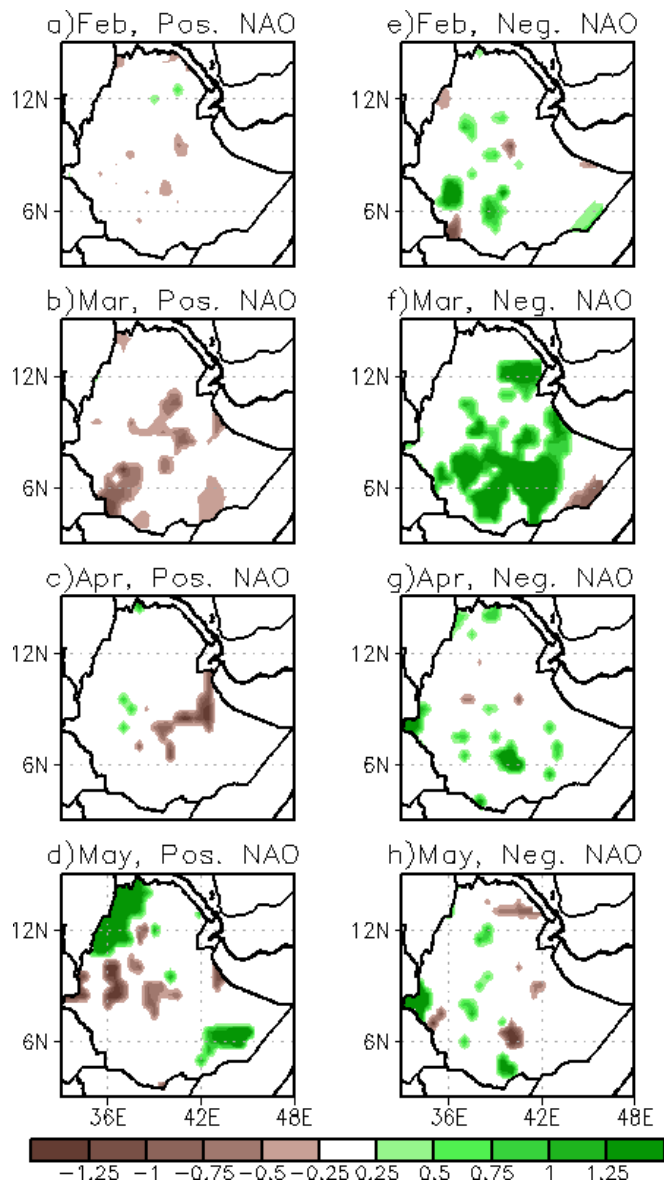


**Fig. 2** (a) - (d), Composites of daily average rainfall anomaly ( $\text{mm day}^{-1}$ ) for NAO positive events, significant at the 95% confidence level (student's *t*-test). (e) - (h), same as (a) - (d) except for NAO negative events.

## Developing an NMME Probability Threshold Based Seasonal Forecast Tool

Mingyue Chen, Arun Kumar, and David DeWitt

*Climate Prediction Center, NOAA/NWS/NCEP, College Park, Maryland*

### ABSTRACT

This study examines the feasibility of developing a seasonal forecast tool based on the North American Multi-Model Ensemble seasonal system (NMME) for different probability thresholds. The probabilistic seasonal forecast skill from the NMME (Kirtman *et al.* 2014) for seasonal anomaly precipitation (PREC) and 2 meter temperature (TEMP), including spatial maps and time series of skill over the Contiguous US (CONUS), and its seasonality, are first assessed. Next, the impact of the threshold probability used to define the regions of forecasts with Equal Chance (EC) on (a) forecast skills and (b) corresponding spatial coverage of region with non Equal Chance (nonEC) forecasts are examined. The skill assessment is based on three category probabilities (above, near, and below normal) for the NMME 0-month-lead seasonal forecast in JFM1995-DJF2016. The verification precipitation data is from the CMAP monthly precipitation analysis (Xie and Arkin 1997) and the land surface temperature from the GHCN-CAMS monthly analysis (Fan and van den Dool 2008). The climatology time period is 1982-2010. The skill measures include the Heide Skill Score (HSS) and the Ranked Probability Skill Score (RPSS).

The results show that relative high forecast skills are located over the southwest US. The areas with high (low) skills of HSS are consistent with high (low) skills of RPSS (Fig. 1). In general, most high skills are related to ENSO episodes. The PREC shows higher skills in spring and fall seasons, while the TEMP shows higher skills in summer season. For both PREC and TEMP, the nonEC forecast HSS increases as the

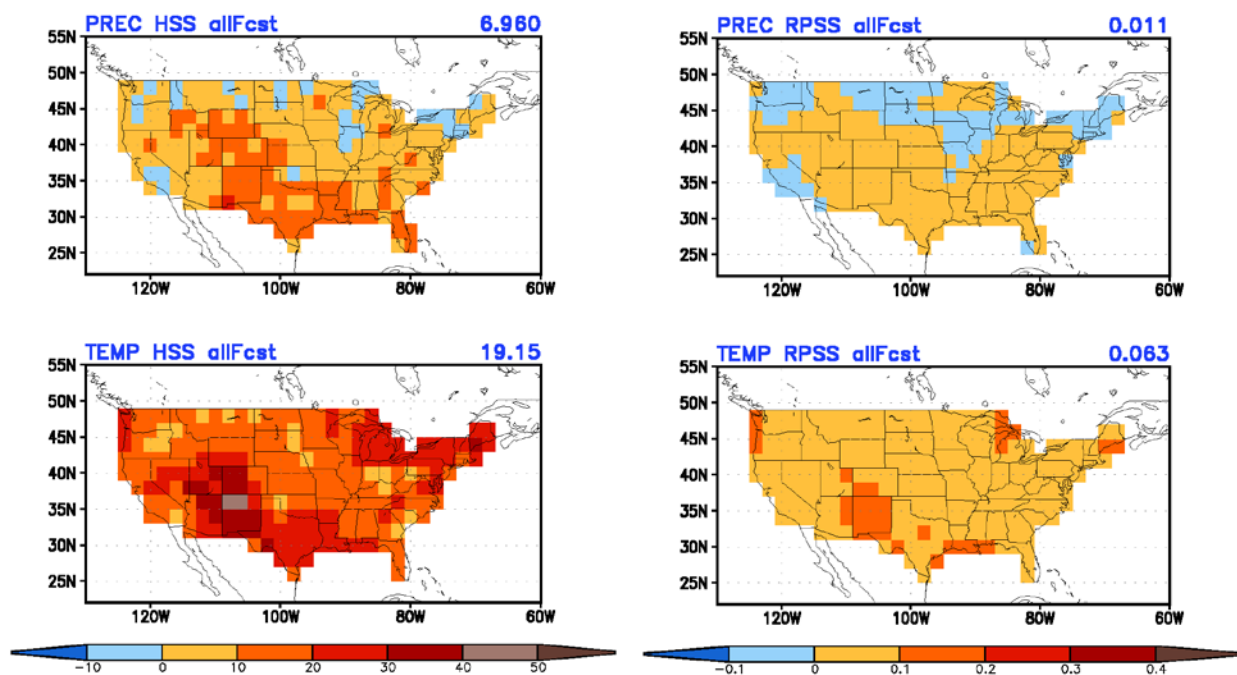


**Fig. 1** Spatial maps of HSS (left panels) and RPSS (right panels) in all seasons in 1995-2016 for PREC (upper panels) and TEMP (lower panels). Skills are based on all forecasts.

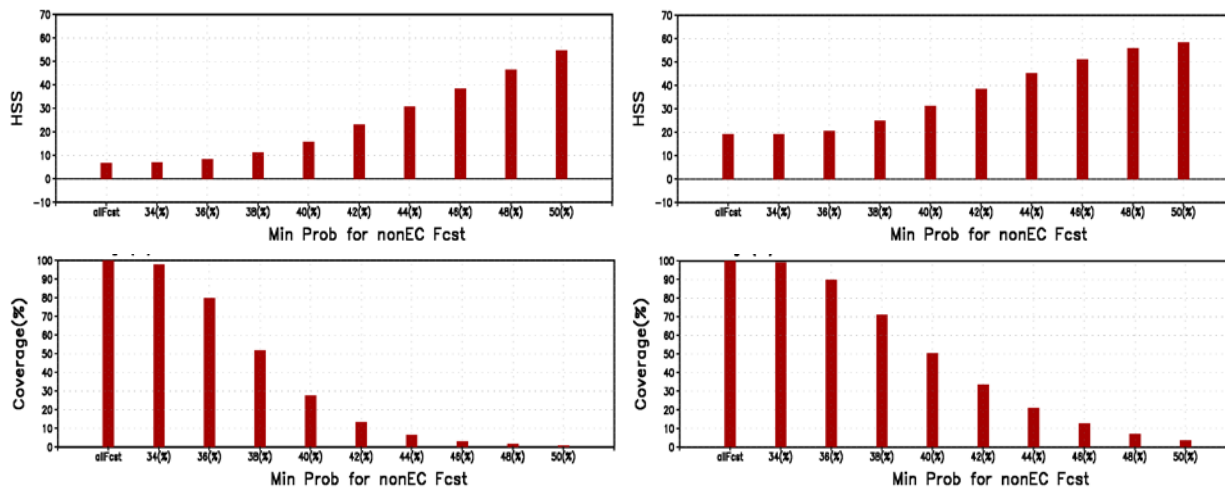


**Fig. 2** HSS averaged over the CONUS for all forecasts and nonEC forecasts with different probability threshold used to define the nonEC forecasts (upper panels), and the corresponding coverage of the nonEC forecasts (lower panels). The left and right columns are for PREC and TEMP, respectively.

probability threshold cutoff value increases, while the areal coverage goes down (Fig. 2). Increasing probability threshold cutoff is equivalent to higher confidence in forecasts, higher signal-to-noise ratio, larger shift in the PDF from climatology, and therefore, should equate to higher skill.

*Acknowledgments.* Thanks to Dr. Emily Becker for providing the NMME seasonal probabilistic forecast data.

## References

- Fan, Y., and D. H. van den Dool, 2008: A global monthly land surface air temperature analysis for 1948-present. *J. Geophys. Res.*, **113**, D01103, doi:10.1029/2007JD008470.
- Kirtman, B. P., and Co-authors, 2014: The North American Multimodel Ensemble: Phase-1 seasonal-to-interannual prediction: phase-2 toward developing intraseasonal prediction. *Bull. Amer. Meteor. Soc.*, **95**, 585-601, doi:10.1175/BAMS-D-12-00050.1.
- Xie, P., and P. A. Arkin, 1997: Global precipitation: A 17-year monthly analysis based on gauge observations, satellite estimates, and numerical model outputs. *Bull. Amer. Meteor. Soc.*, **78**, 2539-2558.

## Seasonal Prediction of North American Temperature and Precipitation Using the Calibration, Bridging, and Merging (CBaM) Method

Sarah Strazzo<sup>1,2</sup>, Dan Collins<sup>1</sup>, Andrew Schepen<sup>3</sup>, Q.J. Wang<sup>4</sup>, Emily Becker<sup>1,2</sup>, and Liwei Jia<sup>1,2</sup>

<sup>1</sup>Climate Prediction Center, NOAA/NWS/NCEP, College Park, MD

<sup>2</sup>Innovim, LLC, Greenbelt, MD

<sup>3</sup>CSIRO Land and Water, Dutton Park, Queensland, Australia

<sup>4</sup>University of Melbourne, Parkville, Victoria, Australia

### 1. Introduction

NOAA's operational seasonal outlooks rely upon forecasts from the North American Multi-Model Ensemble (NMME; Kirtman *et al.* 2014). While the NMME remains a state-of-the-art tool for seasonal forecasting, recent research suggests that the NMME does not consistently reproduce the observed relationship between the El Niño/Southern Oscillation (ENSO) and temperature over North America (Chen *et al.* 2017). As an example, Fig. 1 shows the 1-month lead forecast December–January (DJF) ENSO–temperature teleconnection pattern from the NMME (1b–i) compared to the observed pattern (1a). Several of the NMME member models fail to represent the observed teleconnection pattern over the NMME hindcast period (1982–2010). For example, the CMC2, GFDL, GFDL-FLOR, and NASA models suggest a negative correlation ( $-0.6 < r < -0.2$ ) between ENSO and temperature over portions of the Midwestern United States where the observed correlation is positive ( $0.2 < r < 0.6$ ).

Given the short duration of the NMME hindcast period and the observed variability in both ENSO events and remote responses to ENSO events during this period, it is difficult to evaluate the skill of model teleconnection patterns. Regardless, recent results support the notion that such discrepancies contribute to reduced forecast skill (Chen *et al.* 2017). Prior work has applied Bayesian post-processing to general circulation model (GCM) output to both calibrate GCM forecasts and correct for model misrepresentation of relevant teleconnections (Schepen *et al.* 2014, 2016). Here we test this Bayesian post-processing method – known as Calibration, Bridging, and Merging (CBaM) – using the NMME hindcast dataset with the ultimate goal of improving forecast skill over regions where the NMME misrepresents the ENSO teleconnection.

### 2. Data and methods

The CBaM method for post-processing dynamical model forecasts employs Bayesian joint probability (BJP) modeling (Wang *et al.* 2009). Using NMME reforecasts and observed SST, 2-m temperature, and

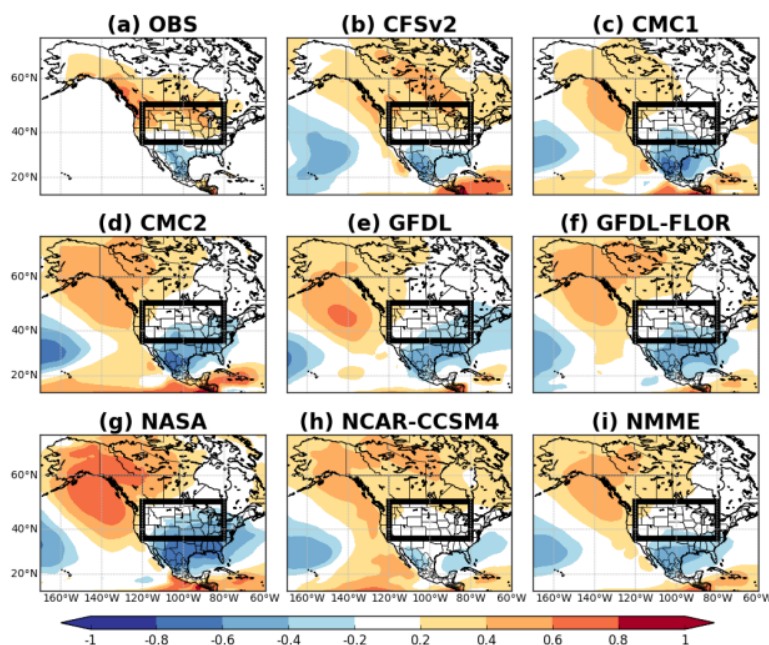


**Fig. 1** Correlation between DJF Niño3.4 SST anomalies and 2-m temperature over North America for the NMME hindcast period 1982–2010, a) observation, b)–h) 1-month lead forecast by ensemble members, and i) by NMME.



precipitation data from the Optimum Interpolation SST (OISST), Global Historical Climatology Network+ Climate Anomaly Monitoring System (GHCN+CAMS), and Climate Prediction Center Merged Analysis of Precipitation (CMAP) datasets, respectively, we develop two types of Bayesian joint probability models: one to model the relationship between NMME-reforecast temperature (precipitation) and observed temperature (precipitation) at each grid point, and another to model the relationship between NMME-reforecast Niño3.4 anomalies and observed temperature or precipitation at each grid point. We refer to the former as a calibration model and the latter as a bridging model. Bivariate normal distributions are at the core of a Bayesian joint probability model. Prior to Bayesian joint probability model development, data transformations are applied to the temperature and precipitation data to ensure that they conform to a bivariate normal distribution. Markov Chain Monte Carlo sampling is employed to obtain a numerical sample of the posterior distribution of the bivariate normal parameters (mean and covariance). For each calibration (bridging) model, we sample 1000 bivariate normal parameters from which we derive an ensemble of 1000 calibrated (bridged) forecasts.

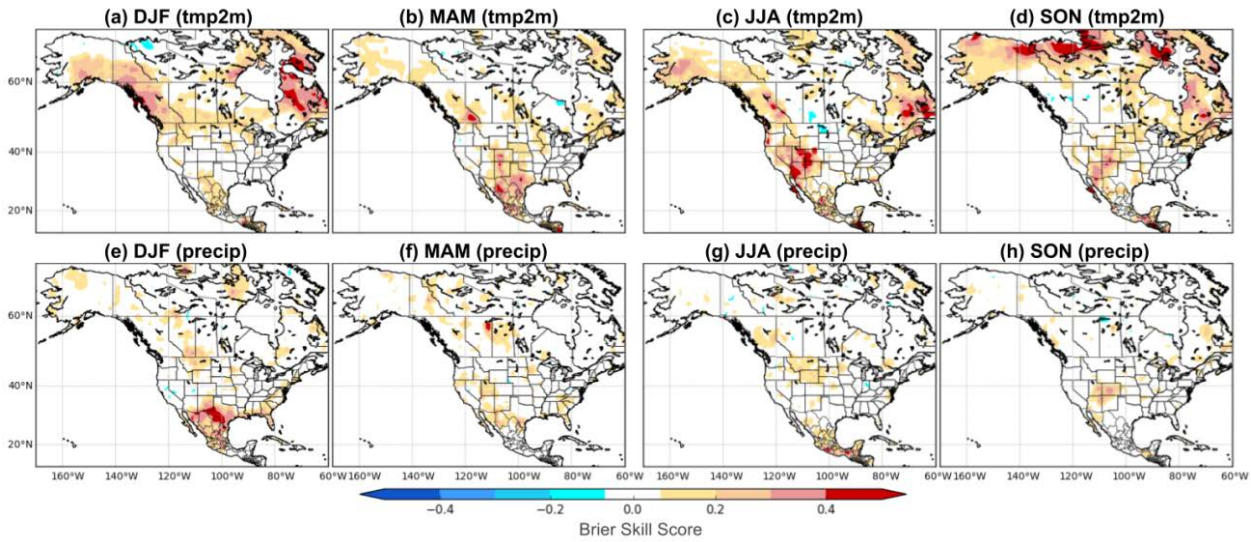


**Fig. 2** Brier skill scores from fully merged CBaM post-processed NMME probabilistic forecasts of below normal temperature (2a–d) and precipitation (2e–h) over the NMME hindcast period.

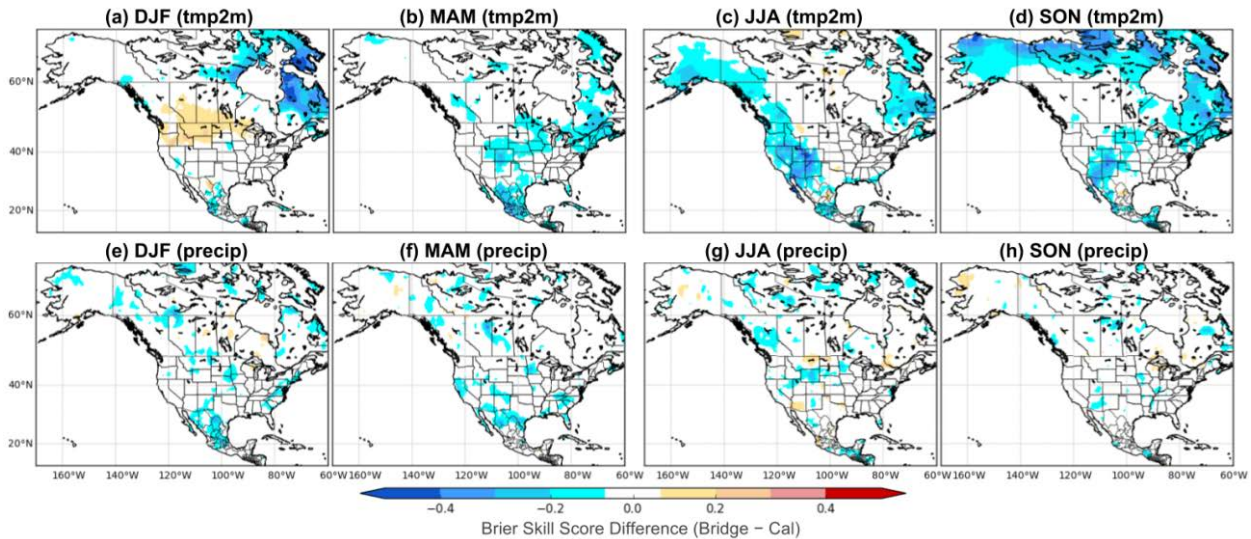


**Fig. 3** Difference maps depicting the difference between bridged and calibrated Brier skill scores for probabilistic forecasts of below normal temperature (3a–d) and precipitation (3e–h) over the NMME hindcast period. Warm shading represents areas for which bridging yielded higher Brier skill scores than calibration.



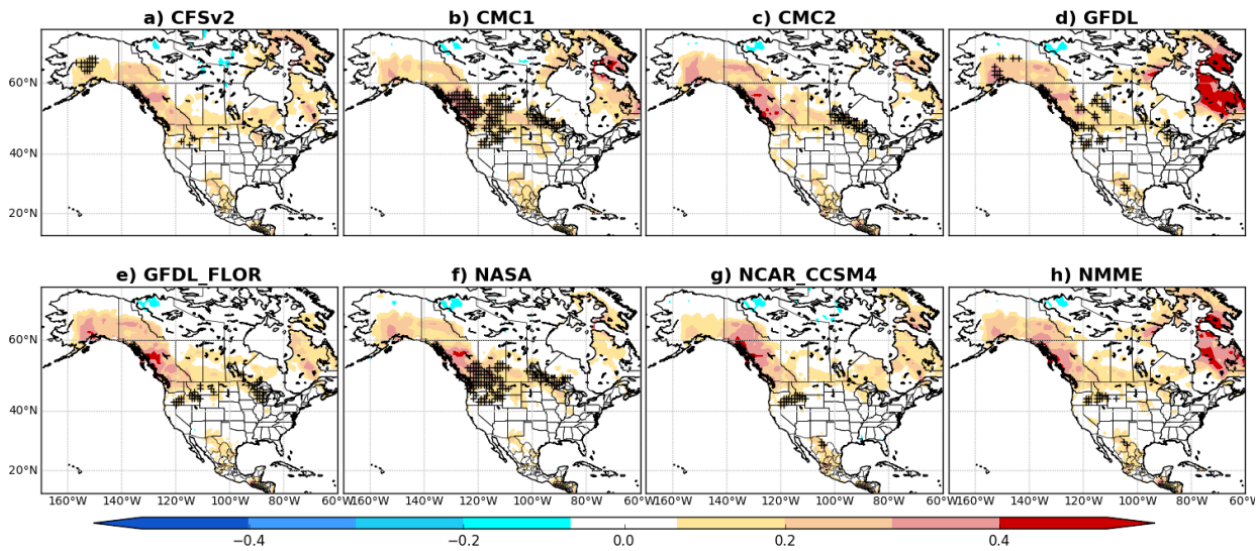


**Fig. 4** Shading indicates Brier skill scores associated with 1-month lead merged CBA forecasts of below normal DJF 2-m temperature for each of the NMME member models and the multi-model mean. Hatching denotes grid cells for which bridging statistically significantly improves forecast skill, where statistical significance is determined using a bootstrap method.

We develop separate bridging and calibration models for each NMME member model of grid point, initial time, and lead; and apply leave-one-year-out cross validation to test the method over the hindcast period. The final step in the CBA method is to merge the bridged and calibrated forecasts using Bayesian model averaging. The resulting merged forecast represents the weighted mean of the calibrated and bridged forecasts.

Finally, we assess probabilistic forecast skill using Brier skill scores and reliability diagrams. For brevity, we only present results for probabilistic forecasts of below normal temperature and precipitation.

### 3. Results

As expected, we find that the fully merged temperature forecasts yield higher Brier skill scores than the fully merged precipitation forecasts (Fig. 2). We additionally find that the calibrated forecasts on average perform better than the bridged forecasts, particularly for temperature (Fig. 3). However, bridging improves DJF temperature forecasts for some regions and seasons. In particular, bridging marginally increases skill over parts of the Midwestern and Northern United States – approximately the same regions where the NMME misrepresents the ENSO-temperature teleconnection pattern.

We apply a bootstrap significance test to determine whether bridging significantly enhances 1-month lead forecast skill of DJF 2-m temperature beyond what skill is achieved through calibration (Fig. 4). Bridging statistically significantly ( $\alpha = 5\%$ ) improves 1-month lead forecast skill over calibration for approximately 10% of North American CMC2 and NASA grids. The degree to which bridging enhances skill varies by NMME member model, season, and lead (not shown). Improvement from bridging is largely confined to winter months, although we find that bridging significantly enhances forecast skill for a small subset ( $\sim 5\%$ ) of grids for CMC1 forecasts of JJA temperature. Overall, these results suggest that bridging is likely a more useful tool for post-processing individual model ensembles rather than multi-model ensembles. Bridging improves forecast skill relative to calibration for fewer than 3% of NMME grids over the hindcast period. Finally, we find that the fully merged CBA forecasts are more statistically reliable than the raw NMME forecasts (Fig. 5), particularly for higher predicted probabilities. Both calibration and bridging yield statistically reliable forecasts, although calibration tends to achieve better reliability in the higher predicted probability bins (not shown).

While these results suggest that the CBaM tool may improve real-time NMME forecast skill, some caveats should be noted. As noted previously, we develop bridging models using a relatively short, 29-year data set. Given this, a small number of extreme ENSO events most strongly influences the statistical relationships. Additionally, we develop separate bridging and calibration models at each grid point and therefore do not take into account spatial correlations among grid points. Future iterations of the tool should account for such spatial autocorrelation, possibly using hierarchical Bayesian modeling. Finally, it remains to be determined how well BJP calibration and bridging models developed from hindcast data will perform using a truly statistically independent real-time forecast. We are currently testing the method to post-process real-time NMME seasonal forecasts of temperature and precipitation to determine its utility as an operational forecast tool. The experimental probabilistic real-time CBaM forecasts can be found at <http://www.cpc.ncep.noaa.gov/products/people/dcollins/cbam/>.

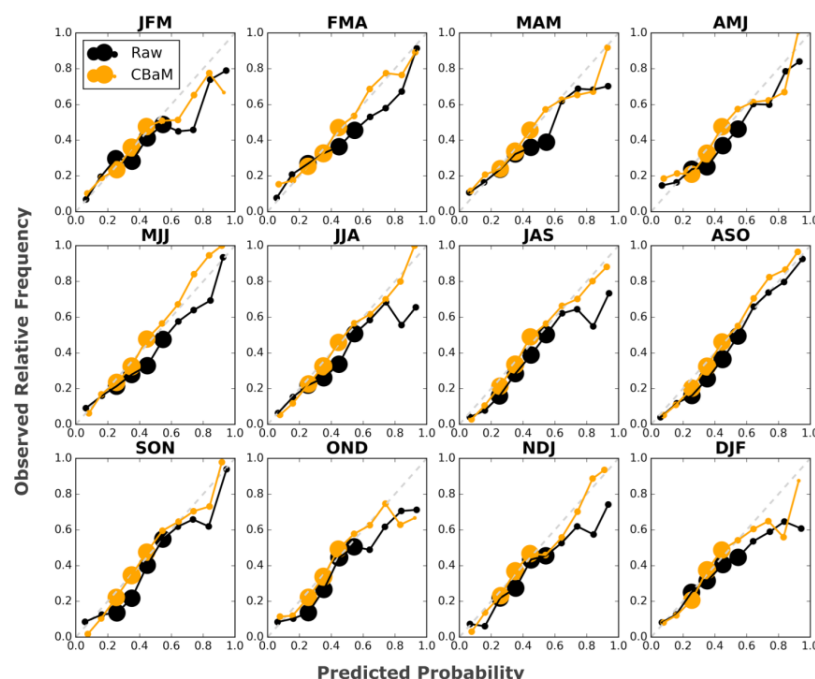


**Fig. 5** Reliability diagrams comparing the statistical reliability of 1-month lead raw (black) versus CBaM (orange) forecasts of 2-m temperature. The CBaM results refer to the fully merged multi-model (NMME) forecast. The raw forecast refers to the multi-model mean forecast, without any bias-correction applied. The horizontal axis denotes the predicted probability while the vertical axis denotes the observed relative frequency. The light gray dashed line corresponds to a perfectly reliable forecast. The size of the plotted circles is proportional to the number of forecast probabilities that fall into a given predicted probability bin.

## References

- Chen, L. C., H. van den Dool, E. Becker, and Q. Zhang, 2017: ENSO precipitation and temperature forecasts in the North American Multimodel Ensemble: Composite analysis and validation. *J. Climate*, **30**, 1103–1125.
- Kirtman, B. P., and Co-authors, 2014: The North American multimodel ensemble: phase-1 seasonal-to-interannual prediction; phase-2 toward developing intraseasonal prediction. *Bulletin of the American Meteorological Society*, **95**, 585–601. doi: <http://dx.doi.org/10.1175/BAMS-D-12-00050.1>
- Schepen, A., Q. J. Wang, and D. E. Robertson, 2014: Seasonal forecasts of Australian rainfall through calibration and bridging of coupled GCM outputs. *Mon. Wea. Rev.*, **142**, 1758–1770.
- Schepen, A., Q. J. Wang, and Y. Everingham, 2016: Calibration, bridging, and merging to improve GCM seasonal temperature forecasts in Australia. *Mon. Wea. Rev.*, **144**, 2421–2441.
- Wang, Q. J., D. E. Robertson, and F. H. S. Chiew (2009), A Bayesian joint probability modeling approach for seasonal forecasting of streamflows at multiple sites, *Water Resour. Res.*, **45**, W05407, doi:10.1029/2008WR007355.

## **Correlation of Regional Sea-level Variability Mechanism, Sub-Mesoscale Dynamics, Climate Variability & Development of Sea-Level Variability Predicting Models (SLVPM)**

Virendra Goswami

*Indian Institute of Technology and Environment and Peace Foundation, New Delhi, India*

### **ABSTRACT**

Lately, researchers in University of Washington, USA and University of Edinburgh found that the pools underneath the glacier, Thwaites, are draining out at an unprecedented rate and emptying themselves (Fig. 1). This unstoppably melting of the glacier into the ocean is mainly because of warmer seawater lapping at its underside. Thwaites is 4000m thick and is considered key to making projections of global sea level rise. Prof. Peter Clark, Oregon State University (OSU), attributed that the Glacier retreat was due to rising levels of carbon dioxide and other greenhouse gases (GHG), as opposed to other types of forces. If this continues, then the most of glaciers would disappear in the next few centuries and the glaciers loss in future will contributing to rising sea levels.

Hence, the present investigation aims to find out the correlation between the rise of GHG level and the sea-level rise vis-à-vis climate variability and can these be controlled through chemical processes, *e.g.* creating the Temperature Absorption Sinks (TAS) to control sea-level rise and unstoppably melting of the glaciers into the ocean mainly because of warmer seawater lapping at its underside and Carbon Absorption Sinks (CAS), GHG Detoxifiers to check the rising levels of carbon dioxide and other GHG by developing the Sea-Level Variability Predicting Models (SLVPM).

Next, an attempt would be made through SLVPM to study the correlation of regional sea-level variability mechanism, sub-mesoscale dynamics, climate variability and its impact on sea-level rise.

Regional variability of the sub-mesoscale dynamics study includes to examine satellite imageries with emphasis on the large scale kinematic and thermodynamic behavior of selected mesoscale convective systems, *e.g.* intense cloud clusters depressions and thunderstorms, to study vertical structure of these system. The values of characteristics, *e.g.* lifetime, distribution, trajectories, size and three dimensional structure, *i.e.*, vertical extent of these systems, would be computed.

Next, the kinematic features of the mesoscale convective systems would be correlated with sea-level variability on time and space scales, at the local, regional and global levels through the extracted sea surface temperature (SSTs) over the grid box, attributing the regional change to natural and anthropogenic radiative forcing agents and to bring out a few optimum values of these to develop (SLVPM)

It would be endeavor to check the melting of glaciers and rise of sea level through Magnetic Refrigeration Techniques (MRT), Magnetic Reactors and harnessing of lunar energy to reduce the temperature at the glaciers and that of sea surface through chemical processes by making use of the correlation of physico-chemical characteristics of catalysts and climate variability as well as through the



**Fig. 1** The Thwaites Glacier part of the West Antarctica Ice Sheet is undergoing accelerated melt along with a number of other glaciers that could see sea levels rise by between 10 and 13 feet. (Graham 2017; photo credit: NASA)

developed Sea-Level Variability Predicting Models (SLVPM).

**References**

Graham, K., 2017: Evidence points to collapse of Pine Island and Thwaites glaciers. *Digital Journal*, Accessed 3 March 2018, <http://www.digitaljournal.com/print/article/508489#ixzz58jkGgtWV>



## APPENDIX

# Photo Gallery

---

42<sup>nd</sup> NOAA Climate  
Diagnostics and  
Prediction Workshop





## **Norman, Oklahoma October 23-26, 2017**

For complete album  
<http://www.nws.noaa.gov/ost/climate/STIP/42CDPW/photos.htm>



**In Session**





## Invited Talks





## **Presentations**



# **Presentations**





## Discussions



Keynote

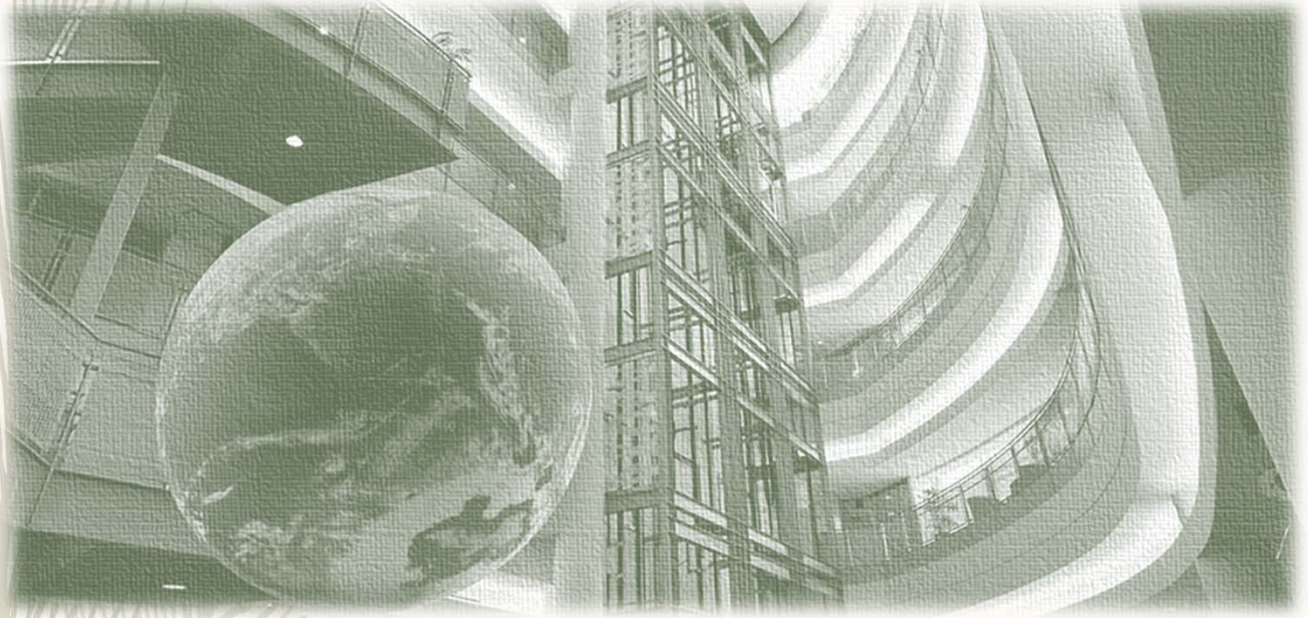






## NWC Tour







# NWS Science and Technology Infusion Climate Bulletin

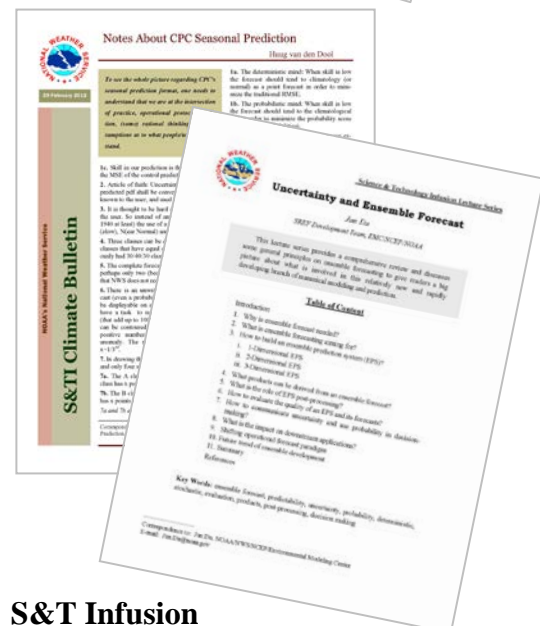
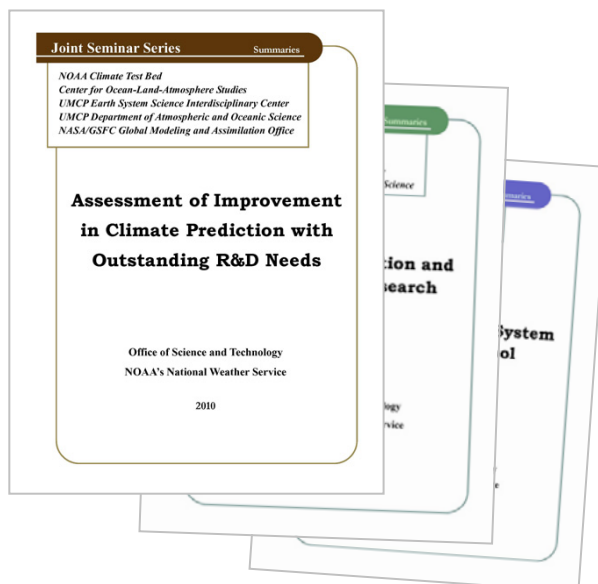
## Featured Special Collections

(<http://www.nws.noaa.gov/ost/climate/STIP/Collections.htm>)

### Climate Prediction Science and Technology Digest



### NOAA Climate Test Bed Joint Seminar Series Extended Summaries Collection Volume



### S&T Infusion Lecture Series & Notes



